Wayne State University Dissertations

January 2021

# Assessing Midbrain Abnormalities In Parkinson's Disease Using Magnetic Resonance Imaging

Kiarash Ghassaban
*Wayne State University*

Follow this and additional works at: https://digitalcommons.wayne.edu/oa_dissertations

Part of the Bioimaging and Biomedical Optics Commons

**ASSESSING MIDBRAIN ABNORMALITIES IN PARKINSON'S DISEASE USING MAGNETIC RESONANCE IMAGING**

by

**KIARASH GHASSABAN**

**DISSERTATION**

Submitted to the Graduate School

of Wayne State University,

Detroit, Michigan

in partial fulfillment of the requirements

for the degree of

**DOCTOR OF PHILOSOPHY**

2021

MAJOR: BIOMEDICAL ENGINEERING

Approved By:

_____
Advisor                                    Date

_____

_____

# DEDICATION

I dedicate this work to my family:

*Javad Ghassaban*

*Shabnam Kordrostami*

*Khashayar Ghassaban*

*Parmida Ghassaban*

# ACKNOWLEDGEMENTS

# TABLE OF CONTENTS

# LIST OF FIGURES

# LIST OF TABLES

# ABBREVIATION LIST

| | |
|---|---|
| AD | Alzheimer's Disease |
| ADC | Analog to Digital Convertor |
| BBB | Blood Brain Barrier |
| BW | Bandwidth |
| CMB | Cerebral Micro-Bleeds |
| CN | Caudate Nucleus |
| CT | Computed Tomography |
| DAT | Dopamine Transporter |
| DGM | Deep Gray Matter |
| DN | Dentate Nucleus |
| EMF | Electromotive Force |
| FA | Flip Angle |
| FID | Free Induction Decay |
| FLAIR | Fluid Attenuation Inversion Recovery |
| GBCA | Gadolinium-Based Contrast Agents |
| GM | Gray Matter |
| GP | Globus Pallidus |
| GRE | Gradient Recalled Echo |
| H&R | Hoehn and Yahr |
| HC | Healthy Control |
| HPF | High Pass Filter |
| ICPMS | Inductively Coupled Plasma Mass Spectrometry |

| | |
|---|---|
| LC | Locus Coeruleus |
| MRI | Magnetic Resonance Imaging |
| MS | Multiple Sclerosis |
| MTC | Magnetization Transfer Contrast |
| NM | Neuromelanin |
| PBP | Parabrachial Pigmented Nucleus |
| PCC | Pearson Correlation Coefficient |
| PD | Parkinson's Disease |
| PET | Positron Emission Tomography |
| PSD | Proton Density |
| PT | Pulvinar Thalamus |
| PUT | Putamen |
| QSM | Quantitative Susceptibility Mapping |
| RBD | Rapid Eye Movement Sleep Bevior Disorder |
| RF | Radiofrequency |
| RII | Regional Iron Analysis |
| RN | Red Nucleus |
| ROC | Receiver Operating Characteristic Curve |
| ROI | Region of Interest |
| RRMS | Relapsing-Remitting Multiple Sclerosis |
| SE | Spin Echo |
| SHARP | Sophisticated Harmonic Artifact Reduction for Phase |
| SN | Substantia Nigra |

| | |
|---|---|
| SNpd | Substantia Nigra Pars Dorsalis |
| SNpr | Substantia Nigra Pars Reticulata |
| SNpr | Substantia Nigra Pars Compacta |
| STAGE | Strategically Acquired Gradient Echo |
| SWI | Susceptibility Weighted Imaging |
| T1W | T1-Weighted |
| T2W | T2-Weighted |
| TBI | Traumatic Brain Injury |
| TE | Echo Time |
| THA | Thalamus |
| TR | Repetition Time |
| tSWI | True SWI |
| UPDRS-III | Unified Parkinson's Disease Rating Scale Part III |
| WM | White Matter |
| XRF | X-Ray Fluorescence |

# Chapter One: Introduction

**Background and Significance**

Parkinson's disease (PD) is one of the fastest growing neurodegenerative disorders in the world and a leading cause of disability. [1] The number of patients with PD was 6.9 million in 2015 and is expected to rise to 14.2 million by 2040. [2] PD is characterized by the classical motor features of parkinsonism with early prominent death of dopaminergic neurons in the substantia nigra (SN). [3] The current diagnostic criteria for clinical PD from the International Parkinson and Movement Disorder Society (MDS) [4] include consideration of ancillary diagnostic tests such as PET imaging which can be used to assess the density of presynaptic dopaminergic terminals within the striatum as a surrogate of SN neurodegeneration. [3] The strength of dopaminergic imaging as a diagnostic biomarker is that it could help differentiate Parkinson's disease from other movement disorders without presynaptic dopaminergic terminal deficiency. [5] However, PET imaging is not widely available, it is expensive, and it uses radioisotopes.

Though still under debate, it is generally believed that neuronal loss and lack of dopamine content in the SN lead to movement disorders in these patients. [6, 7] The loss of neuromelanin in particular has been thought to lead to an increase in iron content in the SN which has been implicated in a number of PD studies. [8-10] In fact, the SN seems to be the only brain structure through which a meaningful relationship with neuronal loss has been consistently found in the literature. [11] Since the onset of PD is generally later and brain iron levels tend to increase as a function of age in deep gray matter (DGM) structures even under normal conditions, [12-14] it is imperative to account for these age–dependent changes as well. [15]

Another alternative qualitative approach that does not measure NM throughout the whole SN but is nonetheless sensitive to the NM in the nigrosome-1 (N1) territory has also been claimed to be a possible means to distinguish between PD subjects and healthy controls (HC) [16-18]. The absence of the N1 sign is a potential marker to the loss of NM as well as an increase in local iron content. [19] However, this approach does not actually measure NM or iron content quantitatively. With that said, the sensitivity and specificity of NM, iron or the N1 may not be sufficient to qualify as diagnostic biomarkers by themselves. [20-22]

On the other hand, however, a clinically reliable, non-invasive biomarker to diagnose PD is still absent. Since MRI is non-invasive, widely available and relatively inexpensive, many researchers have used it to investigate the pathophysiological changes of PD. The most promising biomarker candidates are iron content as seen with susceptibility weighted imaging (SWI) and as measured with R2*, and quantitative susceptibility mapping (QSM) [11] and neuromelanin (NM) content (as measured with NM-MRI) [17]. The literature generally supports the concept that iron content is expected to increase in the pars compacta aspect of the SN at a higher extent in PD patients while NM is expected to decrease [21, 22].

As for the iron deposition, Liu et al. investigated a cohort of 174 healthy adults using QSM with the purpose of assessing the effects of normal aging on the iron levels in seven DGM structures. [12] In addition to their evaluation of mean susceptibility from the entire 3D region covered by each nucleus as a function of age (also known as the global analysis) in the basal ganglia and midbrain, they introduced a new age- and structure-dependent high iron susceptibility-age baseline (also known as the regional analysis). In this technique, age-dependent susceptibility values are chosen from the upper 95% prediction intervals derived from the corresponding global analyses of the normal population. The threshold-dependent high iron (RII) content voxels are then estimated by

having a susceptibility value higher than that specific threshold for a given structure at a given age. [12] The regional analysis appeared to be more robust and sensitive to age-related changes compared against the global analysis. Furthermore, by applying the same methodology, Ghassaban et al. established the global and regional susceptibility-age baselines for the dentate nucleus of the cerebellum as the eighth main DGM structure using 81 healthy adults with a similar age range. [11] Therefore, it is hypothesized that this regional analysis may also be more sensitive in picking up subtler MRI-dependent changes in PD patients as well as possible correlations of these parameters with disease severity.

The NM content also appears to be linked to dopaminergic functions in healthy controls (HCs); positive correlation between dopamine D2 receptor binding and NM accumulation has been observed [23]. In PD patients, however, the loss of NM has been correlated with the loss of dopaminergic neurons in both PET [24] and single photon emission computed tomography (SPECT) studies [25]. It has been shown that the rate of dopaminergic neuronal loss in the SN pars compacta (SNpc) is accelerated for PD patients and 60-80% of neurons may be lost before the manifestation of motor symptoms [26]. The hyperintense signal in the SN associated with in vivo NM-MRI has been shown to correlate with that seen in postmortem measurements [27, 28]. Further, it has been shown that the MRI representation of NM matches that seen in PET and that the intensity of the NM signal in MRI correlates with the dopamine release capacity [24]. High field imaging with tyrosine hydroxylase, a critical indicator of NM production, has also shown a similar spatial match between NM and hydroxylase [27].

In the last few years, NM-MRI has been used in an attempt to diagnose idiopathic PD (IPD) [8, 29-31]  and differentiate it from essential tremor (ET) [32, 33], progressive supra-nuclear palsy (PSP) [34], and multiple system atrophy (MSA) [35] with some success by quantifying the

depigmentation of NM loss. This has been accomplished using magnetization transfer contrast (MTC), [8], NM volume [29, 30], width of the SNpc in the central territory [33, 36] as well as lateral loss of NM volume [31]. It is encouraging that there is a consistent finding that NM volume is significantly reduced in PD patients compared to HCs [10, 29, 34, 37-42]. It is believed that dopaminergic neuronal death in the midbrain is followed by cellular depigmentation leaving behind iron that is then phagocytized and becomes visible in MRI [43]. For this reason, many studies have used iron as measured with R2* or QSM as a means to differentiate PD patients from HCs. [11]

A few prior studies have combined NM and iron measures, but these usually require two different sequences as well as co-registration and interpolation of the data when different resolutions are used [21, 22, 30, 44, 45] and in some cases the use of a NM mask from a template data set. [9] However, the sensitivity and specificity of these individual measures (NM or iron in the SN) may not be good enough for them to qualify as diagnostic biomarkers by themselves [20-22]. Therefore, it is hypothesized that a single MT pulse augmented GRE multi-echo sequence be used that would provide quantitative NM and iron measures simultaneously through which the overlap of NM and SN iron-containing regions is introduced as an additional measure which, in combination with the NM itself, could provide a stronger biomarker to help diagnose and assess the progression of the disease.

Additionally, as another form of potential neuronal loss, idiopathic rapid eye movement (REM) sleep behavior disorder RBD (iRBD) is recognized as the prodromal stage of α-synucleinopathies, particularly PD, with iRBD representing a unique opportunity for potential disease-modifying interventions. [46-48] Similar to PD, previous studies have shown cognitive dysfunction [49, 50] and subtle motor impairment in iRBD patients [51, 52] as well which might be useful in predicting early conversion and the specific type of α-synucleinopathy. With that being said, we hypothesize that

abnormal levels of iron deposition and N1 loss could potentially be correlated with cognitive dysfunction and motor impairment reported in iRBD patients. However, whether global or RII iron accumulation in the cerebral nuclei correlates with cognitive and motor impairment in iRBD patients remains uninvestigated.

Based on the abovementioned background, the following chapters of this dissertation are arranged as the following. Chapter two will discuss the basic concepts of MRI gradient echo magnitude and phase data along with QSM reconstruction and the use of MT pulse for the MTC images. The role of MRI iron quantification and NM visualization in PD pathology will be discussed in detail in chapter three. The next three chapters will build the main body of the dissertation in a retrospective order in terms of PD progression. That is, in chapter four MRI iron quantification will be used to differentiate PD from healthy controls. This will then be followed by chapter five in which a single MT-enabled GRE sequence will be used to quantify iron, evaluate the N1 sign and analyze NM volumetrics simultaneously specifically in PD patients going through the early stages of the disease compared against healthy controls. In chapter six, we take one more step back and evaluate the same criteria in RBD patients to assess the role of brain iron deposition and neuromelanin loss as well as their relationships with cognitive and motor functions as precursor and early biomarkers for PD. Finally, the conclusions and future directions derived from the results of these studies will be discussed in chapter seven.

**Project Aims**

Based on the discussions in the previous section of this chapter, the following summarizes the project specific aims and their corresponding hypotheses:

***Specific Aim 1****:* To assess the global and regional iron deposition in major deep gray matter nuclei of PD patients and healthy controls using QSM and R2* mapping and their correlations with disease severity.

***Hypothesis 1a:*** Substantia nigra will be the only structure consistently showing elevated iron content in PD patients compared to that of healthy controls with the regional analysis being more sensitive in differentiating the two cohorts.

***Hypothesis 1b:*** Patients with more severe clinical scores will tend to develop abnormally elevated iron content in their substantia nigra.

***Specific Aim 2****:* To evaluate the diagnostic accuracy of imaging midbrain NM, N1 and iron simultaneously using a single 3D multi-echo MT augmented GRE sequence in early PD patients and healthy controls.

***Hypothesis 2a:*** The volumetric measurements associated with NM and iron-containing SN will decrease while iron content will increase in the midbrains of PD patients compared to those of age- and sex-matched healthy controls.

***Hypothesis 2b:*** The combination of volumetric measurements including NM and iron-containing SN with the N1 sign and susceptibility-based iron quantification in the SN will provide the highest diagnostic accuracy in early PD.

***Specific Aim 3****:* To investigate volumetrics as well as global and regional high iron content in major deep gray matter nuclei and the N1 loss in the SN of idiopathic RBD patients and their potential correlations with cognitive and motor functions.

*Hypothesis 3a:* Even though not as highly predominant as in PD, some of the RBD patients will show N1 loss as well as higher iron content in the SN.

*Hypothesis 3b:* Iron and volumetric analyses will reveal correlations with cognitive and motor scores in some of the deep gray matter nuclei

## Chapter Two: Basics of MR Gradient Echo, Phase and Magnetic Susceptibility

In this chapter, a review of the basics of magnitude and phase information acquired through a GRE signal is given, followed by the current MRI techniques used to quantify iron deposition as well as visualizing neuromelanin content in the brain.

### MR Signal Acquisition

From the basic physics of a spin (½) particle in an external magnetic field ($\vec{B}$), for a right handed system, the spin precesses around the magnetic field at the Larmor frequency, $\omega$, as given by [53]:

$$\vec{\omega} = -\gamma . \vec{B} \tag{2.1}$$

where $\gamma$ is the gyromagnetic ratio of the particle[1] and $\vec{\omega}$ is the angular frequency. Since the water content makes up a major proportion of the human body components, the proton (present in the ^{1}H hydrogen nucleus with the spin value of +1/2) is the most important source of nuclear interactions of human tissue when exposed to an external magnetic field.

### *Ideal Signal Formation*

In an "isochromat" of spins (i.e., where a microscopic group of many spins are exposed to an approximately constant magnetic field), the sum of magnetic vectors, known as the net magnetization ($\vec{M}$) can be calculated through the Bloch equation [54]:

$$\frac{d\vec{M}}{dt} = \gamma \vec{M} \times B_0 \hat{z} \tag{2.2}$$

---

[1] $\gamma$ is unique for each magnetized particle. For proton, the gyromagnetic ratio is $2.68 \times 10^8$ rad/s/T.

where $B_0$ is the external magnetic field applied along $\vec{z}$, also known as the longitudinal direction. After separating the parallel and perpendicular (transverse) components of the magnetization, equation (2.2) yields:

$$\frac{d\overrightarrow{M_z}}{dt} = 0 \qquad (2.3)$$

$$\frac{d\overrightarrow{M_\perp}}{dt} = \gamma \overrightarrow{M_\perp} \times B_0 \hat{z} \qquad (2.4)$$

Based on equation (2.4), the time-varying $\overrightarrow{M_\perp}$ (or $\overrightarrow{M_{xy}}$) only occurs when the net magnetization has a transverse component, which does not happen under normal conditions. In order to detect the signal originated from the magnetization process, at a given external magnetic field $B_0$, a radiofrequency (RF) pulse "on resonance" with the proton Larmor frequency is applied to the whole spin isochromat, tipping it away from the longitudinal direction and towards the transverse x-y plane. Depending on the degree to which the magnetization is tipped (i.e., "flip angle") the magnitude of $\overrightarrow{M_{xy}}$ is defined. Physically, $\overrightarrow{M_{xy}}$ rotates around $B_0$, inducing a varying flux in a "receive coil" which then creates an electromotive force (EMF) under Faraday's law. The origin of the potentially detectable MR signal is this electrical current created from the EMF, which is then converted to the image format [54]. However, it should be noted that the discussion above holds only under ideal conditions in which there is neither an interaction among the spins nor between the spins and the surrounding "lattice".

### MR Signal Affected by Relaxation Times

Under realistic circumstances, spins interact with each other as well as the lattice. Practically, when our body is put into the magnetic field the spins begin to return to an equilibrium magnetization that takes usually many seconds. At this point, an RF pulse can be applied to create a

transverse magnetization orientation. If the spins are rotated 90º, then the longitudinal magnetization $M_z$ will start to recover toward its equilibrium value along the z axis. The time constant representing this regrowth is called the "spin-lattice relaxation time", also known as T1 [54]. Each tissue has its own T1 which is usually determined by experiment. By taking the T1 effect into consideration, and after applying an RF pulse, equation (2.3) becomes:

$$\frac{dM_z}{dt} = \frac{1}{T1}(M_0 - M_z) \tag{2.5}$$

yielding the following time dependence:

$$M_z(t) = M_z(0)e^{-t/T1} + M_0(1 - e^{-t/T1}) \tag{2.6}$$

The story is quite different for the transverse magnetization. Once there is a transverse component, subtle variations present in the local magnetic field cause the spins to dephase from each other leading to a reduction in $M_{xy}$. The characteristic time during which the transverse magnetization decreases back to its equilibrium level (i.e., $M_{xy} = 0$) is called the "spin-spin relaxation time", also known as T2 [54] (See Figure **2.1**).
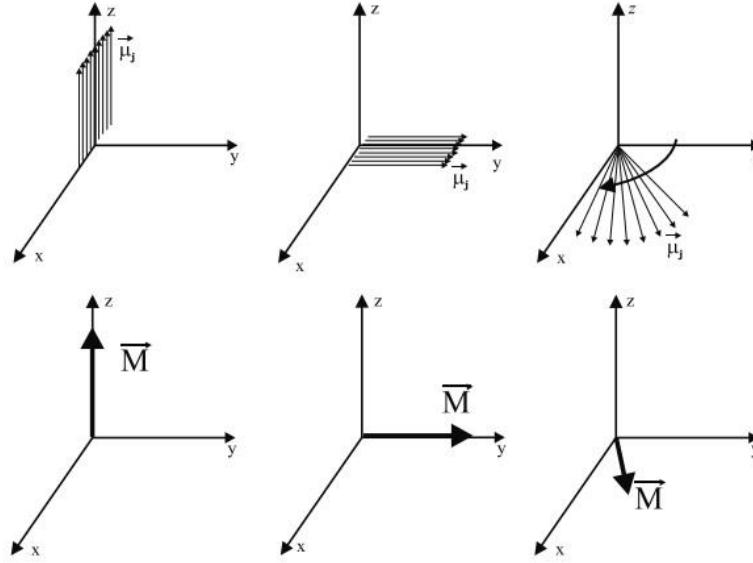
**Figure 2.1** Illustration of the T2 effect on a set of spins. The upper row shows a spin isochromat after being exposed to a 90° RF excitation which is tipped along the y direction and then dephases due to spin-spin interactions. The lower row shows the same effect in the form of the net transverse magnetization. If the T1 effect was also accounted for, the vector $\overrightarrow{M}$ at the bottom right would be shorter.[2]

After taking the T2 effect into account, equation (2.4) becomes:

$$\frac{d\overrightarrow{M_\perp}}{dt} = \gamma \overrightarrow{M_\perp} \times B_0 \hat{z} - \frac{1}{T2} \overrightarrow{M_\perp} \tag{2.7}$$

which after solving leads to:

$$\overrightarrow{M_\perp}(t) = \overrightarrow{M_\perp}(0)e^{-t/T2} \tag{2.8}$$

The time-course representation of equations (2.6) and (2.8) along with the simultaneous combined effect of both T1 growth and T2 decay are shown in Figure **2.2**.

[2] Image taken from 54.        Haacke, E.M., *Magnetic resonance imaging : physical principles and sequence design*. 1999, New York: Wiley. xxvii, 914 p.
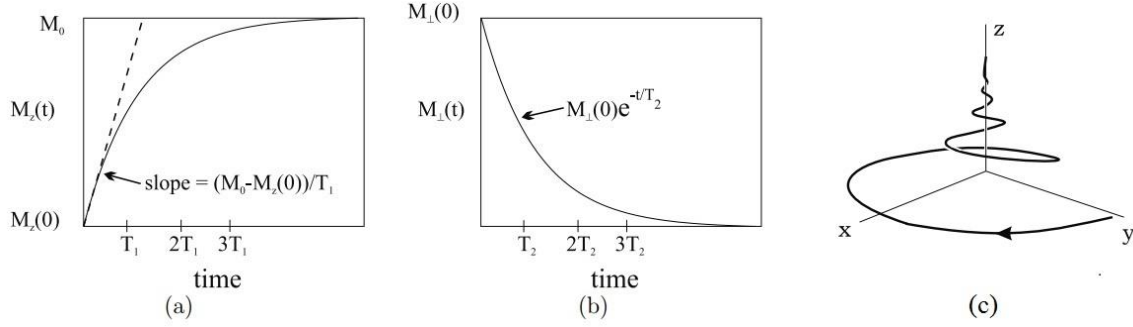
**Figure 2.2** Regrowth of the longitudinal magnetization (a) and decay of the transverse magnetization (b) after applying the RF pulse showing the effects of T1 and T2 relaxation times, respectively. The combined effect is visualized as a typical trajectory of the tip of the magnetization $\overline{M}(t)$ in (c). [54]

The plot in (b) in the figure above shows the profile of the signal in the rotating frame.[3] The actual signal profile, called Free Induction Decay (FID), oscillates with an angular Larmor frequency of $\omega_0$ in the laboratory frame. In other words, the actual detected signal in the laboratory frame is defined as:

$$S(t) = S_0 \, e^{-\frac{t}{T2}} \sin{(\omega_0 t)} \tag{2.9}$$

In addition to the mutual spin-spin interactions which lead to the intrinsic T2 decay, there is another source of dephasing which initially stems from external magnetic field (B₀) global inhomogeneities, known as T2′. As a result, the combined time constant associated with the decay of the transverse magnetization, known as T2*, is defined as:

$$\frac{1}{T2^*} = \frac{1}{T2} + \frac{1}{T2'} \tag{2.10}$$

Defining the relaxation rates to be the inverse of the relaxations times, this expression becomes:

$$R2^* = R2 + R2' \tag{2.11}$$

Therefore, after accounting for the local field heterogeneities, equation (2.9) becomes:

---

[3] This type of reference frame rotates at the Larmor frequency, making the analyses easier for the observer.

$$S(t) = S_0 \, e^{-\frac{t}{T2^*}} \sin{(\omega_0 t)} \qquad\qquad (2.12)$$

Gradient echo imaging, to be discussed next, is sensitive to T2* effects while spin echo imaging (which uses an additional 180º RF pulse) is only sensitive to T2 since it rephases the spins and removes the dephasing effects. It should be noted that in the following sections the signal behavior will be considered in the rotating frame in which the oscillating term is eliminated.

**Gradient Echo Imaging**

With respect to recent technological developments, magnetic field uniformity has reached reasonably minimum levels, making global $B_0$ heterogeneities less problematic and the use of time-consuming SE sequences less common in the clinical setting. Consequently, the 180º pulse can be eliminated and replaced by the usual gradient echo (GRE) rephasing used to create an echo which is subsequently sampled, and Fourier transformed to create an image. Today GRE imaging is commonly used in many clinical applications across all manufacturers. [53]

*GRE Sequence and Signal Acquisition*

In order to differentiate one spin isochromat from another, the object to be imaged is frequency encoded by applying a magnetic field that is different at each location. This can be accomplished by linearly varying the field across the object using, ideally, a constant gradient field. A one-dimensional example is shown in Figure **2.3**. In this implementation, the transverse magnetization is first purposely dephased and then rephased to create an echo at $t = t_4 - \frac{t_4 - t_3}{2}$ $(t' = 0)$. It is important to note that this echo time only refocuses the dephasing effects stemming from applying fields and not those originating from intrinsic spin dephasing at the molecular level [54].
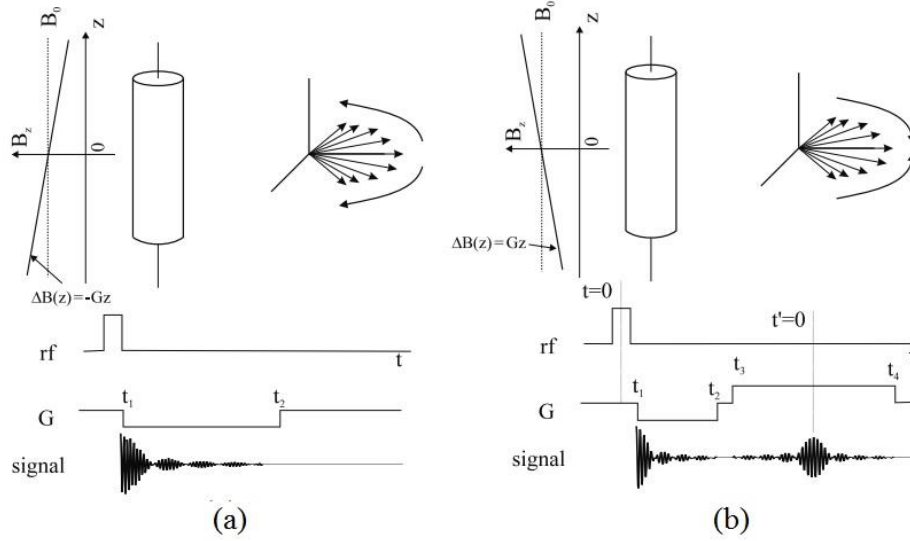
**Figure 2.3** A typical 1D GRE experiment. The cylinders consist of arbitrary spin isochromats located at different locations along the z axis. The dephasing part (a) uses a negative gradient -G and the rephrasing part (b) uses a positive gradient +G with the same amplitude.[4]

For 2D and 3D GRE data acquisition, the concept illustrated in Figure **2.3** should be repeated every TR (i.e., repetition time) and as many times as the number of phase encoding steps. A typical 2D GRE sequence diagram is shown in Figure **2.4**. In 3D experiments, on the other hand, there is another gradient table added to the slice select direction ($G_{z,ss}$).

After allowing the magnetization to reach equilibrium[5], $M_{ze}$ is found to be:

$$M_{ze} = M_0 \frac{1 - e^{-\frac{TR}{T1}}}{1 - cos\theta. e^{-\frac{TR}{T1}}} \qquad (2.13)$$

where $\theta$ is the flip angle and $M_{ze}$ is the equilibrium longitudinal magnetization.

---

[4] Image taken from 54.      Haacke, E.M., *Magnetic resonance imaging : physical principles and sequence design*. 1999, New York: Wiley. xxvii, 914 p..

[5] The number of RF pulses prior to the acquisition can vary from only a few pulses in higher FAs to hundreds of pulses in lower FAs.
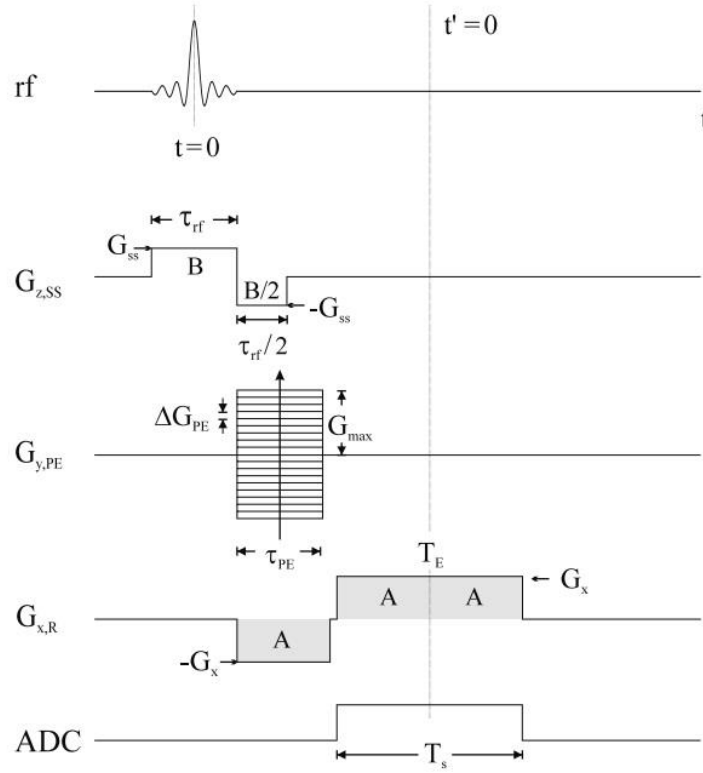
**Figure 2.4** A typical 2D GRE experiment where there is a gradient table along the phase encoding (y in this example) direction. The time difference between the gradient steps $\Delta G_{PE}$ is TR. Analog to Digital Convertor (ADC) is on when the echo time TE occurs during the sampling time along the readout direction (x in this example). [54]

By combining equations (2.8) and

(2.13), the transverse magnetization at the echo time is given by:

$$Signal \propto M_{xy} = M_0 \frac{1 - e^{-\frac{TR}{T1}}}{1 - cos\theta . e^{-\frac{TR}{T1}}} sin\theta . e^{-\frac{TE}{T2^*}} \qquad (2.14)$$

Equation (2.14) is known as the Ernst equation and accounts for the major intrinsic and extrinsic MR tissue properties. This equation tells us that by manipulating the MR parameters, such as flip angle, TE and TR, different contrast mechanisms can be created. For example, at lower flip angles and very short TE, the image is spin-density weighted, while at higher flip angles and short TR relative to T1, the image will be more T1-weighted. A T2* weighted image can be obtained by acquiring the data with longer echo times and lower flip angles (to remove the T1 effect).

## *Complex MR Signal*

From a signal processing perspective, the final image will have both magnitude and phase components. That is, the MR signal acquired by a GRE sequence is complex in nature with the magnitude extracted from equation (2.14) and, for a right handed system, the phase defined as [54]:

$$\phi(\vec{r}, t) = \Delta\omega.t = -\gamma.\Delta B(\vec{r}).t \tag{2.15}$$

where $\Delta B(\vec{r})$ is the field variation experienced by a spin isochromat due to the global and local sources of magnetic field inhomogeneities and chemical shift. Therefore, the complex form of the MR signal can be represented as:

$$S(r, t) = |S(r, t)|e^{i\phi(r,t)} \tag{2.16}$$

which after accounting for equation (2.14) at the echo time can be written as:

$$S(\theta, TE, TR) = S_{xy}(\theta, TE, TR).e^{-i\gamma\Delta B.TE} \tag{2.17}$$

## *Fourier Transform and K-Space*

In order to get an image, the signal picked up by the coil has to be transformed into an image. The time dependent signal is given by a sum over the spin densities, $\rho(\vec{r})$, weighted by the phase induced by the applied gradients:

$$s(t) = \iiint d^3\vec{r}.\rho(\vec{r}).e^{i\phi(\vec{r},t)} = \iiint dxdydz.\rho(x,y,z).e^{i\phi_G(x,y,z,t)} \tag{2.18}$$

where the phase $\phi_G(x, y, z, t)$ is the sum of the accumulated phase in three different directions:

$$\phi_G(\vec{r}, t) = -\gamma\Delta B(\vec{r})t = -\gamma.G(\vec{r}, t)\vec{r}.t \tag{2.19}$$

The total phase imparted to the spins is given by:

$$\phi_G(x,y,z,t) = -\gamma . G(\vec{r},t)\vec{r}.t \tag{2.20}$$

$$= -\gamma \left( \int_0^t dt'\, G_x(t')x + \int_0^t dt'\, G_y(t')y \right.$$

$$\left. + \int_0^t dt'\, G_z(t')z \right) t$$

Therefore, if we define the following "k-space variables" as:

$$k_x(t) = \frac{\gamma}{2\pi} \int_0^t dt'\, G_x(t')x \tag{2.21}$$

$$k_y(t) = \frac{\gamma}{2\pi} \int_0^t dt'\, G_y(t')y \tag{2.22}$$

$$k_z(t) = \frac{\gamma}{2\pi} \int_0^t dt'\, G_z(t')z \tag{2.23}$$

equation (2.18) can be rewritten as:

$$s(k_x,k_y,k_z) = \iiint dx dy dz . \rho(x,y,z). e^{-2\pi i(k_x x + k_y y + k_z z)} \tag{2.24}$$

Equation (2.24) is technically the Fourier transform of the effective spin density. When written as a function of the spatial frequencies, this signal or data is referred to as k-space data.

Figure **2.5** shows how k-space is filled following every step illustrated in Figure **2.4**. Assuming that the starting point is $k_x=k_y=0$, after applying each RF pulse at the corresponding constant phase encoding gradient ($G_{PE}$) the readout gradient moves the k-space point from $-k_{R,max}$ to $+k_{R,max}$ which then creates a line of k-space. After the phase encoding gradient increases by one step ($\Delta G_{PE}$) the same process happens again but this time the simultaneous change of $k_x$ and $k_y$ sweeps over one line higher in k-space. This process continues until the desired k-space is filled with complex sampled points. By applying the inverse Fourier transform, original magnitude and phase information are then extracted in the spatial domain. That reconstructed signal is then represented by equation (2.17).
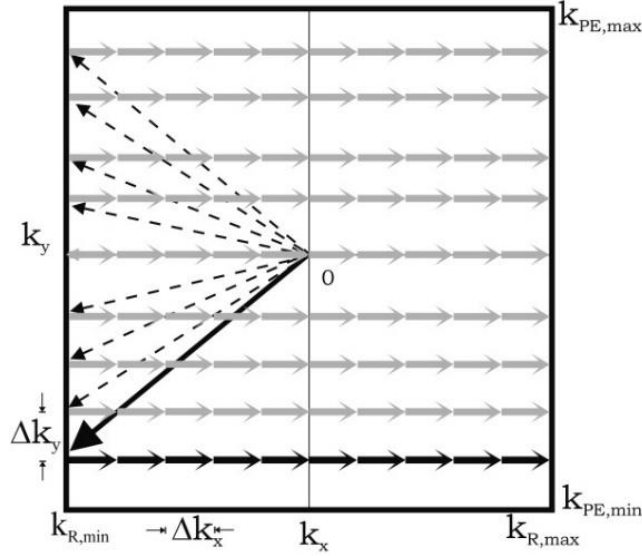
**Figure 2.5** A schematic of a 2D k-space filling trajectory corresponding to Figure **2.4**. Due to the simultaneous changes of readout and phase encoding gradients as a function of time, k-space filling follows a diagonal trajectory when ΔGPE occurs.

### *Susceptibility Weighted Imaging*

Susceptibility Weighted Imaging (SWI) uses a special type of GRE sequence. In order to minimize the phase-dependent artifacts due to blood flow effects, SWI is usually fully flow-compensated in all directions. [54] The logic behind incorporating flow compensation is the fact that we are interested in measuring the phase caused by local field variations, not other unrelated factors.

As in all 3D GRE sequences, complex data are acquired yielding magnitude and phase images. However, in order to reconstruct the final susceptibility-weighted image, further steps are applied to the original phase image to remove phase wraps and low spatial frequency components. From this processed image, a mask is created which is then multiplied into the original magnitude image to enhance the visualization of local susceptibility changes. The post-processing pipeline of SWI image reconstruction is not the main scope of this dissertation. Nevertheless, the use of the original SWI phase image, which plays a key role in QSM, will be discussed in the following sections.

**Magnetic Susceptibility**

Magnetic susceptibility ($\chi$) is an intrinsic property of a tissue which manifests its tendency towards being magnetized when exposed to an external magnetic field. Magnetic properties of a typical substance can be characterized by three different categories; paramagnetism with positive susceptibility ($\chi > 0$) whose magnetic moments align parallel to the external field, diamagnetism with negative susceptibility ($\chi < 0$) whose magnetic moments align anti-parallel to the main field, and ferromagnetism with very high positive susceptibility ($\chi \gg 1$). Iron and calcium are two common paramagnetic and diamagnetic substances, respectively, present abundantly in the human body. However, to date, ferromagnetism has not been reported in living tissues in significant amounts. [53]

A homogeneous external constant magnetic field can be defined as:

$$\vec{B_0} = \mu_0 \vec{H} \tag{2.25}$$

where $\vec{H}$ is the vector form of the magnetic field intensity (Ampere/meter) and $\mu_0$ is the absolute permeability of free space ($4\pi \times 10^{-7}$ Tm/A). When an external static field ($B_0$) interacts with an object, it induces a magnetization vector ($\vec{M}$) inside the object creating a new total field given by:

$$\vec{B} = \mu_0 (\vec{H} + \vec{M}) \tag{2.26}$$

Practically, the induced magnetization (or permanent in case of ferromagnetism) is related to the magnetic field intensity through the magnetic susceptibility:

$$\vec{M} = \chi \vec{H} \tag{2.27}$$

Therefore, using equation (2.27), equation (2.26) can be rewritten as:

$$\vec{B} = \mu_0 \left(\frac{1+\chi}{\chi}\right)\vec{M} \tag{2.28}$$

Assuming that $\chi \ll 1$, then equation (2.28) can be simplified to:

$$\vec{B} = \frac{\mu_0}{\chi}\vec{M} \tag{2.29}$$

or

$$\vec{M} = \frac{1}{\mu_0}\chi\vec{B} \tag{2.30}$$

Equations (2.29) and (2.30) show the relationship between the induced magnetization and perturbed magnetic field inside the exposed object. A magnetic source will produce fields outside itself that depend on the object's geometry and orientation. For example, in the human body, venous blood vessels (which can be modeled as cylinders) and microbleeds (which can be modeled as spheres) will create magnetic fields outside themselves. [53] It should be noted, however, that the susceptibility values reported in the equations above are the absolute values in vacuum. In the case of veins and microbleeds, the measured values will represent the relative susceptibility ($\Delta\chi$) compared to the tissue in which they are embedded. Since the brain is mostly water it is predominantly diamagnetic relative to air.

**Phase Signal and Susceptibility Mapping**

*Phase Image Processing*

Based on equation (2.15), the phase value at echo time TE can be rewritten as:

$$\phi(\vec{r}) = -\gamma.\Delta B(\vec{r}).TE \tag{2.31}$$

Basically, there are two different sources of field variation: first, macroscopic or global sources such as geometric orientation of the structures (e.g. air-tissue and air-bone interface) and external field inhomogeneities. Second, microscopic or local sources of variation which are in the form of

chemical shift and internal susceptibility sources (such as iron in the form of ferritin). Overall, the total field change is made up of all these contributions:

$$\Delta B_{Total} = \Delta B_{External\ Field} + \Delta B_{Chemical\ Shift} \tag{2.32}$$
$$+ \Delta B_{Global\ Geometry} + \Delta B_{Susceptibility}$$

The chemical shift term, $\Delta B_{Chemical\ Shift}$, is a point like effect, while the local susceptibility sources, $\Delta B_{Susceptibility}$, depend on their shape and orientation.[6] Due to the fact that the local susceptibility sources are the target of interest, the confounding external sources need to be removed.

One of the problematic issues present in the original phase images is "phase aliasing". This phenomenon occurs because the phase is limited to [-π π) range. As a result, each value equal to or higher than π wraps back to –π and, accordingly, any phase value lower than -π wraps back to less than π. The actual phase value can be calculated as:

$$\phi_{True}(\vec{r}) = \phi_{Measured}(\vec{r}) + 2\pi . n(\vec{r}) \tag{2.33}$$

where $n(\vec{r})$ is the number of times the pixel-wise phase value has been aliased. Since background field variations have comparatively low spatial frequency, applying a high-pass spatial filter (HPF) is a reliable and robust method to minimize these background field effects inside the brain (although not as effective at the edges of the brain). [55]

In a typical homodyne high-pass filter, a Hanning window is located at the center of the k-space and depending on the filter size, only collects low spatial frequency information. As shown in equation (2.34) and Figure **2.6**, a complex division of the original reconstructed image ($\hat{\rho}$) by the truncated filtered image will then output a homodyne high-pass filtered phase image. [56]

---

[6] In this dissertation, since the focus is on the brain tissue, the local field variation is mostly dominated by the susceptibility distribution.

$$arg(\hat{\rho}_{HighPass}) = arg\left(\frac{\hat{\rho}}{\hat{\rho}_{LowPass}}\right) \tag{2.34}$$
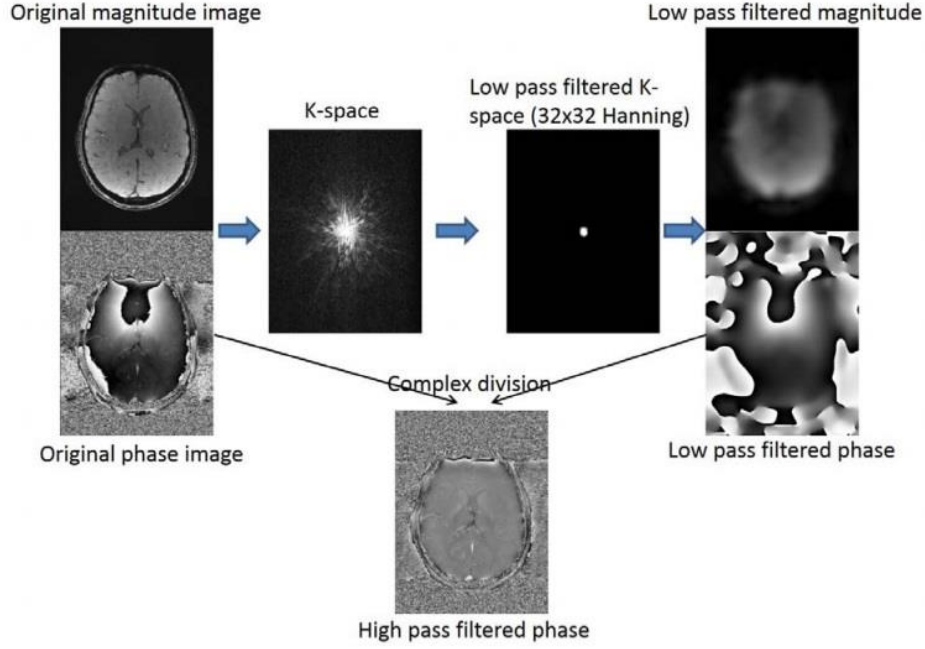


**Figure 2.6** General pipeline of a homodyne high-pass filter.

One of the most important advantages of high-pass filtering is its high execution speed and the fact that it does not require any phase unwrapping steps, making it a suitable choice in both research and clinical settings. However, using a bigger HPF window size (e.g., $128 \times 128$) also removes useful intermediate spatial information in intermediate sized structures underestimating the contribution of the signal itself. For this reason, other background field removal techniques such as variable high-pass filtering (vHPF) [57] and Sophisticated Harmonic Artifact Reduction for Phase data (SHARP) [58] have been suggested for susceptibility quantification purposes.

*Quantitative Susceptibility Mapping*

Assuming that the external static field is along the z-axis, for a right-handed system equation (2.31) can be rewritten as:

$$\phi(\vec{r}) = -\gamma . \Delta B_z(\vec{r}) . TE \tag{2.35}$$

where $\Delta B_z(\vec{r})$ can be derived via [57]:

$$\Delta B_z(\vec{r}) = \frac{\mu_0}{4\pi} \iiint d^3 r' [\frac{3M_z(\vec{r'})(z-z')^2}{|\vec{r}-\vec{r'}|^5} - \frac{M_z(\vec{r'})}{|\vec{r}-\vec{r'}|^3}] \tag{2.36}$$

This expression can be reformulated into a convolution:

$$\Delta B_z(\vec{r}) = \mu_0 M_z(\vec{r}) * G(\vec{r}) \tag{2.37}$$

where $G(\vec{r})$ is called the Green's function and is given by:

$$G(\vec{r}) = \frac{1}{4\pi} \frac{3cos^2\theta - 1}{r^3} \tag{2.38}$$

Here, $\theta$ is the angle between the position vector $\vec{r}$ and the external field direction $\vec{z}$. By incorporating equations (2.29) and (2.37) we can modify equation (2.37) to:

$$\Delta B_z(\vec{r}) = B_0 \chi(\vec{r}) * G(\vec{r}) \tag{2.39}$$

If the susceptibility distribution is known, then equation (2.39) can be used to predict the local changes in magnetic field. This is known as the "forward modeling process".

Practically, it is the phase information that is available and so an inverse process must be used to determine $\chi(\vec{r})$. This can be accomplished by taking the Fourier transform of equation (2.39) yielding:

$$\Delta B_z(\vec{k}) = B_0 . \{\chi(\vec{k}) . G(\vec{k})\} \tag{2.40}$$

and hence:

$$\chi(\vec{k}) = \frac{\Delta B_z(\vec{k}) . G^{-1}(\vec{k})}{B_0} \tag{2.41}$$

The Fourier transform of the Green's function is given by [57]:

$$G(\vec{k}) = \begin{cases} \dfrac{1}{3} - \dfrac{k_z^2}{k^2}, & k \neq 0 \\ 0 & k = 0 \end{cases} \qquad (2.42)$$

where $k^2 = k_x^2 + k_y^2 + k_z^2$ .

Finally, using the available phase information as a representation of the local field changes, the susceptibility distribution in the image domain can be found from:

$$\chi(\vec{r}) = -\frac{FT^{-1}\left(\phi(\vec{k}).G^{-1}(\vec{k})\right)}{\gamma.B_0.TE} \qquad (2.43)$$

A schematic diagram of this quantitative susceptibility mapping (QSM) process is shown in Figure **2.7**. It should be noted that brain masks are not a necessary part of the algorithm but using them improves the susceptibility map by removing streaking artifacts that can be caused by sharp edged parts of the brain if they are not removed.
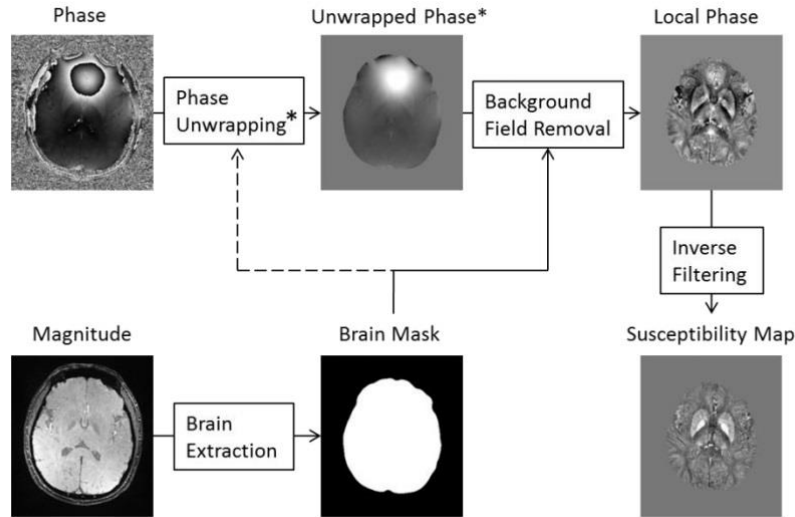


**Figure 2.7** Schematic diagram of general QSM post-processing algorithm. Involvement of the phase unwrapping step depends on the background removal method. Brain extraction step is not mandatory but enhances reconstruction speed and accuracy.[7]

---

[7] Image taken from 56.     Liu, S., *Technical Improvements in Quantitative Susceptibility Mapping*, in *School of Biomedical Engineering*. 2014, McMaster University. with permission.

On the other hand, as seen in equation (2.44), $G^{-1}(\vec{k})$ has zeroes along a conical shape in k-space points rendering the inverse problem ill-posed. A variety of methods have been used to try and overcome these limitations, but most of them have some type of remnant streaking artifacts that corrupt the susceptibility map [59].

## Chapter Three: Iron and Neuromelanin as Seen with MRI

### Neuromelanin in the Brain

*Neuromelanin Physiology*

Neuromelanin (NM), the neuronal version of melanin, is a dark pigment found in the brain that is naturally produced through oxidation of amino acids followed by a polymerization process. NM is believed to in be present in large quantities in catecholaminergic cells of the substantia nigra (SN) pars compacta of the midbrain and locus coeruleus (LC), giving a dark color to these structures. [25] Even one hundred years ago, it was believed that the NM pigment loss in the substantia nigra was associated with PD. [60] This loss has been shown to originate from the dopaminergic neurons in the SN and the noradrenergic neurons of the LC. [61]

Unlike melanin that uses a group of special cells, known as melanocytes (which is almost not present in the SN), NM takes advantage of a different synthetic process, that is, the conversion of norepinephrine. Some types of catecholamines in the cytosol and especially dopamine through oxidative processes are responsible for its dark color as well as NM being an electron-dense pigment. [62] Playing a very important role in both behavioral and physical functions, dopamine is a neurotransmitter (i.e., one of the chemicals responsible for transmitting signals between the nerve cells of the brain) very few of which are produced by the organelles in the brain. Dopaminergic cell groups are collections of neurons in the central nervous system that synthesize dopamine. [26] The NM pigmentation of these organelles appears to be acting as a protector for these neurons under healthy conditions as excessive amounts of dopamine content in the cytosol may induce cell damage

(through reactive types of oxygen) ultimately leading to neuronal death. [63] Sulzer et al. further addresses the synthetic process of NM and defines it as an insoluble pigment stemming from dopamine derived quinones that are present in autophagic lysosomes along with lipid bodies and other soluble proteins. [64] The melanic component of the NM chemical structure is bound to cross-β-sheet peptides making them a major part of the lipid bodies found within the organelles containing NM. [43] While playing a neuroprotective role through removing unnecessary cytosolic dopamine in the midbrain, NM tends to bind high levels of metals and particularly iron forming a paramagnetic NM-iron complex which is crucial for MR signal detection [43] which will be discussed in the following sub-sections.

### *Neuromelanin Interactions with Iron*

As discussed previously, metal ions (e.g., iron, copper and zinc) can be chelated by the NM pigment. In addition to making the NM structure a candidate for MR detection, these metals can contribute to the catecholamine oxidation in the NM synthesis process during the early stages while remaining bound to NM-containing auto-lysosomal organelles. [65] Iron has been seen to be substantially the most abundant metal present in pigmented dopaminergic neurons in the SN. [66] In other words, research shows that under healthy conditions the iron concentration in the SN can vary significantly from 0.1 µg/mg to 6 µg/mg in SN tissue and NM-pigmented intraneuronal content [67] while this value could be as high as 11 µg/mg in an isolated NM pigment. [68] With that being said, these iron measurements suggest that the intraneuronal NM content is not fully saturated and is capable of chelating more iron. It should be noted that this is not necessarily the case for LC. That is, as opposed to SN, the iron concentration of NM pigment isolated from LC is approximately 16% of that measured from NM isolated from SN, most likely due to the fact that the NM content in the LC tends to bind more copper rather than iron to help with norepinephrine synthesis. [67]

Generally speaking, iron complexes in the human body are mostly in the form of $Fe^{2+}$ (ferrous) or $Fe^{3+}$ (ferric) that are chelated by smaller size molecules such as ATP and especially proteins including ferritin, hemoglobin and transferrin. [62, 69] Iron is believed to be a key cofactor in dopamine synthesis in the SN while, as mentioned earlier, copper appears to play the same role in the norepinephrine system in the LC. [43] A more in-depth discussion regarding different forms of iron is given below.

Even though reactive ferric iron content can be seen in non-NM pigmented neurons in a healthy SN, this type of iron deposition is undetectable in pigmented neurons of the SN, most likely due to the efficient sequestration of NM. On the other hand, although the SN is a host to significant amounts of reactive iron content, these iron depositions are almost undetectable in the LC due to the lower levels of total iron content; the synthetic process of NM binding to reactive iron is believed to block the redox activity for the iron to avoid neurotoxicity. [67] However, it is of vital importance to know that even though the presence of NM-containing organelles may be a neuroprotective process, once neuronal death occurs the iron previously bound to NM could turn into extracellular iron and potentially cause toxicity through activating microglia which may then lead to tissue inflammation. [70] In the following sections a more detailed review of different forms of iron and how to visualize and quantify its MR-detectible content will be given.

### *Neuromelanin-Sensitive MRI*

Over the past decade, the ultimate goal of NM-sensitive MRI (NM-MRI) research has been predominantly focused on improving the signal from protons associated with NM while increasing the contrast between NM against the surrounding background tissue. Among some of the early studies in this area, Sasaki et al. were the first group to have successfully implemented an in vivo

visualization of the NM content in the SN and LC using MRI. [71] In this early work, they utilized a T1-weighted multi-slice acquisition taking advantage of relatively short duration turbo/fast spin echo (TSE/FSE) sequence and concluded that NM-dependent MR signal is significantly more visible on the 3T magnet compared to that of 1.5T. Unsurprisingly, they also noted T1 shortening effects due to the presence of metal elements (i.e., mostly iron in SN and copper in LC) associated with the MR signal coming from NM-containing voxels. [71] Since the advent of NM-MRI over a decade ago, a few other T1W TSE-based studies have investigated the NM content in the SN and LC of healthy subjects as well as neurodegenerative conditions where NM depigmentation may occur, especially in PD. [37, 39, 42, 71, 72]

On the other hand, a phenomenon known as magnetization transfer (MT) has caught a lot of attention among researchers aiming for suppression of tissues with high macromolecular content and hence an improved contrast of gray matter to white matter. MT is currently thought to be the primary source of NM-MRI contrast derived from applying MT preparation pulses prior to the actual imaging sequence. [73] By definition, MT is usually referred to a process by which the macromolecules and the water molecules they interact with inside the "bound pool" exchange magnetization with the protons that belong to the "free pool". A magnetization transfer contrast (MTC) can then be created through applying specially designed MT RF pulses prior to the imaging pulse sequence. Nevertheless, in order to avoid frequency interference with the subsequent pulses used for actual free pool spin excitation, the MT pulses are usually followed by spoiling gradients. Upon applying the MT pulse, the bound pool gets excited which then leads to pre-saturation of the MR signal detected from macromolecule-containing tissue. [74] It should be noted, however, that depending on the degree to which these pools are coupled some of the spin isochromats may become partially saturated (i.e., direct saturation) as well through the transfer of energy applied to the bound

water pool over to the free water pool. In other words, when using routine RF pulses to image a given tissue, minor signal reduction may occur due to a secondary MT effect in the free water pool and that is something that should be taken into consideration when interpreting the MR signal. [75]

The frequency at which the MT pulse is applied can be challenging. A study done by Ramani et al. investigated the MT spectrum through which images were acquired at multiple RF offsets shifted from the free water center frequency (i.e., Larmor frequency) and fitted a model to measure MT exchange levels, bound to free pool ratio as well as transverse and longitudinal relaxation measurements associated with each pool. [76] At lower frequency offsets (ranging from a few hundred to a few thousand hertz shifted from the Larmor frequency) the MT pulse will partially saturate the free pool protons as well which means that the final observed signal is attenuated due to a combination of both MT and direct saturation effects. Even though off-resonance MT pulses are commonly used for NM-MRI applications, special binomial or multinomial on-resonance pulses inducing similar MT effects (only in the bound pool since the applied MT pulse in this case has the same frequency as the free pool) can also be used depending on the commercial manufacturer and RF coil hardware design.

As mentioned earlier, paramagnetic substances such as iron and copper are known to cause shortening of relaxation times; this is true in both free protons and protons restricted by macromolecules which consequently results in reduced MT effects in samples in which paramagnetic ions are present. With that said, one can argue that the presence of iron affects the MT spectrum. While the main iron protein in the SN is known to be ferritin which usually shows relatively low paramagnetic characteristics, the dominant iron storage in pigmented dopaminergic neurons of the SN is the NM-iron complex which are highly paramagnetic. The reason for this difference is that the chelating groups in the NM-iron complex are chemical compounds (catechols)

carrying a stable free radical while the chelating groups in ferritin protein are mainly amino acids. Additionally, the NM-iron complex also hosts aliphatic chain compounds that are believed to further impact the MT-induced energy exchange between macromolecules and free water protons that are absent in ferritin. [77]

When using NM-MRI the SN pars compacta (SNpc) shows the highest signal intensity compared to the surrounding tissue due to higher levels of NM pigmented dopaminergic neurons compared to that of the SN pars reticulata (SNpr) which is rich in iron but has less NM-iron complex. [73] Needless to say, due to lack of NM content, other iron-rich deep gray matter structures such as globus pallidus, putamen and caudate nucleus do not show as high signal intensity on NM-MRI images. On the other hand, it has been confirmed that T1 and T2 shortening effects are both significantly higher in melanin-iron complexes compared to those of iron-free melanin or iron by itself. [78] The chemical structure of NM-iron complex causes far more dominant T1 shortening effect compared to that of T2 which further improves the contrast between SNpc and the surrounding gray matter tissue. Therefore, one can conclude that the NM-MRI contrast seen in SNpc is due to a combination of T1 and MT effects put together. [78]

**Quantifying Cerebral Iron Content using MRI**

Iron has long been known for playing a key role in a variety of brain physiologic interactions such as brain metabolism, neuronal maturation, dopamine production, myelin generation, electron and oxygen transport [79, 80] making it the most important transition metal present in the human brain. Additionally, brain iron levels have been seen to correlate with normal aging which could also explain some of the pathophysiological effects in Alzheimer's Disease (AD) [81], PD [82], and Multiple Sclerosis (MS). [83] According to the literature, iron deficiency is also a sign of some other disorders such as Attention Deficit Hyperactivity Disorder (ADHD) [84] and neurodegeneration in

general. [85] On the other hand, living organisms in the human body apply different methods to keep the iron homeostasis level and prevent iron overload or deficiency [86].

### *Different Forms of Iron*

Basically, there are two general categories of iron forms present in the human body; almost 70% of that is in the form of heme-iron (i.e., hemoglobin which is responsible for oxygen transport) while 30% is in the form of non-heme iron (e.g., deposited in the organs, structures, proteins etc.). [13, 87] As the name of "transitional metal" suggests, iron is mostly in the form of Ferric ($Fe^{3+}$) or Ferrous ($Fe^{2+}$) with ferric being comparatively more stable leading to its higher proportion in the human body.

Iron is usually stored in an ubiquitous soluble protein, ferritin, which is naturally produced by living organisms in the body. The major function of ferritin is to make excess iron accumulate in its subunits thereby keeping the iron homeostasis level from changing. Ferritin is a fairy large spherical molecule which consists of 24 sub-units and can store up to 4500 atoms of iron in its central hollow part. (see Figure **3.1** below).
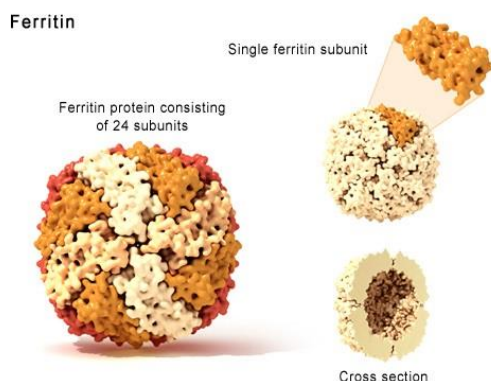


**Figure 3.1** Ferritin protein. The hollow section (mineral core) of the molecule can store up to 4500 iron atoms.

Hemosiderin is another form of iron storage protein; unlike ferritin, hemosiderin is an insoluble molecule which is known to be a fairly immediate product of the ferritin denaturation process. This protein can be found in white blood cells and has been seen to be present in comparatively large proportions in diseased brains associated with cerebral hemorrhages. [88] Stroke [89] and Traumatic Brain Injury (TBI) [90] often show the presence of hemosiderin associated with cerebral hemorrhage.

The last type of the normal non-heme iron proteins is called transferrin. As the name suggests, the major role of this molecule is to deliver iron and iron-related products to different parts of the body. Specifically in the brain, its responsibility is to deliver iron to the brain through the blood brain barrier (BBB). [87, 91] However, since transferrin binds only two iron atoms, the effect of iron on this molecule is not enough to cause considerable magnetic field variation which makes it practically undetectable via MR methods.

From a distribution standpoint, different types of non-heme iron have been shown to be heterogeneously distributed in different parts of the brain. [87] Histochemical research has reported both iron atoms (mostly $Fe^{3+}$) and ferritin molecules to be almost equally distributed in gray matter and white matter, while transferrin showed more notable presence in the white matter. [92] However, in deep gray matter structures, ferritin appears to be the dominant type of iron and shows spatially and temporally variable levels with the highest average values being in the Globus Pallidus and the highest age-dependency rate in the Putamen. Moreover, as reported by a well-known study by Hallgren and Sourander, the highest concentration of non-heme iron content in the cortical regions was found in the motor cortex followed by occipital cortex and sensory cortex. [13]

### *Iron in the Aging Brain*

Iron deposition in the brain as a function of normal aging has been investigated for a long time. Back in the 1950s, from a cadaver brain study, Hallgren and Sourander showed that the brain iron levels change in different parts of the brain as a function of age generally with very low values in infants, followed by an almost exponential increase in the first two decades and leveling off or a linear trend afterwards. [13] These findings have been validated in other studies using in vivo MR techniques in which the same conclusions have been drawn [93-95]. For instance, deep gray matter nuclei showed different exponential and linear trends of iron deposition as a function of age; in a study done by Li et al., some structures such as the putamen, dentate nucleus, and caudate nucleus have been reported to show an almost linear iron-age increasing behavior across the lifespan, while other nuclei such as the globus pallidus, red nucleus, and substantia nigra revealed an exponential growth pattern with higher increase rate in the first two decades followed by an almost constant levels of iron in subsequent decades. [94] However, by using a novel method called regional high iron content analysis, there are also some new subtle susceptibility-age trends revealed that were not investigated in previous studies. [12] Generally speaking, basal ganglia, midbrain and cerebellum nuclei tend to have higher levels of iron concentration in the elderly, while the thalamic regions and cortical white matter are believed to have more iron storage in younger people. [96] Although iron presence is believed to be mostly dominated by deep gray matter nuclei, a whole-brain study has shown that in addition to these regions, frontal lobes also tend to build up excessive iron content as a function of age. [97]

Several MRI techniques are available for quantifying in vivo iron content, including various methods based on mapping T2, T2*, T2′, phase and magnetic susceptibility of the tissue. [54, 98, 99]

The optimal technique for a given clinical application is dependent on the amount or concentration of iron.

### *Determining T2, T2\* and T2′*

As discussed earlier in this chapter, the transverse relaxation time, T2, can be determined using data collected with a multi-echo, spin echo sequence or multiple single-echo spin echo sequences, [100] by modeling the signal at different echo times (TEs) as:

$$S(TE) = \rho_0 e^{-TE/T2} \tag{3.1}$$

where $\rho_0$ is the effective spin density. Similarly, T2\* can be determined using data collected with a multi-echo gradient echo sequence, using the same exponential decay model except that T2 is replaced with T2\* in the equation above. However, when multiple types of tissues with different T2 or T2\* values are present in the same pixel, more complex models such as a bi-exponential model may be required. T2′ is derived via $\frac{1}{T2^*} = \frac{1}{T2} + \frac{1}{T2'}$ (or R2\* = R2 + R2′) and can be obtained by calculating the difference between R2\* and R2. This can be done by either estimating T2 and T2\* using two separate sequences or by using sequences such as gradient echo sampling of the free induction decay and echo (GESFIDE) or gradient echo sampling of a spin echo (GESSE) to obtain T2 and T2′ simultaneously. [101, 102]

However, to do a good job in estimating T2, T2\* and T2′, the gradient echo sequence must be run with a high enough resolution, low enough echo time and high enough bandwidth (BW) to minimize dephasing and geometric distortion. [103] Estimating T2′ can be done through the GESFIDE sequence along with T2, T2\* and SWI. Once R2′ is measured, the local susceptibility due to sources such as iron, calcium or blood can be found if the volume fraction of that substance is known via:

$$R2' = \kappa\lambda\gamma\Delta\chi B_0 \qquad\qquad (3.2)$$

where κ is 0.42, λ is the volume fraction, $\gamma$ is the gyromagnetic ratio, and $\Delta\chi$ is the change in local susceptibility.[101] If the source of susceptibility change is capillary blood, then the hematocrit and the level of deoxyhemoglobin would be required to estimate the blood's susceptibility.

*Determining phase*

The phase contains key information about the field variations inside the tissue, that is the changes that occur from a perfectly homogeneous field caused either by an imperfect field or by changes in tissue susceptibility. [57, 102] The phase from a gradient-echo sequence can be written as:

$$\phi(TE) = \gamma\Delta B \cdot TE + \phi_0 \qquad\qquad (3.3)$$

for a left-handed system, where $\Delta B$ is the field variation and the offset $\phi_0$ is related to coil-sensitivity and tissue conductivity. [54] At a given echo time, the more the iron concentration, the higher the local field variation and the more rapidly the phase accumulates. In theory, iron concentration can be quantified using local phase information. [104] Practically, when imaging the human body, the field variation $\Delta B$ can be considered as a combination of the global field variation induced by the air-tissue interfaces and the local field variations induced by tissue susceptibility changes. Usually, the background field components should be removed before the phase images can be used for iron quantification. This is done by using various background field removal algorithms, [105-107] including high-pass filtering, [108] methods based on the spherical mean value properties of harmonic functions, [58] as well as solving the background field removal as a Laplacian boundary value problem. [109] The advantages and disadvantages are discussed in detail in a few recently published review papers on SWI and quantitative susceptibility mapping (QSM). [57, 98, 102, 110]

It has been shown that the phase shifts correlate with the iron content measured using X-ray fluorescence (XRF). [111] This technique has been used in several studies to quantify cerebral iron content in normal controls and in patients affected by neurodegenerative diseases such as PD and MS. [104, 112, 113] However, it is also known that phase can be affected by the orientation of the structures and by imaging parameters such as the main field strength and echo time. [102] Fundamentally, since phase is induced by the changes of magnetic susceptibility, it would be better to quantify the source directly, as introduced in the next section.

### *Determining susceptibility*

As previously discussed, quantifying $\chi(\vec{r})$ is an ill-posed problem. This problem can be solved by using the straight-forward thresholded k-space division algorithm, [59, 114] or by using more sophisticated algorithms in which the geometries of interest extracted from magnitude, phase and an initial reconstruction of susceptibility maps are utilized as constraints. [115-120] One advantage of using susceptibility for iron quantification, instead of using phase directly, is that susceptibility is not dependent on imaging parameters such as main field strength and echo time. [57] Moreover, unlike phase, which is geometry and orientation dependent, the susceptibility of structures with iron overload (e.g., deep grey matter structures) is generally not dependent on the orientation of the object. [102, 121] Nonetheless, the susceptibility of the white matter can be orientation dependent due to structural and magnetic susceptibility anisotropy. [118, 122, 123] Finally, and clinically very important, QSM provides information via the sign of the susceptibility as to whether a given structure is paramagnetic (containing more iron) or diamagnetic (containing calcium).

The relationship between susceptibility and iron content has been investigated in several studies, based on ferritin phantoms and/or postmortem studies where the iron content can be verified using

XRF and inductively coupled plasma mass spectrometry (ICPMS). [124, 125] Linear relationships between susceptibility and iron content have been shown in earlier studies, with slopes varying from 0.6 to 1.3 ppb/(µgFe per g wet tissue). [125] A recent paper suggests that 1ppb in susceptibility is roughly equivalent to a value closer to 1 µgFe per g wet tissue. [12] The variation in the slopes is partly due to the differences in the QSM reconstruction algorithm. [125] QSM based iron quantification has been quite successful especially for the basal ganglia, midbrain and dentate nucleus (DN) structures. [12, 94, 126] However, when interpreting the measured susceptibility values in white matter, the contribution of myelin content and susceptibility anisotropy should be considered. [127-130]  A summary of the linear correlations of R2* and QSM with cerebral iron concentration is provided in Table **3.1**. One key point to be aware of is that the coefficient relating susceptibility to iron content will depend on the QSM method and choice of threshold.

It has been shown that R2* is more sensitive to the changes of cerebral iron content than R2, and QSM has even superior sensitivity than R2*. [124, 131, 132] Compared with R2*, QSM shows better reproducibility due to its independence of main field strength and imaging parameters. Although slightly different due to reconstruction algorithms, the reproducibility of QSM can be reflected by the consistent slopes in the relationships between susceptibility and iron concentration found in different studies conducted at different field strength, whereas the slopes found in studies using R2* showed a clear dependence on the main field strength, as shown in Table **3.1**. This makes QSM a better choice in longitudinal studies or studies comparing results obtained from other imaging sites using different data acquisition protocols. [133] Nonetheless, studies involving the differentiation or separation of the effects of cerebral iron and myelin content may benefit from a combination of R2* mapping and QSM [134, 135] Because iron content is paramagnetic and myelin is diamagnetic, while both can increase the R2*. [134, 136, 137] Using R2* mapping and QSM

together, the investigation of the properties of tissue and the underlying pathological mechanisms become possible. The advantages of the joint use of R2* and QSM has been demonstrated in several recent studies focusing on MS lesions. [138-140] However, care should be taken when interpreting the R2* and QSM results in the white matter, since both R2* and susceptibility may be dependent on fiber orientation. [127, 141-144]

Furthermore, as seen in Table **3.1**, there is a clear and strong linear correlation between both QSM and R2* with direct measurements of iron concentration in the brain, validated by several in vivo and in vitro studies over the past decade. [12, 58, 114, 124-126, 136, 145-159] This implies that, with R2* (being careful to use the conversion factor at a given field strength) and susceptibility mapping techniques, abnormal iron levels in the brain structures of neurodegenerative diseases such as MS and PD can be associated with elevated levels of iron concentration in different regions of a diseased brain.

### *Other Techniques*

In addition to the T2, T2*, T2′ and susceptibility mapping based methods introduced above, there are some other techniques which can also be used to measure iron, including T1 mapping, field dependent R2 increase (FDRI), [160] magnetic field correlation (MFC), [161] as well as direct saturation based method such as water-saturation shift-referencing (WASSR). [162] These methods, although less frequently used due to technical challenges, may provide unique information about tissue properties and can be used as reference methods. For example, compared to T2* mapping, T1 mapping is less susceptible to the field inhomogeneity, and hence, it has the potential to improve both the accuracy and reproducibility of in vivo iron quantification although it is much less sensitive to iron than T2*. [163-165] Ge et al. demonstrated the quantification of iron content in grey matter

in multiple sclerosis patients using MFC. [166] Pfefferbaum et al. compared FDRI with SWI phase imaging for cerebral iron quantification and showed that FDRI has higher specificity to non-heme iron than SWI. [96]

**Table 3.1** Review of studies investigating the linear correlation of R2* and QSM with iron concentration in different brain structures.

| Study[a] | Sample Size | Iron Quantification Method | Field Strength (Tesla) | Linear Regression Parameters | Linear Correlation Equation A×[Fe]+B [d] | Brain Structures Included |
|---|---|---|---|---|---|---|
| Yao et al. [145] | 9 HC | R2* | 1.5 T | PCC = 0.79, P < 0.01 | A = 0.06, B = 1.08 | CN, PUT, GP |
| Ning et al. [146] | 56 Infants | R2* | 1.5 T | PCC = 0.75 (CN) PCC = 0.66 (PUT) PCC = 0.67 (GP) P < 0.001 | NA | CN, PUT, GP |
| Uddin et al. [147] | 17 HC | R2* | 1.5 T | PCC = 0.85, P < 0.0001 | A = 0.06 ± 0.003 B = 12.81 ± 0.42 | CN, PUT, GP, RN, SN, THA, FWM, CGM |
| Martin et al. [148] | 13 HC | R2* | 3 T | PCC = 0.91, P = 0.01 | NA | CN, PUT, GP, RN, SN, FWM |
| Péran et al. [149] | 30 HC | R2* | 3 T | PCC = 0.96, P < 0.001 | A = 0.14, B = 11.31 | CN, PUT, GP |
| Yao et al. [145] | 9 HC | R2* | 3 T | PCC = 0.87, P < 0.01 | A = 0.12, B = 1.41 | CN, PUT, GP |
| [b] Langkammer et al. [124] | 7 DS | R2* | 3 T | PCC = 0.95, P < 0.001 | A = 0.27, B = 14.3 | CN, PUT, GP, THA, FWM, TWM, OWM |
| [b] Langkammer et al. [136] | 6 DS | R2* | 3 T | PCC = 0.37, P < 0.01 | A = 0.12, B = 22.38 | FC, FWM, OC, OWM |
| Yan et al. [150] | 24 HC | R2* | 3 T | PCC = 0.98, P < 0.001 | NA | CN, PUT, GP, RN, SN, THA, FWM |
| Sedlacik et al. [151] | 66 HC | R2* | 3 T | PCC = 0.94, P = NA | A = 0.11 ± 0.006, B = 10.69 ± 0.80 | CN, PUT, GP |
| Barbosa et al. [126] | 30 HC | R2* | 3 T | PCC = 0.79, P = NA | A = 0.13, B = 20.0 | CN, PUT, GP, THA, RN, SN, GM |
| Uddin et al. [147] | 17 HC | R2* | 4.7 T | PCC = 0.95, P < 0.0001 | A = 0.196 ± 0.005, B = | CN, PUT, GP, RN, SN, THA, |

| | | | | | 16.87 ± 0.71 | FWM, CGM |
|---|---|---|---|---|---|---|
| Yao et al. [145] | 9 HC | R2* | 7 T | PCC = 0.92, P < 0.0001 | A = 0.32, B = 1.98 | CN, PUT, GP |
| Shmueli et al. [114] | 1 HC | R2* | 7 T | PCC = 0.83, P = 0.042 | NA | PUT, RN, SN |
| Bilgic et al. [152] | 23 HC | QSM | 1.5 T | PCC = 0.88, P = 0.02 | NA | CN, PUT, GP, THA, RN, SN, DN, FWM |
| Persson et al. [153] | 183 HC | QSM | 1.5 T | PCC = 0.97, P < 0.001 | A = 0.95. B = -24.50 | CN, PUT, GP, THA, RN, SN, DN |
| Liu et al. [12] | 174 HC | QSM | 1.5 T | PCC = 0.98, P < 0.01 | A = 0.89 ± 0.03, B = -48.51 ± 4.09 | GP, PUT, THA |
| Schweser et al. [58] | 5 HC | QSM | 3 T | PCC = 0.86, P < 0.001 | A = 1.3 ± 0.2 [e] B = NA | CN, PUT, GP, THA, RN, SN, DN, FWM |
| [b] Langkammer et al. [155] | 13 DS | QSM | 3 T | PCC = 0.87, P < 0.001 | A = 0.97 ± 0.03, B = -37.0 ± 2.0 | CN, PUT, GP, THA, FWM, TWM, OWM |
| [c] Zheng et al. [125] | 1 MS | QSM | 3 T | PCC = 0.87, P = NA | A = 0.80 ± 0.01, B = 10.8 ± 2.9 | CN, PUT, GP (Left Hemisphere) |
| Lim et al. [154] | 5 HC | QSM | 3 T | PCC = 0.99, P = NA | A = 0.73, B = -44.15 | CN, PUT, GP |
| Chai et al. [156] | 45 HC | QSM | 3 T | PCC = 0.90, P = 0.037 | A = 0.55, B = -18.80 | CN, PUT, GP, THA, RN, SN, DN, FWM |
| He et al. [157] | 35 HC | QSM | 3 T | PCC = 0.90, P = 0.007 | NA | CN, PUT, GP, RN, SN |
| Xia et al. [158] | 31 HC | QSM | 3 T | PCC = 0.84, P = 0.01 | NA | CN, PUT, GP, THA, RN, SN, DN, FWM |
| Barbosa et al. [126] | 30 HC | QSM | 3 T | PCC = 0.83, P = NA | A = 0.65, B = -13.8 | CN, PUT, GP, THA, RN, SN. GM |
| Shmueli et al. [114] | 1 HC | QSM | 7 T | PCC = 0.92, P < 0.01 | NA | PUT, RN, SN |

| Wharton et al. [159] | 5 HC | QSM | 7 T | PCC = 0.96, P = NA | A = 0.75 ± 0.1, B = NA | CN, PUT, GP, RN, SN, THA, FC |
|---|---|---|---|---|---|---|

HC: healthy controls, PCC: Pearson Correlation Coefficient (R), DS: Deceased Subjects, PD: Parkinson's Disease, MC: Myelin Corrected, CN: Caudate Nucleus, PUT: Putamen, GP: Globus Pallidus, SN: Substantia Nigra, RN: Red Nucleus, THA: Thalamus, GM: Gray Matter, WM: White Matter, FWM: Frontal White Matter, TWM: Temporal White Matter, OWM: Occipital White Matter, FC: Frontal Cortex, OC: Occipital Cortex, CGM: Cortical Grey Matter, MS: Multiple Sclerosis

[a] The in vivo iron concentration was estimated based on the study by Hallgren and Sourander (1958), unless otherwise stated.

[b] The iron concentration in this study was determined using Inductively Coupled Plasma Mass Spectroscopy (ICPMS).

[c] The iron concentration in this study was determined using X-Ray Fluorescence (XRF).

[d] For the relationship between R2* and iron, the unit of the slope (A) is s-1 per µg Fe / g wet tissue, and the unit of the intercept (B) is s-1. For the relationship between susceptibility and iron, the unit of the slope (A) is ppb per µg Fe / g wet tissue, and the unit of the intercept (B) is ppb.

[e] In this study, the slope was obtained by correcting the contribution of myelin content with magnetization transfer saturation map.

**The Role of MRI in Parkinson's Disease**

As pointed out in the previous chapters, with the current technology the clinical diagnosis of PD can only occur when 30-40% of the dopaminergic neurons have already been lost in the midbrain, particularly in the SN which introduces a significant challenge to PD therapeutics since such treatments are ideally required to be started before most of the dopaminergic neurons are dead. To date, no useful clinical test has been established to detect PD prior to the onset of motor symptoms. However, it is worth mentioning that it is common for PD patients to often show early symptoms that may develop to become PD-related later on. Loss of smell, anxiety, depression, restless leg syndrome and especially REM sleep behavior disorder are among the more common ones, even though they may also be associated with many other disorders. Specifically, it has been reported that a high percentage of RBD patients may develop synucleinopathies with more aggressive progression over a few years to a few decades. Nevertheless, it should also be noted that not all patients who develop PD have a history of RBD. [47]

Some studies suggest that the damage to the axons of dopaminergic neurons may occur prior to cell death, with SPECT and PET based imaging for dopamine-dependent labels such as dopamine transporter (DAT) supporting such findings. [167] However, these modalities are usually very expensive and require radiation exposure which have made researchers look for less costly and safer in vivo alternatives, particularly MRI, with the ultimate goal of detecting PD before the onset of the disease.

*Quantifying Abnormal Iron in Parkinson's Disease*

As discussed earlier, QSM has recently played a major role in research and clinical studies investigating iron deposition in deep grey matter structures of both healthy and diseased conditions.

[57] One of the most common forms of neurodegeneration is PD which is known to be associated with elevated iron content in deep gray matter and the brain regions responsible for motor function. [6, 7] Although other advanced post-processing MR techniques such as phase, R2 and R2* maps have been utilized to quantify iron content, QSM has proven to be a more promising and reliable method in terms of sensitivity and specificity. [57, 126, 168-170] Iron deposition has been found to be heterogeneously distributed in the brains of PD patients. [113, 171] However, the most prominent deficit is the degeneration of dopaminergic interactions in the SN which leads to high levels of non-heme iron in this midbrain structure. [172, 173] Cross-sectional and longitudinal research studies have quantitatively investigated this abnormality by monitoring the patients' iron-rich brain structures, particularly in the SN. In this dissertation, we only focus on R2* and QSM techniques which are the most widely used iron quantification methods in PD.

Using R2* maps, several studies have found abnormally elevated R2* rates, putatively indicative of higher iron deposition, across different subcortical brain regions in PD patients either in comparison with healthy control groups or after a specific period of time when monitored longitudinally. In the form of a cross-sectional study, Gorell et al. demonstrated higher R2* values in the SN of a non-demented PD group compared to a healthy cohort. [173] Rossi et al. showed increased levels of R2* not only in the SN, but also in the globus pallidus compared to a normal group. [174] In another article, however, Hopes et al. claimed that nigrostriatal structures including the SN, caudate nucleus and putamen had significantly greater R2* values in untreated PD patients compared to a healthy cohort. [175] Esterhammer et al. demonstrated a significant increase of R2* in the putamen and globus pallidus only in the early stages of PD with the SN maintained significant in both early and advanced stages. [176] On the other hand, two longitudinal R2* studies by Ulla et al. and Wieler et al. have both reported an increase in the R2* rate of SN over a 3-year time period

indicating that the iron content in the PD patients progresses over time. [177, 178] Ulla et al. also reported a significant progression of iron deposition in the caudal putamen.[177]

Over the past decade, QSM has been used to investigate iron related pathology and progression of PD. Similar to R2*, QSM has also shown higher levels of iron accumulation in the brains of PD patients, particularly in the SN. [126, 168-170] Guan et al. showed that susceptibility values are directly correlated with the disease stage and claimed that substantia nigra pars compacta (SNpc) is characterized by significantly higher iron content only in the early stages, whereas in more advanced stages of PD other structures such as substantia nigra pars reticulate (SNpr), red nucleus and globus pallidus also tend to develop high levels of iron deposition. [179] Elevated iron content in the SNpc was also reported in a 7T high resolution QSM study done by Lotfipour et al. in which significantly higher magnetic susceptibility values were seen for this substructure in the PD patients compared to the control group. [180] In Azuma et al.'s work, QSM was found to be a useful technique for quantitatively assessing lateral asymmetries in the SN of PD patients where the hemisphere differences were more prominent compared to those of the healthy controls. [181] Another study by Guan et al. showed that depending on the type of PD, the structures characterized by high iron accumulation vary; they claimed that iron accumulation in the nigral regions is the dominant effect in PD regardless of the disease type, whereas excessive iron deposition in the DN and red nucleus was seen only in patients with tremor symptoms. [182] Similarly, in a study done by He et al. the DN was shown to be the structure of choice that could be a potential biomarker to differentiate tremor-dominant PD from other types due to the increased magnetic susceptibility values only in this cerebellar structure. [183] Conversely, Acosta-Cabronero et al. reported that although magnetic susceptibility is expectedly higher in the dorsal SN, iron content in the DN decreases in idiopathic PD compared to healthy controls. [15]

To date, the high iron content of the SN appears to serve as the only reliable biomarker to characterize PD as has been consistently reported in the literature. [6, 15, 126, 157, 168-170, 173-181, 184, 185] Moreover, in a few studies where both R2* and QSM techniques were used to quantify iron content in PD patients, QSM showed superior sensitivity and accuracy in terms of diagnostic performance as well as detecting significant differences between PD and healthy groups making it the preferred iron quantification technique and a reliable imaging biomarker for PD. [126, 168-170] This could be due in part to the fact that increased water content can confound increases in iron content making R2* less sensitive. On the other hand, increased water content does not affect the susceptibility from the local iron content making QSM potentially more valuable in the assessment and quantification of iron content.

Under normal conditions, non-heme iron levels also change in the aging brain. Assessing quantified iron content against normal aging across brain structures dates back to the 1950s when Hallgren and Sourander investigated iron concentration in cadaver brains. [13] Over the past few decades, several research groups have tried to quantify normal brain iron content versus age with in vivo MR post-processing techniques. By using QSM, Li et al. introduced baselines of magnetic susceptibility changes as a function of age over the lifespan in cortical and subcortical brain regions. [94] In addition to validating their normal susceptibility-age baselines through a 3D ROI-based algorithm (known as the global analysis) for different deep gray matter nuclei, Liu et al. developed a new algorithm by which the local high iron content can be detected depending on the structure of interest and the age of the subject. [12] In this algorithm, the upper 95% prediction interval from the susceptibility-age global analysis of each nucleus is used to define an age-dependent threshold. Any voxel within the associated 3D ROI with a susceptibility value higher than that threshold would be considered as a high iron content (RII) voxel. The mean RII susceptibilities as a function of age for

different deep gray matter structures then establish new normal baselines, known as the regional analysis, which is claimed to have higher sensitivity, reliability and robustness for monitoring age-dependent changes in iron content compared to the global analysis. [12]

Table **3.2** reviews the studies investigating the brain iron content in cohorts of PD patients compared to healthy controls using R2* and QSM techniques. As seen in the table, the SN is the only deep gray matter nucleus which is consistently showing significantly elevated iron deposition in PD patients compared to healthy controls across all the reported studies. [126, 157, 168-170, 174-182, 184-188] Furthermore, in a few studies this significance expands to substructures of the SN, particularly the SNpc. [126, 169, 174, 177-182, 187] By taking the mean of the increased rates in the SN and SNpc in the studies which provided statistical information, the average increased rates were 10.3±8.5% and 13.6±4.0% in the R2* values of the SN and SNpc, respectively, in the PD patients compared to the healthy controls. However, these changes are reflected in considerably higher rates when QSM techniques were used. Specifically, the average increase rates were 28.2±14.6% and 35.2±2.7% for the SN and SNpc, respectively. These increased rates in R2* and QSM reflects the increase in iron concentration. However, these may be an under-estimation of the actual changes of the iron content in the SN, since the voxels with low levels of iron content were included in those studies and because all PD patients were included not just those showing high iron content in the SN.

**Table 3.2** Recent studies on R2* and QSM comparing different brain structures in PD patients and healthy controls.

| Study | Sample Size (N) | Iron Quantification Method | Field Strength | Brain Structures Assessed | Brain Structures with Significant Differences | (Mean ± SD in HC, Mean ± SD in PD)[a] |
|---|---|---|---|---|---|---|
| Péran et al. [184] | 22 HC<br>30 PD | R2* | 3 T | CN, GP, PUT, THA, RN, SN | SN | NA |
| Du et al. [185] | 16 HC<br>16 PD | R2* | 3 T | **SN** | SN | NA |
| Rossi et al. [174] | 21 HC<br>34 PD | R2* | 3 T | SN, GP | Medial SNpc, Lateral SNpc | Medial SNpc: (43 ± 7, 51 ± 10)<br>Lateral SNpc: (42 ± 6 , 50 ± 10) |
| [b] Ulla et al. [177] | 26 HC (8 M, 18 F)<br><br>27 PD (13 M, 14 F) | R2* | 1.5 T | GP, PUT, SN, GM, WM | SNpc, SNpr | SNpc-M: (20.2 ± 0.41 , 22.7 ± 0.48)<br>SNpc-F: (20.9 ± 0.39 , 22.5 ± 0.61)<br>SNpr-M: (25.3 ± 1.10 , 28.7 ± 0.95)<br>SNpr-F: (25.1 ± 0.4 , 25.5 ± 0.50) |
| [c] Ulla et al. [177] | 18 HC<br>14 PD | ΔR2* | 1.5 T | GP, PUT, SN, GM, WM | SNpc, SNpr, PUT | NA |
| Wieler et al. [178] | 13 HC<br>19 ES-PD | R2* | 3 T | GP, PUT, RN, SN | SNpc | NA |
| Murakami et al. [168] | 21 HC<br>21 PD | R2* | 3 T | CN, GP, PUT, THA, RN, SN | SN | SN: (29.0 ± 2.0 , 30.1 ± 1.5) |
| Esterhammer et al. [176] | 38 HC<br>82 PD | R2* | 1.5 T | CN, GP, PUT, THA, SN, CC | SN | SN: (20.58 [17.4–23.9] , 21.25 [15.8–29.4]) [d] |
| He et al. [157] | 35 HC<br>44 ES-PD | R2* | 3 T | CN, GP, PUT, RN, SN | SN | SN: (34.9 ± 4.41 , 38.9 ± 5.91) |
| Barbosa et al. [126] | 30 HC<br>20 PD | R2* | 3 T | CN, GP, PUT, THA, RN, SN | SNpc | SNpc: (47.7 ± 8.4 , 52.8 ± 11.7) |
| Du et al. [169] | 47 HC<br>47 PD | R2* | 3 T | SN | SNpc | SNpc: (32.8 ± 5.0, 37.8 ± 4.3) |
| Hopes et al. [175] | 20 HC<br>15 LS-PD | R2* | 3 T | CN, GP, PUT, SN | L-SN, R-SN | L-SN: (37.7 [36–39] , 50.2 [45–52]) [d]<br><br>R-SN: (36.8 [35–39] , 47.8 [45–52]) [d] |

| Study | Subjects | Method | Field | Regions | Significant Regions | Values |
|---|---|---|---|---|---|---|
| Ji et al. [186] | 28 HC<br><br>54 PD | R2* | 3 T | CN, GP, PUT, THA, RN, SN | L-SN, R-SN, L-RN, R-RN | L-SN: (34.2 ± 0.85 , 37.0 ± 0.74)<br>R-SN: (34.6 ± 0.97, 37.3 ± 0.69)<br>L-RN: (29.7 ± 0.61 , 31.7 ± 0.64)<br>R-RN: (29.3 ± 0.68 , 31.7 ± 0.54) |
| Langkammer et al. [170] | 58 HC<br><br>66 PD | R2* | 3 T | CN, GP, PUT, THA, RN, SN | SN | SN: (37.6 ± 5.8 , 41.1 ± 8.7) |
| Guan et al. [179] | 40 HC<br>45 ES-PD<br>15 LS-PD | R2* | 3 T | CN, GP , PUT, THA, RN,SN, DN | SNpc | NA |
| Guan et al. [182] | 40 HC<br>27 TD-PD<br>27 AR-PD | R2* | 3 T | CN, GP , PUT, THA, RN,SN, DN | SNpc | NA |
| Lotfipour et al. [180] | 11 HC<br>6 TD-PD<br>3 PIGD | QSM | 7 T | SN | SNpc | NA |
| Murakami et al. [168] | 21 HC<br><br>21 PD | QSM | 3 T | CN, GP, PUT, THA, RN, SN | SN | SN: (199.0 ± 14.0 , 224.0 ± 14.0) |
| He et al. [157] | 35 HC<br><br>44 ES-PD | QSM | 3 T | CN, GP, PUT, RN, SN | SN, RN | SN: (83.7 ± 15.6 , 100.0 ± 18.3)<br>RN: (81.0 ± 14.5 , 93.0 ± 18.9) |
| Barbosa et al. [126] | 30 HC<br><br>20 PD | QSM | 3 T | CN, GP, PUT, THA, RN, SN | SN, SNpc | SN: (114.7 ± 32.5 , 150.9 ± 41.5)<br>SNpc: (140.1 ± 38.5 , 186.7 ± 53.2) |
| Du et al. [169] | 47 HC<br><br>47 PD | QSM | 3 T | SN | SNpc | SNpc: (108.0 ± 33.0 , 148.0 ± 44.0) |
| Acosta-Cabronero et al. [187] | 50 HC<br><br>25 PD | QSM | 3 T | Whole-brain pattern, SN | SN, vSN, dSN, LOC, PPC, RMPC, MTC, DN, HIP | NA |
| [e] Azuma et al. [181] | 25 HC<br><br>24 PD | QSM | 3 T | CN, GP, PUT, RN, SN | SN, mSN, pSN | SN: (104.7 ± 31.0, 158.0 ± 47.6)<br>mSN: (104.6 ± 28.7, 166.6 ± 53.2)<br>pSN: (66.5 ± 25.6, 120.8 ± 38.7) |
| Langkammer et al. [170] | 58 HC<br><br>66 PD | QSM | 3 T | CN, GP, PUT, THA, RN, SN | SN, RN, GP, THA | SN: (90.0 ± 30.0, 114.0 ± 40.0)<br>RN: (89.0 ± |

| | | | | | | 30.0, 105.0 ± 40.0) GP: (112.0 ± 30.0, 126.0 ± 30.0) THA: (0.0 ± 10.0, 5.0 ± 10.0) |
|---|---|---|---|---|---|---|
| Guan et al. [179] | 40 HC 45 ES-PD | QSM | 3 T | CN, GP , PUT, THA, RN,SN, DN | SNpc | NA |
| Guan et al. [179] | 40 HC 15 LS-PD | QSM | 3 T | CN, GP , PUT, THA, RN,SN, DN | SNpc, SNpr, RN, GP | NA |
| Guan et al. [182] | 40 HC 27 TD-PD | QSM | 3 T | CN, GP , PUT, THA, RN,SN, DN | SNpc, RN, DN | NA |
| Guan et al. [182] | 40 HC 27 AR-PD | QSM | 3 T | CN, GP , PUT, THA, RN,SN, DN | SNpc | NA |
| He et al. [183] | 48 HC 19 TD-PD | QSM | 3 T | DN | DN | DN: (63.0 ± 16.0 , 74.0 ± 18.0) |

M: male, F: female, L: left, R: right, HC: healthy control, PD: Parkinson's disease, SN: substantia nigra, TD-PD: tremor dominant PD, AR-PD: akinetic-rigid dominant PD, PIGD: postural instability gait disorder, LS-PD: late stage PD, ES-PD: early stage PD, SNpc: SN pars compacta, SNpr: SN pars reticulata, mSN: middle part of the SN , pSN: posterior part of the SN, vSN: ventral SN, dSN: dorsal SN, PUT: putamen, DN: dentate nucleus, RN: red nucleus, THA: thalamus, GP: globus pallidus, GM: gray matter, WM: white matter, HIP: hippocampus, LOC: lateral occipital cortex, PPC: posterior parietal cortex, MTC: middle temporal cortex, RMPC: rostral middle prefrontal cortex. CC: corpus callosum

a Units of $R2^*$ and QSM are in $s^{-1}$ and ppb, respectively.

b In this study, by combining male and female groups, an analysis of variance (ANOVA) showed a significant increase of $R2^*$ in PD compared to HC group in both SNpr and SNpc.

c $\Delta R2^*$ corresponds to the difference in the $R2^*$ value between the baseline and a follow up time-point after 3 years.

d In this study, $R2^*$ values are quoted as median [range].

e In this study, QSM values for the PD patients were quoted from the more affected hemibrain.

*Neuromelanin Loss in Parkinson's Disease*

A century after the first definition of PD, this movement disorder was seen to be somewhat associated with NM pigmented neuronal loss in the midbrain area which was then found to belong to dopaminergic neurons. [43] Fast forward to almost two decades ago, by measuring NM concentration levels in the SN of normal subjects and PD patients, Zecca et al. claimed that NM seems to be a good biomarker of the neuronal damage in the SNpc. [189]

Following the advent of early NM-MRI techniques, TSE-based MRI methods have been utilized to examine NM changes in the SN and LC of PD patients. [37, 39, 42, 71, 72] In a validation study, Kawaguchi et al. compared DAT-sensitive radioligand PET imaging with NM-MRI and suggested that the accumulation of NM in the SN may be dependent upon actual dopamine concentration maintained by DATs associated with nigral dopaminergic neurons. [190]

Early neuropathological findings confirm a close correlation between the number of NM-containing dopaminergic neurons in the SNpc and the NM-MRI signal derived from the corresponding regions. [28] As previously pointed out, the signal intensity derived from NM-MRI is expected to decrease in PD patients due to NM loss. Figure **3.2** shows two examples, one from a HC and the other from a PD patient, where an MT-prepared NM-MRI sequence was used to highlight the NM content in the SNpc. As seen in this Figure, the CNR between the SNpc and cerebral peduncle (as the reference region) is noticeably lower compared to that of the HC which according to Sulzer et al. represents about 25% reduction in contrast. [43]
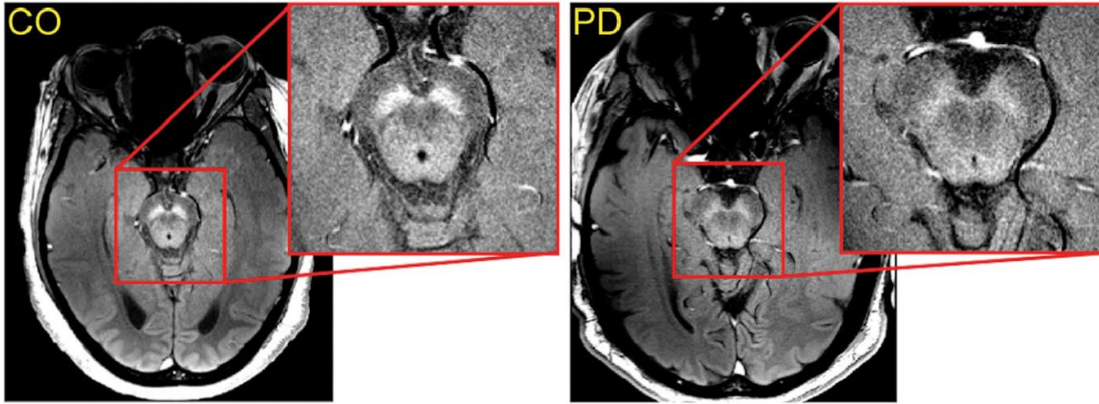
**Figure 3.2** A comparison between NM contrast in the SNpc of a HC (left) and a PD patient (right) derived from an MTC sequence. The PD patient shows approximately 25% CNR reduction. Images courtesy of Sulzer et al. [43]

In order to compare different NM-sensitive sequences used for MRI in vivo evaluation of SN degeneration in PD, one may argue that MTC is a better choice. In other words, TSE/FSE sequences usually depend on incidental MT effects derived from multi-slice and mostly 2D interleaved image acquisition to receive the NM signal. [73] This approach is not as effective as using an explicit MT pulse to saturate the signal from macromolecules and generate an efficient NM-sensitive contrast. Additionally, though also seen in MTC to a lesser extent, TSE/FSE MR sequences usually deposit substantial amounts of energy in the brain tissue, to the point that specific absorption rate (SAR) on the scanner may be an issue forcing the operator to either collect fewer slices, lengthen the TR and total acquisition time or shorten the echo train. [191] Longer total scan times may turn into a serious technical issue in PD patients, especially those going through late or terminal stages of the disease with sever motor symptoms.

With respect to pre-symptomatic stages of PD, it has been shown that patients suffering from RBD have also shown SNpc volume comparable to those from IPD patients [10, 192] which is in agreement with potential reduction of dopamine loss in PD. Another study has also noted a loss of MR hyperintensity in dorsolateral aspect of the SN in two-thirds of patients with RBD. [193] These

pathophysiological changes in RBD as a relatively undiscovered disorder opens the door to more extensive investigations to find MR-dependent in vivo biomarkers prior to arrival of PD-specific symptoms.

In the next three chapters, a comprehensive analysis of abnormal NM and iron content in PD and RBD patients will be discussed in much more detail in a backwards order starting from intermediate stage of PD towards early stages and finally RBD as the pre-symptomatic prodromal phase of PD. In Chapter Four abnormal levels of iron content in IPD patients will be discussed as a function of age and also compared against an age-matched healthy population. In Chapter Five iron, NM and N1 will be evaluated using a single MT-prepared 3D GRE sequence strictly in early IPD patients and their correlations with clinical scores. Finally, Chapter Six will specifically assess iron and N1 changes in RBD patients and age-matched HCs as well as their relationships with cognitive and motor function scores.

## Chapter Four: Regional high iron in the substantia nigra differentiates Parkinson's disease patients from healthy controls

**Introduction**

Parkinson's disease (PD) is believed to be the second most common neurodegenerative disease in developed countries. [194] Research has shown that the substantia nigra (SN) is one of the most important structures playing a vital role in the pathophysiology of PD patients. [11] Neuronal loss and lack of dopamine content in this midbrain nucleus generally lead to movement disorders in these patients. [6, 7] The loss of neuromelanin in particular has been thought to lead to an increase in iron content in the SN which has been implicated in a number of PD studies. [8-10] In fact, the SN seems to be the only reliable brain structure through which a meaningful relationship with neuronal loss has been found. [11] Since the onset of PD is generally late and brain iron levels tend to increase as a function of age in deep gray matter (DGM) structures even under normal conditions, [12-14] it is important to account for these age–dependent changes. [15]

A number of magnetic resonance imaging (MRI) techniques can be used to quantify iron content in the human body. Conventionally, R2 and R2* relaxation rate mapping along with phase information have been utilized to measure iron deposition in different regions of the human body *in vivo*. [11] However, one of the most popular approaches today is the use of quantitative susceptibility mapping (QSM); a post-processing technique that generates susceptibility maps using phase information and, unlike other conventional quantification techniques, is independent of imaging parameters such as geometry, echo time, spatial resolution, field strength and signal-to-

---

noise ratio (SNR). [57] QSM also appears to have the greatest reliability and robustness compared to other MR-based *in vivo* methods. [57, 169, 170] Specifically, in terms of consistency, QSM has been shown to have high repeatability and less variability compared to R2*. [11]

Liu et al. investigated a cohort of 174 healthy adults using QSM with the purpose of assessing the effects of normal aging on the iron levels in seven DGM structures. [12] In addition to their evaluation of mean susceptibility from the entire 3D region covered by each nucleus as a function of age (also known as the global analysis) in the basal ganglia and midbrain, they introduced a new age- and structure-dependent high iron susceptibility-age baseline (also known as the regional analysis). The regional analysis appeared to be more robust and sensitive to age-related changes compared to the global analysis. [12] Furthermore, by applying the same methodology, Ghassaban et al. established the global and regional susceptibility-age baselines for the dentate nucleus using 81 healthy adults. [11] Therefore, we hypothesized that this regional analysis may also be more sensitive to changes in iron for PD patients.

In this study, using QSM and R2* techniques, we compare the iron content in the DGM structures between a cohort of PD patients and a group of healthy controls (HC). Additionally, using QSM maps we investigate the iron deposition rates of PD patients compared to the corresponding global and regional normal baselines established by Liu et al. [12] and Ghassaban et al. [11] Similarly, R2* maps are used to compare global measurements to those of the healthy population established by Li et al. [94] Also, susceptibility measurements in terms of increased iron deposition are compared to the clinical status of PD patients. Finally, the QSM data are compared directly to the R2* across the different DGM nuclei using the HC data. This study could potentially pave the way for developing future iron-based diagnostic studies and better understanding the etiology of PD.

**Methods**

*Data Collection*

This study was approved by the local ethics committee at Ruijin Hospital and all subjects signed

consent forms. A total of 49 subjects were evaluated: 25 PD patients ($61.8 \pm 6.4$ years old) and 24

HC subjects ($63.4 \pm 8.0$ years old). All of the PD patients were recruited from local movement

disorder clinics. The inclusion criteria were: 1) a diagnosis of idiopathic PD, 2) Mini-Mental State

Exam (MMSE) score equal to or more than 24 and 3) Hoehn and Yahr (H&Y) scale of 1 through 3

as patients with higher scores had more severe symptoms and would have trouble staying still in the

magnet for the duration of the scans. The exclusion criteria were: 1) symptoms of secondary or

atypical parkinsonism or 2) a history of cerebrovascular disease, seizures, brain surgery, brain tumor,

moderate-to-severe head trauma or hydrocephalus or 3) treatment with antipsychotic drugs or with

any other drug possibly affecting clinical evaluation. Data were collected using a 16 echo, gradient

echo imaging sequence on a 3T GE Signa HDxt from an eight-channel receive-only head coil with

the following imaging parameters: TE1 = 2.69ms with $\Delta$TE = 2.87ms, TR = 59.3ms, pixel

bandwidth = 488 Hz/pixel, flip angle = 12°, slice thickness = 1mm, matrix size = 256 × 256 and an

in-plane resolution of $0.86 \times 0.86$ mm$^2$.

*QSM Processing*

The susceptibility maps were created using the first 8 echoes and were reconstructed for each

echo individually using SMART v2.0 (MRI Institute for Biomedical Research, Bingham Farms, MI,

USA) followed by a weighted average of the resultant QSM images based on their SNRs. Only 8

echoes were used because of severe frontal signal loss at echo times longer than roughly 20ms. The

reconstruction steps included the brain extraction tool (BET) to segment only the brain tissue using

the fourth echo magnitude data, [195] quality guided 3D phase unwrapping algorithm (3DSRNCP) for phase unwrapping, [196] sophisticated harmonic artifact reduction for phase data (SHARP) for background field removal with a threshold of 0.05 and a deconvolution kernel of 6, [58] and a truncated k-space division (TKD) approach (threshold = 0.1) referred to as susceptibility weighted imaging and mapping (SWIM) for inverse filtering. [59] The DGM nuclei included in this study were: the head of the caudate nucleus (CN), putamen (PUT), globus pallidus (GP), thalamus (THA), pulvinar thalamus (PT), red nucleus (RN), substantia nigra (SN) and dentate nucleus (DN). Multislice 3D regions-of-interest (ROI) representing these structures were manually traced on QSM slices using SPIN (Signal Processing in NMR, SpinTech, Inc., Bingham Farms, MI, USA) by the author with more than 5 years of relevant experience. Original magnitude and phase images were used as references to ensure accurate boundary drawings. An illustration of the 3D ROIs is given in Figure **4.1**. Mean susceptibility values from the entire structures of both cohorts were then extracted and plotted as a function of age, also known as the global analysis. Similar to Liu et al.'s work, age-dependent susceptibility values were chosen as thresholds from the upper 95% prediction intervals based on their global analysis of 174 controls from which regional high iron (RII) content voxels were then estimated for a given structure at a given age for all the nuclei except the DN. [12] For the DN, a similar process was performed on the global analysis established by Ghassaban et al.'s study from 81 healthy adults. [11] Similarly, mean susceptibilities of the RII regions were calculated and plotted as a function of age, also known as the regional analysis. The global and regional analyses of both PD and HC cohorts were then superimposed on the corresponding plots introduced by Liu et al and Ghassaban et al. [11, 12] Additionally, the average values were compared for both global and RII susceptibilities between the PD and HC cohorts in both hemispheres and in all DGM nuclei.
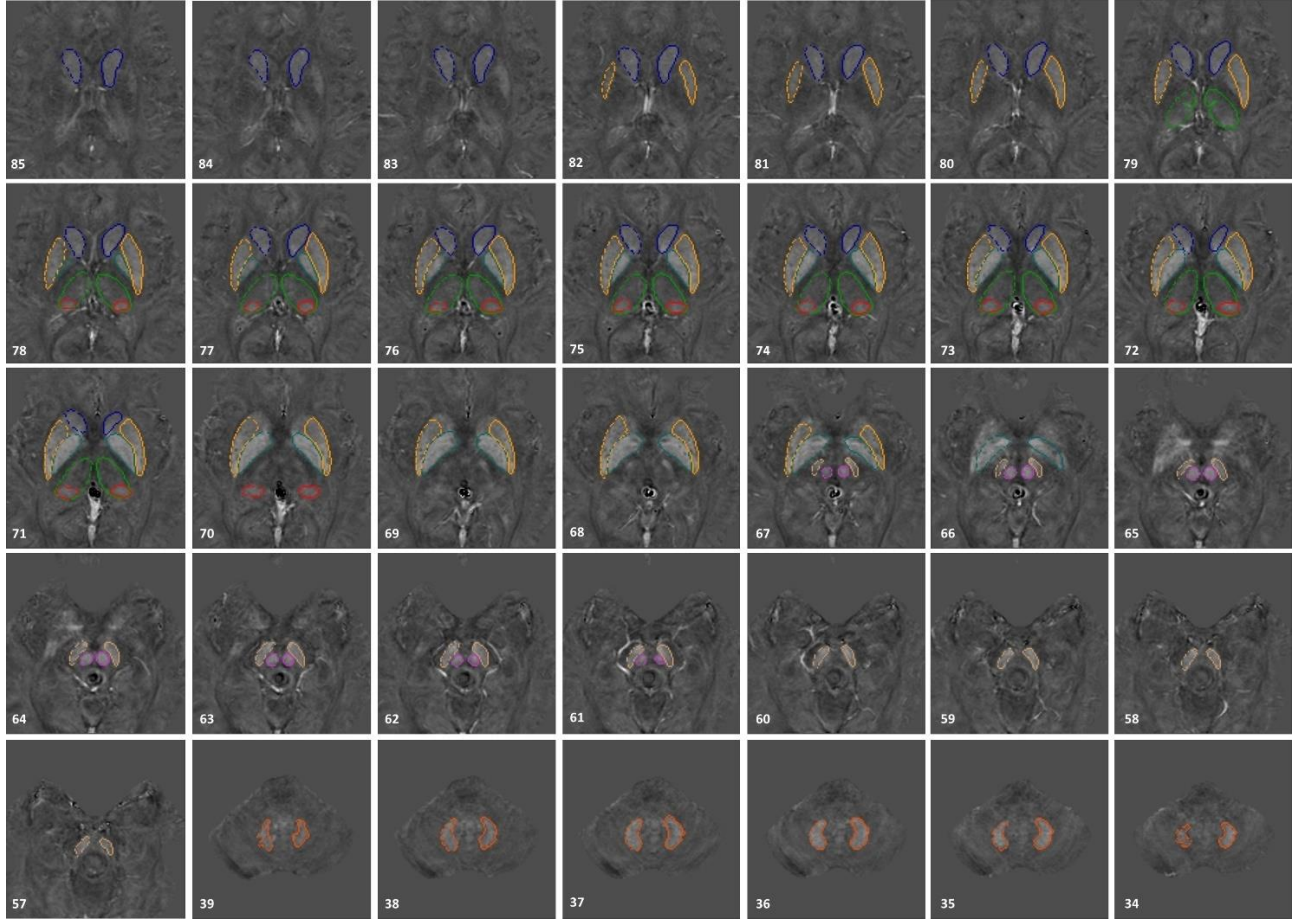
**Figure 4.1.** 3D regions of interest (ROIs) traced on susceptibility maps of a 65-year-old male. Structures include the head of caudate nucleus (CN), globus pallidus (GP), putamen (PUT), thalamus (THA), pulvinar thalamus (PT), red nucleus (RN), substantia nigra (SN) and dentate nucleus (DN). The numbers in the lower left corner represent the slice numbers from 132 slices collected in this example.

*R2\* Processing*

The R2\* maps were also reconstructed using the first 8 echoes through a pixel-by-pixel fit to an exponential curve. The exact same 3D ROIs traced on the QSM maps were also used on R2\* maps. Similar to QSM data analysis, mean R2\* values were extracted from each structure and plotted as a function of age (i.e., global analysis). These values were then superimposed and visually compared to the corresponding R2\*-age baselines established by Li et al for 6 DGM structures including the CN, GP, PUT, RN, SN and DN. [94] For each structure the fitted exponential regression equation

and 95% confidence intervals provided by Li et al were used to predict the mean R2* values as a function of age for the normal population. [94] Moreover, similar to the analysis done in QSM processing, R2* values of both PD and HC cohorts were compared to each other in both hemispheres for all DGM structures.

*Correlation between Susceptibility and R2\**

With both the QSM and R2* data available and in order to assess the relationship between these two parameters in the DGM structures, a linear regression model was fitted to the mean R2* as a function of mean susceptibility in all the nuclei. To avoid any sources of bias, only the healthy cohort was included for this correlation, the results of which were compared to those of Li et al.'s study. [94]

*Statistical Analysis*

All statistical analyses were carried out using Microsoft Excel 2013 (Microsoft Corporation, Redmond, WA) with a two-tailed significance level of 0.05. Two-sample t-test analyses were performed to compare the average global (for QSM and R2*) and regional (for QSM only) values of PD and HC cohorts in both hemispheres. Furthermore, paired sample t-tests were performed to compare susceptibility and R2* values between the left and right hemisphere of each DGM structure. Additionally, a comparison between the mean susceptibility values of the SN and clinical status of the PD patients was performed. The parameters to which SN global and regional susceptibility values were compared included the unified Parkinson's disease rating scale part III (UPDRS-III) and H&Y scores as well as the disease duration. Finally, the same clinical status parameters along with patients' ages were used to compare a sub-group of PD patients with

abnormal RII susceptibility values (i.e., higher than the corresponding upper 95% prediction interval from the susceptibility-age baseline [12]) to another sub-group whose RII susceptibilities fall within the normal ranges of the baseline.

**Results**

Figure **4.2** and Figure **4.3** show the QSM global and regional analyses for the right hemisphere of both groups, respectively, superimposed on the corresponding previously established normal populations. These susceptibility-age baselines were published by Ghassaban et al. (for the DN only) [11] and Liu et al. (for the rest of the DGM structures). [12] The SN is the only structure showing elevated susceptibility values in both global and regional analyses (see Figure **4.4**).
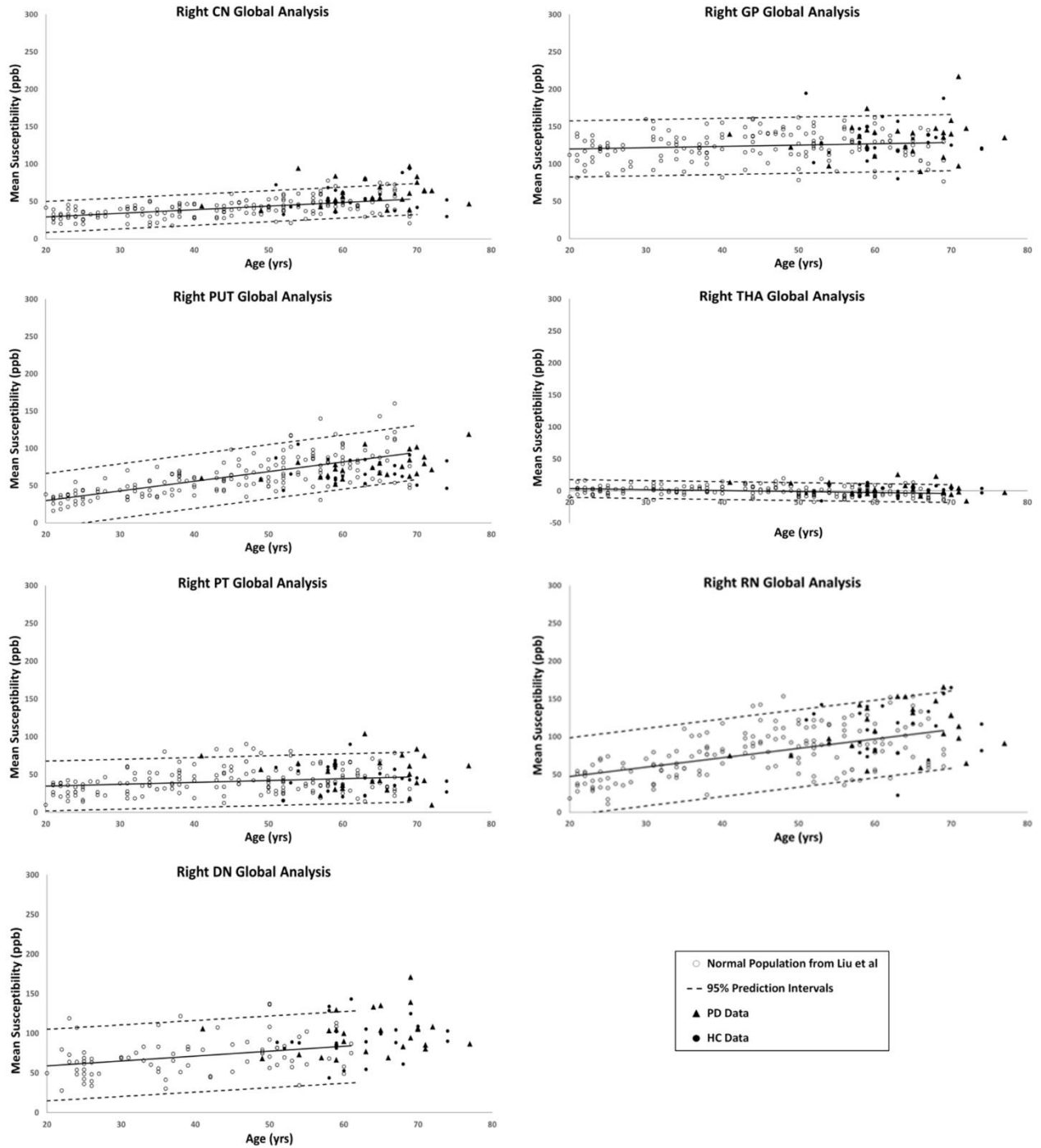
**Figure 4.2**. Right hemisphere global analyses of HC and PD cohorts superimposed on the susceptibility-age baselines for different deep gray matter structures published by Ghassaban et al. [11] for the dentate nucleus and Liu et al. for the other seven nuclei. [12] CN: caudate nucleus, GP: globus pallidus, PUT: putamen, THA: thalamus, PT: pulvinar thalamus, RN: red nucleus, DN: dentate nucleus. Hollow circles: normal baselines, solid circles: HC data from this study, triangles: PD data from this study, solid lines: linear regression models associated with the normal population, dashed lines: 95% prediction intervals associated with the normal population.
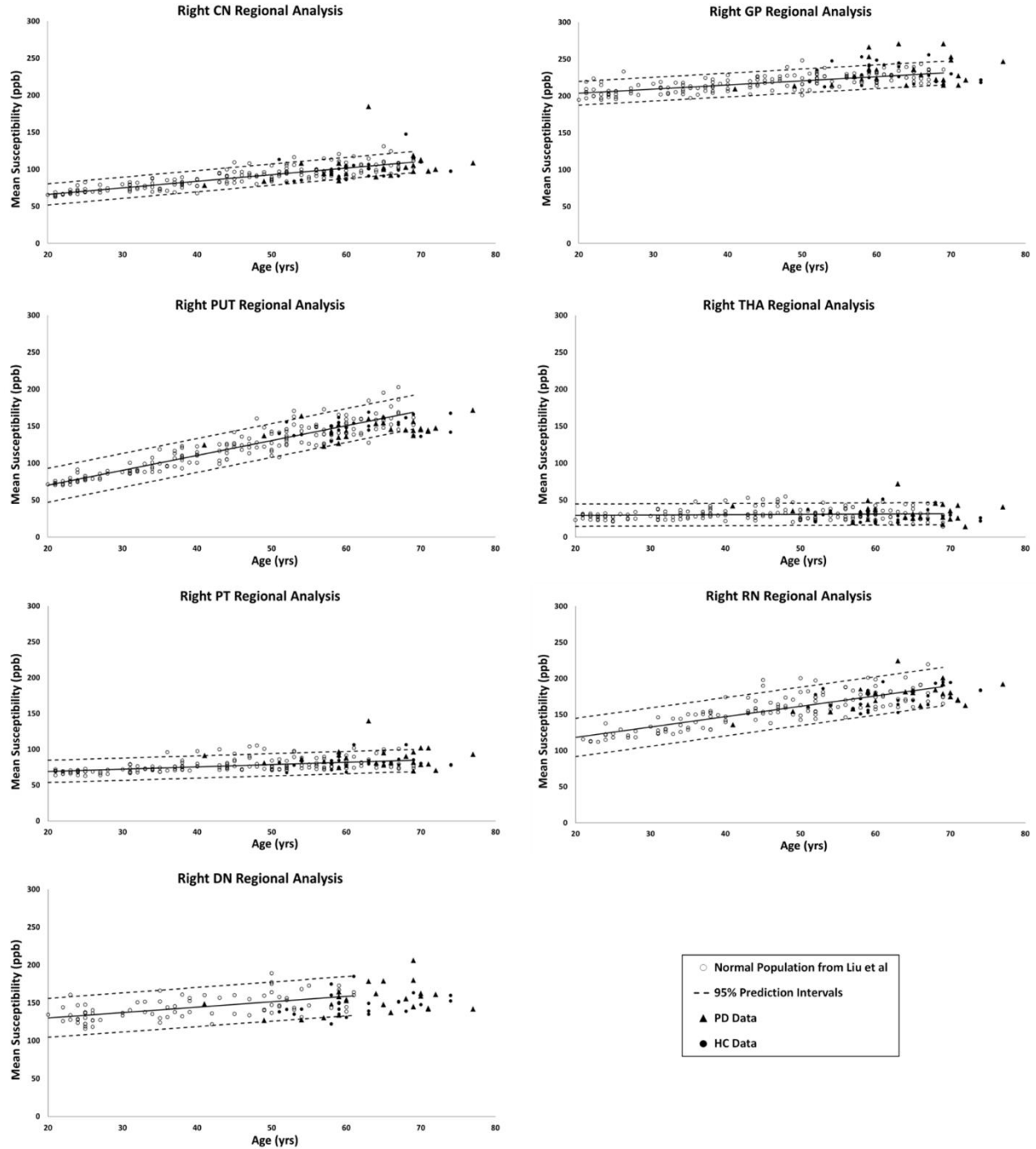
**Figure 4.3**. Right hemisphere regional high iron (RII) analyses of HC and PD cohorts superimposed on the susceptibility-age baselines for different deep gray matter structures published by Ghassaban et al. [11] for the dentate nucleus and Liu et al. for the other seven nuclei. [12] CN: caudate nucleus, GP: globus pallidus, PUT: putamen, THA: thalamus, PT: pulvinar thalamus, RN: red nucleus, DN: dentate nucleus. Hollow circles: normal baselines, solid circles: HC data from this study, triangles: PD data from this study, solid lines: linear regression models associated with the normal population, dashed lines: 95% prediction intervals associated with the normal population
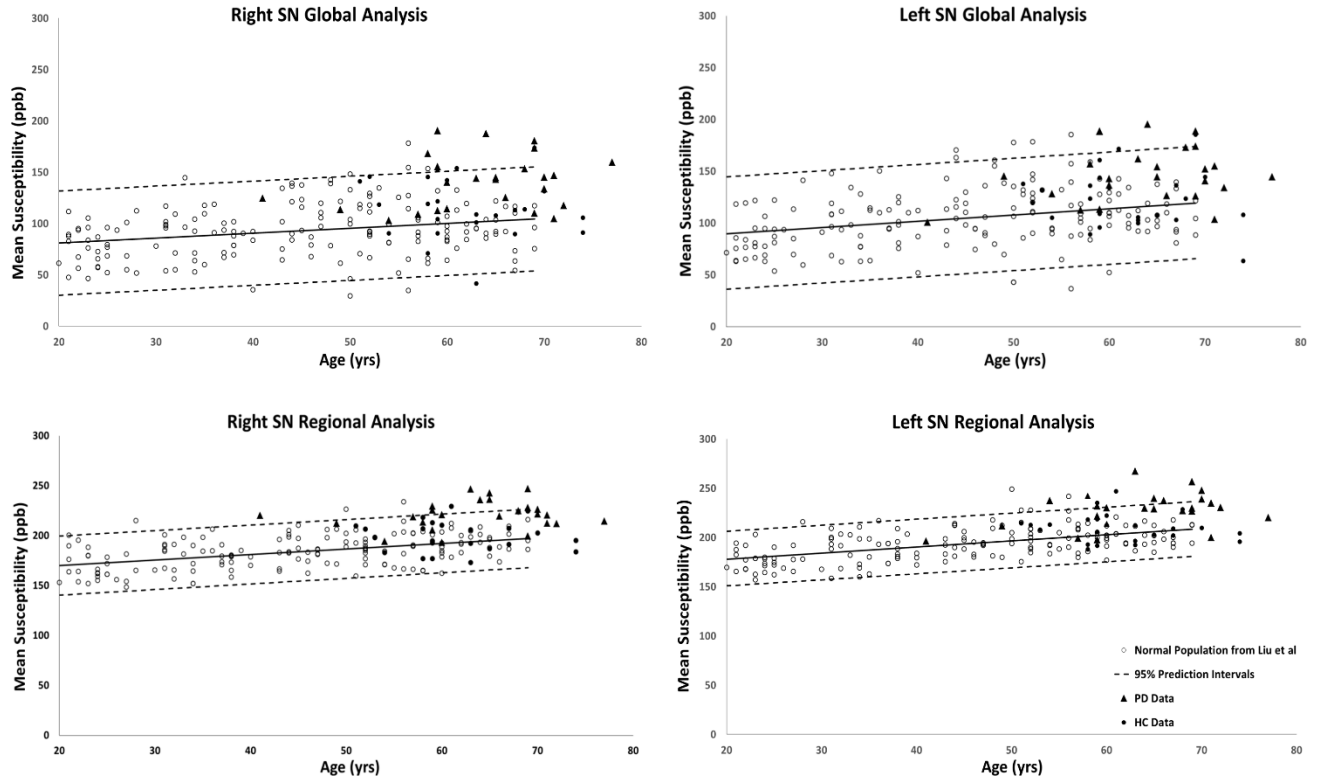
**Figure 4.4**. Substantia nigra global (entire structure) and regional (RII high iron) analyses of HC and PD cohorts superimposed on the susceptibility-age baselines published by Liu et al. [12] Hollow circles: normal baselines, solid circles: HC data from this study, triangles: PD data from this study, solid lines: linear regression models associated with the normal population, dashed lines: 95% prediction intervals associated with the normal population.

The results of the two-sample and paired-sample t-tests comparing the susceptibility means of HC and PD cohorts within and between the two hemispheres of different DGM structures are summarized in Table **4.1**. Only the SN showed significantly higher susceptibility values in PD patients when compared with the HC cohort, with the regional analysis (PD: 221±18 ppb, HC: 200±14 ppb, p<0.001 for the right and PD: 223±17 ppb, HC: 210±15 ppb, p<0.001 for the left hemisphere) revealing more prominent differences compared to those of the global analysis (PD: 140±27 ppb, HC: 116±30 ppb, p<0.01 for the right and PD: 144±26 ppb, HC: 122±28 ppb, p<0.01 for the left hemisphere). The SN was also the only structure showing significant differences between the two hemispheres in both cohorts using both global and regional analyses. On the other hand, in

addition to the SN, significant differences were seen between the hemispheres in both PD and HC groups in the THA, RN and DN only using the regional analysis. Among all affected nuclei, the left hemisphere showed significantly higher susceptibility values.

**Table 4.1.** Two-sample t-test statistics comparing susceptibility means of the global and regional analyses between the two cohorts in both hemispheres.

| Iron Analysis | | Global Analysis | | | RII Analysis | | |
|---|---|---|---|---|---|---|---|
| Hemisphere | | Right | Left | P-value | Right | Left | P-value |
| CN | HC | 54.6 ± 6.6 | 52.4 ± 7.6 | 0.27 | 99.1 ± 5.6 | 97.3 ± 6.1 | 0.32 |
| | PD | 59.3 ± 6.7 | 54.7 ± 6.9 | 0.16 | 102.0 ± 7.8 | 97.7 ± 8.6 | 0.03 |
| | P-value | 0.35 | 0.67 | NA | 0.56 | 0.95 | NA |
| GP | HC | 133.1 ± 10.1 | 127.8 ± 7.8 | 0.15 | 231.8 ± 5.2 | 231.1 ± 6.9 | 0.82 |
| | PD | 133.7 ± 10.0 | 127.6 ± 9.9 | 0.11 | 232.3 ± 7.2 | 231.6 ± 7.9 | 0.86 |
| | P-value | 0.94 | 0.97 | NA | 0.92 | 0.92 | NA |
| PUT | HC | 68.7 ± 6.4 | 72.8 ± 7.0 | 0.25 | 150.5 ± 4.3 | 144.9 ± 5.0 | 0.08 |
| | PD | 75.8 ± 6.6 | 73.6 ± 7.8 | 0.32 | 145.1 ± 4.8 | 142.1 ± 6.1 | 0.12 |
| | P-value | 0.15 | 0.87 | NA | 0.19 | 0.10 | NA |
| THA | HC | 2.3 ± 2.8 | 2.8 ± 2.9 | 0.71 | 30.2 ± 3.2 | 36.5 ± 3.0 | **<0.001** |
| | PD | 3.1 ± 3.7 | 2.2 ± 3.7 | 0.59 | 33.3 ± 4.8 | 36.8 ± 3.8 | **<0.001** |
| | P-value | 0.24 | 0.66 | NA | 0.30 | 0.88 | NA |
| PT | HC | 45.3 ± 7.0 | 45.6 ± 6.9 | 0.90 | 83.3 ± 3.7 | 85.4 ± 2.8 | 0.10 |
| | PD | 51.8 ± 8.8 | 47.7 ± 7.2 | 0.12 | 87.5 ± 5.5 | 86.4 ± 4.7 | 0.45 |
| | P-value | 0.27 | 0.68 | NA | 0.22 | 0.74 | NA |
| RN | HC | 108.1 ± 13.0 | 102.9 ± 12.9 | 0.31 | 173.2 ± 5.4 | 177.5 ± 6.1 | **0.03** |
| | PD | 112.8 ± 13.1 | 112.2 ± 13.8 | 0.85 | 175.8 ± 6.8 | 179.3 ± 6.8 | **0.01** |
| | P-value | 0.61 | 0.36 | NA | 0.55 | 0.69 | NA |
| SN | HC | 115.4 ± 11.6 | 127.5 ± 10.8 | **0.04** | 200.1 ± 6.1 | 210.3 ± 5.7 | **<0.001** |
| | PD | 139.8 ± 10.4 | 147.5 ± 10.5 | **0.01** | 220.7 ± 5.6 | 234.7 ± 5.9 | **<0.01** |
| | P-value | **<0.01** | **<0.01** | NA | **<0.001** | **<0.001** | NA |
| DN | HC | 93.1 ± 9.7 | 95.3 ± 11.0 | 0.41 | 147.6 ± 5.4 | 155.9 ± 6.2 | **<0.001** |
| | PD | 99.4 ± 10.2 | 102.1 ± 10.8 | 0.41 | 153.7 ± 7.2 | 159.1 ± 7.4 | **<0.01** |
| | P-value | 0.38 | 0.39 | NA | 0.20 | 0.52 | NA |

Numbers are reported in Mean ± 95% confidence intervals. CN: caudate nucleus, GP: globus pallidus, PUT: putamen, THA: thalamus, PT: pulvinar thalamus, RN: red nucleus, SN: substantia nigra, DN: dentate nucleus. P-values in bold show significant differences between the means.

The relationship between mean global and regional susceptibility changes in the SN of PD patients and clinical status parameters (i.e., disease duration and UPDRS-III) resulted in no significant correlations (all p-values > 0.05). However, as shown in Table **4.2**, dividing the PD cohort in two sub-groups with normal and abnormal RII susceptibility values showed that there were

significantly higher UPDRS-III scores in patients with elevated RII iron content (p < 0.05 in both hemispheres).

**Table 4.2**. Comparison of clinical status between two sub-groups of the PD cohort with normal and abnormal RII iron content in the substantia nigra.

| Hemisphere | Right | | | Left | | |
|---|---|---|---|---|---|---|
| Group | Abnormal Iron (N=10) | Normal Iron (N=14) | p-value | Abnormal Iron (N=10) | Normal Iron (N=14) | p-value |
| Age (years) | $62.5 \pm 8.6$ | $64.9 \pm 7.8$ | 0.51 | $63.9 \pm 5.6$ | $63.1 \pm 9.7$ | 0.80 |
| Duration (years) | $4.7 \pm 2.8$ | $3.8 \pm 3.3$ | 0.49 | $5.1 \pm 3.4$ | $3.4 \pm 2.9$ | 0.29 |
| UPDRS-III | $30.4 \pm 14.3$ | $17.8 \pm 9.6$ | **0.03** | $28.6 \pm 12.9$ | $16.6 \pm 9.7$ | **0.03** |
| H&Y | $1.8 \pm 0.6$ | $1.4 \pm 0.5$ | 0.17 | $2.0 \pm 0.75$ | $1.5 \pm 0.55$ | 0.10 |

Normal and abnormal sub-groups are separated based on RII susceptibility values higher and lower than the baseline upper 95% prediction intervals, respectively. P-values in bold show significant differences between the means.

The global measurements of R2* values superimposed on the corresponding age-dependent baselines published by Li et al [94] resulted in no abnormal values with most of the means falling within the 95% confidence intervals. The only exception was the SN of the PD patients with R2* values slightly skewed upward but still most subjects were below the upper 95% confidence interval, as shown in Figure **4.5**. Also, the two-sample t-tests between PD and HC cohorts revealed significant differences in the SN in both hemispheres (PD: $42\pm4$ s$^{-1}$, HC: $39\pm4$ s$^{-1}$, p=0.01 for the right and PD: $43\pm4$ s$^{-1}$, HC: $39\pm4$ s$^{-1}$, p=0.01 for the left hemisphere). The paired sample t-tests showed no significant differences between the hemispheres for any of the structures in either cohort.

Figure **4.6** shows the linear regression model fitted to the R2* values as a function of the corresponding QSM values for the HC group plotted for all the nuclei included in this study. The Pearson correlation coefficient (PCC) value of 0.87 is indicative of a strong linear relationship between these two parameters. Also, the linear slope of 0.123 s$^{-1}$/ppb is very close to the slope of 0.126 s$^{-1}$/ppb reported by Li et al. [94]
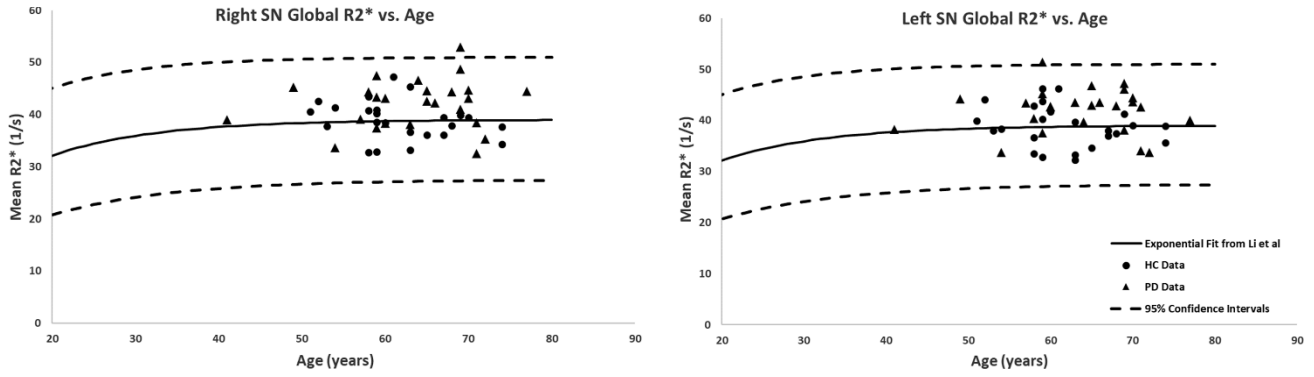
**Figure 4.5**. Global analysis of the R2* measurements in the substantia nigra of PD patients and healthy adults superimposed on the corresponding R2*-age exponential fits provided by Li et al. [94] Although most of the subjects fall within the 95% confidence intervals, the PD patients showed higher R2* values compared to those of the HC. Solid circles: HC data from this study, triangles: PD data from this study, solid lines: exponential regression models from the normal population, [94] dashed lines: 95% confidence intervals associated with the fitted curves.
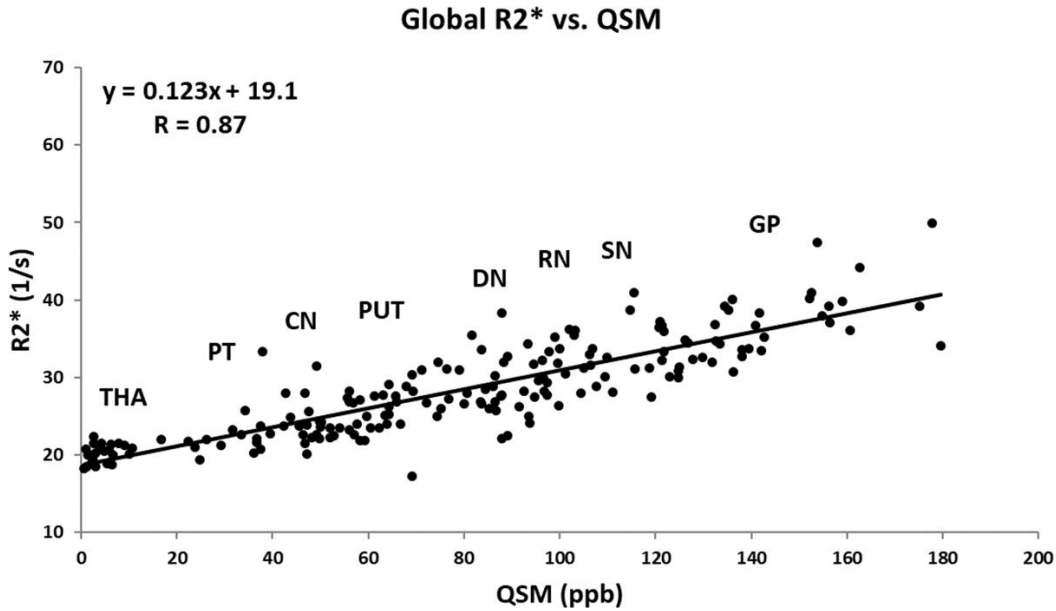


**Figure 4.6**. Mean R2* as a function of mean QSM in deep gray matter nuclei of the HC group fitted by a linear regression model. The data points are the average means between the two hemispheres. Based on the estimated mean values, the labels show the approximate locations around which each structure falls. The regression parameters are shown on the plot. CN: caudate nucleus, GP: globus pallidus, PUT: putamen, THA: thalamus, PT: pulvinar thalamus, RN: red nucleus, DN: dentate nucleus. Solid circles: HC data from this study, solid line: linear regression fit.

## Discussion and Conclusions

To date, there is no clear answer to the contributing factors in the pathogenesis of Parkinson's

disease. It is generally believed that the loss of neuromelanin content may initiate the process of

increasing non-heme iron deposits in the midbrain which then leads to different forms of parkinsonism. [8-10] On the other hand, there is also the hypothesis arguing that the depigmentation of the nigrosome-1 content in the posterolateral part of the SN might lead to the subsequent increase in iron deposition in this midbrain structure. [197]

In this chapter, we have shown that there is an increase in iron in the SN over and above the normal increase due to age in PD patients. Although the average susceptibility value of the SN is seen to increase in the PD cohort, especially in the thresholded regions characterized by high iron content, we also note that there may, in fact, be two populations of PD patients, those that do not change iron content and those that do. For the abnormally high iron content group, there was a significantly higher UPDRS-III than the group showing normal iron content. Nevertheless, to draw a stronger conclusion will require investigating a considerably larger sample size.

The global and regional analyses in the SN of PD patients has previously been evaluated in Ghassaban et al. and Sethi et al. in which similar QSM reconstruction techniques were adopted using different scanners and field strengths. [11, 198] The regional analysis being more sensitive to local high iron content changes seen in the SN in this study is in accordance with their findings. This validates the consistency and reliability of using gradient echo imaging and the use of the threshold based QSM reconstruction for data from different MR manufacturers' systems

The comparison between the two hemispheres revealed significantly higher iron deposition in the left hemispheres of both PD and HC cohorts in the THA, RN, SN and DN in the regional (RII) analysis and only in the SN for the global analysis. However, the largest effects in terms of absolute shifts in susceptibility were seen in the SN where the differences were on the order of 20 ppb

compared to all other cases where the differences are on the order of less than 8 ppb. This is consistent with Liu et al.'s study where they showed that, except in the SN, small but significant differences between the hemispheres of all DGM structures would vanish if other sources of error (in their case excluding one slice from the top and/or bottom of the structures or changing the definition of RII from upper 95% to 99% prediction interval of the global analysis) were taken into account when measuring the susceptibility values. [12] However, simulation results for the SN show that QSM has a systematic error of roughly 12 ppb in the SN due to streaking artifacts generated by the QSM reconstruction. [57] Additionally, low spatial frequency undulations seen in QSM techniques could also lead to asymmetry in the brain. [57] Therefore, by taking into consideration all these sources of systematic error, the asymmetries seen in the SN may disappear as well. Another QSM study in which lateral asymmetry was found in the SN of PD patients was done by Azuma et al. where the mean susceptibility was seen to be significantly higher in the more affected hemisphere compared to that of the less affected hemisphere although they had much larger errors compared to our data due in part to the distribution of iron and the small sample size. [181] They also do not account for the other sources of systematic error mentioned above which may again remove any remaining small differences between left and right values of iron in the SN.

Evaluating R2* maps led to two major findings: first, in accordance with the literature, iron content characterized by R2* values was seen to be higher in the SN of PD patients compared to the healthy group. Second, even though these differences were statistically significant, considerably lower p-values from QSM results (both between the two groups and between the hemispheres within each group) showed higher sensitivity and reliability of susceptibility-based techniques to pick up more subtle changes in brain iron. Additionally, the error analysis from both of these iron

quantification techniques reveals that the variability of measurements associated with QSM is considerably less compared to that of R2*, [199] especially in the high iron content (RII) region. Despite the fact that R2* correlates well with QSM measures of iron content, R2* measurements (especially from a limited number of echo times) is more prone to noise. One major advantage of QSM is that it is in theory independent of echo time, but the SNR of the R2* maps depends critically on the echo time. [57] Practically an echo time of roughly 20ms is enough to give excellent susceptibility maps and in this case with 8 echoes excellent measurements of the DGM is possible.

Another key finding that validates previous results is the tightness (higher $r^2$ values) of the iron growth with age in the different DGM structures in the regional iron content measures. The fact that regional changes are much tighter than global changes opens the door to a better separation of patient types, specifically in terms of separating high iron content patients from normal iron content patients. Averaging over all patients, especially in the global analysis, will reduce the shift in the mean iron content and may be the reason that some of the previous studies failed to show increased iron content in the SN. [200] RII iron content may provide a new means to evaluate the role of regional changes in iron deposition. For example, it is believed that the loss of neuromelanin in the nigrosome-1 territory of the SN pars compacta leaves behind MR-visible iron. [201] Localizing where this high iron content occurs anatomically may help to answer this question.

Further, in this work, the ability to separate the high and normal RII iron content patients using QSM data led to the finding that there are in fact group differences in UPDRS-III scores. Similarly, by using R2*, Pesch et al. found a correlation between iron content and UPDRS-III scores in the SN of 35 PD patients. [202] However, their R2* measurements were not corrected for age. Since R2*

has been seen to increase as a function of normal aging, [94] it is imperative to take this factor into account in iron quantification studies.

There are a number of limitations to this study. First, the number of samples is small and a much larger population should be studied to best demonstrate the presence of two groups of PD patients. Second, no clinical phenotypes were considered while analyzing imaging data. Third, ROI tracings were done manually which might have induced some unwanted errors when demarcating different DGM nuclei especially around the edges; this source of error, however, gets substantially reduced when thresholded low susceptibility values are excluded in the regional analysis. Nonetheless, the undesired errors associated with manual ROI tracing in the global analysis could be effectively minimized by using atlas-based automated DGM segmentation techniques. [203] Finally, the fairly low in-plane resolution used in the GRE sequence made it difficult to evaluate the sub-structures, especially the SNpc whose abnormally high iron deposition is believed to be correlated with NM degeneration in the midbrain. [8-10] Higher spatial resolution is recommended in future studies for this purpose. In conclusion, the increase in iron in the SN in some PD patients is higher than the normal range in HC as found in both regional and global analyses. Using regional high iron content may provide a means to separate two populations of PD patients; one with and one without iron increases in the SN. Separating the PD population into two groups may prove useful in understanding the etiology of the disease as well as monitoring the disease progression.

**Chapter Five: Imaging Iron and Neuromelanin Simultaneously Using a Single 3D Magnetization Transfer Sequence: Combining Neuromelanin, Iron and the Nigrosome-1 Sign as Complementary Imaging Biomarkers in Early Stage Parkinson's Disease**

**Introduction**

Parkinson's disease (PD) is one of the fastest growing neurodegenerative disorders in the world and a leading cause of disability. Early PD diagnosis is still challenging and motivates an increasing need for non-invasive imaging biomarkers. Although Datscan can be used as an absolute exclusion criterion for diagnosing PD, [204] it is not widely available, it is expensive, and it uses radioisotopes.

PD is characterized by the classical motor features of parkinsonism with early prominent death of dopaminergic neurons in the substantia nigra pars compacta (SNpc). The SNpc (referring to the dorsal part of SN) and the SN pars reticulata (SNpr, referring to the ventral part of the SN) are anatomically and functionally distinct (see Supplementary Section 9.1 for further anatomical details). The SNpr contains higher levels of iron than the SNpc in normal subjects, while the SNpc is rich in dopaminergic neurons which are known to accumulate neuromelanin (NM). Consequently, in most previous neuroimaging studies, [205] the SNpr is usually detected as a $T_2^*W$ hypointense region due to high iron content while the SNpc has both hypointense regions with high iron and hyperintense regions such as the nigrosome-1 NM rich area (due to its high $T_2^*$ values and lower iron content) as validated in NM-sensitive MRI (NM-MRI). [9] As a result, while the SNpc is characterized by NM content, the SNpr is usually responsible for regional high iron content in the

---

SN. Practically, it is very difficult to differentiate SNpr and SNpc with MRI. However, similar to other major deep gray matter nuclei of the brain, and complicating the issue, is the fact that total iron content in the SN increases as a function of age with a relatively large spread in values. [12, 198]

Anatomically, the NM-containing dopaminergic neurons are not restricted to the SNpc region. According to histological studies, [206] the dopaminergic neurons in the midbrain are located in three different groups referred to as A8, A9 and A10. Apart from the SNpc (group A9), the overall ventral tegmental area (VTA) region (located in A8 and A10) contain dopaminergic neurons. [205] The parabrachial pigmented nucleus (PBP) or SN pars dorsalis (SNpd) is located ventromedially to dorsolaterally between the red nucleus and the SNpc while the VTA nucleus lies ventral to the RN at the ventromedial limit of the PBP. The PBP together with the midline VTA nucleus constitute the dorsal tier of the dopaminergic neurons in the midbrain. Due to the variability of anatomical and neurochemical properties within the overall VTA region, it is difficult to separate the SNpc and the overall VTA region both histologically in humans and in-vivo on MR images. [207] However, using multi-contrast MRI, particularly using QSM, it is possible to differentiate the SNpc from the overall VTA region as a whole. [45] A schematic of the midbrain summarizing these structures is shown in Figure **5.1**.

It is believed that dopaminergic neuronal death in the SNpc is followed by NM depigmentation leaving behind iron that is then phagocytized and becomes visible in MRI. [43] Therefore, the most promising clinical MR biomarker candidates are iron content as seen with $R_2^*$ or quantitative susceptibility mapping (QSM) [11] and NM as measured with NM-MRI. [17] QSM provides a quantitative measure of the iron in the total SN, including the SNpc and SNpr, while the hyperintense signal seen in NM-MRI is spatially associated with the SNpc and the overall VTA

region inclusive of the SNpd as well as with the NM seen in postmortem histological studies. [27] It has been shown that the MRI representation of NM matches the dopaminergic territory seen in PET and that the intensity of the NM signal in MRI correlates with the dopamine release capacity. [24] The literature generally supports the concept that iron content is expected to increase in the SNpc in PD subjects while NM is expected to decrease in PD subjects. [21, 22, 184] An alternate approach that does not measure NM throughout the SN but rather is sensitive to just the NM in the nigrosome-1 (N1) territory has also been promoted as a possible means to discriminate between PD subjects and healthy controls (HC). [16-18] The disappearance of the N1 sign is a surrogate marker to the loss of NM overall as well as an increase in local iron content, [19] but this approach does not actually measure NM or iron content quantitatively. However, the sensitivity and specificity of either NM, iron or the N1 sign in the SN may not be good enough for them to qualify as diagnostic biomarkers by themselves. [20-22]

Some studies have combined NM and iron measures, but they used two different sequences which required co-registration and data interpolation [21, 22, 30, 44, 45] and, sometimes, the use of a NM template mask. [9] Only one group used a single two-echo 2D gradient echo (GRE) sequence to study NM and susceptibility weighted imaging (SWI). [73] Apart from the volume and intensity measures of SN or NM usually used in PD neuroimaging studies, a prior study [208] showed that the overlap between the iron content as determined by $R_2^*$ mapping and the neuromelanin mask of the SNpc provided good diagnostic performance to differentiate PD from HC. Also, during the past few years, the N1 sign which is usually imaged with a 3D SWI scan [18] is gaining attention as a potential imaging biomarker of pathophysiologic changes in PD subjects. Our hypothesis is that the combination of these imaging measures will provide a comprehensive understanding about

pathophysiological changes in the SN underlying PD and outperform each single measure by themselves.

Therefore, our goal in this chapter is to use a single sequence to evaluate four metrics as imaging biomarkers to differentiate early stage PD subjects from HCs: the NM complex volume (SNpc plus PBP), SN volume (SNpc plus SNpr), SN iron content (as measured using susceptibility in QSM) and N1 sign. This innovative approach uses a 3D multi-echo, GRE, magnetization transfer contrast (MTC) sequence that can be run in a clinical setting in less than 5 minutes.

**Materials and Methods**

*Subjects*

This study was approved by the local ethics committee at Ruijin Hospital and consent forms were signed by all subjects. Forty subjects with early-stage idiopathic PD and 40 sex- and age-matched HCs were recruited consecutively from the Ruijin movement disorder clinic and local advertisements from May 2018 to January 2019. All subjects were on medication. The diagnosis and severity of motor symptoms were assessed by two neurologists based on the Movement Disorders Society (MDS) PD criteria, [204] the Hoehn & Yahr (H&Y) stage and the MDS Unified Parkinson's Disease Rating Scale Part-III (UPDRS-III), [209] Symptom laterality was determined by measuring the difference between the right and left UPDRS-III sub scores, [210] The exclusion criteria of PD were as follows: (1) H&Y scale more than 2.5; (2) Mini-Mental State Examination (MMSE) score less than 24; (3) a history of cerebrovascular disease, brain tumor, head trauma or any other type of psychiatric disorders; (4) a history of medication known to cause parkinsonism or affect clinical assessment; (5) contraindications to an MRI examination, and (6) younger than 40 years of age. The inclusion criteria for the HCs were as follows: (1) no family history of movement disorders; (2) no

neurological or psychiatric disorders; (3) an MMSE score of at least 24 and (4) older than 40 years of age. PD subjects were evaluated one year later to confirm the diagnosis using the same MDS-PD diagnostic criteria as used at the baseline for PD diagnosis.

*MRI Data Collection*

All data were collected on a 3T Ingenia scanner (Philips Healthcare, Netherlands) using a 15-channel head coil. A seven-echo 3D SWI sequence with an MTC pulse was collected using: TE = 7.5 ms and $\Delta$TE = 7.5 ms, TR = 62 ms, flip angle = 30˚, pixel bandwidth = 174 Hz/pixel, matrix size = 384 $\times$ 144, slice thickness = 2 mm, in-plane resolution = 0.67 mm $\times$ 1.34 mm and total scanning time = 4 min 47 s for 64 slices. The MTC pulse was an on-resonance [211] 90$^o$ flip angle with 3 block pulses of 1.91ms which is part of the Philips product sequence. [212] To validate that the phase images from the MTC scan can also provide normative QSM data, a separate multi-echo SWI sequence was acquired as part of the strategically acquired gradient echo (STAGE) protocol [213-215] using: TEs = 7.5 and 17.5 ms, TR = 25 ms, flip angles = 6˚ and 24$^o$, pixel bandwidth = 220 Hz/pixel, imaging matrix size = 384 $\times$ 144, slice thickness = 2 mm, an in-plane resolution = 0.67 mm $\times$ 1.34 mm and a scanning time of 1 min 53 s for 64 slices per scan. In both cases, the images were interpolated to an in-plane resolution of 0.67 mm $\times$ 0.67 mm. The axial slice orientation was the anterior commissure posterior commissure (ACPC) line for all scans.

*MTC and QSM Data Processing*

The NM signal was evaluated from the first echo (TE = 7.5 ms) of the MTC data while the susceptibility maps (denoted as MTC-QSM) were calculated using the second echo (TE = 15 ms) data to avoid more severe aliasing at the longer echo times. The MTC-QSM process included the following steps: a brain extraction tool  was applied (threshold = 0.2, erode = 4 and island = 2000)

[195] using the first echo magnitude data; a 3D phase unwrapping algorithm (3D sorting by reliability following a non-continuous path or 3DSRNCP) was used to unwrap the original phase data [196]; sophisticated harmonic artifact reduction (SHARP) was used to remove unwanted background fields (threshold = 0.05 and deconvolution kernel size = 6) [58]; and a truncated k-space division based inverse filtering technique (threshold = 0.1) [59] was used with an iterative approach (iteration threshold = 0.1 and number of iterations = 4) to reconstruct the susceptibility maps. [117] The same QSM processing pipeline was used to reconstruct the second echo (TE = 17.5 ms) data from the STAGE sequences, denoted as STAGE-QSM. Finally, the MTC-QSM and the magnitude image of the second echo were used to create true SWI (tSWI) data for the detection of the N1 sign. [121]

*Defining the NM and iron boundaries and quantification of volumes and susceptibility*

Two sets of regions of interest (ROIs) were outlined separately one for NM on the MTC images and one for iron on the MTC-QSM images. The images were first zoomed by a factor of four to more easily and accurately draw the boundaries for NM and iron. The iron-based SN ROIs were traced starting from one slice below the most cranial slice where the subthalamic nucleus was visible and continued for four to five consecutive slices to the most caudal slice. The NM boundaries, however, were traced from the last caudal slice (which corresponds to the most caudal slice showing iron content in the SN) for four to five slices cranially until the NM was no longer visible as shown in Figure **5.1**. The NM complex used in this study was defined as the region showing NM contrast in the midbrain but excluding the midline VTA nucleus (as shown in the central dark gray area in Figure **5.1** fourth column).
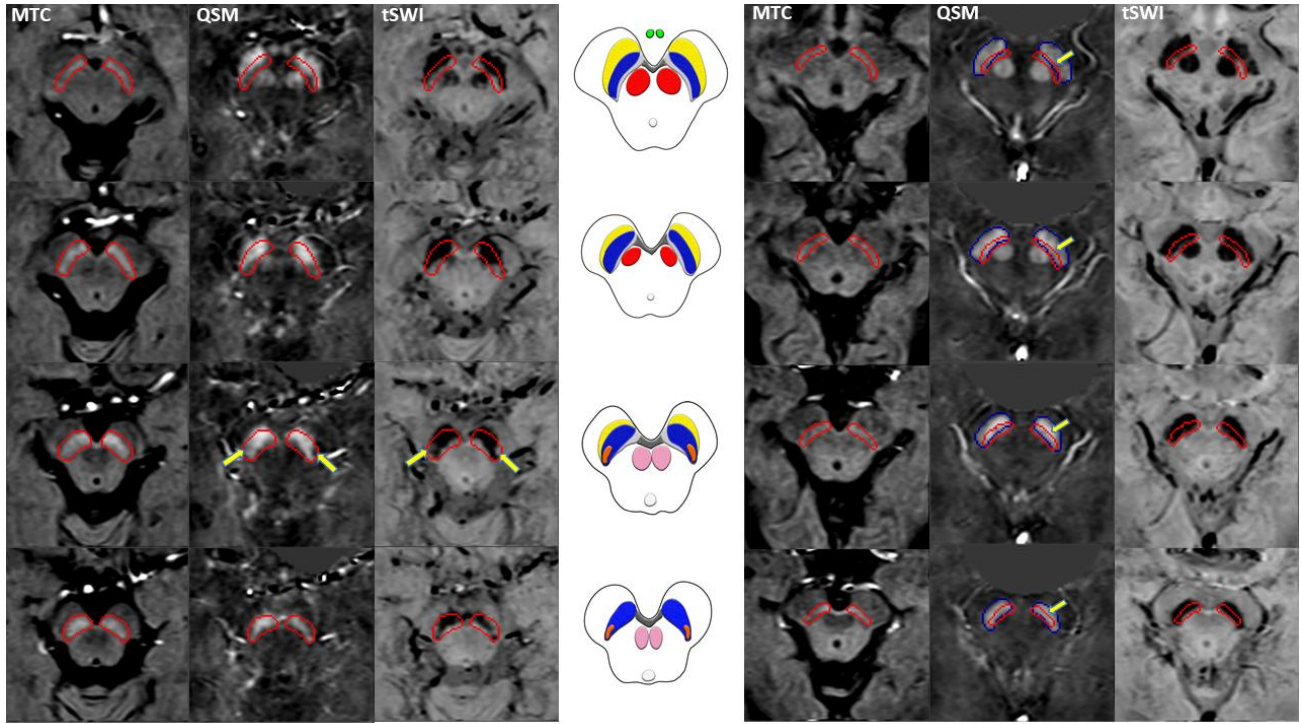
**Figure 5.1**. Neuromelanin, iron and N1 in the SN as represented by MTC magnitude, MTC-QSM and MTC-tSWI data**.** From left to right the first three columns show four consecutive slices from a 63-year-old healthy control followed by the schematic of different midbrain structures and the same contrasts from a 62-year-old PD subject shown in the last three columns. The top and bottom rows show the most rostral and most caudal slices, respectively. The red ROIs representing the NM complex were drawn on the MTC magnitude data and then overlaid on the corresponding MTC-QSM and MTC-tSWI datasets. It should be noted that the overlap between the NM complex and the iron containing SN (i.e., the SNpc in controls) increases towards the caudal slices in the HC subject while this area is substantially smaller in the PD subject on a slice-by-slice basis ($p = .040$ for all the slices where both NM and the iron containing SN are present). The yellow arrows in the second and third columns show the N1 territory located in the ventral-lateral aspect of the NM complex while the yellow arrows in the right column represent the directionality of the NM loss (and overlap) starting from the ventral tier and continuing towards the dorsal tier of the SNpc. The regions shown by the NM boundaries but that lie outside the SN as highlighted in the QSM data represent the PBP (also known as the SNpd). The highlighted regions in the schematic represent: green: mammillary bodies; pink: superior cerebellar peduncles; red: red nucleus, orange: Nigrosome-1 territory; yellow: SN pars reticulata (SNpr); blue: SN pars compacta (SNpc); light gray: SN pars dorsalis (SNpd)/parabrachial pigmented nucleus (PBP); and dark gray: ventral tegmental area (VTA) nucleus.

Finding the final boundaries was done with a two-step process. First, all initial input boundaries were reviewed by three raters and then an intermediate set of boundaries was chosen by consensus. These boundaries were initially traced a few pixels outside what would have otherwise been drawn manually by any of the raters while avoiding the hyperintense structures such as veins outside the desired final ROI. Second, to remove the human element completely, a dynamic programming algorithm was used to determine the final boundaries [216] (see Supplementary Section 9.2 and

Supplementary Figure **9.3** for more details). This semi-automated approach provides a means to generate a mathematically determined user independent boundary. DICE similarity coefficients associated with different sets of results from the raters before reaching consensus were calculated as .89 and .84 for the $SN_{VOL,MTC}$ and .91 and .88 for the $SN_{VOL,QSM}$ in the HC and PD subjects, respectively. A partial volume correction of the most caudal slice was performed on the NM, QSM and overlap fraction data. The partial volume effect was calculated based on the contrast of the most caudal slice and of the second and third most caudal slices via:

$$Volume\ of\ the\ slice\ with\ partial\ volume\ effect \qquad (5.1)$$

$$= measured\ volume\ of\ the\ slice$$

$$\times \frac{contrast\ of\ the\ slice}{average\ contrast\ of\ the\ two\ middle\ slices}$$

A volumetric analysis was performed using the boundaries from all slices covering both the NM and iron containing SN. The results were then compared between the PD and HC groups as well as between the two hemispheres for each group for the NM complex and iron containing SN total volumes. The overlap between the NM complex volume (SNpc plus PBP) and iron containing SN volume (SNpc plus SNpr) was evaluated by superimposing the two ROIs from the MTC and MTC-QSM data, respectively. This overlap was normalized by the iron containing SN volume creating an overlap fraction measure which basically represents the SNpc fraction with respect to the entire SN volume (Figure **5.1**), as given below:

$$Overall\ Overlap\ Fraction \qquad (5.2)$$

$$= \frac{\sum_{slices\ where\ SN_{pc}\ is\ present} volume\ of\ the\ intersection\ between\ NM\ and\ SN}{\sum_{slices\ where\ SN_{pc}\ is\ present} volume\ of\ the\ iron\ containing\ SN}$$

For ease of reference, hereafter we define $SN_{VOL,MTC}$ as the SNpc plus PBP volume measured from the MTC data in $mm^3$; $SN_{VOL,QSM}$ as the total SN volume (SNpc plus SNpr) measured on MTC-QSM in $mm^3$; $SN_{\Delta\chi}$ as volumetric mean susceptibility from MTC-QSM in ppb; and $SN_{OVERLAP}$ as the intersection of the $SN_{VOL,MTC}$ and $SN_{VOL,QSM}$ normalized to $SN_{VOL,QSM}$ in percent.

The mean susceptibility of the SN was measured and compared between the two groups in both hemispheres. These global values were plotted as a function of age against the corresponding baselines from a normal population established by Liu et al. [12]. To demonstrate that MTC-QSM and the normative STAGE-QSM (without the MT pulse) are equivalent to each other, the same SN boundaries traced on MTC-QSM were superimposed on the STAGE-QSM data for the HCs. The two datasets acquired with the same resolution and brain coverage were aligned to each other by the magnitude images using SPM software (V12, Functional Imaging Laboratory, UCL, London, UK), and the QSM data were then transformed according to the geometric displacement matrix. For each case, the mean susceptibility was extracted from the whole 3D ROI and averaged over the two hemispheres. A linear regression model was applied to evaluate the correlation between the averaged mean susceptibility between these two sequences for all the HCs and PD subjects. (see Supplementary Section 9.3)

In order to assess the potential dependence of volumetric analyses to brain tissue atrophy and spread of the data in both cohorts, a normalization of $SN_{VOL,MTC}$ and $SN_{VOL,QSM}$ to the whole midbrain volume was done by manually tracing 3D boundaries on the first echo magnitude data. (see Supplementary Section 9.6)

*N1 sign evaluation*

The N1 sign evaluation (no loss, unilateral loss or bilateral loss) was performed in a blinded manner using the MTC-tSWI data (which has been found to be the best modality to show the N1 sign in previous works) [18, 217] and the MTC-QSM data by two reviewers separately. The consensus results between the two reviewers were then used for the final analyses. To validate the interpretation of the data, each slice where the N1 sign was found was compared with the boundaries from the MTC data to ensure that the interpretation of the N1 sign was correct in that it was situated in the ventral-lateral side of the NM complex. This has not been possible previously when just using QSM by itself as the N1 sign is usually recognized either by the swallowtail or ovoid sign and a hyperintense area remaining inside. Using the MTC boundaries assures a correct interpretation of the data.

*Statistical Analysis*

Subject characteristics are presented as mean ± standard error of the mean (SEM). Two-sample and paired t-tests were used for inter-group comparisons between the two groups and intra-group comparisons between the two hemispheres as well as the comparison between the ipsilateral and contralateral sides in the PD group, respectively. The area under the curve (AUC) for receiver operating characteristic (ROC) analysis was calculated to evaluate the overall diagnostic performance of the $SN_{\Delta\chi}$, $SN_{VOL,QSM}$, $SN_{VOL,MTC}$ and $SN_{OVERLAP}$, as independent predictors. Then, the diagnostic performances for PD were compared using the DeLong test. Binary logistic regression was used to integrate information from different combinations of these measures to produce associated ROC curves. We performed partial correlation analysis to explore relationships between each image feature and the clinical variables (disease duration and UPDRS-III) using age and sex as

covariates. All statistical analyses were performed using IBM SPSS Statistics Version 25 (International Business Machines Corporation, Armonk, NY, USA). A *p*-value < .05 for two-sided tests was considered significant. The Bonferroni correction was used to correct the partial correlations when multiple comparisons were used in the correlation analyses (p-value threshold for significance: .006) and ROC comparisons (p-value threshold for significance: .003).

**Results**

Demographic and clinical characteristics are shown in Table **5.1**. There was no significant difference in sex or age between the two groups. For any of the imaging measures discussed herein, there were no significant differences between the ipsilateral and contralateral side for the PD group, or between the left side and right side for the HC group.

**Table 5.1.** Comparison of clinical status between two sub-groups of the PD cohort with normal and abnormal RII iron content in the substantia nigra.

| | Parkinson's disease | Healthy controls | *p*-value |
|---|---|---|---|
| **Sex, man:woman** | 20:20 | 20:20 | - |
| **Age, years[a]** | 63.10 ± 8.05 [43 - 76] | 65.50 ± 8.19 [44-81] | .19 |
| **Disease duration, years** | 2.55 ± 2.92 [0.08 - 15] | | |
| **UPDRS-III** | 22.73 ± 14.26 [6 - 64] | | |
| **Hoehn and Yahr scale** | 1.78 ± 0.52 [1 - 2.5] | | |
| **Symptom laterality, left:right** | 14:26 | | |

Values represent mean ± standard deviation [range]. The UPDRS-III was administered while subjects were in the ON medicated state. [a]Significant differences were tested using independent t-test.

*NM complex and iron containing SN volume comparison between early stage PD subjects and healthy controls*

An example set of the slices evaluated is shown pictorially in Figure **5.1**. These boundaries were used to calculate $SN_{VOL,MTC}$ and $SN_{VOL,QSM}$. The $SN_{VOL,MTC}$ were $(322.85 \pm 4.72)$ mm$^3$ and $(234.58 \pm 6.22)$ mm$^3$ averaged between the right and left hemispheres of the HC and PD groups, respectively. This example also highlights the fact that the N1 sign shown in the caudal slices lies within the ventral-lateral tier of the NM boundary. The PD group had significantly lower NM complex volumes

than those of the HC group ($p < .001$). There was no significant correlation of SN$_{VOL,MTC}$ with age for either group. (see Supplementary Section 9.4 and Supplementary Figure **9.6**) The SN$_{VOL,QSM}$ were ($477.53 \pm 12.63$) mm$^3$ and ($395.38 \pm 9.61$) mm$^3$ averaged over the right and left hemispheres of the HC and PD groups, respectively, with the PD group showing lower volumes ($p < .001$). There was a decreasing trend in SN$_{VOL,QSM}$ as a function of age (Supplementary Figure **9.6**) which reached significance for PD ($p = .001$) but not for HCs ($p = .070$). The mean SN$_{OVERLAP}$ values were ($39.96 \pm 1.05$)% and ($36.49 \pm 1.29$)% averaged over the right and left hemispheres of the HC and PD groups, respectively, with the PD group showing lower overlap percentages ($p = .040$) (Supplementary Table **9.1**). There were no significant differences between male and female results in any of the measures ($p > .050$ in all cases).

The scatter plots for SN$_{VOL,MTC}$ versus SN$_{OVERLAP}$, SN$_{VOL,QSM}$ and SN$_{\Delta\chi}$ are presented in Figure **5.2**A-C, respectively. Figure **5.2**A shows the SN$_{VOL,MTC}$ as a function of SN$_{OVERLAP}$ in all 4 to 5 slices where both NM and SN are present. However, there is a larger overlap of PD and HC cases between SN$_{VOL,MTC}$ and either SN$_{OVERLAP}$ or SN$_{VOL,QSM}$ (Figure **5.2**A-B) compared to that of SN$_{VOL,MTC}$ and SN$_{\Delta\chi}$ (Figure **5.2**C). The sensitivity, specificity and accuracy associated with the relationship between SN$_{VOL,MTC}$ and SN$_{\Delta\chi}$ (Figure **5.2**C) provided slightly better, although statistically insignificant, performance in separating the two cohorts compared to the other two metrics. ($p = .292$ comparing SN$_{VOL,MTC}$/SN$_{\Delta\chi}$ to SN$_{VOL,MTC}$/SN$_{OVERLAP}$ and $p = .470$ comparing SN$_{VOL,MTC}$ to SN$_{VOL,MTC}$/SN$_{VOL,QSM}$).
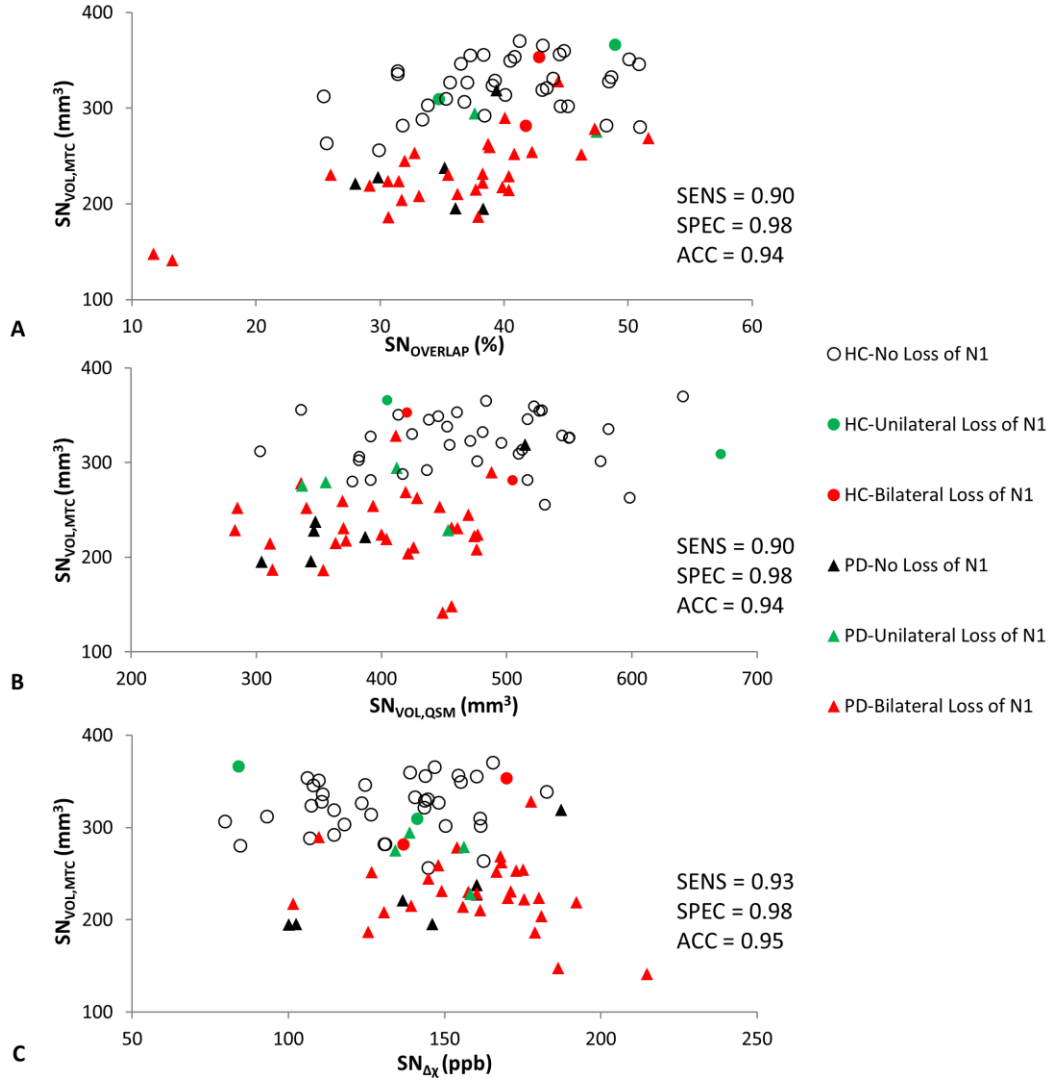
**Figure 5.2**. Distinguishing between the two groups using NM complex volume and three other measures. $SN_{VOL,MTC}$ volume as a function of (A) $SN_{OVERLAP}$, (B) $SN_{VOL,QSM}$, and (C) $SN_{\Delta\chi}$. The data indicate the loss of N1 for both groups. Sensitivity (SENS), specificity (SPEC) and accuracy (ACC) values are also shown for each plot.

*Using MTC-QSM to quantify iron in PD*

The relationship for the HCs between the two QSM approaches is shown in Supplementary Figure **9.4** and Supplementary Figure **9.5** in Supplementary Section 9.3. The results confirm a strong positive relationship ($R^2 = .751$, $p < .001$, slope = 1.11, $p < .001$) between them indicating that MTC-QSM provides similar susceptibility values compared to the normative STAGE-QSM and, therefore, MTC-QSM is suitable to estimate regional brain iron levels.

*SN iron deposition in PD*

Using MTC-QSM, there was a higher iron content for early stage PD subjects compared to HCs in both hemispheres ($p < .001$). The data for the SN susceptibility analyses superimposed on the corresponding susceptibility-age baselines [12] are shown in Figure **5.3**. The $SN_{\Delta\chi}$ values were $(132.12 \pm 4.01)$ ppb and $(155.30 \pm 4.09)$ ppb averaged over the right and left hemispheres of the HC and PD groups, respectively, with the PD group showing higher $SN_{\Delta\chi}$ ($p < .001$). Not only did the PD group show higher iron content, within the PD group, the presence of bilateral loss of N1 sign was most evident in those cases with the highest iron content. Specifically, a total of 21 out of 25 PD cases on the right and 14 out of 15 cases on the left that lay above the 95% prediction interval for the iron distribution had bilateral loss of the N1 sign (Figure **5.3**). We also note that the more caudal the slice the more the NM overlaps with the iron (representing the SNpc) until at the last slice where it is almost a complete overlap showing that caudally the SN is predominantly the SNpc (see Figure **5.1**).

*The added information from the N1 sign*

The results from the N1 analysis reveal that 36 out of 40 HC cases showed bilateral presence of N1 while N1 loss, either unilaterally or bilaterally, was detected in 34 out of 40 PD cases. The N1 sign information included in Figure **5.2** shows that some PD cases that appear in the HC region are in fact bilateral loss of the N1 sign, making it possible to remove them from the HC region and further improve the sensitivity of the NM and SN volume. The N1 sign performed reasonably well by itself (AUC = .891) but was significantly improved when merged with $SN_{VOL,MTC}$ (AUC= .979; $p < .001$) and $SN_{\Delta\chi}$ (AUC =.953; $p = .056$). However when the N1 sign was merged with $SN_{VOL,MTC}$ and $SN_{VOL,QSM}$, , the highest AUC of .983 ($p = .003$) was obtained.
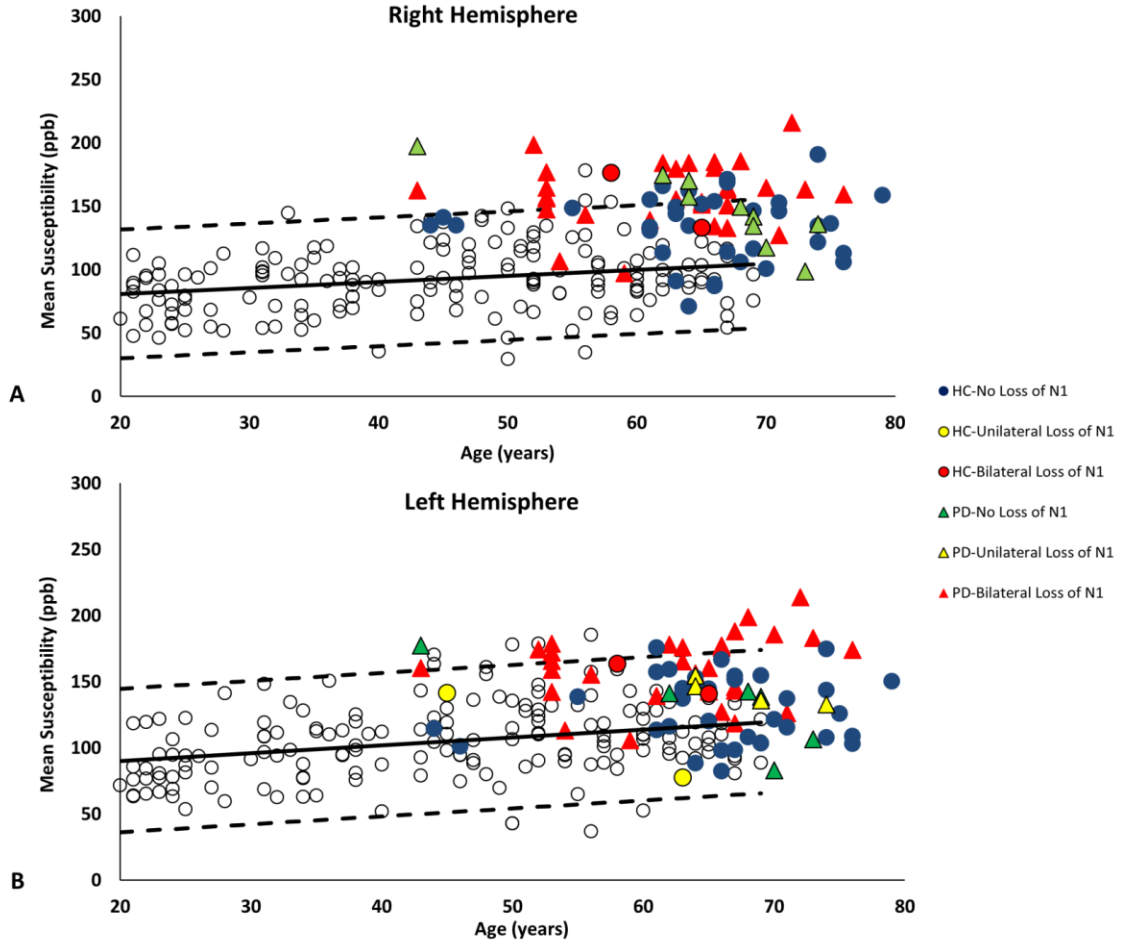
**Figure 5.3**. Mean susceptibility as a function of age for a large normal population as well as HC and Parkinson's cases in this study. SN global iron content of the HC and Parkinson's disease groups associated with the (A) right and (B) left hemisphere. The bilateral, unilateral, and no loss of Nigrosome-1 for each group are also shown. The data are superimposed on the corresponding normal baselines established by Liu et al. illustrated by open circles. [12] The solid line and dashed lines show the linear regression model associated with the normal baseline and its corresponding 95% prediction intervals, respectively.

*Diagnostic performance for early stage PD*

The AUC values associated with the average of the right and left hemispheres were .960 for the $SN_{VOL,MTC}$; .788 for the $SN_{VOL,QSM}$; .740 for the $SN_{\Delta\chi}$ and .629 for the $SN_{OVERLAP}$. However, combining the two QSM related measures, $SN_{VOL,QSM}$ and $SN_{\Delta\chi}$, yielded AUC values of .859 and adding $SN_{OVERLAP}$ brought these values to .911. Normalizing the $SN_{VOL,MTC}$ and $SN_{VOL,QSM}$ volumes to the whole midbrain volume did not improve the classification performance associated with any of

the measured values. To support this claim, the $p$-values associated with the un-normalized versus normalized ROC curves corresponding to the combination of $SN_{VOL,MTC}$ with each of $SN_{VOL,QSM}$, $SN_{\Delta\chi}$ and $SN_{OVERLAP}$ were found to be .38, .36 and .49, respectively, indicating that the normalized data showed no significant improvement over the un-normalized data (see Supplementary Section 9.6 and Supplementary Figure **9.9**).

The ROC curves associated with the $SN_{VOL,MTC}$, $SN_{VOL,QSM}$, $SN_{\Delta\chi}$ and $SN_{OVERLAP}$ are illustrated in Figure **5.4**A. As suggested in these plots and with respect to the above-mentioned AUC values, the $SN_{VOL,MTC}$ had a significantly higher AUC compared to those of the $SN_{VOL,QSM}$, $SN_{\Delta\chi}$ or $SN_{OVERLAP}$ for the average of the right and left hemispheres in differentiating early stage PD subjects from HCs ($p < .001$ for all), respectively (Figure **5.4**A). The ROC curves associated with the combination of $SN_{VOL,MTC}$ and the three other measures are shown in Figure **5.4**B. The corresponding AUC values were .969 for the combination of $SN_{VOL,MTC}$ and $SN_{VOL,QSM}$, .965 for $SN_{VOL,MTC}$ and $SN_{OVERLAP}$, and .976 for $SN_{VOL,MTC}$ and $SN_{\Delta\chi}$ for the average of the right and left hemispheres, respectively. The AUCs associated with all of the measure combinations are shown in Supplementary Table **9.2**. Although we obtained a higher AUC value for the combination of all four measures than any individual measure, the difference was not significant ($p = .222$) compared to $SN_{VOL,MTC}$ alone, but was significant when compared to the rest of the individual measures ($p < .001$). Also, the AUC from the combination of $SN_{\Delta\chi}$ and $SN_{VOL,QSM}$ measures showed a low p value of .020 compared to $SN_{VOL,MTC}$ alone but not low enough to be significant at the .003 level (Supplementary Table **9.3**).
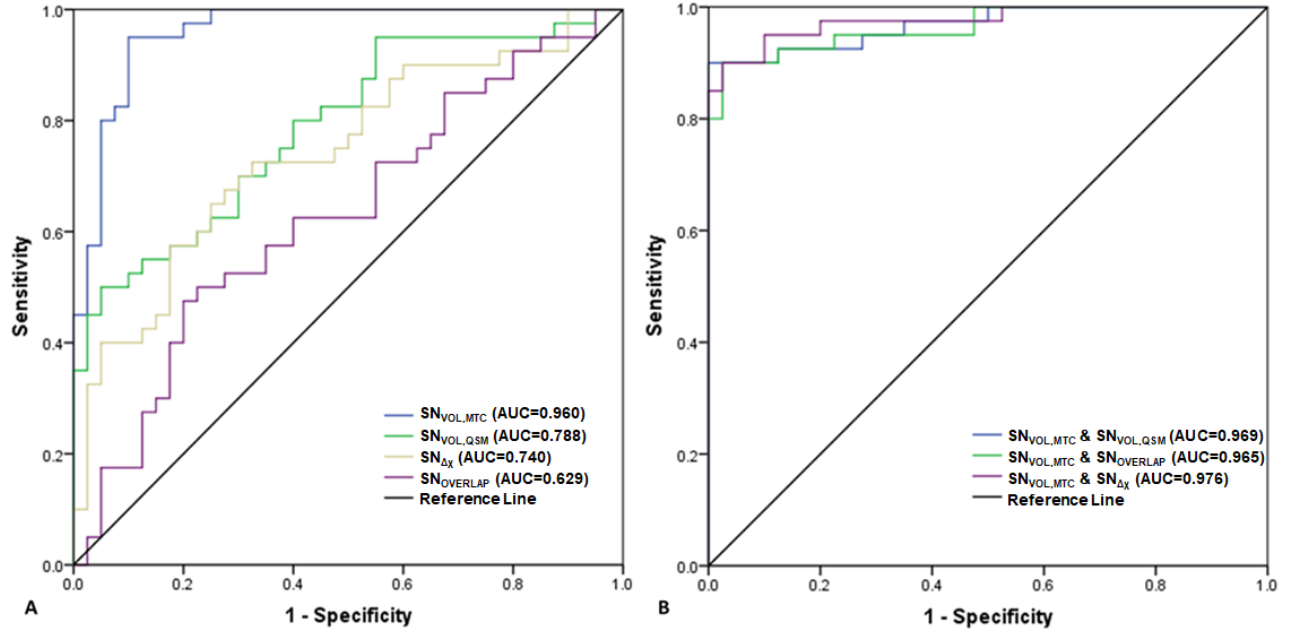
**Figure 5.4**. ROC analyses of diagnostic performance using different neuroimaging measurements. (A) ROC analyses of the different combinations of NM complex volume (SNVOL,MTC), SN volume (SNVOL,QSM), global mean iron content (SN$\Delta\chi$,) and overlap fraction (SNOVERLAP) for the individual measures. (B) The combination of NM complex volume with the three other measures was calculated via a binary logistic regression analysis. The data are averaged over both hemispheres.

*Correlation analysis between imaging features and clinical scales*

There was a significant loss of SN$_{VOL,QSM}$ with increasing UPDRS-III score ($R^2 = .22$, $p = .002$) (Figure **5.5**A). The correlation was not significant between the SN$_{\Delta\chi}$ and disease duration for the whole group ($R^2 = .12$, $p = .027$) (Figure **5.5**B), but there was a positive correlation between SN$_{\Delta\chi}$ and disease duration ($R^2 = .32$, $p < .001$) in the subgroup of PD patients with disease duration less than or equal to 5 years which is considered as early PD. [204] There were no other significant correlations with any of the other quantitative MRI measures or clinical scales.
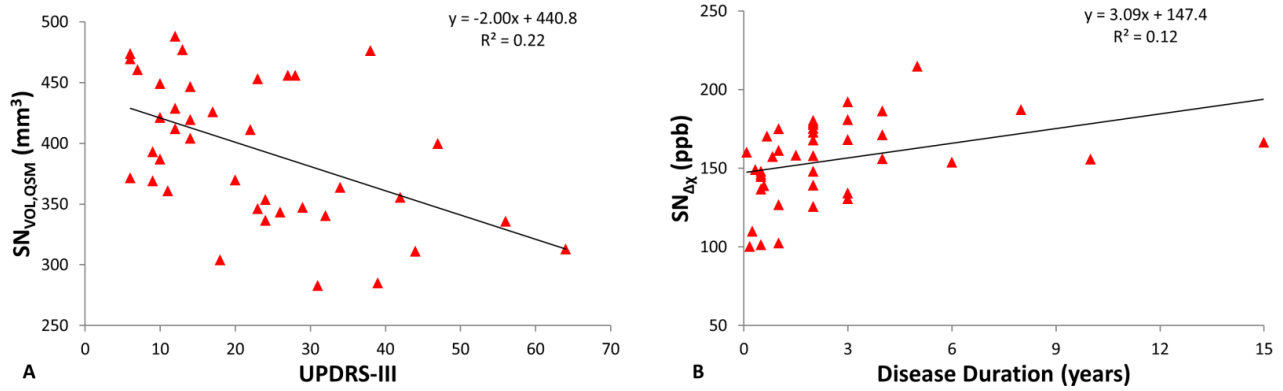
**Figure 5.5**. The correlations of SN volume and iron content with clinical characteristics of Parkinson's disease. (A) $SN_{VOL,QSM}$ (averaged over both hemispheres) versus UPDRS-III. There is a significant reduction in the $SN_{VOL,QSM}$ as UPDRS-III increases ($p = .002$). (B) The correlation between $SN_{\Delta\chi}$ (averaged over both hemispheres) and disease duration in PD subjects ($p = .027$) is not significant after Bonferroni correction ($p$-value threshold for significance: .0125). There appears to be a rapid rise in the iron content in the first 5 years (with $y = 11.8x + 133.4$, $R^2 = .32$, and $p < .001$) and then it levels off for the early stage PD group.

## Discussion and Conclusions

To our knowledge, the integration of NM, iron, iron-NM overlap and the N1 sign derived from a single sequence to differentiate early stage PD from healthy controls has not been presented in the literature. In this study, the $SN_{VOL,MTC}$ provided the highest single measure diagnostic accuracy while the N1 sign provided the second highest diagnostic performance. Merging the $SN_{VOL,MTC}$ and $SN_{VOL,QSM}$ with the N1 sign yielded the highest AUC among all singular predictors and all combinations of predictors. We also found $SN_{VOL,QSM}$ negatively correlated with UPDRS-III and the $SN_{\Delta\chi}$ increased with disease duration in PD subjects during the first 5 years after showing clinical symptoms.

Previous studies have shown that diagnostic AUC for individual measures (NM contrast, $SN_{VOL,MTC}$, $SN_{\Delta\chi}$ and the width of SNpc) can vary from .65 to .92 [8, 10, 21, 22, 29-31, 34, 218-220] whereas our results for the combination of $SN_{VOL,MTC}$, $SN_{VOL,QSM}$, $SN_{\Delta\chi}$ and the N1 sign generated an AUC of up to .98. The main advantages of this single MTC sequence approach include:

simultaneous NM and iron content information; rapid acquisition time (less than 5 minutes); no need for co-registration or the creation of templates; and high contrast data which is critical for boundary detection. [212] Further, the semi-automated DP boundary detection approach we used in this study brought the boundaries traced by the raters in line with each other. This rapid approach to obtain both the iron and NM information simultaneously opens the door to its potential practical use in a clinical setting.

The results of this study showed an AUC for $SN_{\Delta\chi}$ and $SN_{VOL,QSM}$ measures together (which are both derived from QSM data) of .859 in differentiating early stage PD subjects from HCs. A similar approach comparing the NM and QSM data (but derived from two sequences) was used by Takahashi et al. using QSM and $SN_{VOL,MTC}$ derived from the SNpc component (VTA volumes removed); they found an AUC of .86 in both studies. [21, 22] The $SN_{OVERLAP}$ by itself performed poorly, likely due to the fact that the $SN_{VOL,MTC}$ and $SN_{VOL,QSM}$ can both be reduced leaving the overlap fraction invariant. On the other hand, it should be noted that even though under normal circumstances there is an almost complete overlap between $SN_{VOL,MTC}$ and $SN_{VOL,QSM}$ in the most caudal slice delineating the SNpc, the NM loss in PD patients appears to be happening mostly in the posterolateral aspect of the SNpc where the N1 territory is anatomically located.

Prior studies have shown that the N1 sign could be used to differentiate PD from HCs with reasonably good accuracy. [16, 17] Although this method is attractive because of its visual nature in the images, it is not trivial as there is still overlap of the N1 appearance between PD subjects and HCs and none of the approaches introduced to date take the volume of the N1 sign into account. [18] Our study for the first time incorporated the N1 sign along with other quantitative measures such as the $SN_{VOL,MTC}$, $SN_{VOL,QSM}$, $SN_{OVERLAP}$ and $SN_{\Delta\chi}$ resulting in a comprehensive analysis of the

pathological changes in PD. Although the N1 sign performs well by itself (AUC = .891), similar to the findings in Cheng et al, [18] it can be improved by combining this data with either $SN_{VOL,MTC}$, $SN_{VOL,QSM}$, or $SN_{\Delta\chi}$. This is not surprising since the N1 sign detection is not infallible. Further, the N1 sign does not quantitatively represent either iron or NM despite the fact that the absence of iron helps define the N1 sign appearance. We note that those PD cases with very high iron content turned out to show bilateral loss of the N1 sign. This is not surprising either as the loss of the N1 sign is generally assumed to mean that there is higher iron content in that area. [18] Based on the aforementioned discussion, it is imperative to understand the role of each of these potential biomarkers by themselves. Ideally, in future studies, one may use all of this complementary information to have a more comprehensive picture of the pathology behind what is actually happening in the midbrain of PD patients in terms of volumetric changes, N1 loss and iron deposition.

We found a significant correlation between the $SN_{VOL,QSM}$ and UPDRS-III total score. A number of studies have also shown a negative association between clinical measures such as UPDRS-III and $SN_{VOL,MTC,}$ [30] area [34] and width. [36] It should be noted that, from a pathological perspective, the loss of pigmented neurons in the SNpc is associated with disease duration and severity in PD [221] and that detecting atrophy of the contralateral SNpc side may allow earlier diagnosis as suggested by longitudinal PET studies. [222] Therefore, it is reasonable to expect such clinical correlations with the $SN_{VOL,QSM}$. The correlation was not significant between the global iron content and disease duration in the whole PD group but only significant in the sub-group during the first 5 years of disease duration. The increase in iron content is most likely due to the loss of at least the N1 and the increase in iron in that territory. [18]

However, no correlation was found between $SN_{VOL,MTC}$ and clinical scales even though it provided the highest AUC to differentiate early stage PD subjects from controls. The question of clinical correlation with imaging biomarkers is complicated since PD is a heterogeneous neurodegenerative condition with different genetics, pathology, clinical phenotypes and disease duration. In this work, only early stage PD subjects were recruited which means that a correlation with clinical data may not necessarily exist for these subjects. Ideally, we should be able to see correlations as subjects progress towards later stages of the disease. Furthermore, there is contradictory evidence in the literature regarding the correlation between NM measures and UPDRS-III scores. Some previous neuroimaging studies have shown significant correlations of NM volume with either UDPRS-III and/or disease duration [30, 36, 37, 42, 223] while a few other papers were unable to find any clinical correlations with NM volume. [10, 42, 192] Several pathological studies showed a loss of NM with the severity of the disease or disease duration in PD subjects. [221, 224-226] These findings are consistent with a loss of NM as a representation of pathological changes in the SN of PD patients. On the other hand, while other studies have shown weak or moderate correlations between UPDRS-III scores and the NM signal area [227] or NM volume, [40] another paper shows no association between the NM content and any of the above-mentioned clinical scores. [41] Therefore, given that we have a relatively small sample size of PD subjects going through their early stages and the fact that these clinical manifestations may vary across different populations, it is not surprising that we do not see such correlations. (see Supplementary Section 9.4) We found no correlation of QSM values with UPDRS-III in this study, although such correlation has been seen before in the literature. [228]  However, in general, inconsistent results have been reported across studies with some papers reporting no correlation of QSM values with

UPDRS-III. [169, 170] Since UPDRS-III measures motor performance at the time of the examination, [229] this discrepancy of the correlation between QSM values and UPDRS-III scores among different studies can be partly caused by residual treatment effects at the time of motor examination.

The semi-automatic DP approach used in this study provides a means to obtain consistent final boundaries using different initial ROIs for the NM complex and SN. However, it should be noted that any automated or semi-automated method still has certain constraints associated with them that can potentially lead to changes in volumetric results. Specifically, one study by Ogisu et al. found that by using a region-growing semi-automated technique the NM volumes can substantially decrease as a function of increasing thresholds leading to poor separation between PD and HC at lower threshold values. [29] Given the CNR associated with the MTC and QSM images as well as the nature of the DP algorithm used here, this technique tends to produce boundaries and volumes close to those from the full width half maximum and, hence, will have an intermediate volume compared to methods using low or high thresholds. We also reviewed the DP boundaries to ensure that no artifacts or errors in the boundaries occurred. This was unlikely given that the initial boundaries were manually drawn. See the supplementary material (Supplementary Section 9.7 in particular) for a more in-depth discussion of volume measurements compared across different methods and different papers.

There are a few limitations in this work. First, the lack of definite diagnostic confirmation by neuropathologic assessment is a potential limitation. Nevertheless, all the PD subjects were followed up clinically for at least 12 months and the clinical diagnoses were confirmed. Second, the sample size was relatively small and for clinical adoption of this methodology; a much larger number of

subjects will be required. Third, in order to accurately define the initial boundaries outside the final ROIs, the DP algorithm proposed in this study requires a priori knowledge of the anatomy of the structures in the midbrain. Fourth, one could use higher in-plane resolution to better define the boundaries of the ROIs, but it would come at the expense of increased scan time and less signal-to-noise as well as increased potential for patient motion. Fifth, this study only focused on differentiating early stage PD subjects from HCs but not differential diagnosis among parkinsonian disorders which is more challenging clinically. In the future, it will be interesting to investigate the differential diagnosis performance using this approach between PD and atypical parkinsonian syndromes.

In summary, we have introduced a rapid 3D imaging approach to depict NM degeneration and iron deposition simultaneously using a semi-automated boundary detection algorithm. Although the $SN_{VOL,MTC}$ had the highest AUC of the individual measures followed by the N1 sign with the second highest AUC, each measure plays a complementary role in evaluating PD with the $SN_{VOL,QSM}$ specifically correlating with UPDRS-III. This approach provides a practical MR imaging method to differentiate early stage subjects with PD from HCs with an AUC as high as .98. With minor changes in the sequence design, this multi-contrast GRE-based single MRI sequence has the potential to be implemented across all major manufacturers' equipment with a total acquisition time on the order of 5 minutes.

**Chapter Six: Assessing brain iron and volume of subcortical nuclei in idiopathic rapid eye movement sleep behavior disorder**

**Introduction**

Rapid eye movement (REM) sleep behavior disorder (RBD) is characterized by vocalizations, jerks and abnormal motor behavior during REM sleep, often associated with REM-related dream content. [230] Idiopathic RBD (iRBD) is recognized as the prodromal stage of α-synucleinopathies including Parkinson's disease (PD), PD dementia (PDD), dementia with Lewy bodies (DLB), and multiple system atrophy (MSA). Therefore, iRBD represents a unique opportunity for potential disease-modifying interventions. [46-48] Previous studies have shown cognitive dysfunction [49, 50] and subtle motor impairment in iRBD patients [51, 52] which might be useful in predicting early conversion and the specific type of α-synucleinopathy.

Iron metabolism has been a research focus in studying movement disorders such as idiopathic PD (IPD). [11] Local changes in iron content have been measured in different structures for different disorders. [198] More specifically, increased iron deposition has been found in the substantia nigra (SN) of IPD subjects. [148, 184, 231, 232] Given the iron deposition that takes place in the SN of IPD subjects and the loss of the nigrosome-1 (N1) sign, one can postulate that abnormal iron deposition may also occur in iRBD subjects. To date, only two studies have explored brain iron deposition in iRBD patients. A study by Lee et al. has reported that no differences were found in iron-related $R_2^*$ values between 15 iRBD patients and 20 healthy controls (HCs). [233] However, $R_2^*$ mapping is not as sensitive to iron content as quantitative susceptibility mapping (QSM) and it

can be affected by some confounding factors such as water and calcium content. [134] QSM can be used to overcome these limitations and provide better signal-to-noise in mapping iron content. [11, 98, 156, 234-237] Using QSM, a second study found significantly increased iron deposition in the SN of iRBD patients compared to HCs. [238] They explored iron deposition in the SN, globus pallidus (GP), red nucleus (RN), head of the caudate nucleus (CN), and putamen (PUT), but did not include the dentate nucleus (DN). [238] It has been reported that iron deposition in the DN is a potential biomarker for tremor-dominant PD [183] and it is considered appropriate to evaluate iron deposition in the DN for iRBD patients as well. Neither of these two studies evaluated the regional high iron content (RII iron) which may also be useful in differentiating iRBD from HCs. [239]

Recently, loss of the N1 sign has been reported as a potential imaging biomarker of pathophysiological changes in PD patients. [18] The N1 sign, also known as the swallowtail sign, has been described as a hyperintense signal in the middle of the posterior SN with two hypointense lateral and medial tails on susceptibility weighted imaging (SWI) or $T_2^*$ weighted imaging ($T_2^*$WI) and the opposite contrast on QSM and $R_2^*$ data. [240] A loss of the N1 sign has been associated with an increase in iron deposition. [197] Using QSM, SWI and true-SWI (tSWI, where instead of using filtered phase data the QSM maps are used as masks to generate susceptibility-weighted images [102, 121]) it is possible to monitor the presence of the N1 sign, [18, 121] although this has not been done yet for iRBD patients. The loss of the N1 sign is believed to be caused by the depigmentation of the neuromelanin content in that region resulting in an increase in MR visible iron as seen by susceptibility-dependent contrast imaging methods. [43] Of interest is the association between iron deposition and cognitive or motor impairment in PD, [157, 241] PDD, [234] Alzheimer's disease[242] and subcortical vascular mild cognitive impairment. [243] With that said, we

hypothesized that abnormal iron deposition could also be correlated with cognitive dysfunction and subtle motor impairment reported in iRBD patients. However, whether global or RII iron accumulation in the cerebral nuclei correlates with cognitive and motor impairment in iRBD patients remains uninvestigated.

Therefore, the aims of this chapter are: 1) to investigate the difference in the incidence of the N1 sign between iRBD patients and HCs using QSM, SWI and tSWI; 2) to measure global and RII iron deposition and volume changes of cerebral nuclei in iRBD patients using QSM; and 3) to investigate the correlations between global and RII iron in the cerebral nuclei with cognitive and motor function.

**Materials and Methods**

*Participants*

This prospective study was approved by the Tianjin Medical University General Hospital Review Board and Ethics Committee. All participants signed the informed consent. Twenty-nine iRBD patients were enrolled from Tianjin Medical University General Hospital from October 2016 to January 2020. The iRBD patients were diagnosed according to the standards described in the International Classification of Sleep Disorders criteria. [244] Patients with the following features were excluded: 1) age less than 18 years; 2) not right-handed; 3) history of psychiatric disorders, stroke, head trauma, unstable hypertension or diabetes, chronic obstructive pulmonary disease, or electroencephalographic abnormalities suggesting epilepsy, encephalitis, or any other neurologic disorders. All patients were observed with overnight video polysomnography (v-PSG) using a digital sleep laboratory system (Nicolet v32) and were instructed to go to sleep at their usual bedtimes. Twenty-eight age-, gender- and education-matched HCs were enrolled from Tianjin Medical University General Hospital staff or community members by advertisement. All HCs were right-

handed and eighteen years or older. The main demographic and clinical characteristics including age, sex, and disease duration were recorded for each subject. In order to evaluate the disease severity, iRBD patients were evaluated using the Rapid Eye Movement Sleep Behavior Disorder Questionnaire–Hong Kong (RBDQ-HK).

**Neuropsychological and Motor Function Evaluation**

Neuropsychological and motor function evaluations were performed by a trained neurologist in an evaluator-blinded fashion (X.Z. with 5 years of experience) in a quiet environment on the same day prior to MRI scanning. The neuropsychological evaluations included the following: 1) visuospatial function using the Rey Complex Figure Test (RCFT) [245] for score and time; 2) memory function using the Auditory Verbal Learning Test (AVLT), [246] including the total score, short delay recall, long delay recall, recognition, and RCFT delayed recall test; 3) attention-executive function with the Trail Making Test (TMT) A, TMT B, Stroop Color-Word Test (modified version) (Stroop A, Stroop B, Stroop C and Stroop interference effect which equals the time of Stroop C minus the time of Stroop B), and verbal fluency test, [247] and 4) language function using the Boston Naming Test. [247] The neuropsychological tests are listed in Table **6.1**. In our study, all 29 patients and 28 HCs underwent the same battery of neuropsychological tests. For each of the domains, the raw neuropsychological test scores were converted into z-scores according to the mean and standard deviations of the scores in the HC cohort. Subsequently, an average cognition z-score was calculated by averaging the z-scores of all separate cognitive domains.

The motor function tests included: 1) part III of the Movement Disorder Society revised Unified Parkinson's Disease Rating Scale (MDS UPDRS-III), 2) the alternate tap test, [248] 3) the 3-meter Timed Up and Go test [249] to evaluate the speed and flexibility of movement, and 4) the Flamingo

test [250] to assess the ability of the patient to balance on one leg for 1 minute. In our study, a subset of 21 iRBD patients and 16 HCs underwent the motor function tests while the others refused to take these tests due to the relatively long testing time.

**Table 6.1.** Comprehensive battery of neuropsychological tests used to evaluate cognitive status.

| Cognitive function | Tests |
|---|---|
| **Visuospatial function** | Rey Complex Figure Test for score and time |
| **Memory function** | Auditory Verbal Learning Test (AVLT) for total learning score short-delay and long-delay free recall and recognition<br>Rey Complex Figure Test (RCFT) delayed recall test |
| **Attention-executive function** | Trial making test<br>Stroop color-word test<br>Verbal fluency test |
| **Language function** | Boston naming test |

*MRI Data Acquisition*

All Twenty-nine iRBD patients and 28 HCs underwent MRI examinations. The MRI data were acquired using a 3.0T MRI scanner (MAGNETOM Prisma, Siemens Healthcare, Erlangen, Germany) equipped with a 20-channel phased-array head coil. Foam pads were used to keep the head motionless, and earplugs were used to reduce noise during scanning. All axial images were acquired parallel to the anterior–posterior commissural line from the middle sagittal plane of the MRI positioning image. The sequences run included: conventional axial $T_1$-weighted images ($T_1$WI) and $T_2$WI to exclude subjects with congenital cerebral structural abnormalities, cerebrovascular diseases, and space-occupying lesions followed by a high-resolution, 3D flow-compensated gradient-echo (GRE) as a part of the MR angiography and venography (MRAV) sequence [251] to acquire both original magnitude and phase images. The imaging parameters of the sequences were: 1) $T_1$WI: repetition time/echo time (TR/TE) = 250/2.43 ms, matrix size = 384 × 312; flip angle =

85$^o$, number of slices = 22, slice thickness = 5 mm, in-plane spatial resolution = 0.6 × 0.6 mm$^2$; FOV = 240 × 195; receiver bandwidth/pixel = 350 Hz/pixel and a total acquisition time = 1 minute and 4 seconds; 2) T$_2$WI: TR/TE = 3500/89 ms, matrix size = 384 × 312; flip angle = 150$^o$, number of slices = 22, slice thickness = 5 mm, in-plane spatial resolution = 0.6 × 0.6 mm$^2$; FOV = 240 × 195 mm$^2$; receiver bandwidth/pixel = 221 Hz/pixel and a total acquisition time = 1 minute and 1 second; 3) high-resolution 3D flow-compensated MRAV sequence: TR/TE = 20/12.5 ms, matrix size = 384 × 288; flip angle = 12$^o$, number of slices = 64, slice thickness = 2 mm, in-plane spatial resolution = 0.67 × 0.67 mm$^2$; FOV = 256 × 192; receiver bandwidth/pixel = 240 Hz/pixel and a total acquisition time = 6 minutes and 8 seconds.

*Postprocessing of QSM and Measurement of Susceptibility*

The post-processing of QSM from magnitude and phase images was performed with SMART (Susceptibility Mapping and Phase Artifacts Removal Toolbox, Detroit, MI) software. The following are the post-processing steps of the QSM reconstruction: First, the Brain Extraction Tool (BET) in the FMRIB Software Library (FSL) was employed to eliminate the skull and other regions with low signals. [195] Second, a 3D best-path algorithm was employed to exclude the phase wraps in the original phase images. [196] Third, the sophisticated harmonic artifact reduction for the phase data (SHARP) algorithm was employed to remove the background phase information. [58] Finally, the QSM images were reconstructed using the truncated k-space division algorithm using a k-space threshold of 0.1. [59]

The mean susceptibility values for the global iron (calculated from the whole structure) and RII regional high iron (calculated by using structure-specific thresholds to extract pixel values above the upper 95% prediction intervals of the corresponding global susceptibility-age normal baselines

established by Liu et al. [12]) were measured from the QSM data using SPIN (Signal Processing in Nuclear Magnetic Resonance, SpinTech MRI, Inc., Bingham Farms, MI, US) software. Two of the authors (CC with 9 years of experience in neuroradiology; KG with 6 years of experience in MR imaging, respectively) were responsible for these measurements; both were blinded to the clinical and epidemiological information. The cerebral nuclei in our study included: bilateral substantia nigra (SN), red nucleus (RN), dentate nucleus (DN), head of the caudate nucleus (CN), putamen (PUT), globus pallidus (GP), thalamus (THA) and pulvinar thalamus (PT). Considering that the size and shape of the cerebral nuclei are slightly different in different people and to ensure that the susceptibility was measured as accurately as possible, 3D regions of interests (ROIs) were outlined manually on the continuous slices of cerebral nuclei to include the entire volume of each structure visible on the QSM maps (Figure **6.1**). The large identifiable cerebral vessels in the cerebral nuclei were excluded when drawing the ROIs. The mean and standard deviation of the susceptibility values were measured for both left and right hemispheres from each structure. Finally, when analyzing the global and regional susceptibility measurements from each cohort, the effect of age-related iron changes of both hemispheres in all deep gray matter nuclei was corrected for by subtracting the measured susceptibilities from the corresponding values derived from the linear regression models established by Liu et al. [12]
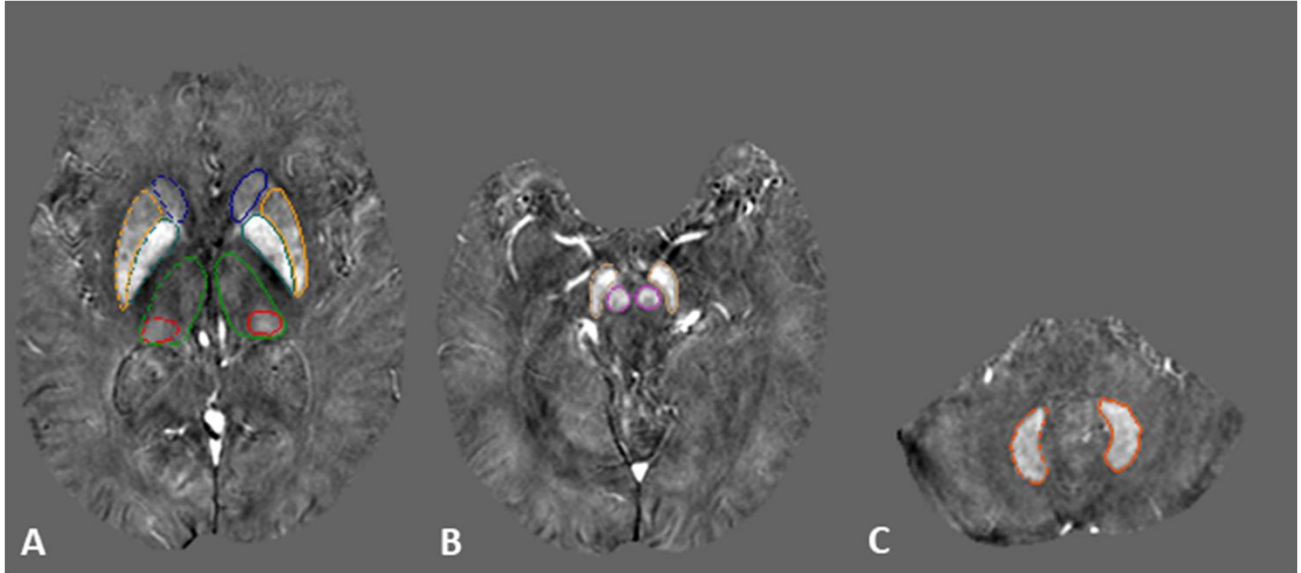
**Figure 6.1**. Regions of interest traced on quantitative susceptibility maps on three representative slices showing deep gray matter nuclei. A) the basal ganglia; blue: caudate nucleus, orange: putamen, cyan: globus pallidus, green: thalamus, red: pulvinar thalamus. B) midbrain; purple: red nucleus, yellow: substantia nigra. C) cerebellum; orange: dentate nucleus.

*Postprocessing of tSWI and Evaluation of the N1 Sign*

To review the N1 sign throughout the SN, four types of images were visually evaluated: the original $T_2$*WI magnitude images, SWI, QSM and tSWI data. The tSWI data were created using a mask generated from QSM to augment susceptibility-dependent contrast in the original magnitude data. [121] The application of tSWI is not affected by the orientation dependence inherent in the phase images, which negatively affects the SWI data. The data were reviewed from the most caudal SN slice to the most cranial slice abutting the sub-thalamic nucleus. This usually included 4 to 5 slices covering the SN with a 2mm slice thickness. The loss of the N1 sign was defined as either bilateral or unilateral. To be called bilateral loss, there had to be no evidence of the sign in any of the slices, while to be defined as unilateral loss, it had to be seen in at least one caudal slice of either hemisphere. [18] In our study, the presence or absence of the N1 sign was reviewed based on

consensus by two experienced raters (one with 6 and one with 35 years of experience in MR imaging).

*Statistical Analysis*

The statistical analyses were performed using SPSS 16.0 (SPSS Inc. Chicago, Ill., USA). The normal distribution of data was explored with the Shapiro-Wilk test. The reproducibility and reliability between the two raters for the N1 sign and global susceptibility were explored using the intraclass correlation (ICC) analysis. The diagnostic test for the N1 sign loss between iRBD patients and HCs was investigated with Fisher's exact test. The differences in the distribution of age, education and gender between the iRBD patients and HCs were explored using two independent sample t-tests and the Chi-square test, respectively. The differences in the cognitive scores, Alternate-tap test, 3-meter Timed Up and Go test and the global and RII susceptibility of the cerebral nuclei were investigated using two independent sample t-tests. The difference in the Flamingo test was investigated using the rank sum test. The relationships between the global and RII susceptibility of the cerebral nuclei and the neuropsychological and motor function measures in the iRBD patients were investigated using Pearson's correlation analysis. Furthermore, stepwise multiple linear regression analysis was used to explore the predictive risk factor of global and RII susceptibility for the neuropsychological and motor function. In the stepwise regression analysis, F-to-enter 0.05 and F-to-Remove 0.1 were applied.

It is commonly known that iRBD patients are inherently unaware of RBD-related behavior since they occur during sleep and only in the case of awakening due to dream-enactment-related impact or injury is this behavior usually noticed. [46] If these events are not serious, they are easily ignored, making patient recruitment clinically challenging. For this reason, the sample size in our study was

relatively small. Nevertheless, it was still of interest to perform an exploratory analysis without adjusting for multiple comparisons at first, especially when testing for iron effects in the SN and DN where there is ample evidence of changes in PD. [252] To err on the safe side, when evaluating the significance of all tested variables, the false discovery rate (FDR) correction to $P < 0.05$ was considered to be statistically significant.

## Results

*Demographic and Clinical Characteristics of iRBD Patients and Healthy Controls*

The demographic and clinical characteristics of the iRBD patients and HCs are presented in Table **6.2** and Table **6.3**.

**Table 6.2.** Demographic, clinical characteristics and cognitive tests of all the participants.

| | iRBD patients (n = 29) | HCs (n = 28) | *P* value | *P*FDR value |
|---|---|---|---|---|
| **Age, yr** | 64.6 ± 7.6 | 62.7 ± 4.2 | 0.255 | 0.255 |
| **Gender, F/M** | 9/20 | 9/19 | 0.928 | 0.928 |
| **Education, yr** | 11.0 ± 4.5 | 11.5 ± 3.1 | 0.653 | 0.653 |
| **iRBD duration, yr** | 6.1 ± 4.9 | -- | -- | |
| **RBDQ-HK** | 42.2 ± 14.8 | -- | -- | |
| **Cognitive tests, z scores** | | | | |
| **visuospatial function** | -0.60 ± 1.21 | 0.04 ± 0.12 | **0.009#** | **0.045*** |
| **memory function** | -0.41 ± 0.88 | 0.00 ± 0.80 | **0.034#** | 0.085 |
| **attention-executive function** | -0.19 ± 0.96 | 0.00 ± 0.60 | 0.304 | 0.380 |
| **language function** | 0.18 ± 0.81 | 0.00 ± 0.98 | 0.419 | 0.419 |
| **Average cognition** | -0.27 ± 0.67 | 0.01 ± 0.64 | 0.080 | 0.133 |

Plus-minus values are means ± SD. iRBD = idiopathic rapid eye movement sleep behavior disorder, HCs = healthy controls, F = female, M = male, RBDQ-HK = RBD Questionnaire–Hong Kong,
#, *P* value <0.05 without FDR correction
*, *P*FDR value <0.05 with FDR correction

The average disease duration of the iRBD patients was 6.1 ± 4.9 years. The average RBDQ-HK score of the iRBD patients was 42.2±14.8 and they also performed worse in visuospatial function (*P* =0.009) and memory function (*P* =0.034) compared with the HCs before FDR correction (Table

**6.2**). After FDR correction, the only significant difference was in the visuospatial function (*P* =0.045). For the motor function tests, the iRBD patients performed worse in the Alternate-tap test (left: *P* =0.010; right: *P* =0.013; Average: *P* =0.010) and the 3-meter Timed Up and Go test (*P* =0.007) compared with the HCs before FDR correction. After FDR correction, all the differences in the Alternate-tap test (left: *P* =0.016; right: *P* =0.016; Average: *P* =0.016) and the 3-meter Timed Up and Go test (*P* =0.016) remained significant (Table **6.3**).

**Table 6.3.** Demographic, clinical characteristics and motor function tests.

| | iRBD patients (n = 21) | HCs (n = 16) | P value | P$_{FDR}$ value |
|---|---|---|---|---|
| **Age, yr** | 65.3 ± 7.0 | 62.9 ± 5.1 | 0.253 | 0.253 |
| **Gender, F/M** | 6/15 | 7/9 | 0.338 | 0.338 |
| **Education, yr** | 11.7 ± 4.5 | 11.2 ± 3.1 | 0.719 | 0.719 |
| **iRBD duration, yr** | 5.7 ± 5.0 | -- | -- | |
| **RBDQ-HK** | 44.0 ± 13.1 | -- | -- | |
| **UPDRS III** | 4.40 ± 4.3 | -- | -- | |
| **Alternate-tap test (Taps/min)** | | | | |
| **Left** | 180.2 ± 35.8 | 216.5 ± 44.7 | **0.010#** | **0.016*** |
| **Right** | 190.9 ± 45.3 | 228.6 ± 41.4 | **0.013#** | **0.016*** |
| **Average** | 185.6 ± 39.6 | 222.5 ± 41.3 | **0.010#** | **0.016*** |
| **3-meter Timed Up and Go (s)** | 7.3 ± 1.7 | 6.0 ± 0.8 | **0.007#** | **0.016*** |
| **Flamingo test, median (P25, P75)** | 2.8 (0, 5.5) | 1.5 (0.5, 3) | 0.403 | 0.403 |

Plus-minus values are means ± SD. iRBD = idiopathic rapid eye movement sleep behavior disorder, HCs = healthy controls, F = female, M = male, RBDQ-HK = RBD Questionnaire–Hong Kong,
#, *P* value <0.05 without FDR correction
*, P$_{FDR}$ value <0.05 with FDR correction

*Reproducibility and Reliability of N1 Sign Evaluation and Iron Deposition*

The ICC values between the two raters for N1 sign evaluation was calculated to be 0.87 for the combined HC and iRBD groups. The final choice of which cases showed the N1 sign was reached based on consensus between the two raters. The ICC values between the two raters for the global and regional susceptibility measurements of cerebral nuclei were calculated to be 0.87 and 0.98, respectively, derived from both HC and iRBD groups combined.

*Loss of the N1 Sign in iRBD Patients and Healthy Controls*

Based on the consensus results between the two raters, out of 29 iRBD patients, 8 patients had bilateral loss and 4 patients had unilateral loss (3 on the left and 1 on the right) of the N1 sign. Out of 28 HCs, only two had unilateral loss of the N1 sign while the rest showed the N1 sign on both sides (Figure **6.2**). As a result, the number of iRBD patients with N1 loss was significantly higher than that of HCs (P=0.005).
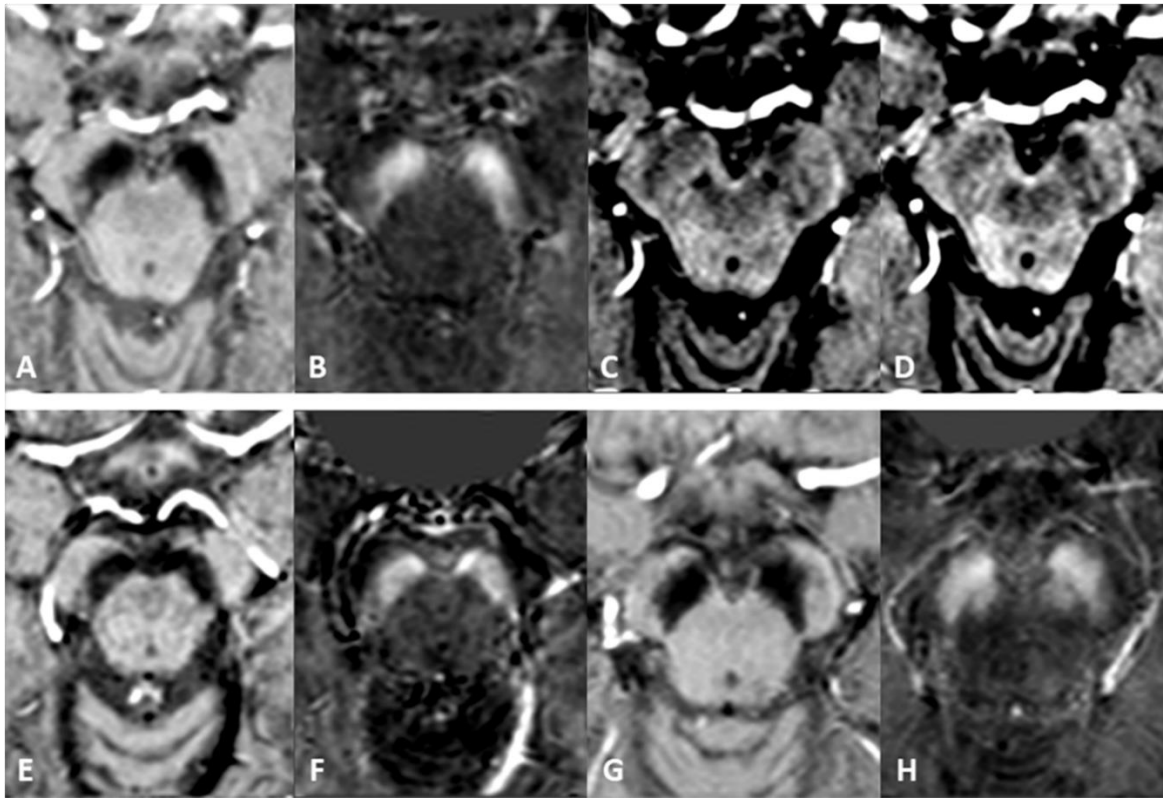


**Figure 6.2.** Nigrosome-1 sign in the substantia nigra. The top row shows bilateral presence of N1 in A) tSWI, B) QSM, C) SWI and D) $T_2$*WI of a healthy control. E, F) tSWI and QSM images of an iRBD patient with unilateral loss of N1 in the left hemisphere. G, H) tSWI and QSM images of an iRBD patient with bilateral loss of N1.

*Susceptibility and Volumes of the Cerebral Nuclei in iRBD Patients and Healthy Controls*

In order to explore the relationship between N1 loss and elevated iron deposition in the SN, we compared the global and RII susceptibility of the SN among the iRBD patients with bilateral N1 sign loss (n=8), iRBD with no N1 loss (n=17) and HCs with no N1 loss (n=26). There were no significant

differences in the global and RII susceptibility of the SN among these three groups (Supplementary

Table **10.1** and Figure **6.3**).
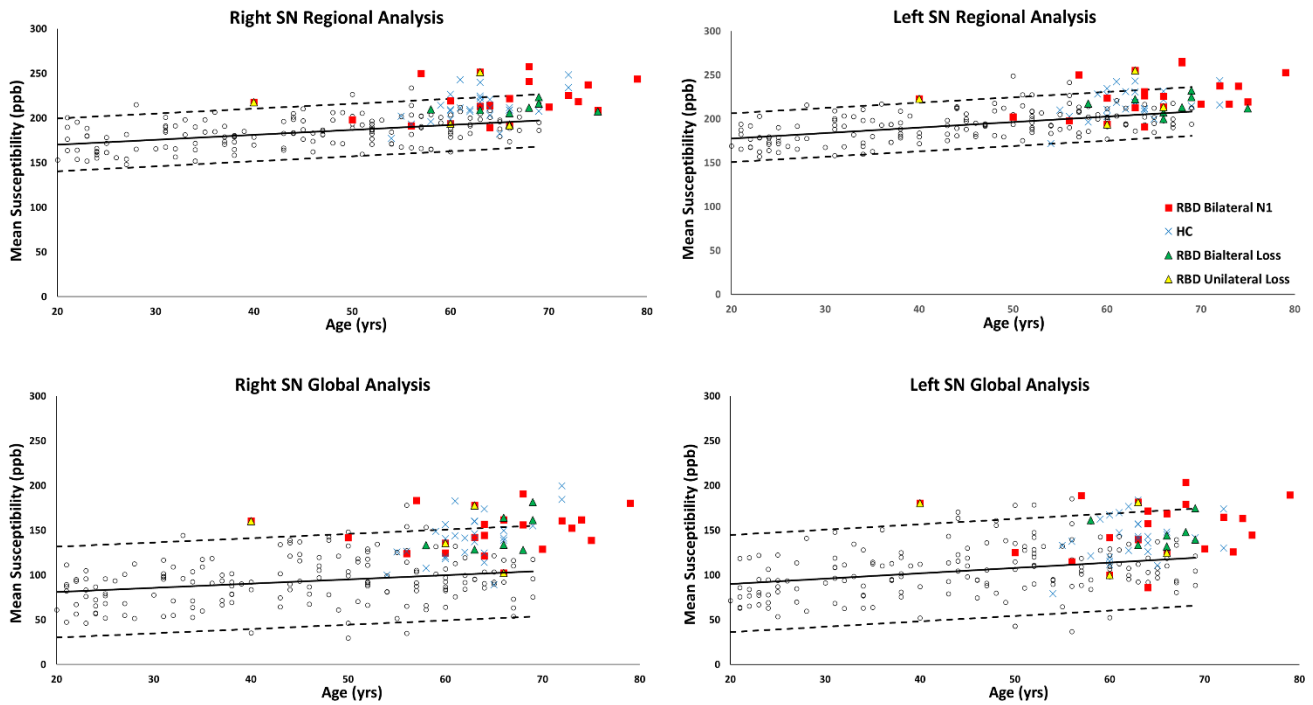


**Figure 6.3.** Distribution of global and regional mean susceptibility values of the SN in HCs and iRBD groups based on the appearance of N1 sign. Red squares: iRBD patients with bilateral presence of N1; green triangles: iRBD patients with bilateral loss of N1; yellow triangles: iRBD patients with unilateral loss of N1; blue x's: healthy controls. Hollow circles, solid lines and dashed lines are associated with the normal population data, the linear regression model and 95% prediction intervals, respectively. [12]

The comparison of global and RII susceptibility of the cerebral nuclei between the HC and

patient groups before and after correcting for age are summarized in Table **6.4** and Table **6.5**,

respectively.

**Table 6.4.** Comparison of the global and RII susceptibility of cerebral nuclei between the iRBD patients and HCs.

| Iron Analysis | | Global analysis (ppb) | | RII analysis (ppb) | |
|---|---|---|---|---|---|
| Hemisphere | | Right | Left | Right | Left |
| CN | HCs | 43.8 ± 16.7 | 47.1± 17.3 | 106.6 ± 12.9 | 103.1 ± 12.0 |
| | iRBD | 49.0 ± 13.6 | 46.9± 12.3 | 107.5 ± 11.5 | 102.8 ± 11.2 |
| | *p-value* | 0.200 | 0.953 | 0.783 | 0.912 |
| | *P_{FDR}-value* | 0.626 | 0.984 | 0.912 | 0.912 |
| GP | HCs | 133.0 ± 23.2 | 125.8 ± 25.2 | 240.0 ± 36.4 | 232.2 ± 34.4 |
| | iRBD | 134.9 ± 26.7 | 128.7 ± 27.0 | 246.5 ± 38.1 | 240.7 ± 38.5 |
| | *p-value* | 0.780 | 0.676 | 0.515 | 0.379 |
| | *P_{FDR}-value* | 0.960 | 0.901 | 0.749 | 0.726 |
| PUT | HCs | 56.5 ± 19.3 | 61.3 ± 20.8 | 138.8 ± 12.8 | 134.4 ± 12.1 |
| | iRBD | 62.0 ± 26.2 | 68.5 ± 27.6 | 147.1 ± 19.7 | 139.8 ± 19.7 |
| | *p-value* | 0.365 | 0.274 | 0.062 | 0.221 |
| | *P_{FDR}-value* | 0.649 | 0.626 | 0.384 | 0.589 |
| THA | HCs | -7.1 ± 10.3 | -6.9 ± 9.3 | 28.0 ± 7.7 | 32.2 ± 7.7 |
| | iRBD | -9.3 ± 9.7 | -9.3 ± 9.1 | 28.3 ± 9.6 | 32.8 ± 8.8 |
| | *p-value* | 0.421 | 0.320 | 0.912 | 0.777 |
| | *P_{FDR}-value* | 0.674 | 0.640 | 0.912 | 0.912 |
| PT | HCs | 38.9 ± 17.0 | 36.2 ± 17.7 | 87.5 ± 8.8 | 84.7 ± 8.7 |
| | iRBD | 38.8 ± 26.9 | 36.0 ± 25.0 | 87.1 ± 13.4 | 86.7 ± 11.7 |
| | *p-value* | 0.984 | 0.978 | 0.905 | 0.454 |
| | *P_{FDR}-value* | 0.984 | 0.984 | 0.912 | 0.726 |
| SN | HCs | 141.9 ± 25.8 | 140.3 ± 23.3 | 212.5 ± 16.4 | 217.5 ± 15.6 |
| | iRBD | 149.1 ± 21.7 | 150.7 ± 27.9 | 216.8 ± 18.7 | 223.7 ± 19.8 |
| | *p-value* | 0.259 | 0.133 | 0.355 | 0.190 |
| | *P_{FDR}-value* | 0.626 | 0.532 | 0.726 | 0.589 |
| RN | HCs | 132.8 ± 34.2 | 130.8 ± 37.2 | 185.7 ± 17.4 | 189.2 ± 16.8 |
| | iRBD | 148.2 ± 30.1 | 137.0 ± 27.6 | 192.8 ± 21.3 | 192.6 ± 15.6 |
| | *p-value* | 0.077 | 0.479 | 0.171 | 0.420 |
| | *P_{FDR}-value* | 0.512 | 0.697 | 0.589 | 0.726 |
| DN | HCs | 99.0 ± 23.8 | 109.1 ± 26.4 | 151.8 ± 13.1 | 162.8 ± 15.7 |
| | iRBD | 114.4 ± 27.1 | 121.9 ± 30.1 | 162.5 ± 17.2 | 171.5 ± 19.8 |
| | *p-value* | **0.027**[#] | 0.096 | **0.011**[#] | 0.072 |
| | *P_{FDR}-value* | 0.432 | 0.512 | 0.176 | 0.384 |

Plus-minus values are means ± SD. CN = caudate nucleus, GP = globus pallidus, PUT = putamen, THA = thalamus, PT = pulvinar thalamus, SN = substantia nigra, RN = red nucleus, DN = dentate nucleus. #, $P$ value <0.05 without FDR correction

The results of volumetric measurements from each nucleus are also summarized in Table **6.6**.

The global and RII susceptibility values in the right DN of the iRBD patients were both significantly higher than those in the HCs (global: P = 0.027 and RII: P = 0.011, without FDR correction) but these differences were not significant after the FDR correction was applied.

**Table 6.5.** Comparison of the age-corrected global and RII susceptibility of cerebral nuclei between the iRBD patients and HCs

| Iron Analysis | | Global analysis (ppb) | | RII analysis (ppb) | |
|---|---|---|---|---|---|
| Hemisphere | | Right | Left | Right | Left |
| CN | HCs | -5.9 ± 16.7 | 1.5 ± 17.3 | 2.8 ± 12.4 | 3.6 ± 11.1 |
| | iRBD | -1.8 ± 11.8 | -0.3 ± 11.5 | 1.5 ± 8.3 | 1.3 ± 8.4 |
| | *p-value* | 0.294 | 0.751 | 0.634 | 0.371 |
| | *P$_{FDR}$-value* | 0.866 | 0.910 | 0.920 | 0.920 |
| GP | HCs | 5.8± 23.1 | -1.5 ± 25.2 | 12.5 ± 36.0 | 8.8 ± 34.3 |
| | iRBD | 7.2 ± 26.5 | 1.1 ± 26.9 | 17.6 ± 36.6 | 16.5 ± 37.4 |
| | *p-value* | 0.829 | 0.702 | 0.601 | 0.425 |
| | *P$_{FDR}$-value* | 0.910 | 0.910 | 0.920 | 0.920 |
| PUT | HCs | -28.3 ± 18.6 | -18.9 ± 20.5 | -17.0 ± 11.9 | -10.6 ± 10.2 |
| | iRBD | -26.0 ± 23.8 | -14.7 ± 24.5 | -13.7 ± 16.3 | -9.6 ± 16.1 |
| | *p-value* | 0.682 | 0.479 | 0.384 | 0.783 |
| | *P$_{FDR}$-value* | 0.910 | 0.894 | 0.920 | 0.920 |
| THA | HCs | -6.0 ± 10.3 | -10.2 ± 9.3 | -3.2 ± 7.7 | -8.0 ± 7.7 |
| | iRBD | -7.7 ± 9.3 | -12.3 ± 8.6 | -3.1 ± 9.7 | -7.4 ± 8.9 |
| | *p-value* | 0.503 | 0.382 | 0.946 | 0.805 |
| | *P$_{FDR}$-value* | 0.894 | 0.873 | 0.965 | 0.920 |
| PT | HCs | -6.1 ± 16.8 | -10.6 ± 17.7 | 4.7 ± 8.4 | 1.2 ± 8.4 |
| | iRBD | -6.8 ± 27.2 | -11.3 ± 25.4 | 3.5 ± 13.4 | 2.5 ± 11.7 |
| | *p-value* | 0.906 | 0.910 | 0.698 | 0.644 |
| | *P$_{FDR}$-value* | 0.910 | 0.910 | 0.920 | 0.920 |
| SN | HCs | 4.2 ± 24.8 | 2.6 ± 22.7 | 18.6 ± 15.3 | 13.6 ± 14.8 |
| | iRBD | 4.8 ± 21.4 | 3.5 ± 27.8 | 21.5 ± 18.2 | 18.3 ± 19.2 |
| | *p-value* | 0.325 | 0.190 | 0.512 | 0.303 |
| | *P$_{FDR}$-value* | 0.867 | 0.760 | 0.920 | 0.920 |
| RN | HCs | 32.7 ± 33.8 | 24.2 ± 37.8 | 6.2 ± 16.9 | 7.3 ± 16.5 |
| | iRBD | 45.0 ± 30.0 | 27.0 ± 28.5 | 9.8 ± 21.0 | 7.2 ± 15.5 |
| | *p-value* | 0.152 | 0.758 | 0.489 | 0.965 |
| | *P$_{FDR}$-value* | 0.760 | 0.910 | 0.920 | 0.965 |
| DN | HCs | 13.6 ± 23.9 | 15.8 ± 26.5 | -8.5 ± 13.3 | -6.6 ± 15.9 |
| | iRBD | 27.5 ± 26.9 | 26.6 ± 29.7 | 0.5 ± 17.0 | -0.1 ± 18.6 |
| | *p-value* | **0.046#** | 0.156 | **0.032#** | 0.165 |
| | *P$_{FDR}$-value* | 0.736 | 0.760 | 0.512 | 0.920 |

Plus-minus values are means ± SD. CN = caudate nucleus, GP = globus pallidus, PUT = putamen, THA = thalamus, PT = pulvinar thalamus, SN = substantia nigra, RN = red nucleus, DN = dentate nucleus. #, *P* value <0.05 without FDR correction

Additionally, the volumes of the bilateral CN were significantly lower than those of the HCs (right: P = 0.003, left: P = 0.021, without FDR correction). After FDR correction, only the right CN showed a significant difference between iRBD patients and HCs (P = 0.048, with FDR correction).

**Table 6.6.** Comparison of the volume of cerebral nuclei between iRBD patients and HCs.

| Structure | Hemisphere | Right | Left |
|---|---|---|---|
| CN | HCs | 2080.0 ± 266.0 | 2101.2 ± 306.5 |
| | iRBD | 1788.5 ± 345.6 | 1839.4 ± 390.6 |
| | *p-value* | **0.003#** | **0.021#** |
| | *P_FDR-value* | **0.048*** | 0.153 |
| GP | HCs | 2103.1 ± 271.1 | 2130.3 ± 261.4 |
| | iRBD | 1929.8 ± 276.0 | 1966.0 ± 280.9 |
| | *p-value* | 0.052 | 0.057 |
| | *P_FDR-value* | 0.153 | 0.153 |
| PUT | HCs | 3150.7 ± 368.0 | 2988.5 ± 369.1 |
| | iRBD | 2947.2 ± 497.8 | 2782.2 ± 474.6 |
| | *p-value* | 0.224 | 0.197 |
| | *P_FDR-value* | 0.326 | 0.315 |
| THA | HCs | 4010.6 ± 619.0 | 3808.3 ± 566.5 |
| | iRBD | 3876.4 ± 478.5 | 3668.9 ± 419.1 |
| | *p-value* | 0.067 | 0.372 |
| | *P_FDR-value* | 0.153 | 0.496 |
| PT | HCs | 673.6 ± 116.4 | 619.1 ± 110.7 |
| | iRBD | 610.2 ± 123.4 | 550.5 ± 125.9 |
| | *p-value* | 0.067 | 0.063 |
| | *P_FDR-value* | 0.153 | 0.153 |
| SN | HCs | 618.3 ± 79.9 | 590.8 ± 82.8 |
| | iRBD | 570.0 ± 107.0 | 548.3 ± 92.1 |
| | *p-value* | 0.089 | 0.096 |
| | *P_FDR-value* | 0.171 | 0.171 |
| RN | HCs | 208.2 ± 27.3 | 208.9 ± 35.6 |
| | iRBD | 212.1 ± 40.7 | 212.7 ± 36.5 |
| | *p-value* | 0.680 | 0.593 |
| | *P_FDR-value* | 0.725 | 0.725 |
| DN | HCs | 679.0 ± 154.3 | 680.6 ± 152.9 |
| | iRBD | 658.2 ± 125.4 | 678.7 ± 132.1 |
| | *p-value* | 0.660 | 0.944 |
| | *P_FDR-value* | 0.725 | 0.944 |

Plus-minus values are means ± SD. CN = caudate nucleus, GP = globus pallidus, PUT = putamen, THA = thalamus, PT = pulvinar thalamus, SN = substantia nigra, RN = red nucleus, DN = dentate nucleus. #, $P$ value <0.05 without FDR correction

*Correlation between Magnetic Susceptibility and Clinical Features in iRBD Patients*

In order to evaluate the correlation between susceptibility and clinical measures and since it is well known that the susceptibility of deep gray matter structures changes as a function of age, [12, 94] we corrected the mean susceptibility values in both analyses for age in all the structures by using the projected age-matched values taken from the corresponding linear regression models. [12]

Before FDR correction, the global susceptibilities of the bilateral DN were positively correlated with the time in the Stroop C test (left: r = 0.411, P = 0.030; right: r = 0.520, P = 0.005); the global susceptibility of the right DN was negatively correlated with the AVLT short-delay free recall (r = -0.466, P = 0.012); the global susceptibility of the left PUT (r = -0.406, P = 0.032) and left CN (r = -0.376, P = 0.049) were negatively correlated with the memory score of the RCFT test.

The RII susceptibility of the bilateral DN were positively correlated with the time in the Stroop C test (left: r = 0.525, P = 0.004; right: r = 0.614, P = 0.001); the RII susceptibility of the right DN was negatively correlated with the AVLT short-delay free recall (r = -0.392, P = 0.035); the RII susceptibility of the left GP was negatively correlated with the AVLT short-delay free recall (r = -0.381, P = 0.041); and the RII susceptibilities of the bilateral PUT (left: r = -0.404, P = 0.033, right: r = -0.426, P = 0.024) were negatively correlated with the memory score of the RCFT test. After FDR correction, only RII susceptibility of the right DN was found to be positively correlated with the time in the Stroop C test (r = 0.614, P = 0.032). These results are summarized in Figure **6.4**. The corresponding correlations between the susceptibility values from ROI results and cognitive function scores in the HCs are given in Supplementary Figure **10.1**.
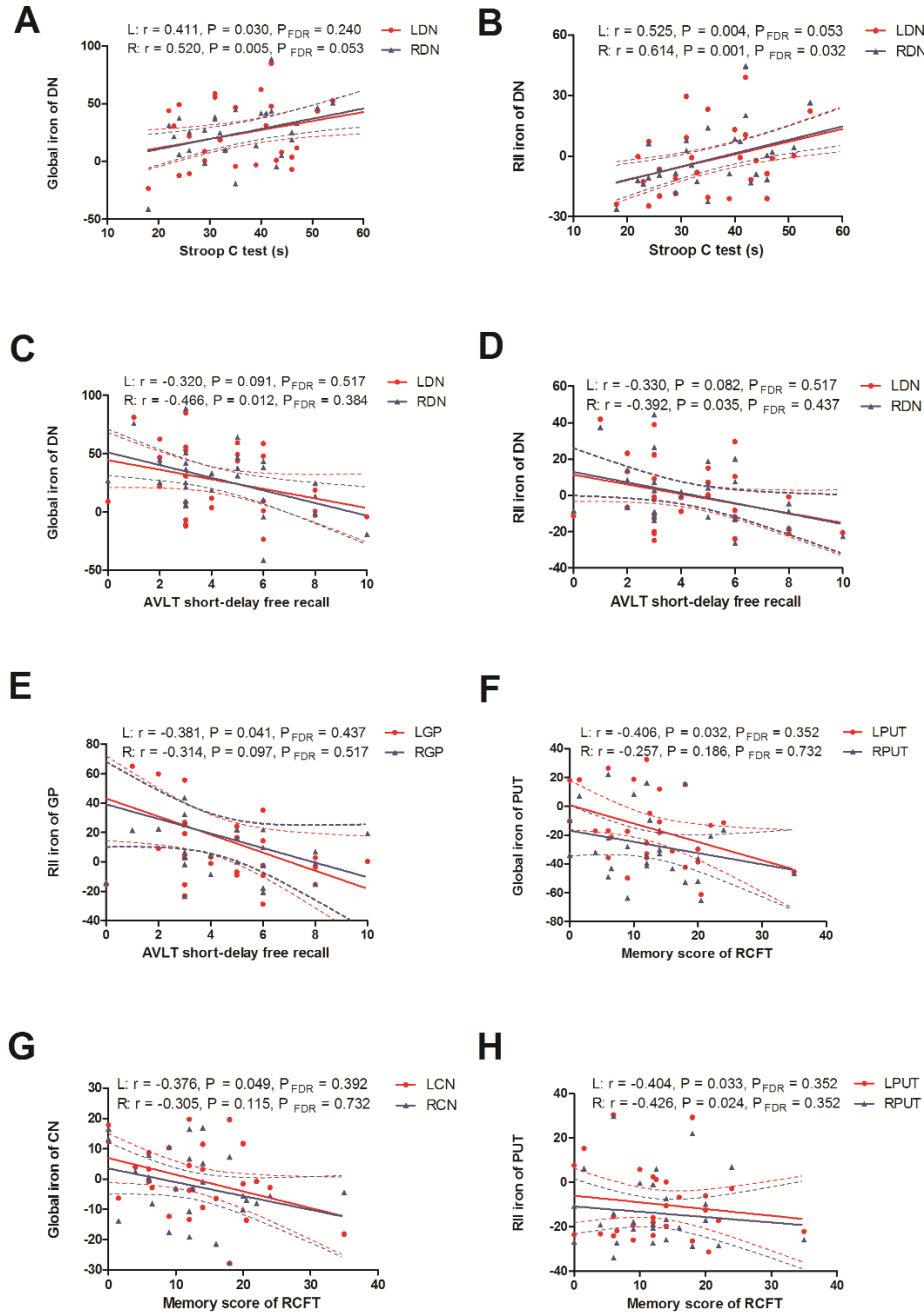
**Figure 6.4**. Correlations between age-corrected iron deposition and cognitive scores in the iRBD patients. The global iron deposition of the bilateral DN were positively correlated with the time in the Stroop C test (A). The RII iron deposition of the bilateral DN were positively correlated with the time in the Stroop C test (B). The global (C) and RII (D) iron deposition of the right DN were negatively correlated with the AVLT short-delay free recall. The RII iron of the left GP was negatively correlated with the AVLT short-delay free recall (E). The global iron of the left PUT (F), the global iron of the left CN (G), the RII iron of the bilateral PUT (H) were negatively correlated with the memory score of the RCFT test. AVLT = Auditory Verbal Learning Test; RCFT = Rey Complex Figure Test; LDN = left dentate nucleus; RDN = right dentate nucleus; LGP = left globus pallidus; RGP = right globus pallidus; LPUT = left putamen; RPUT = right putamen; LCN = left caudate nucleus; RCN = right caudate nucleus.

Before FDR correction, the global susceptibility of the bilateral CN and DN were negatively correlated with the average taps from the Alternate-Tap test (for CN: left: r = -0.569, P = 0.001; right: r = -0.502, P = 0.020 and for DN: left: r = -0.507, P = 0.019; right: r = -0.537, P = 0.012); the global susceptibility of the bilateral GP and right SN were positively correlated with the time of the 3-meter Timed Up and Go test (for GP: left: r = 0.622, P = 0.003; right: r = 0.437, P = 0.048 and for right SN: r = 0.454, P = 0.039); the global susceptibility of the right CN was positively correlated with the time of the 3-meter Timed Up and Go test (r = 0.472, P = 0.031). The RII susceptibility of the bilateral DN and CN were negatively correlated with the average taps from the Alternate-Tap test (for DN: left: r = -0.554, P = 0.009; right: r = -0.523, P = 0.015 and for CN: left: r = -0.494, P = 0.023; right: r = -0.502, P = 0.020); the RII susceptibility of the left GP was positively correlated with the time of the 3-meter Timed Up and Go test (r = 0.499, P = 0.021); and the RII susceptibility of the bilateral SN were positively correlated with the time of the 3-meter Timed Up and Go test (left: r = 0.488, P = 0.025; right: r = 0.493, P = 0.023). After FDR correction, the global susceptibility of the left CN remained significantly negatively correlated with the average taps from the Alternate-Tap test (r = -0.569, P = 0.032). These results are summarized in Figure **6.5**. The corresponding correlations between the susceptibility values from the ROIs and motor function scores in the HCs are shown in Supplementary Figure **10.2**.
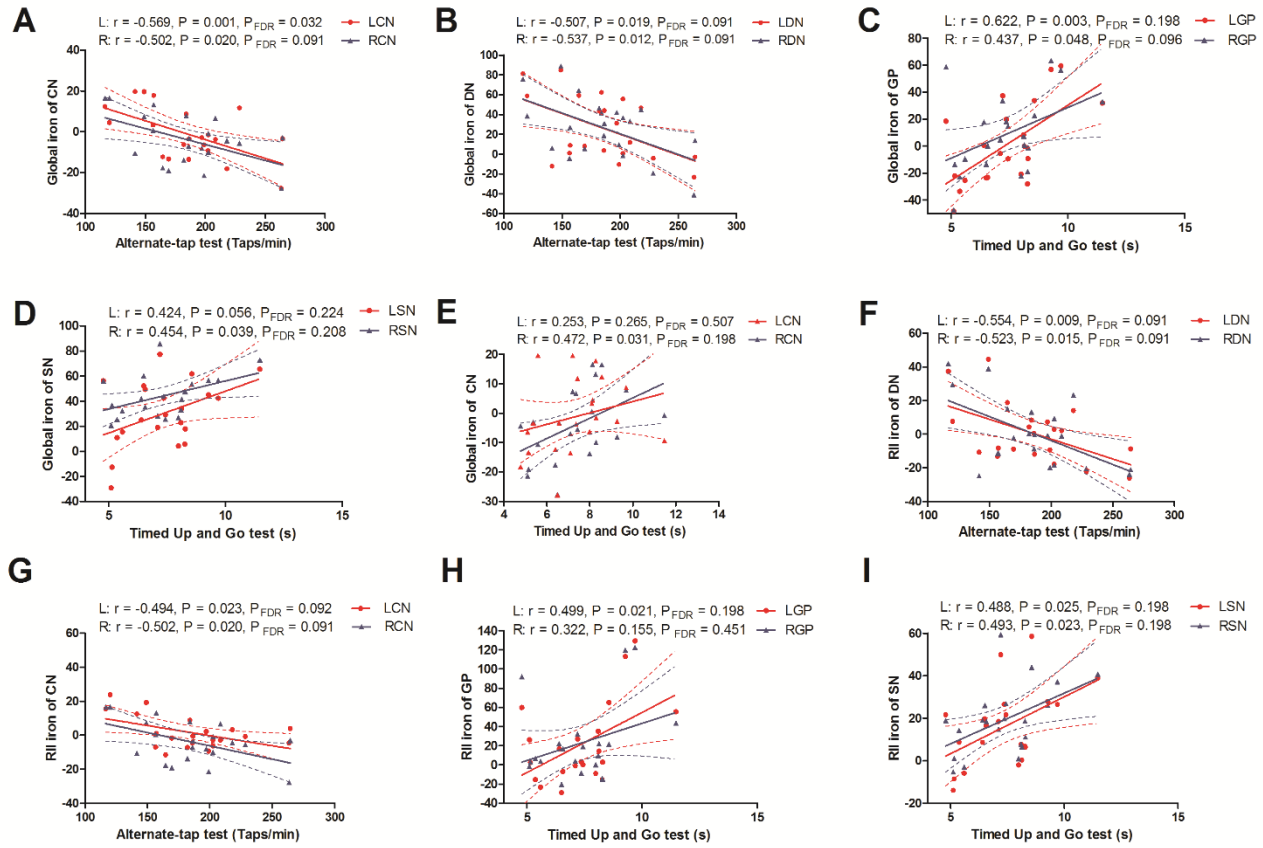
**Figure 6.5.** Correlations between age-corrected iron deposition and motor scores in the iRBD patients. The global susceptibility of the bilateral CN (A) and DN (B) were negatively correlated with the average taps from the Alternate-Tap test. The global susceptibility of the bilateral GP (C), right SN (D) and CN (E) were positively correlated with the time of the 3-meter Timed Up and Go test. The RII susceptibility of the bilateral DN (F) and CN (G) were negatively correlated with the average taps from the Alternate-Tap test. The RII susceptibility of the left GP (H) and bilateral SN (I) were positively correlated with the time of the 3-meter Timed Up and Go test. LCN = left caudate nucleus; RCN = right caudate nucleus; LDN = left dentate nucleus; RDN = right dentate nucleus; LGP = left globus pallidus; RGP = right globus pallidus; LSN = left substantia nigra; RSN = right substantia nigra.

Finally, the global susceptibility of the right SN was positively correlated with disease duration ($r = 0.420$, $P = 0.029$); the global and RII susceptibility of the right GP was positively correlated with the RBDQ-HK score ($r = 0.428$, $P = 0.021$; $r = 0.424$, $P = 0.022$). However, these two correlations did not remain significant after FDR correction. These results are summarized in Figure **6.6**. The correlations between the susceptibility values from the other ROIs and cognitive, motor, disease duration and RBDQ-HK scores are shown in Supplementary Figure **10.3**-9.
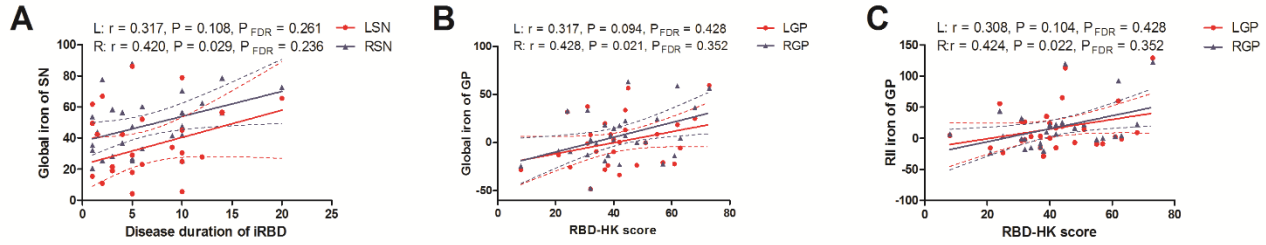
**Figure 6.6.** Correlations between age-corrected iron deposition and clinical features in the iRBD patients. The global iron of the right SN was positively correlated with disease duration of iRBD (A). The global and RII iron deposition of the right GP were positively correlated with the RBDQ-HK score (B and C). iRBD = idiopathic rapid eye movement sleep behavior disorder; RBDQ-HK = RBD Questionnaire-Hong Kong; LSN = left substantia nigra; RSN = right substantia nigra; LGP = left globus pallidus; RGP = right globus pallidus.

We explored the predictive risk factor of global and RII iron of subcortical nuclei for cognitive/motor performance tests using stepwise multiple linear regression analysis. Regarding the cognitive performance, we found that the RII iron of the right CN was the predictive factor for the visuospatial function and the global iron of the right DN was the predictive factor for the memory function (all $P<0.05$, FDR correction) (Table **6.7**).

**Table 6.7**. The relationship between RII iron of the cerebral nuclei and cognitive scores in iRBD patients using stepwise multiple regression analysis

| Cognitive function | Iron of cerebral nuclei (global/RII) | 95% Confidence interval | Partial correlation | Collinearity statistics VIF | $P$ value | $P_{FDR}$ value |
|---|---|---|---|---|---|---|
| **Visuospatial function** | RII iron of RCN | (-0.716, -0.152) | -0.535 | 1.002 | **0.004#** | **0.004\*** |
| **Memory function** | Global iron of RDN | (-0.848, -0.194) | -0.549 | 1.232 | **0.003#** | **0.004\*** |

#, $P$ value <0.05 without FDR correction
\*, $P_{FDR}$ value <0.05 with FDR correction

Regarding the motor performance, we found that the RII iron of the left DN and global iron of the left CN were predictive factors for the Alternate-Tap test (left, average), the global iron of the left DN was the predictive factor for the Alternate-Tap test (right), and the global iron of the left GP was the predictive factor for the 3-meter Timed Up and Go test (all $P<0.05$, FDR correction) (Table

**6.8**). The variance inflation factor (VIF) ranged from 1.002 to 1.927, indicating that there was no multicollinearity among the global and RII iron of subcortical nuclei in the multiple stepwise regression analysis.

**Table 6.8**. The relationship between global/RII iron of cerebral nuclei and motor scores in iRBD patients using stepwise multiple regression analysis

| Motor function | Iron of cerebral nuclei (global/RII) | 95% Confidence interval | Partial correlation | Collinearity statistics VIF | P value | $P_{FDR}$ value |
|---|---|---|---|---|---|---|
| Alternate-Tap test (Left) | RII iron of LDN | (-2.003, -0.866) | -0.791 | 1.691 | <0.001# | 0.002* |
| | Global iron of LCN | (-1.973, -0.449) | -0.430 | 1.125 | 0.004 | 0.004* |
| Alternate-Tap test (Right) | Global iron of LDN | (-3.324, -0.767) | -0.609 | 1.000 | 0.003# | 0.004* |
| Alternate-Tap test (Average) | RII iron of LDN | (-2.258, -1.098) | -0.838 | 1.927 | <0.001# | 0.002* |
| | Global iron of LCN | (-2.788, -1.209) | -0.802 | 1.322 | <0.001# | 0.002* |
| 3-meter Timed Up and Go test | Global iron of LGP | (0.014, 0.055) | 0.628 | 1.000 | 0.002# | 0.003* |

#, P value <0.05 without FDR correction
*, $P_{FDR}$ value <0.05 with FDR correction

**Discussion and Conclusions**

This study compares the N1 sign, global and RII iron deposition and the correlations between iron deposition with cognitive and motor impairment in iRBD patients. The most important findings in this study are: 1) the number of iRBD patients with the N1 sign loss was significantly higher than that of HCs; 2) the global and RII susceptibility values of the right DN were significantly higher than those of the HCs before FDR correction while losing their significance after FDR correction. Although not significant after FDR correction, increases in iron deposition in the DN should be further investigated with a larger sample size in the future; 3) the volume of the right CN was significantly lower than that of the HCs before and after FDR correction; and 4) linear correlation

analysis showed that the RII susceptibility of the right DN was correlated with poor attention-executive function and the global susceptibility of the left CN was significantly correlated with poor motor performance (after FDR correction). Furthermore, multiple regression analysis revealed the following for cognitive and motor performances: for the cognitive performance, the RII iron of the right CN was the predictive factor for the visuospatial function and the global iron of the right DN was the predictive factor for memory function (after FDR correction). For the motor performance, the RII iron of the left DN and global iron of the left CN were predictive factors for the Alternate-Tap test (left, average), the global iron of the left DN was the predictive factor for the Alternate-Tap test (right), and the global iron of the left GP was the predictive factor for the 3-meter Timed Up and Go test (after FDR correction). Taken together, these results suggest that global and regional high iron deposition may be potential imaging biomarkers for early evaluation of cognitive and motor impairment in iRBD patients. It should be noted that before FDR correction, there were more significant results while after FDR correction, most of these results lost their statistical significance. The reason for this may be due to the small sample size and the number of variables included. A bigger sample size and fewer statistical variables would warrant a more meaningful analysis of potential correlations between iron measures and clinical scores.

It should also be noted that similar relationships have been investigated in more advanced stages of neurodegeneration in the literature. In addition to motor impairment being a common characteristic of Parkinsonism, [253, 254] it is of great interest that correlations between iron content and cognitive impairment in some brain structures have also been studied. [234, 241, 255, 256] Specifically, Uchida et al. reported a negative correlation between magnetic susceptibility (i.e., global iron content) and Montreal cognitive assessment (MoCA) scores in the CN of PD patients.

[256] In a separate study by the same group and through a voxel-based QSM technique, the same negative relationship between global susceptibility and MoCA scores was replicated in PD patients with mild cognitive impairment. [241] Additionally, Li et al. have also reported negative correlations between QSM values in bilateral hippocampus and Mini-Mental State Examination (MMSE) scores. [234] Hence, one may argue that the correlations seen between motor and cognitive impairment and global and regional analyses in the brain structures of iRBD patients may then be reflected into such abnormalities seen in different forms of Parkinsonism.

*Global and RII iron changes in iRBD patients*

Our exploratory analysis also found that iRBD patients had significantly increased global and RII mean susceptibility values of the right DN compared with those in the HC group before correction, indicating that increased iron deposition in the DN of iRBD patients may be a potential biomarker for early identification of α-synucleinopathies before clinical extrapyramidal and cerebellar symptoms begin. The findings of our study were different from those of Sun et al.'s study, [238] in which they found significantly increased iron deposition in bilateral SN in iRBD patients. This could be due to smaller errors in measuring the iron content which then would lead to a decreased and possibly significant p-value. Furthermore, in Sun et al.'s study, the global iron content in the DN and regional iron content for any of the deep gray matter structures were not investigated. With that said, one may also argue that the reason for different findings between Sun et al.'s and our study could be due to different subtypes of α-synucleinopathies (such as PD, MSA and DLB) exhibiting different patterns of brain iron accumulation in this early stage. Previous studies found that MSA and PD patients had a wider range of excessive iron deposition; MSA patients tend to have increased iron content in the PUT and SN compared to HCs while PD patients show increased

iron deposition in the SN, GP and RN compared to HCs. [231, 238] Iron deposition of the DN in the PD patients, however, remains controversial. [11] That is, in a study by Guan et al. it has been reported that even though elevated nigral iron content is present regardless of disease type, abnormal iron deposition in the RN and DN appears to be only seen in tremor-dominant patients. [182] Similarly, He et al. reported abnormally high iron deposition of the bilateral DN to be the only biomarker separating tremor-dominant PD from other disease types as well as the HCs, [183] wheras Acosta-Cabronero et al. claimed to have found a decrease of magnetic susceptibility in the DN of idiopathic PD patients compared to that of HCs. [187] Nevertheless, based on the literature and with respect to the fact that Acosta-Cabronero did not include tremor-dominant PD patients in their study, there seems to be some evidence that the high iron deposition in the DN may be a potential biomarker specific to tremor-dominant PD. It should also be noted that in our study these differences in iron deposition between iRBD patients and HCs lost their statistical significance after FDR correction, possibly due to the small sample size and number of comparisons included. Nonetheless, the above mentioned studies along with the results from this work suggest that there might be abnormal iron deposition in the DN of iRBD patients which requires further investigation.

*Volume changes of cerebral nuclei in iRBD patients*

In this work, iRBD patients had significantly decreased volumes of the right CN compared to those of the HC cohort. Previous voxel-based morphometry results showed lower gray matter volume in the CN of iRBD patients, [257, 258] which is consistent with our study. Furthermore, decreased volume of the CN was also found in patients with PD [259-262] and MSA [260, 263] compared to the HCs. This suggests that degeneration of the CN in patients with iRBD may be an early biomarker for α-synucleinopathies. Abnormal iron homoeostasis can induce cellular damage,

[264] which may then lead to a decrease of volume in the deep gray matter nuclei. Additionally, greater atrophy of the caudate nucleus in patients with PD has been associated with poor cognitive function, [262, 265] although no correlation between the CN volume and cognitive/motor function was found in iRBD patients in our study. Further studies are needed to understand the significance of decreased volumes of the CN in early stage iRBD subjects.

*N1 sign loss in the SN of iRBD patients*

We found the incidence of the N1 sign loss in the SN of iRBD patients was significantly higher than that of the HCs, indicating that the iRBD patients may be showing signs of neuromelanin loss in the N1 territory of the SN. It has been reported that the N1 sign loss is correlated with increased iron deposition over time [197] and that it is a potential imaging biomarker of pathophysiological changes in PD patients. [18] In a recent study, Cheng et al. created a robust high quality and rapid imaging protocol for clinical detection of the N1 sign in 80 parkinsonism and related disorders and found that about 79% of the IPD patients had loss of the N1 sign. [18] In our study, about 41.4% (12/29) of iRBD patients showed loss of the N1 sign. This increased number of subjects showing N1 loss relative to HCs seems reasonable given that the iRBD subjects are in a much earlier stage compared to PD. However, we did not find any significant differences in the global and RII susceptibility of the SN among the iRBD patients with bilateral N1 sign loss (n=8), iRBD patients with no N1 loss (n=17) and HCs with no N1 loss (n=26). The volume of the N1 territory is small relative to the entire SN and the standard error in measuring the iron was quite large making it difficult to detect subtle changes in iron content.

*Correlation between iron deposition and clinical features in iRBD patients*

Our study found that increased iron deposition in the right DN not only correlated with motor function, but also correlated with poor attention-executive and memory function in both linear and multiple regression analysis. The cerebellum has been shown to influence nonmotor function such as working memory. [266] In the cerebrocerebellar circuitry, the cerebellum is interconnected with the cerebral cortex, including prefrontal and posterior parietal cortex, as well as the cortical motor areas. [267, 268] Thus, the disruption in these circuits could lead not only to motor deficits but also to cognitive, attentional, and affective impairments. [269] Our study also found that the iron deposition of the CN was correlated with poor visuospatial function in iRBD patients. The CN is an important part of the striatum and plays an important role in cognitive functions. [270] Dopamine loss in the CN and ventral striatum is closely associated with attention/working memory, frontal/executive, and visuospatial dysfuction in early-stage PD. [271] Corticostriatal, pallidal, thalamic and cortical re-entrant neural circuits are thought to promote certain domains of cognition, emotion and behavior. [272] Therefore, abnormal iron accumulation in the right CN and right DN may be associated with the disruption of the corticostriatal networks in iRBD patients, and may be a valuable marker representing the severity of cognitive dysfunction.

Compared with HCs, iRBD patients showed significantly decreased movement speed and lack of flexibility in motor function tests, indicating subclinical changes in their motor systems. Subtle motor impairment has been reported to be frequent in iRBD patients. [51, 52] However, we did not find a significant difference in the ability of balance on one leg measured by the Flamingo test, which is inconsistent with Barber et al.'s study. [273] Studies with imaging modalities such as transcranial sonography, [274, 275] neuromelanin-sensitive MRI, [276] and SWI [193, 277] have identified changes in the SN neuromelanin and iron content in iRBD patients. Our study

demonstrated that the RII iron deposition of the left DN and the global iron deposition of the left CN, left DN and left GP were negatively correlated with poor motor performance in the iRBD patients. In accordance with our findings, Guan et al. have also reported significant correlations between magnetic susceptibility (i.e., global analysis) in the DN and tremor severity as well as between magnetic susceptibility in the CN and akinetic/rigid severity. [182, 256] The GP has also been reported to play an important role in monitoring of motor function in PD. The GP externa can affect the processing of motor information by virtue of its widespread projections to all basal ganglia nuclei. [278] The GP interna is also a target for deep brain stimulation to treat motor complications in PD.[279] Such dependence could serve as a potential biomarker to monitor the severity of motor function abnormalities in iRBD patients which may then be reflected in more advanced manifestations of neurodegeneration.

Excessive iron likely contributes to the dysfunction of the nigrostriatal pathway, [66] which may underlie the subtle motor impairments in iRBD patients. Some PD studies have shown that the susceptibility in the SN and GP were significantly correlated with motor impairment measured by UPDRS. [157, 169, 179] On the other hand, as part of the motor system, the cerebellum controls the body's movements and balance. However, iron content of the DN has not been studied previously in iRBD patients. Our study shows that the iron content in the DN was associated with poor movement flexibility in iRBD patients. We also found increased iron deposition in the GP was positively correlated with RBDQ-HK score before correction, which was consistent with Sun et al.'s study, suggesting that increased iron deposition of the GP correlated with the severity of iRBD.

There are a number of limitations in our study. First, this was a cross-sectional design; a longitudinal study with a larger sample size is warranted to validate the current findings and

investigate the relationship between iron deposition with cognitive and motor impairment in iRBD patients over time. Second, not all patients and HCs had motor function evaluations due to their unwillingness or objective reasons, such as the relatively long testing times. This limited the power of the statistical analysis for all the variables. Third, due to the small sample size and too many variables included in our study, many of the significant differences were lost after FDR correction, with the remaining significant differences being the volume of the right CN between iRBD patients and HCs and some correlations between iron deposition and clinical features in iRBD patients. Fourth, we did not collect neuromelanin-sensitive imaging data which could have helped with evaluating potential neuromelanin loss in the iRBD patients against N1 sign localization.

The exploratory analysis in this study shows that iRBD patients had a higher incidence of N1 sign loss and reduced right CN volume relative to HCs after FDR correction. Cognitive and motor impairment in iRBD patients were also associated with iron deposition of several cerebral nuclei after FDR correction. Future studies with a larger sample size may help reveal further relationships that lost their significance here due to multiple comparison corrections.

## Chapter Seven: Conclusions and Future Directions

In this thesis, multiple qualitative and quantitative MRI techniques have been used to evaluate abnormal levels of iron and neuromelanin in the brains of PD and RBD patients compared against age-matched healthy populations. In Chapter Four, global and regional susceptibility measurements were performed in eight major deep gray matter nuclei of PD patients and age-matched HCs. These evaluations revealed an increase in iron deposition in the SN of PD patients over and above the increasing trend due to normal aging, with the regional analysis being more sensitive in picking up such abnormalities. The regional analysis was also seen to separate the PD population into two sub-groups from which the cohort with abnormal RII iron showed significantly higher UPDRS-III scores than those from the other sub-group with RII iron levels within the normal ranges. Finally, and in agreement with previous literature, even though the higher global R2* in the SN of PD patients were found to be statistically significant from those of HCs, they all fell within normal ranges in the literature making QSM a more reliable choice for iron quantification purposes. [239] However, it should be noted that the sample size for the patient group was relatively small (25 PD patients) in which most recruited subjects were going through intermediate stages of the disease. In order to have a more meaningful and comprehensive evaluation of iron behavior, especially RII iron, a much larger patient population is required.

Taking it one step further and by focusing only on the midbrain area in Chapter Five, we utilized a single multi-echo MT-augmented 3D GRE sequence to simultaneously visualize the NM content and N1 sign in the SN as well as quantifying iron deposition in this structure. Based on the results from this study, combining NM volume from MTC, SN volume from QSM and N1 data from tSWI yields an AUC as high as 0.98 when separating PD patients from age-matched HCs. It should be

emphasized, however, that unlike the PD cohort used in Chapter Four, in this study almost all of the recruited subjects in the patient group were going through early stages of the disease with a mean disease duration of only 2.55 years since clinical diagnosis. [280] With that said, and with respect to what has been discussed previously in the chapter, only the global iron analysis seems to have played a role in separating PD patients from the HC cohort (AUC = 0.74); one may argue that this may be due to the SN not having developed enough abnormal iron to survive the RII thresholds in earlier stages of the disease. Therefore, a potential future study could use the same analyses as what used in this chapter, but on PD patients specifically going through intermediate and later stages of the disease. The hypothesis here is that by the time these patients get to those stages, more NM depigmentation and higher iron deposition will occur, paving the way for RII analysis to distinguish between the two cohorts with an even higher accuracy.

Another step towards understanding pathogenesis of PD was taken in Chapter Six where iron and volumetric measurements along with the N1 sign were assessed in RBD patients and an age-matched HC cohort. In addition to volume shrinkage in the CN and abnormal iron in the DN (as well as other correlations between these MRI measurements and cognitive and motor functions) being consistent with what has been reported in the literature for both RBD and PD, the most interesting and novel finding in this study was the significantly higher number of RBD patients showing N1 loss compared to that of HCs. [281] Since the N1 territory is included in the NM complex in the SN, one may postulate that NM loss may start during pre-symptomatic stages of PD, especially RBD. Unfortunately, NM-MRI data were not collected in this study. However, the promising results reported in this study warrants further investigation of changes in iron, NM, volume and N1 of RBD patients, ideally using the same MT-enhanced 3D GRE sequence discussed in Chapter Five.

Another very interesting area as a potential future direction is the correlations between in vivo MR measures and SPECT/PET DAT scans highlighting localized dopamine loss. As mentioned in the previous chapters, DAT scan is currently the gold standard for clinical diagnosis of PD. In fact, in separate individual studies a reduction in striatal dopamine levels have been seen to be correlated with NM loss in the SNpc [25, 40] as well as iron overload in SNpc [30] with no evidence of such relationships between DAT and N1 to date. It is of great interest to simultaneously evaluate the potential correlations between striatal DAT and all the MR biomarkers discussed in this thesis. It is anticipated that by combining DAT and MRI, not only will a higher diagnosis accuracy be achieved differentiating PD from HC, but it is also expected to see a substantial improvement in picking up subtle changes in RBD (as a prodromal stage of PD) leading to a better understanding of the nigrostriatal pathology and degeneration of dopaminergic pathway.

Furthermore, another somewhat undiscovered research realm appears to be the spatial growth of iron content as a function of age. Over the lifespan, in addition to being temporally variable, iron deposition in the human brain is believed to be spatially changing as a function of age as well [97, 282]. Given the promising results seen in iron behavior in the SNpc and its relationship with the NM complex in PD, there is a great potential for the newly developed RII high iron analysis to be spatially assessed in the midbrain. The spatial RII iron trajectory in patients both longitudinally from a given subject over a certain period of time and cross-sectionally between patients at different stages of the disease could provide insight for a better interpretation of disease monitoring and progression.

In addition to dopaminergic neuronal death in the SN of PD patients, the loss of noradrenergic neurons in the LC has also been found to be associated with the disease with limited evidence stating

that LC neurodegeneration might occur prior to SNpc NM loss. [283] Being able to detect the NM signal in the LC could be a powerful imaging tool to help with PD diagnosis especially in early stages of the disease and ideally when the patients are still at the pre-symptomatic phase. [284] However, the LC is a very small structure (with a diameter and length of roughly 2.5 mm and 8 mm, respectively) and hard to image at clinical level spatial resolution. To be fair, it should also be noted that collecting MR data at higher resolution may come at a cost of longer acquisition time which could become a hurdle with the data covering the NM content in both SN and LC, particularly for PD patients showing sever symptoms and potential motion artifacts. To address this, Liu et al. have introduced a variant of STAGE technology known as MTC-STAGE from which synthetic MTC data at virtually any flip angle is achievable at a reasonable scan time of under 15 minutes. [212] Taking advantage of imaging the NM content in both SN and LC, coupled with other in vivo biomarkers (global and regional iron, N1, DAT etc.), could pave the way for a much more comprehensive interpretation of underlying PD pathophysiology.

## Chapter Eight: Supplementary Material I (Multi-Center QSM Validation)

As previously pointed out QSM has been proven many times to have a higher reliability over other iron quantification techniques, especially R2* and phase. However, a multi-center approach to validate the consistency of susceptibility mapping could be of great interest to researchers. In this chapter, we will discuss the consistency of QSM measurements in the SN across all the studies included in this thesis. We will be seeking to answer two major questions in this regard: 1) under normal circumstances, how do QSM measurements from each of these studies compare to one another as well as to the gold standard normal population? and 2) how does iron behave in the SN upon neurodegeneration in PD and RBD in subjects with bilateral loss of N1 compared to those with no bilateral loss?

We put together all QSM measurements from three studies in Chapters 4-6 and superimposed the results from HC, PD and RBD subjects onto the global and regional susceptibility-age normal baselines established by Liu et al. [12] In order to strengthen the analyses, we have added a fourth group that only includes 22 PD patients (17 males and 5 females) whose data were collected at a different center. These 22 patients were scanned on a 3.0 T Skyra MR system (Siemens, Germany) with a twenty-channel head/neck coil. The 3D SWI imaging parameters were: TE/TR = 20/30 ms, flip angle = 15°, slice thickness = 2mm, pixel bandwidth = 121 Hz/pixel and an in-plane resolution of $0.2 \times 0.2$ mm$^2$. The average ± standard deviation for disease duration, H&Y and UPDRS-III scores for these patients are 7.1 ± 5 years, 2.0 ± 0.3 and 28.5 ± 2, respectively. ROI tracings, iron quantification and N1 analysis were performed on these data using the same algorithm discussed in Chapter Five. The following summarizes the MR scanners and subject groups from the five studies including: 174 HCs on a 1.5T GE Signa (normal baselines), 24 HCs and 25 PD patients on a 3T GE

Signa (Chapter Four), 40 HCs and 40 PD patients on a 3T Philips Ingenia (Chapter Five), 28 HCs

and 29 RBD patients on a 3T Siemens Prisma (Chapter Six) and finally 22 PD patients on a 3T

Siemens Skyra. Therefore, excluding the HCs in the healthy baseline population, a total of 92 HC,

87 PD and 29 RBD patients are included whose data were collected on five separate scanners from

three manufacturers and two field strengths. The datapoints associated with all these studies are

shown in Supplementary Figure **8.1**.
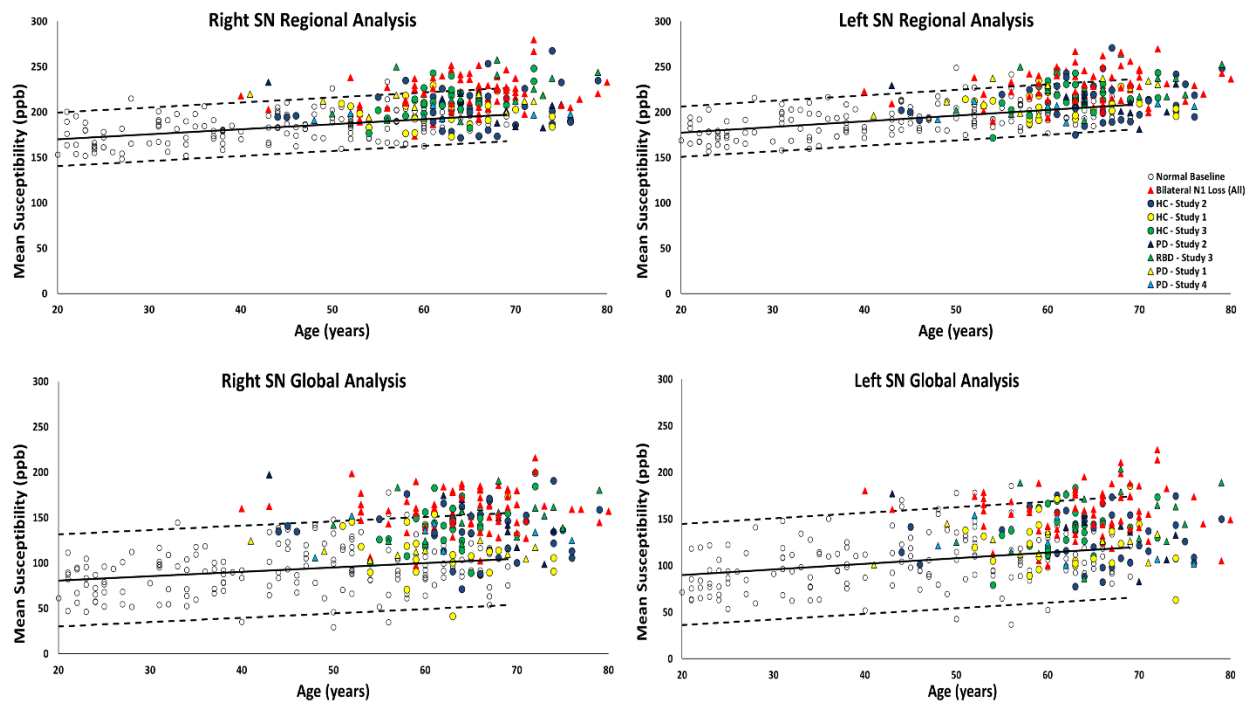


**Supplementary Figure 8.1** Overlay of HC, PD and RBD data on the global and regional baselines from Liu et al. [12] in the SN. Colored solid circles: HC data from each corresponding study, colored solid triangles: PD and RBD data from each corresponding study, red triangles: PD and RBD data with bilateral N1 loss from all studies combined.

There are two important takeaways from this figure. First, by looking at the solid circles

representing the normal subjects from each study, it is clearly seen that the majority of both global

and regional QSM results associated with the HC data fall within the normal range restricted by the

lower and upper bands of the corresponding baselines. Out of a 92 HCs across all four studies, 80

(87%) and 86 (93%) subjects from the global analysis and 81 (88%) and 82 (89%) subjects from the

regional analysis fell between the lower and higher 95% intervals in the right and left hemisphere, respectively. This essentially validates the fact that both global and regional susceptibility values derived from all HCs are consistently within the normal ranges regardless of the manufacturer. Furthermore, in addition to higher sensitivity and reliability, these results confirm QSM superior performance over R2* in terms of being dependent upon field strength.

Second, it appears that the majority of PD and RBD cases with bilateral loss of the N1 sign (red triangles) are located above the linear regression model associated with global and regional susceptibility-age trends. Out of 72 PD/RBD cases with bilateral N1 loss across all four studies, 70 (97%) and 69 (96%) subjects from the global analysis and 68 (94%) and 66 (92%) subjects from the regional analysis had susceptibility values higher than the corresponding linear regression models from the healthy population in the right and left hemisphere, respectively. Additionally, the majority of subjects with abnormally high iron content in both analyses (i.e. susceptibility values above the upper 95% interval) also appear to be PD and RBD subjects with bilateral N1 loss. Out of 46 and 30 patients with abnormally high global iron, 39 (85%) and 23 (77%) subjects and out of 36 and 30 patients with abnormally high regional iron, 27 (75%) and 24 (80%) subjects had bilateral loss of N1 in the right and left hemisphere, respectively. The fact that patients with bilateral N1 loss seem to do worse in terms of abnormal iron deposition in their SN is another novel finding in this thesis which could potentially lead to a better understanding of underlying pathogenesis in Parkinsonism at its earlier stages. Nevertheless, these observations warrant further investigation evaluating the relationships between elevated levels of iron these patients with NM signal and volume as well as clinical scores.

## Chapter Nine: Supplementary Material II (Chapter Five)

**Visualizing the midbrain structures**

Imaging neuromelanin and iron as biomarkers in Parkinson's disease depends not only on imaging these two components with MRI but also on identifying them in the midbrain. Understanding the anatomy and its associated nomenclature is a major part of this process. However, there seems to be some confusion in the field in terms of the anatomy of the SN and what the iron and neuromelanin provide in terms of the SN sub-structures (SNpc and SNpr). In fact, a recent paper was published solely to discuss the nomenclature and understanding of the ventral tegmental area (VTA) in the midbrain. [207]

The first consideration in mapping iron and neuromelanin is their relationship to the SN. From an anatomical perspective, as one goes from superior towards inferior slices, the SN is located in the midbrain and starts where the nigrostriatal pathway ends in the subthalamic nuclei. It appears from about the middle of the RN to directly below the RN usually for 4 to 5 slices with a 2 mm thickness (roughly 8 mm) depending on the partial volume effect in the caudal slices. Rostrally, from the middle of the RN, the subthalamic nucleus (STN) branches off and can be seen in the two upper slices covering about 4mm. Both the STN and SN make an angle to the x-axis and z-axis making it difficult to choose any particular optimal imaging plane. However, with isotropic or near isotropic resolution, the size of the SN can be reasonably accurately measured. The SN consists of two parts, the SNpc and SNpr. The SNpr is predominantly ventral and rostral while the SNpc is predominantly dorsal and caudal. Visualizing that difference is difficult on one single sequence at 3 T although some progress differentiating them has been made at 7 T. [285] They show the usual N1 region as an oval loop surrounded by iron. In the gradient echo data of the cadaver brain shown in their Figure 2,

centrally the signal is bright highlighting the N1 sign. These N1 findings are found more caudally in the SNpc. Since the neuromelanin content present in the N1 region does not show paramagnetic characteristics like iron, the N1 sign can be seen with an opposite intensity on susceptibility-sensitive contrast methods. For example, the contrast between iron and neuromelanin can be seen on SWI/QSM where the lateral and medial portions of the SN show hypointense/hyperintense signal in most cases while the NM in N1 shows hyperintense/hypointense signal for healthy controls because it has less MR visible iron content.

**Supplementary Table 9.1.** The p-values for the various imaging variables for HCs and PD subjects. In these measures, a p-value less than .05 is considered significant and shown in bold.

| Measures | Mean ± Standard error | | |
|---|---|---|---|
| | HC | PD | *P* Value |
| $SN_{VOL,MTC}$ (mm³) | 322.85 ± 4.72 | 234.58 ± 6.22 | **< .001** |
| $SN_{VOL,QSM}$ (mm³) | 477.53 ± 12.63 | 395.38 ± 9.61 | **< .001** |
| $SN_{\Delta\chi}$ (ppb) | 132.12 ± 4.01 | 155.30 ± 4.09 | **< .001** |
| $SN_{OVERLAP}$ (%) | 39.96 ± 1.05 | 36.49 ± 1.29 | **.040** |

Naming the different parts of the SN has been somewhat confusing since people use the usual x, y and z coordinates as lateral/medial, anterior/posterior and cranial/caudal, respectively, as well as rostral/caudal, ventral/lateral and superior/inferior. These various terminologies in themselves can be confusing. Further, a careful naming of the different parts of the midbrain in the transverse plane is quite complicated because of the many small unclear structures. VTA visualization is complicated in that there are no clear anatomical borders to delineate the structure because the VTA consists of a heterogeneity of nuclei which exhibit gradual transitions, and until the recent paper by Trutti et al, there has been no consensus about the anatomical nomenclature to define the VTA territory as a whole in the literature. [207] In this work, for the clarity of terminology, the term NM complex is used to refer to the entire NM hyperintensity region in the midbrain. Given there is still considerable

inconsistency in the terminology of the VTA as a nucleus [286] versus VTA as a region, [287] we refer to the VTA as the midline VTA nucleus and SNpd (also referred to as the parabrachial pigmented (PBP) nucleus) to the area located ventromedially to dorsolaterally between the red nucleus and the SNpc as used in previous histological studies. [286] To help clarify these concerns we presented a cartoon at the end of Figure **5.1** in the main text which we reproduce here as Supplementary Figure **9.1**.

**Supplementary Table 9.2**. Statistics for the various combinations of imaging variables. Sensitivity (SENS), specificity (SPEC), area under the curve (AUC) and accuracy (ACC) for the individual features as well as different combinations of the studied measures $SN_{VOL,MTC}$, $SN_{OVERLAP}$, $SN_{VOL,QSM}$, $SN_{\Delta\chi}$ and Nigrosome 1 (N1). Accuracy here is defined as (true positive + true negative) / (healthy controls + Parkinson's patients).

| Individual/Combinations of Features | SENS | SPEC | AUC | ACC |
|---|---|---|---|---|
| $SN_{VOL,MTC}$ | .863 | .913 | .960 | .888 |
| $SN_{VOL,QSM}$ | .738 | .825 | .788 | .781 |
| $SN_{\Delta\chi}$ | .581 | .888 | .740 | .734 |
| $SN_{OVERLAP}$ | .613 | .775 | .629 | .694 |
| N1 | .913 | .838 | .891 | .875 |
| $SN_{VOL,MTC}$ / $SN_{VOL,QSM}$ | .900 | .975 | .969 | .938 |
| $SN_{VOL,MTC}$ / $SN_{OVERLAP}$ | .900 | .975 | .965 | .938 |
| $SN_{VOL,MTC}$ / $SN_{\Delta\chi}$ | .925 | .975 | .976 | .950 |
| $SN_{VOL,MTC}$ / $SN_{VOL,QSM}$ / $SN_{\Delta\chi}$ | .913 | .950 | .981 | .931 |
| $SN_{VOL,MTC}$ / $SN_{VOL,QSM}$/ N1 | .969 | .950 | .983 | .959 |
| $SN_{VOL,MTC}$ / $SN_{OVERLAP}$ / $SN_{\Delta\chi}$ | .856 | .950 | .976 | .903 |
| $SN_{VOL,MTC}$ / $SN_{VOL,QSM}$/ $SN_{OVERLAP}$ | .888 | .938 | .969 | .913 |
| $SN_{VOL,QSM}$/ $SN_{OVERLAP}$ / $SN_{\Delta\chi}$ | .825 | .913 | .911 | .869 |
| $SN_{VOL,MTC}$ / $SN_{VOL,QSM}$/ $SN_{OVERLAP}$ / $SN_{\Delta\chi}$ | .913 | .950 | .981 | .931 |
| $SN_{VOL,MTC}$ / $SN_{VOL,QSM}$/ $SN\Delta\chi$ / N1 | .969 | .950 | .980 | .959 |
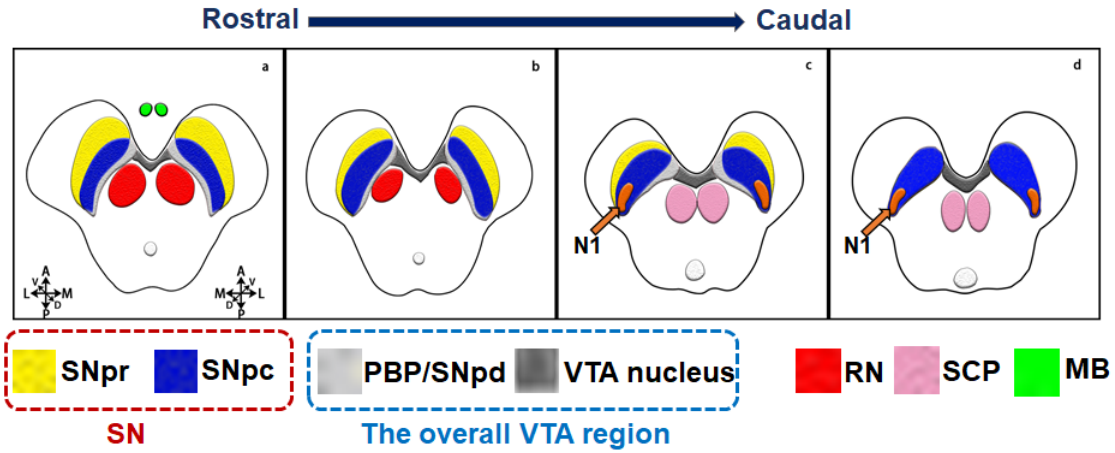
**Supplementary Figure 9.1.** Schematic representation of the midbrain. Here we show a cartoon of the four representative transverse levels (a, b, c, d) based on iron-NM contrasts and landmarks from previous human post-mortem works. SNpr = substantia nigra pars reticulata, SNpc = substantia nigra pars compacta, PBP= parabrachial pigmented nucleus, SNpd=substantia nigra pars dorsalis, VTA=ventral tegmental area, N1 = nigrosome-1, RN=red nucleus, SCP=superior cerebellar peduncles and MB=mammillary body. For the direction labels, L=lateral, M=medial, V=ventral, D=dorsal, A=anterior and P=posterior.

Four separate examples showing the N1 sign are shown in Supplementary Figure **9.2.** The N1 sign appears in the ventral lateral part of the NM boundary and is usually evident in HCs.
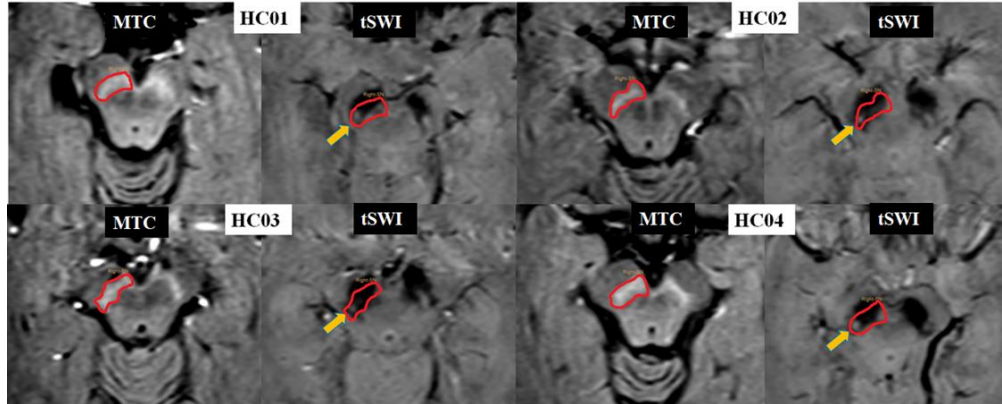


**Supplementary Figure 9.2.** Demonstration of the location of the N1 sign. NM-MRI and tSWI for 4 different healthy controls showing the overlay of the NM boundary (traced using DP semi-automated technique) onto the tSWI. The yellow arrows show the hyperintense region in tSWI data presumably highlighting the N1 territory which is also located in the ventrolateral aspect of the NM boundaries (as drawn on the NM-MRI data).

**Supplementary Table 9.3.** The p-values for the various combinations of imaging variables. The Bonferroni correction yields a significance threshold of 0.003 for the p-values. The significant p-values are shown in bold.

| Measures | Comparison Between the ROC Curves (reported numbers are p-values) | | | |
|---|---|---|---|---|
| | $SN_{VOL,MTC}$ | $SN_{VOL,QSM}$ | $SN_{\Delta\chi}$ | $SN_{OVERLAP}$ |
| $SN_{VOL,MTC}$ | - | **.001** | **< .001** | **< .001** |
| $SN_{VOL,QSM}$ | **< .001** | - | .570 | .070 |
| $SN_{\Delta\chi}$ | **< .001** | .570 | - | .157 |
| $SN_{OVERLAP}$ | **< .001** | .070 | .157 | - |
| $SN_{VOL,QSM}$ / $SN_{\Delta\chi}$ | .020 | - | - | - |
| $SN_{VOL,MTC}$ / $SN_{VOL,QSM}$ / $SN_{OVERLAP}$ / $SN_{\Delta\chi}$ | .222 | **< .001** | **< .001** | **< .001** |

## Dynamic programming to determine the boundaries of the SN and NM

The initial regions-of-interest (ROIs) associated with neuromelanin and substantia nigra were drawn outside the objects on the MTC and QSM images, respectively, which were then used as input to the dynamic programing algorithm (DPA) to determine the final boundaries. To keep the shape of the object, the centerline associated with the initial boundary was detected first. [288] The edge detection occurs using a cost function which is evaluated along the centerline. The rays originate from each selected point on the sorted centerline points, towards the drawn boundary point, which move clockwise. The cost function consists of a derivative term as well as a radius of curvature term which avoids the leakage of the structure of interest into the adjacent objects although we usually limit the search radius outside the boundary as well. [216] The cost function is given by:

$$C(r,m) = \frac{G(r,m) + G_{pre}}{G_{max}} - \alpha * \frac{|R(r,m) - R_{avg}|}{R_{avg}}$$

$$G_{pre} = \sum_{t=m-3}^{m-1} G(t)_{max}$$

where the gradient and the radius along the m<sup>th</sup> ray at the r<sup>th</sup> point are denoted by $G(r,m)$ and $R(r,m)$, respectively. The term $G_{max}$ represents the maximum derivative inside the image and $R_{avg}$ is the average radius over the previous three radii.

For each ray, the calculations are done based on the average radius of curvature associated with the previous three rays, except for the first three which are chosen to start at the center of the centerline. The search process then encircles the entire boundary and iterates five times around the boundary. The candidate points for the new boundary are selected by maximizing the above-mentioned cost function for each ray. Besides the derivative and radius of curvature, the cost function is also dependent on parameters such as the maximum derivative along each ray, and α was set to 0.4. In this work, since the raters drew the initial boundaries a few pixels outside the objects, the algorithm was set to search inside only. An example of the proposed DPA used by two independent raters on both MTC magnitude and MTC-QSM is shown in Supplementary Figure **9.3**.
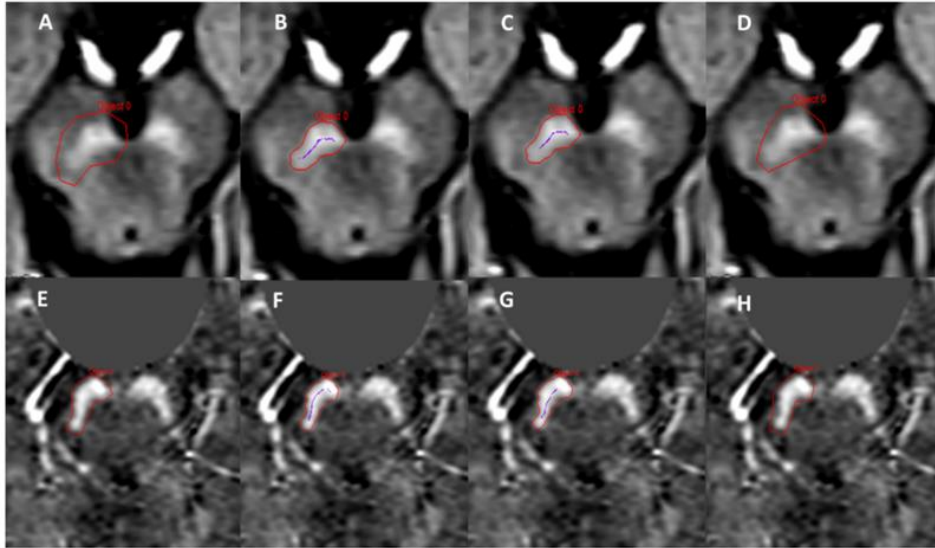


**Supplementary Figure 9.3.** Dynamic programming boundary detection on MTC and QSM images. An example of two different manually drawn boundaries (A, D) on MTC, and (E, H) QSM images. The final boundaries, which were found by dynamic programming (B,C) and (F,G), are almost identical with the number of pixels being (B) 1339 and (C) 1349 for MTC, and (F) 1960 and (G) 1975 for QSM. The average signal intensity changed from 20,730 (B) versus 20,717 (C) for MTC. For QSM, the average susceptibility for these boundaries were (F) 143 ppb and (G) 140 ppb, respectively.

## MTC-QSM can be used to quantify iron in PD

Our approach uses a single sequence to obtain iron and neuromelanin measures. One of the advantages of phase and QSM is that, apart from SNR in both cases, the former is independent of flip angle and the latter is independent of echo time. We compared the usual STAGE gradient echo sequence without an MTC pulse and with an MTC pulse and found that the susceptibility measurements were similar (Supplementary Figure **9.4**). Paired-sample t-tests revealed no significant difference between the mean susceptibility values measured using these two sequences ($p = .452$). An example comparison of the QSM results for the two methods (along with the R2* maps and SWI results from the MTC data) is shown in Supplementary Figure **9.4**.
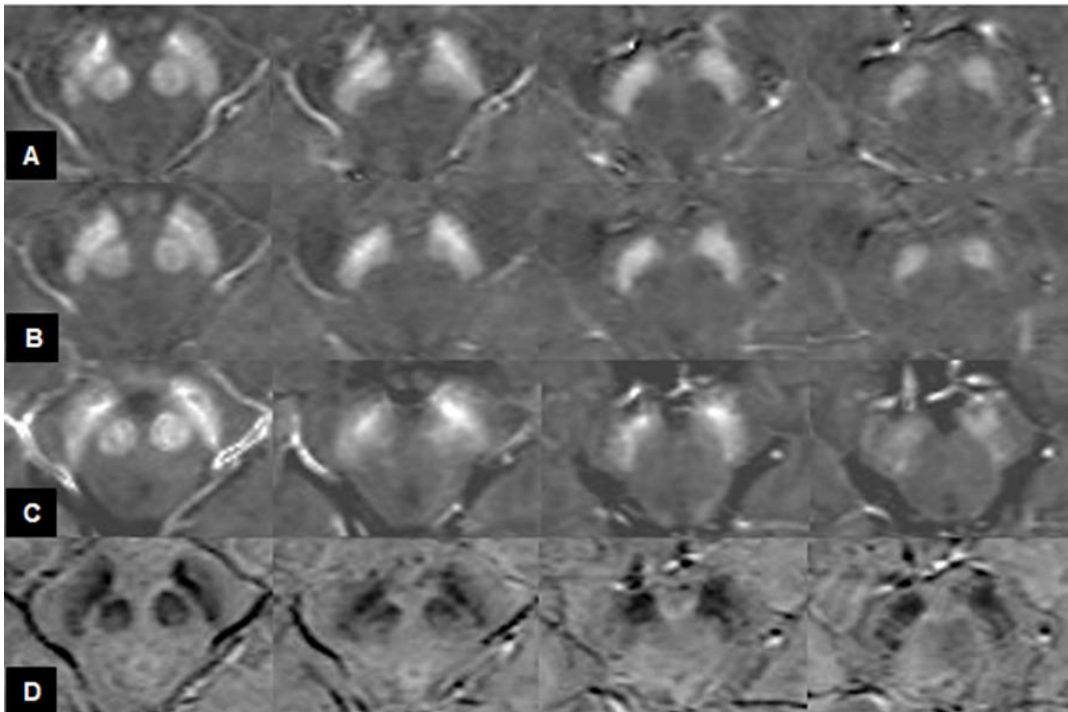


**Supplementary Figure 9.4.** Comparison of the susceptibility maps from the non-MT STAGE data and the MTC-STAGE data. (A) QSM data using TE = 15ms from the MTC-GRE data. (B) QSM data using TE = 17.5 ms from STAGE non-MT GRE scans. (C) $R_2^*$ map from the 5 echoes of the MTC data ($\Delta$TE = 30 ms). It can be seen that both echo times provide QSM measures that are very similar in their overall contrast as the plots in the paper also show in their equivalent quantification of iron content. The $R_2^*$ maps show similar results for the high iron content regions for the 5-echo MTC data. It should also be borne in mind that $R_2^*$ will show high iron regions larger than they really are because of the dipole effects in the image leading to edge signal loss. (D) SWI from the MTC 22.5 ms echo time data. Here the N1 sign is seen clearly in the last two caudal slices for the left SN.

The boundaries from the QSM data from the MTC sequence were copied over to the STAGE QSM data after co-registration of the two data sets and then the DPA was run again. A plot of the measured susceptibility values between these two methods is shown in Supplementary Figure **9.5** where there is a good linear relationship (slope = 1.11, $R^2$=0.751, $p$ < .001) between the susceptibility values measured from MTC-QSM and STAGE-QSM in both HC and PD cohorts combined.
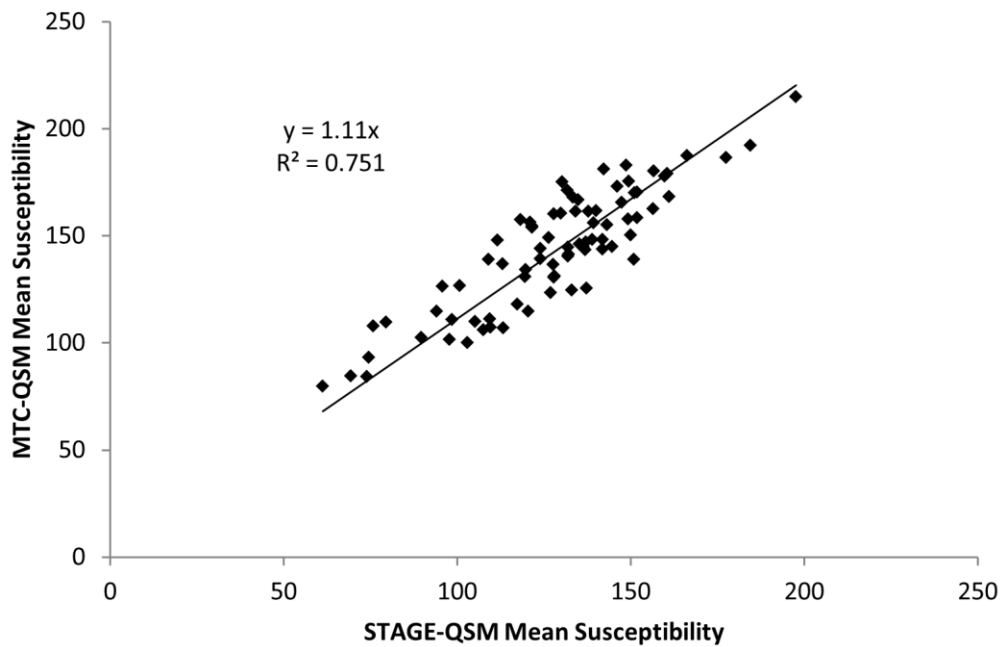


**Supplementary Figure 9.5.** Plot of susceptibility from MTC-QSM and STAGE-QSM for all 80 cases (40 HCs and 40 PDs). This plot shows a good correlation between these two methods using a linear regression model ($p < .001$). The data points show the average mean susceptibility values between the two hemispheres. The intercept of the linear regression model was set to the origin leading to a slope of 1.11 and an $R^2$ of .751.

**The relationship between iron volume, NM volume and NM contrast in the SN with age**

As discussed in this study, some papers have shown a change in signal intensity for NM as a function of disease and age. We saw no significant correlation of $SN_{VOL,MTC}$ with age for either group but a significant correlation with age was seen for the contrast of the NM with respect to the

background for the HC group ($p$ = .048) and for $SN_{VOL,QSM}$, for the PD group ($p$ = .001). (Supplementary Figure **9.6**).
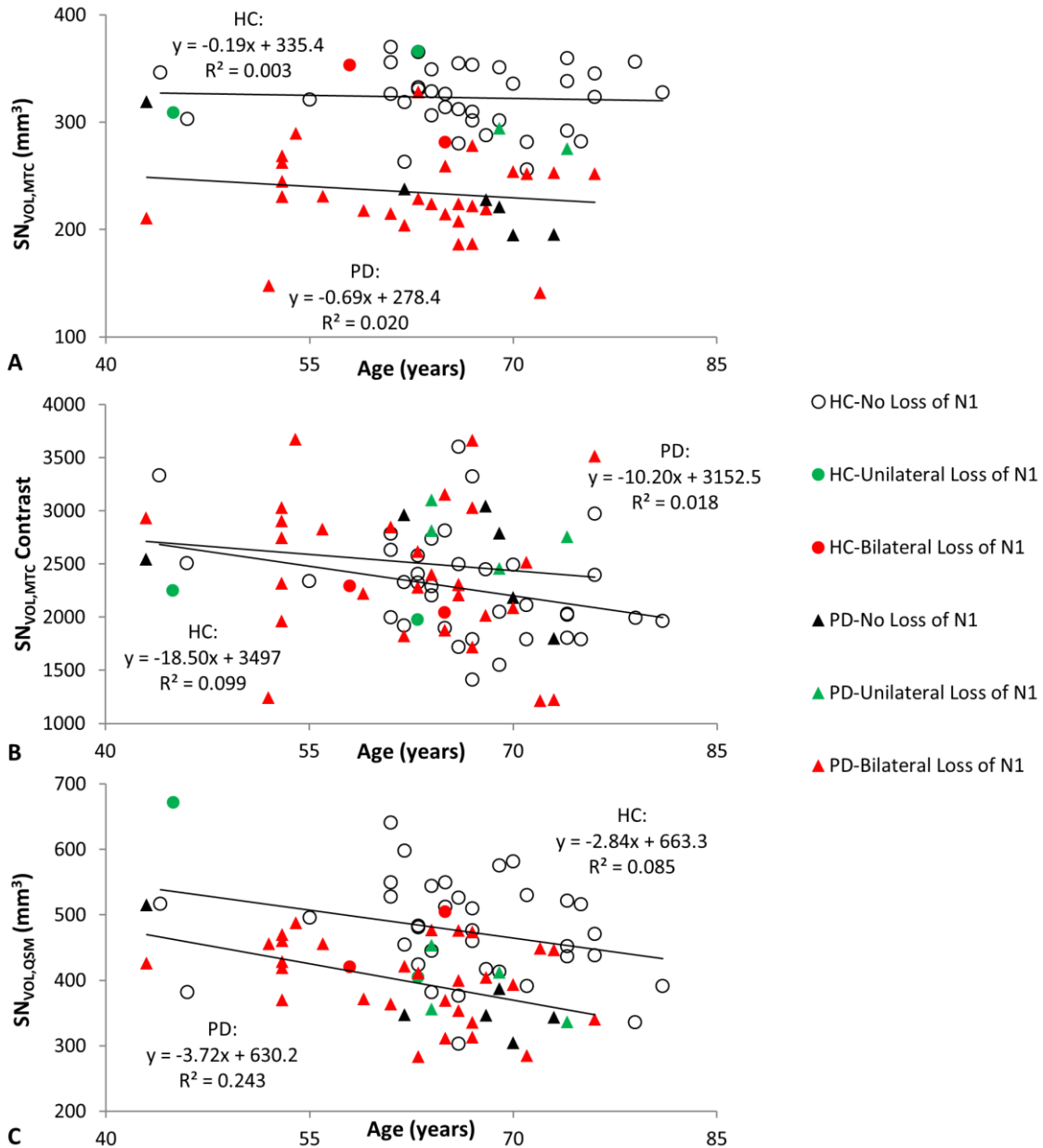


**Supplementary Figure 9.6.** The change in NM volume, NM contrast and SN volume with age. (A) $SN_{VOL,MTC}$ (averaged over both sides) showed no correlation with age for both HCs and early stage PD patients ($p$ = .746 and $p$ = .382, respectively). (B) $SN_{VOL,MTC}$ contrast (averaged over both sides) relative to the background (the crus cerebri) as a function of age. There is a trend downward in contrast for the HCs ($p$ = .048) but not the PD patients ($p$ = .415) as a function of age. (C) $SN_{VOL,QSM}$ (averaged over both sides) as a function of age. There is a significant trend seen in the change of $SN_{VOL,QSM}$ as a function of age for the PD patients ($p$ = .001) but not for the HC group ($p$ = .069). PD = Parkinson's disease, HC=healthy control.

**PBP volume**

It is interesting to note that the PBP (or SNpd) volume can be found by subtracting the overlap volume from the $SN_{VOL,MTC}$. There appears to be a linear downward trend of PBP volume with overlap volume increase (Supplementary Figure **9.7**A) and $SN_{VOL,QSM}$ (Supplementary Figure **9.7**B).
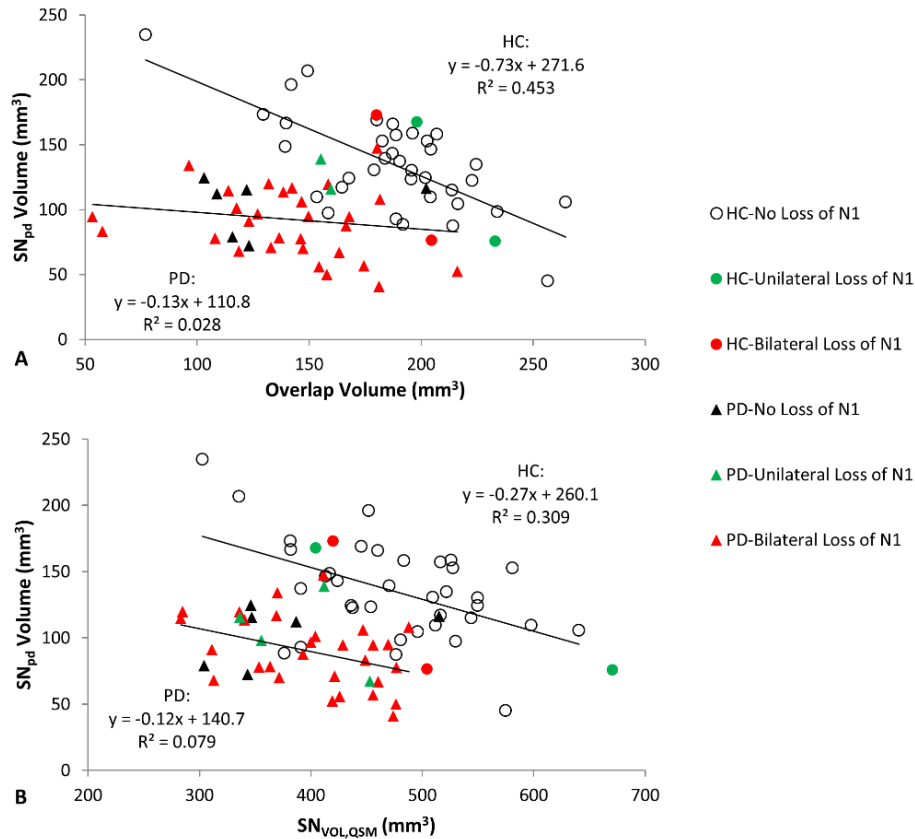


**Supplementary Figure 9.7**. PBP volume as a function of overlap volume and SNVOL,QSM volume for both groups. (A) HC showed a correlation of PBP with overlap volume (p < .001) while PD did not (p = .306). (B) HC showed a correlation of PBP with SNVOL,QSM (p < .001) while PD did not (p = .078). PD = Parkinson's disease and HC = healthy controls.

Also of interest is the fact that the average PBP volume can be estimated in the limit that the overlap volume vanishes for the Parkinson's disease cases (the intercept shown in Supplementary Figure **9.8**A) and is found to be $110.81 \pm 18.10$ mm$^3$. Finally, the reduction in $SN_{VOL,QSM}$ is mirrored by the $SN_{VOL,MTC}$ (Supplementary Figure **9.8**B).
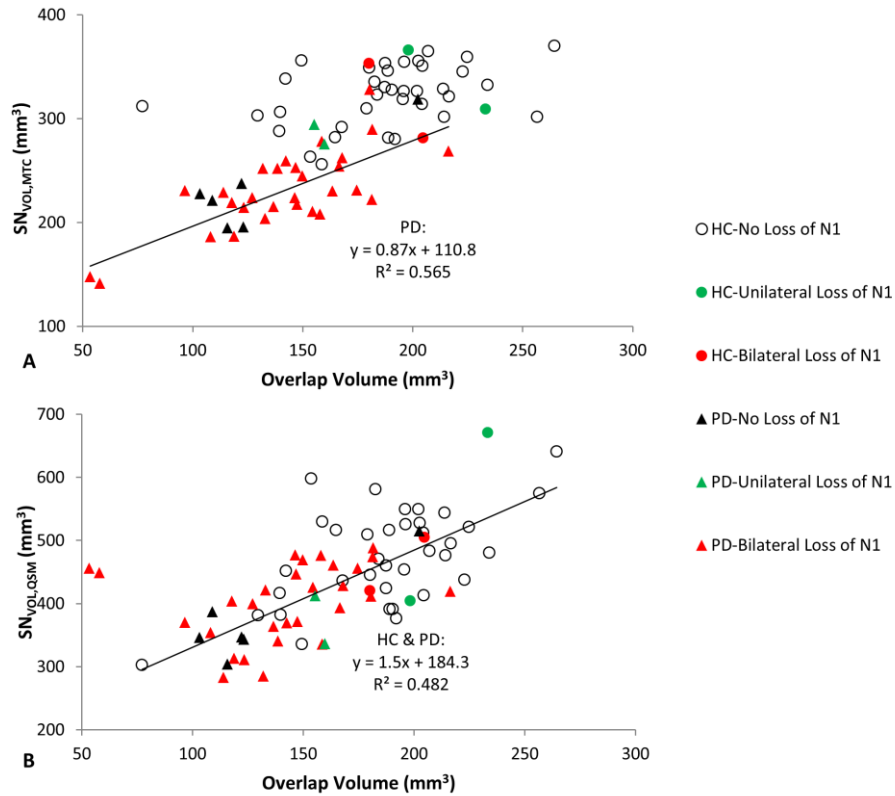
**Supplementary Figure 9.8.** The correlation between $SN_{VOL,MTC}$ and $SN_{VOL,QSM}$ and overlap volume for both groups. (A) $SN_{VOL,MTC}$ as a function of overlap volume to determine average SNpd volume for early stage PD patients ($p < .001$). (B) $SN_{VOL,QSM}$ as a function of overlap volume ($p = .032$). The trend line in (B) is fitted on all the data points of both groups except the two PD outliers showing very low overlap volume. Assuming the loss of volume occurs in the SNpc, when the overlap is zero, the $SN_{VOL,QSM}$ would be 184.3 mm$^3$, which one could interpret as the average SNpr. PD = Parkinson's disease. SNpc = SN pars compacta. SNpr = SN pars reticulata.

## Normalization by the midbrain volume

One could argue that the volumes of the NM complex and iron containing SN could be more spread out in terms of their absolute values because of different brain sizes or at least different midbrain sizes. Therefore, we also normalized the NM and iron containing SN volumes for all cases by the midbrain volume and replotted Figure **5.2** from the main body of the paper (see Supplementary Figure **9.9**).
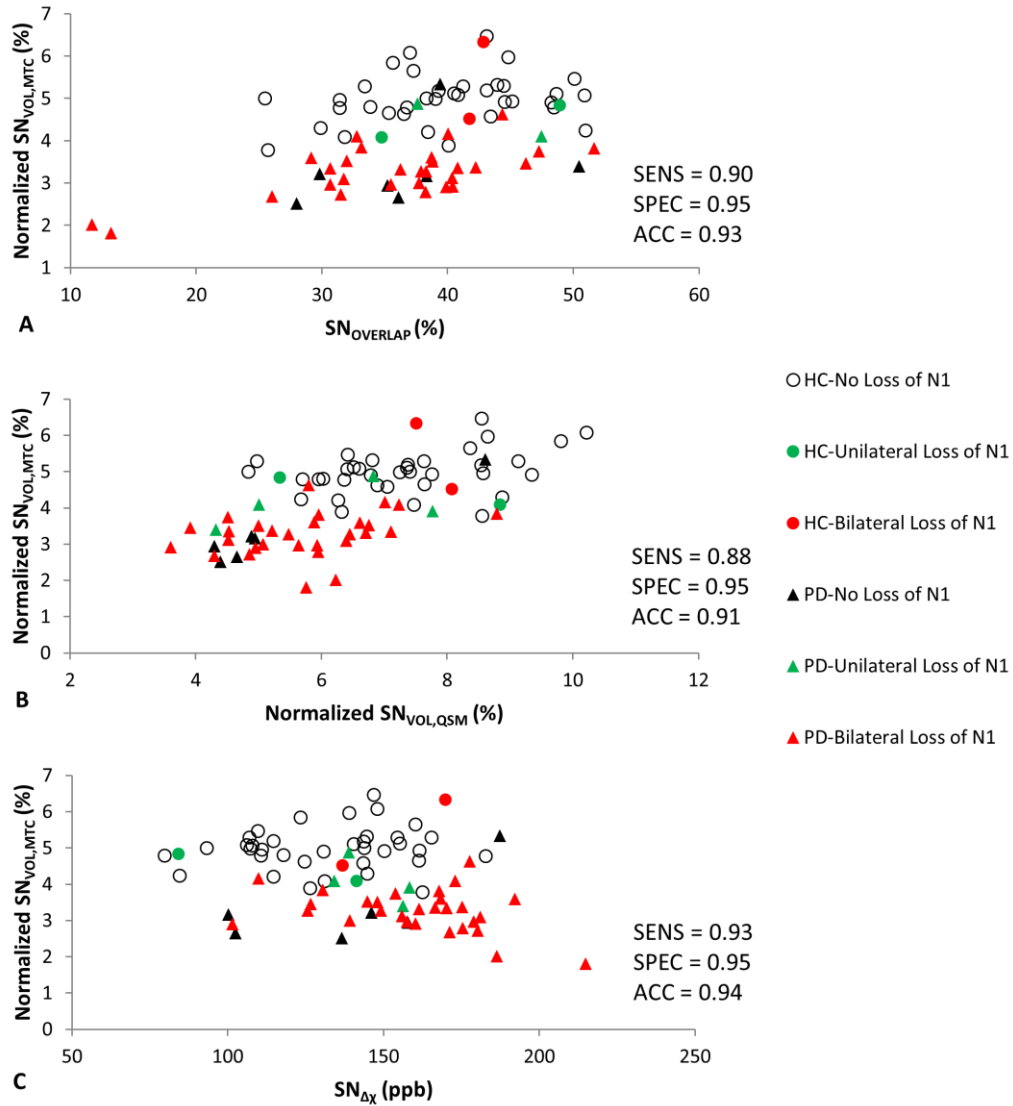
**Supplementary Figure 9.9.** Distinguishing between the two groups using normalized $SN_{VOL,MTC}$ and three other measures. Normalized $SN_{VOL,MTC}$ by midbrain volume as a function of (A) $SN_{OVERLAP}$, (B) normalized $SN_{VOL,QSM}$, and (C) $SN_{\Delta\chi}$. Sensitivity (SENS), specificity (SPEC) and accuracy (ACC) values are shown for each plot. PD = Parkinson's disease. HC = healthy control.

For the healthy controls, the ratio of the mean over standard deviation for un-normalized and normalized $SN_{VOL,QSM}$ was 5.98 and 5.53, respectively. For the Parkinson's disease patients, the ratio of the mean over standard deviation for un-normalized and normalized $SN_{VOL,QSM}$ was 6.50 and 4.56, respectively. For the HCs, the ratio of the mean over standard deviation for un-normalized and normalized $SN_{VOL,MTC}$ was 10.82 and 7.95, respectively. For the Parkinson's disease patients, the

ratio of the mean over standard deviation for un-normalized and normalized $SN_{VOL,MTC}$ was 5.96 and 4.80, respectively. The higher values seen in the un-normalized data indicate that there was less spread of the data without normalization. This could be due to the fact that the normalization process itself can introduce error into the volume measurements. According to these findings, we did not see any significant improvement in the results associated with the normalized $SN_{VOL,QSM}$ or $SN_{VOL,MTC}$ compared to the un-normalized scenario. The results for sensitivity, specificity, and accuracy confirm that normalization of the $SN_{VOL,MTC}$ does not make a significant improvement in separation of the two groups (the *p*-values associated with the un-normalized versus normalized ROC curves corresponding to the combination of $SN_{VOL,MTC}$ with each of $SN_{VOL,QSM}$, $SN_{\Delta\chi}$ and $SN_{OVERLAP}$ were calculated as .381, .363 and .492, respectively, which do not show any significant improvement in the normalized data).

**Discussion on the behavior of NM complex volume between PD subjects and HCs**

In this study, the $SN_{VOL,MTC}$ dropped roughly 25% for PD subjects relative to HCs. This reduction in volume is lower than the pathological changes of NM depigmentation in PD seen with postmortem studies which is thought to be on the order of 50-60% [10, 42, 189, 221]. However, the SNpd volume was estimated to be almost 111 mm$^3$ and if we subtract this from $SN_{VOL,MTC}$ for PD (238 mm$^3$ for right and 232 mm$^3$ for left hemispheres) and HCs (323 mm$^3$ for left and right hemispheres) yields a net SNpc volume for PD of 127 mm$^3$ (121 mm$^3$) for the right (left) side and for HCs of 212 mm$^3$ (left and right). This assumes the PBP (or SNpd) volume is the same for both PD and HCs which is not an unreasonable assumption. Now the apparent NM loss increases from 25% to 40% because the PBP contribution has been removed and this is more representative of the SNpc NM volume loss.

There is a broad range of NM volumes quoted in the literature. The most common values range from 112 to 370 mm$^3$ for HC and 52 to 215 mm$^3$ for PD subjects, the larger of these being consistent with our results [10, 29, 30, 38-42, 289]. The larger volumes were from a 3D Turbo Field Echo (TFE) sequence [29] using a semi-automated determination of the SNpc volumes (using a threshold of 2.0) which found NM volume results similar to ours using a higher resolution of 0.67 mm×1 mm× 1 mm. Two other studies quote volumes of more than 1000 mm$^3$ and 900 mm$^3$ for HC and PD subjects, respectively [21, 22]. These discrepancies most likely result from one or all of the following: the different resolutions that were used; the different contrast-to-noise ratios available for visualizing these structures; whether manual versus automated drawing methods were used; the threshold and the type of imaging sequence used as 2D methods usually have thick slices and slice gaps while 3D methods have contiguous thinner slices; and finally whether the upper levels of NM showing only VTA were included [10, 21, 22, 30, 38-42, 289]. These results should be compared to $SN_{VOL,QSM}$ determined from histological studies. A postmortem study shows that the SN consists of approximately 68% pigmented neurons and they find the SN volumes to be $(512 \pm 117)$ mm$^3$ and $(390 \pm 136)$ mm$^3$ for HCs and PD subjects, respectively. [290] Therefore, one can estimate $SN_{VOL,MTC}$ to be $(348 \pm 80)$ mm$^3$ and $(265 \pm 92)$ mm$^3$ for HCs and PD subjects, respectively, again in line with what we measured.

# Chapter Ten: Supplementary Material III (Chapter Six)

The correlations between age-corrected susceptibility values from ROI results with cognitive and motor function scores in the HCs are given in Supplementary Figure 10.1 and Supplementary Figure 10.2, respectively. Additionally, as shown in Supplementary Table 10.1, there were no significant differences in the global and RII susceptibility of the SN between the RBD group with N1 loss and those of the RBD group without N1 loss and HCs.
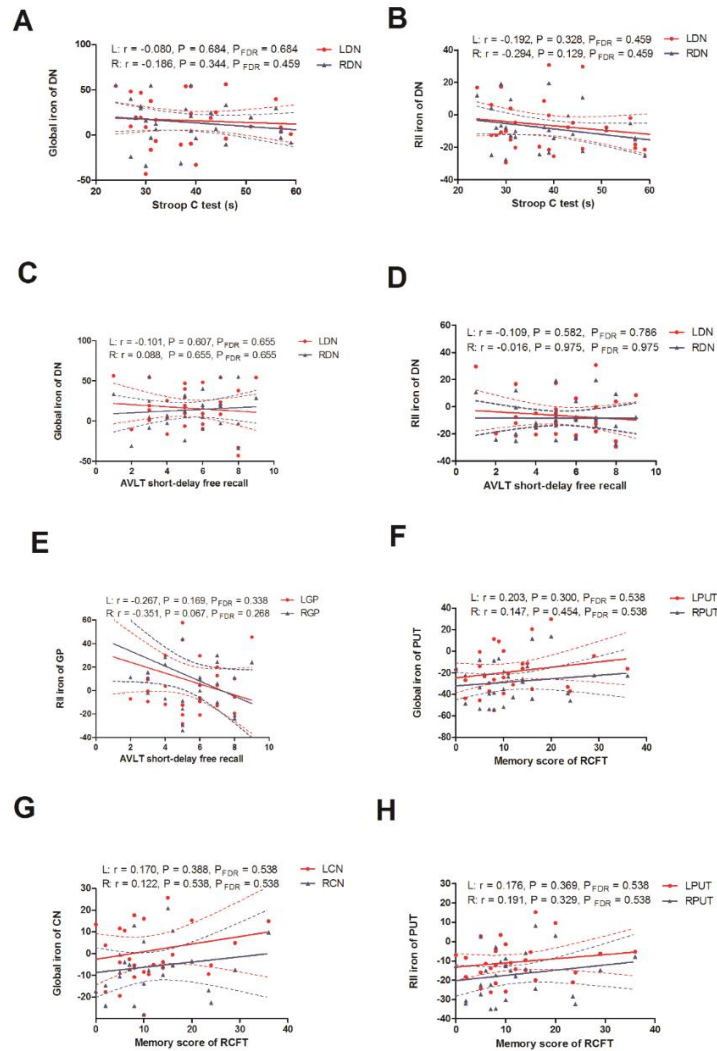


**Supplementary Figure 10.1**. Correlations between age-corrected iron deposition and cognitive functions in the HCs. Solid lines: linear regression model, dashed lines: 95% confidence intervals, DN: dentate nucleus, GP: globus pallidus, PUT: putamen, CN: caudate nucleus.
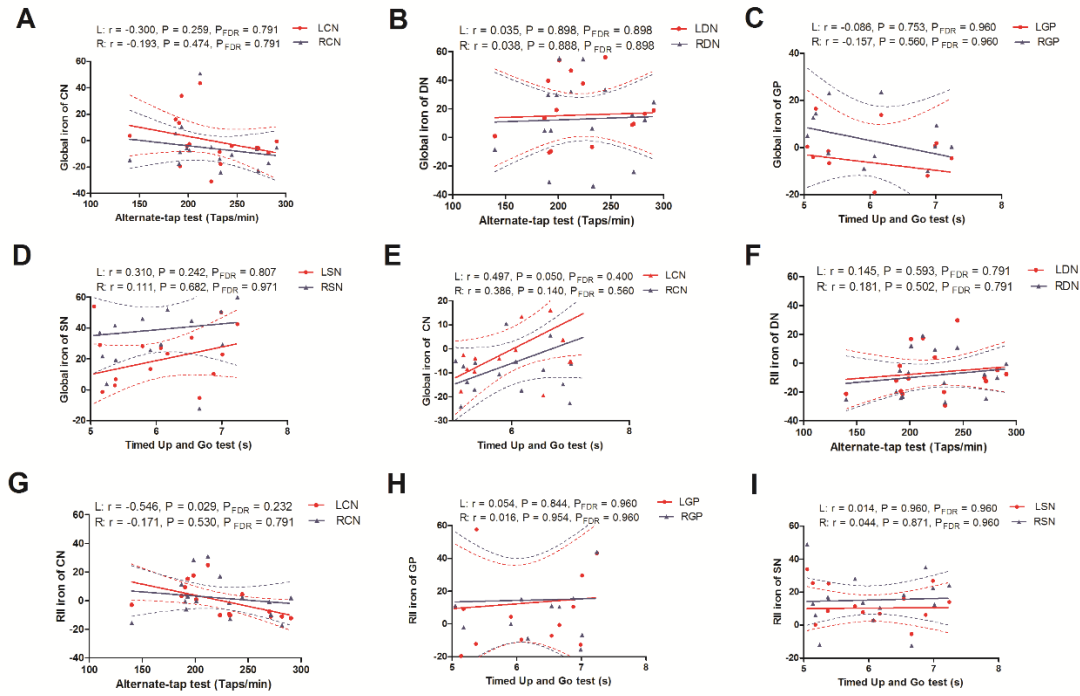
**Supplementary Figure 10.2.** Correlations between age-corrected iron deposition and motor functions in the HCs. Solid lines: linear regression model, dashed lines: 95% confidence intervals, CN: caudate nucleus, DN: dentate nucleus, GP: globus pallidus, SN: substantia nigra.

**Supplementary Table 10.1.** The global and RII susceptibility (ppb) of substantia nigra among groups of iRBD with bilateral N1 loss, iRBD with no N1 loss and HCs with no N1 loss.

| Structure | iRBD with bilateral N1 loss (N = 8) (A) | iRBD with no N1 Loss (N = 17) (B) | HCs with no N1 Loss (N = 26) (C) | P value | | |
|---|---|---|---|---|---|---|
| | | | | A vs. B | B vs. C | A vs. C |
| **Global** | | | | | | |
| **Right SN** | $45.3 \pm 19.0$ | $49.5 \pm 20.1$ | $40.6 \pm 24.9$ | 0.665 | 0.215 | 0.614 |
| **Left SN** | $31.8 \pm 14.6$ | $36.2 \pm 29.7$ | $25.1 \pm 22.3$ | 0.674 | 0.146 | 0.494 |
| **average** | $38.5 \pm 14.4$ | $42.8 \pm 24.2$ | $32.8 \pm 21.7$ | 0.645 | 0.146 | 0.520 |
| | | | | | | |
| **RII** | | | | | | |
| **Right SN** | $13.3 \pm 8.8$ | $25.1 \pm 18.4$ | $18.4 \pm 15.8$ | 0.091 | 0.185 | 0.434 |
| **Left SN** | $9.7 \pm 10.7$ | $21.7 \pm 20.3$ | $13.3 \pm 15.0$ | 0.095 | 0.108 | 0.591 |
| **average** | $11.5 \pm 9.6$ | $23.4 \pm 19.0$ | $15.8 \pm 14.8$ | 0.084 | 0.131 | 0.498 |

Plus-minus values are means ± SD. RII = high-iron thresholded region; SN = substantia nigra; iRBD = idiopathic rapid eye movement behavior disorder; HCs = healthy controls, ppb = part per billion.

Finally, the correlations between the susceptibility values from the rest of the ROIs and cognitive, motor, disease duration and RBDQ-HK scores are shown in Supplementary Figure 10.3-9.
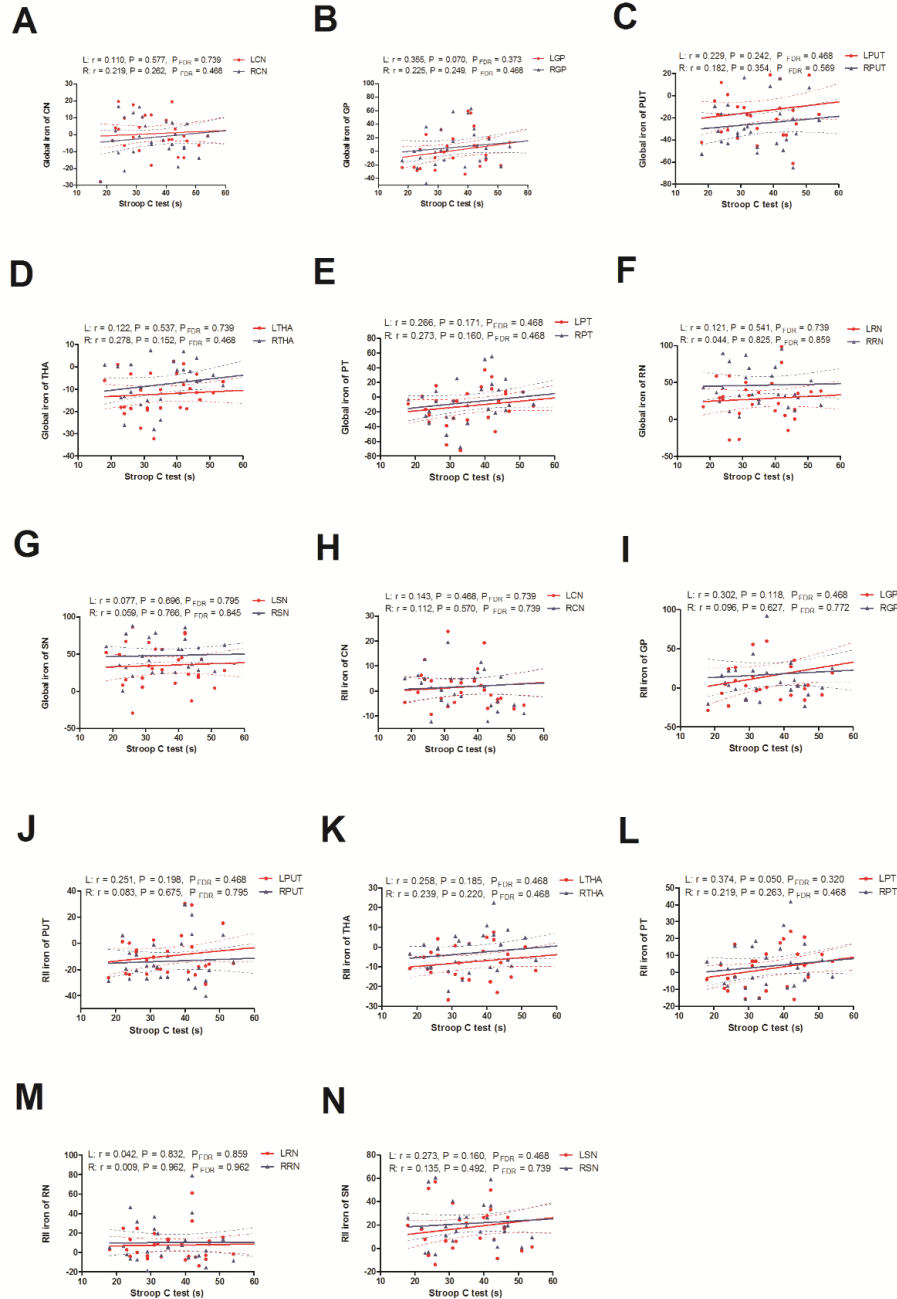


**Supplementary Figure 10.3.** Correlations between age-corrected iron deposition and attention-executive function in the iRBD patients. Solid lines: linear regression model, dashed lines: 95% confidence intervals, DN: dentate nucleus, GP: globus pallidus, PUT: putamen, CN: caudate nucleus, SN: substantia nigra, RN: red nucleus, THA: thalamus, PT: pulvinar thalamus.
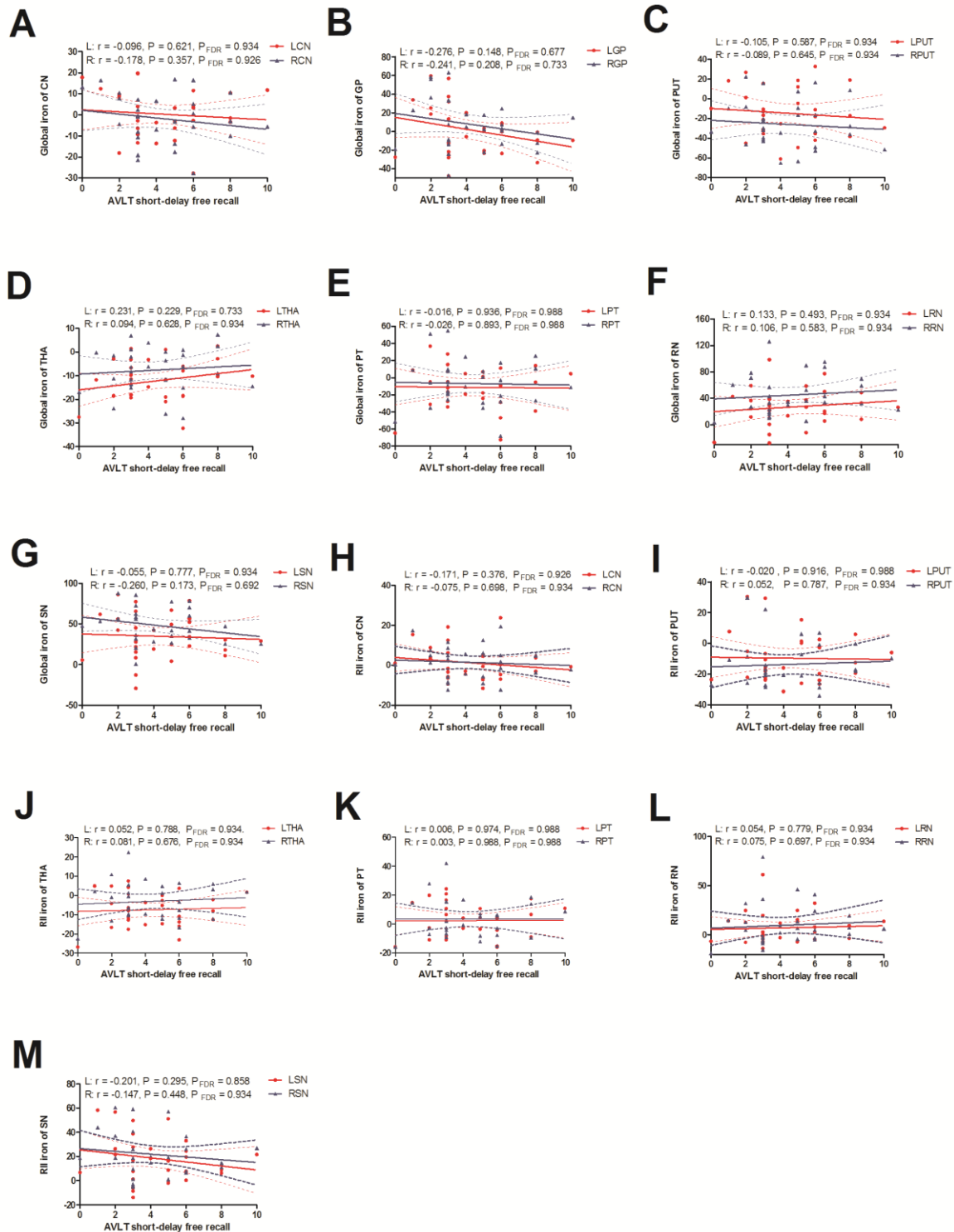
**Supplementary Figure 10.4.** Correlations between age-corrected iron deposition and verbal memory function in the iRBD patients. Solid lines: linear regression model, dashed lines: 95% confidence intervals, GP: globus pallidus, PUT: putamen, CN: caudate nucleus, SN: substantia nigra, RN: red nucleus, THA: thalamus, PT: pulvinar thalamus.
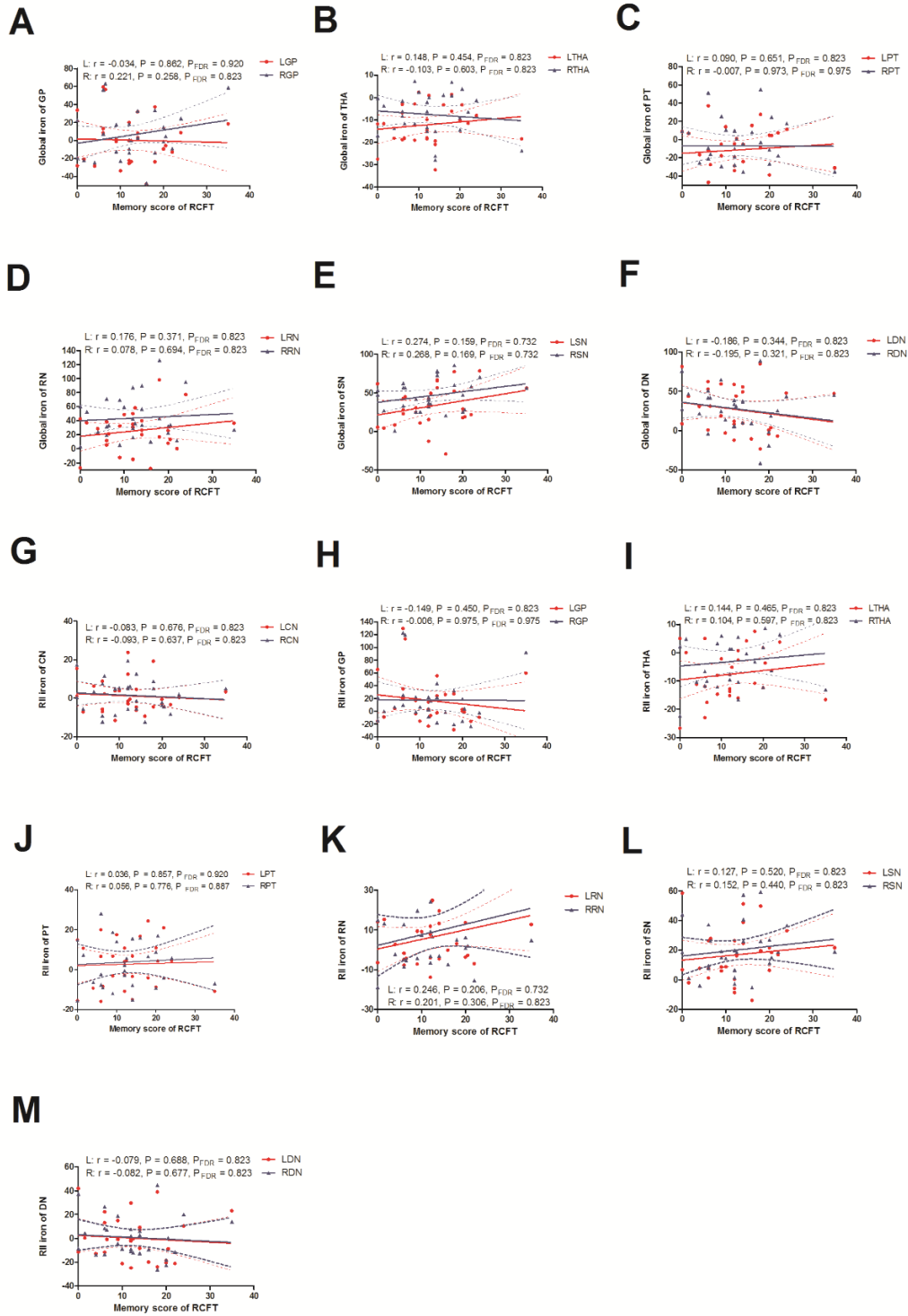
**Supplementary Figure 10.5.** Correlations between age-corrected iron deposition and visuospatial memory function in the iRBD patients. Solid lines: linear regression model, dashed lines: 95% confidence intervals, DN: dentate nucleus, GP: globus pallidus, CN: caudate nucleus, SN: substantia nigra, RN: red nucleus, THA: thalamus, PT: pulvinar thalamus.
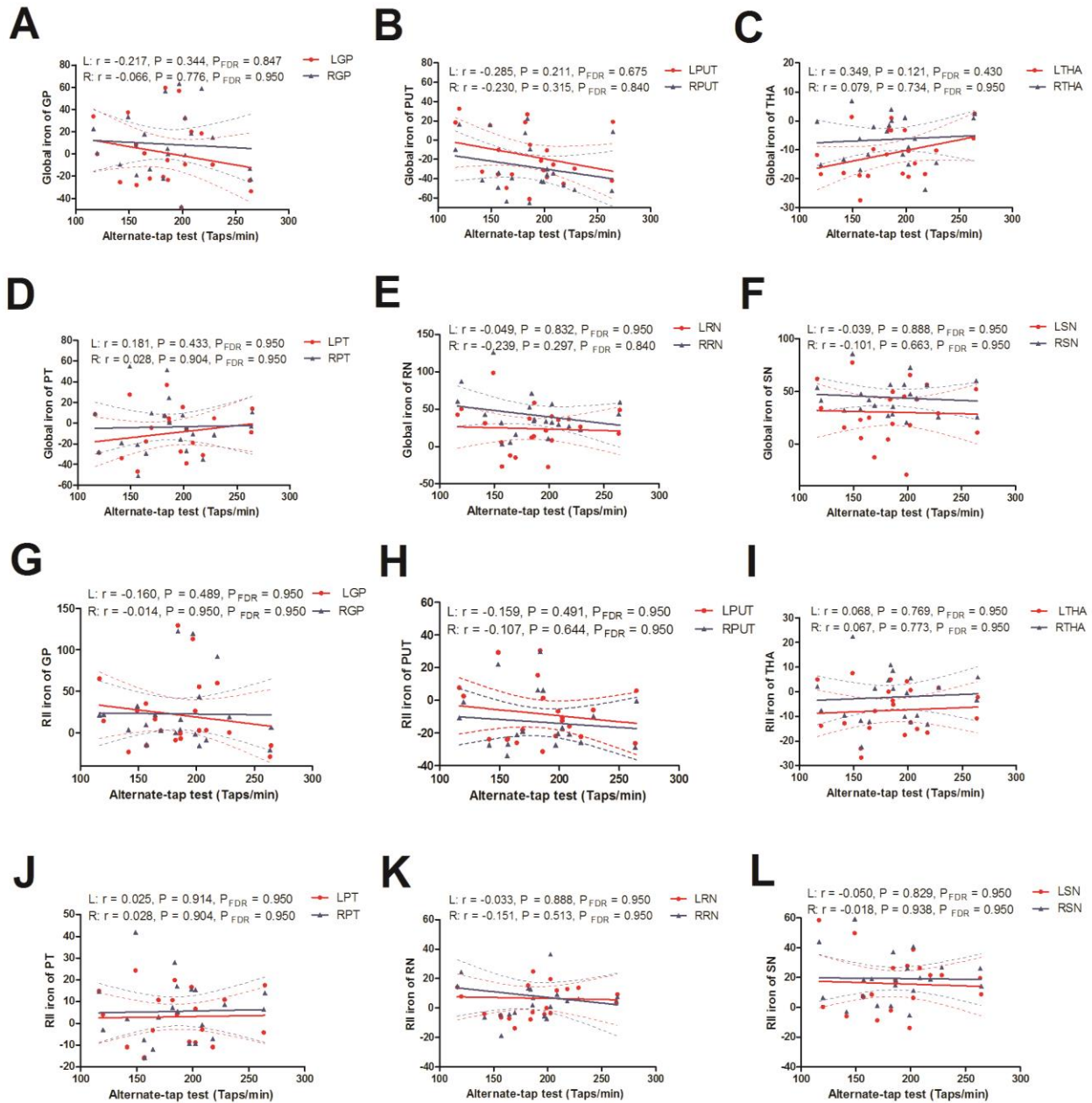
**Supplementary Figure 10.6.** Correlations between age-corrected iron deposition and scores of the alternate-tap test in the iRBD patients. Solid lines: linear regression model, dashed lines: 95% confidence intervals, GP: globus pallidus, PUT: putamen, SN: substantia nigra, RN: red nucleus, THA: thalamus, PT: pulvinar thalamus.
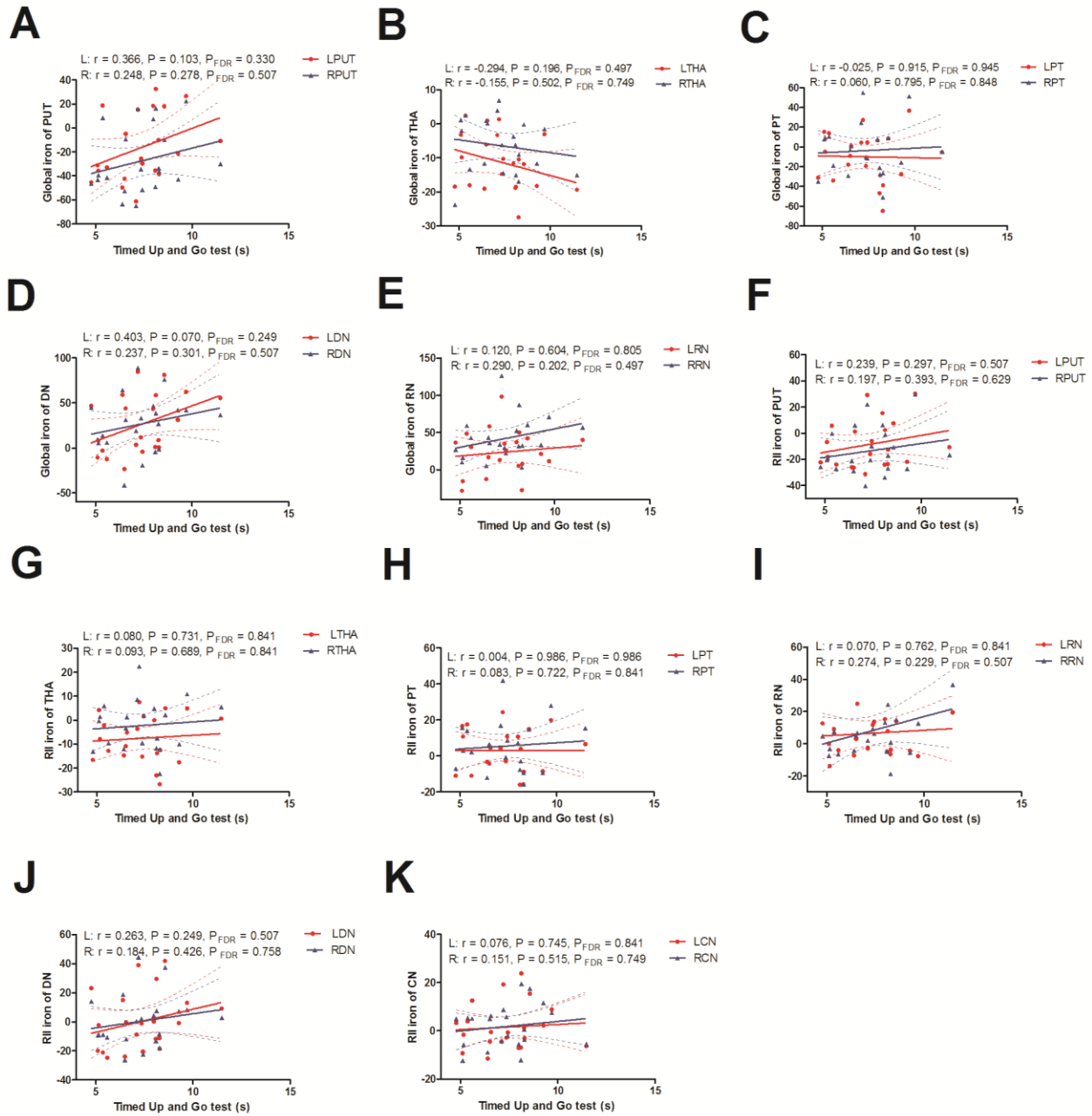
**Supplementary Figure 10.7.** Correlations between age-corrected iron deposition and scores of the 3-meter Timed Up and Go test in the iRBD patients. Solid lines: linear regression model, dashed lines: 95% confidence intervals, DN: dentate nucleus, GP: globus pallidus, PUT: putamen, CN: caudate nucleus, RN: red nucleus, THA: thalamus, PT: pulvinar thalamus.
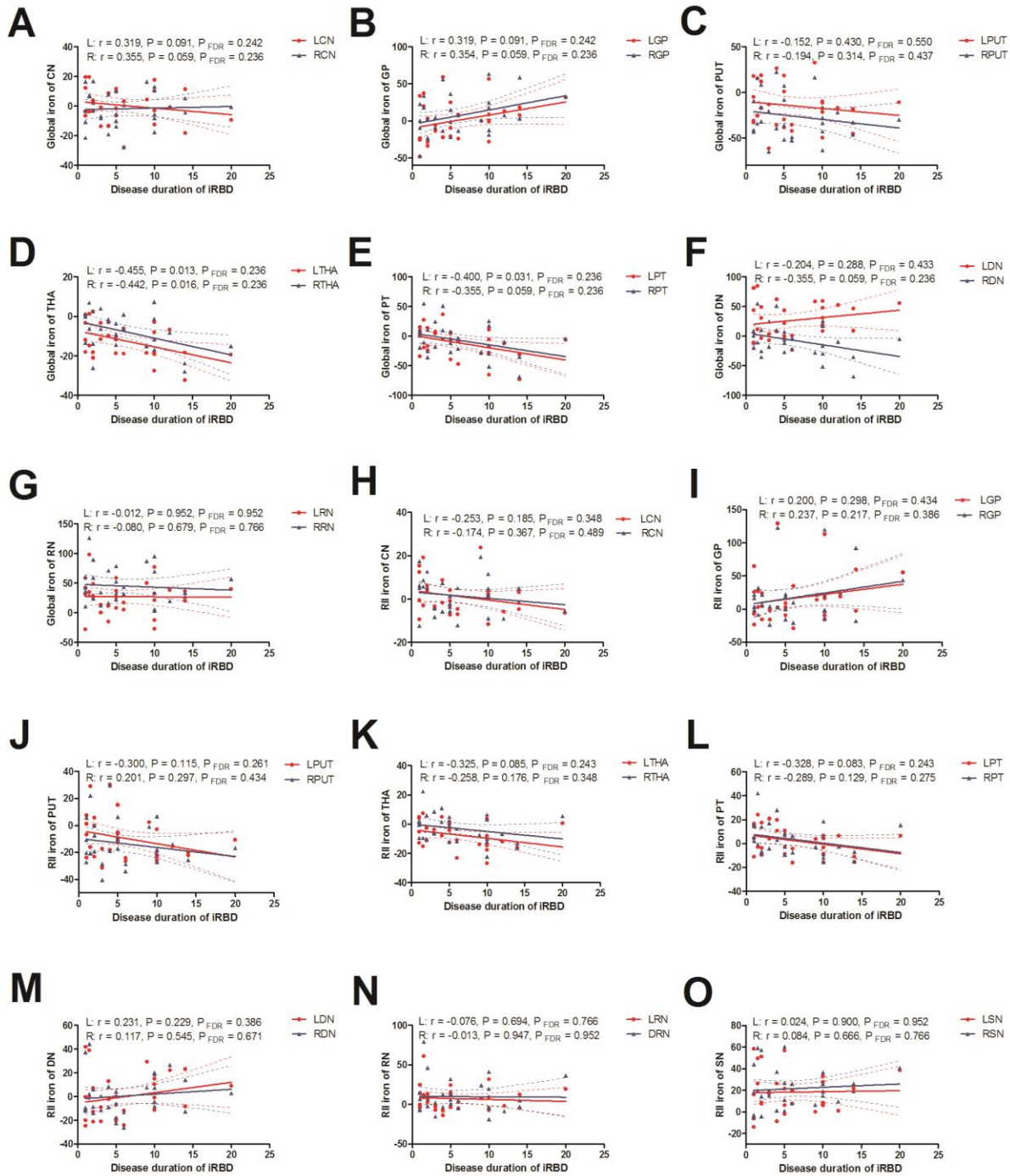
**Supplementary Figure 10.8.** Correlations between age-corrected iron deposition and disease duration of iRBD. Solid lines: linear regression model, dashed lines: 95% confidence intervals, CN: caudate nucleus, DN: dentate nucleus, GP: globus pallidus, PUT: putamen, SN: substantia nigra, RN: red nucleus, THA: thalamus, PT: pulvinar thalamus.
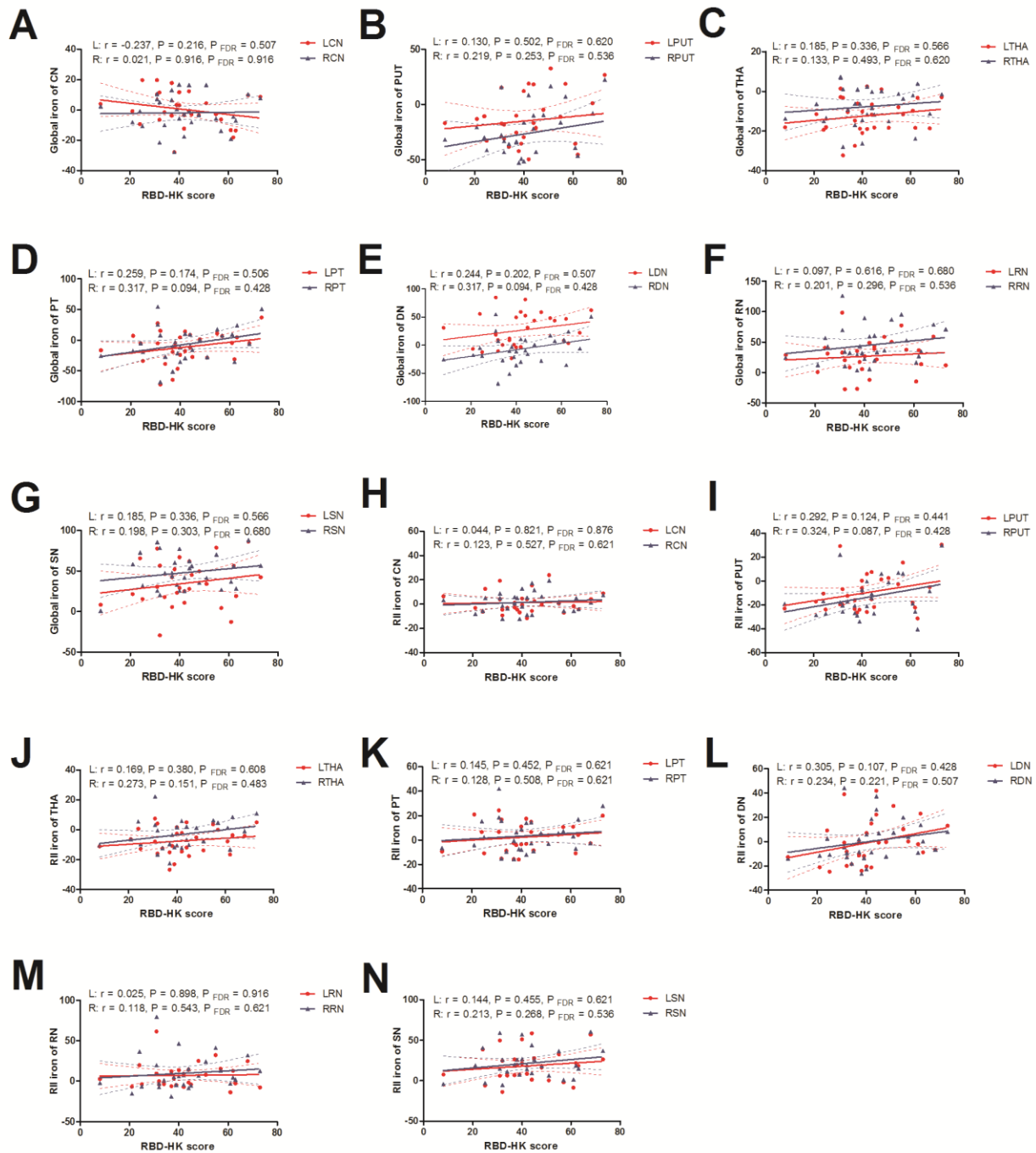
**Supplementary Figure 10.9**. Correlations between age-corrected iron deposition and scores of RBDQ-HK in the iRBD patients. Solid lines: linear regression model, dashed lines: 95% confidence intervals, CN: caudate nucleus, DN: dentate nucleus, PUT: putamen, SN: substantia nigra, RN: red nucleus, THA: thalamus, PT: pulvinar thalamus.

# REFERENCES

1.  Group, G.B.D.N.D.C., *Global, regional, and national burden of neurological disorders during 1990-2015: a systematic analysis for the Global Burden of Disease Study 2015.* Lancet Neurol, 2017. **16**(11): p. 877-897.

2.  Dorsey, E.R. and B.R. Bloem, *The Parkinson Pandemic-A Call to Action.* JAMA Neurol, 2018. **75**(1): p. 9-10.

3.  Kalia, L.V. and A.E. Lang, *Parkinson's disease.* Lancet, 2015. **386**(9996): p. 896-912.

4.  Postuma, R.B., et al., *MDS clinical diagnostic criteria for Parkinson's disease.* Mov Disord, 2015. **30**(12): p. 1591-601.

5.  Saeed, U., et al., *Imaging biomarkers in Parkinson's disease and Parkinsonian syndromes: current and emerging concepts.* Transl Neurodegener, 2017. **6**: p. 8.

6.  Wang, J.Y., et al., *Meta-analysis of brain iron levels of Parkinson's disease patients determined by postmortem and MRI measurements.* Sci Rep, 2016. **6**: p. 36669.

7.  Martin-Bastida, A., et al., *Motor associations of iron accumulation in deep grey matter nuclei in Parkinson's disease: a cross-sectional study of iron-related magnetic resonance imaging susceptibility.* Eur J Neurol, 2017. **24**(2): p. 357-365.

8.  Huddleston, D.E., et al., *In vivo detection of lateral-ventral tier nigral degeneration in Parkinson's disease.* Hum Brain Mapp, 2017. **38**(5): p. 2627-2634.

9.  Langley, J., et al., *Parkinson's disease-related increase of T2\*-weighted hypointensity in substantia nigra pars compacta.* Mov Disord, 2017. **32**(3): p. 441-449.

10. Castellanos, G., et al., *Automated neuromelanin imaging as a diagnostic biomarker for Parkinson's disease.* Mov Disord, 2015. **30**(7): p. 945-52.

11. Ghassaban, K., et al., *Quantifying iron content in magnetic resonance imaging.* Neuroimage, 2019. **187**: p. 77-92.

12. Liu, M., et al., *Assessing global and regional iron content in deep gray matter as a function of age using susceptibility mapping.* J Magn Reson Imaging, 2016. **44**(1): p. 59-71.

13. Hallgren, B. and P. Sourander, *The effect of age on the non-haemin iron in the human brain.* J Neurochem, 1958. **3**(1): p. 41-51.

14. Li, W., et al., *Differential developmental trajectories of magnetic susceptibility in human brain gray and white matter over the lifespan.* Hum Brain Mapp, 2013.

15. Acosta-Cabronero, J., et al., *The whole-brain pattern of magnetic susceptibility perturbations in Parkinson's disease.* Brain, 2017. **140**(Pt 1): p. 118-131.

16. Mahlknecht, P., et al., *Meta-analysis of dorsolateral nigral hyperintensity on magnetic resonance imaging as a marker for Parkinson's disease.* Mov Disord, 2017. **32**(4): p. 619-623.

17. Pavese, N. and Y.F. Tai, *Nigrosome Imaging and Neuromelanin Sensitive MRI in Diagnostic Evaluation of Parkinsonism.* Mov Disord Clin Pract, 2018. **5**(2): p. 131-140.

18. Cheng, Z., et al., *Imaging the Nigrosome 1 in the substantia nigra using susceptibility weighted imaging and quantitative susceptibility mapping: An application to Parkinson's disease.* Neuroimage Clin, 2020. **25**: p. 102103.

19. Blazejewska, A.I., et al., *Visualization of nigrosome 1 and its loss in PD: pathoanatomical correlation and in vivo 7 T MRI.* Neurology, 2013. **81**(6): p. 534-40.

20. Wang, X., et al., *The diagnostic value of SNpc using NM-MRI in Parkinson's disease: meta-analysis.* Neurol Sci, 2019.

21. Takahashi, H., et al., *Quantifying changes in nigrosomes using quantitative susceptibility*

*mapping and neuromelanin imaging for the diagnosis of early-stage Parkinson's disease.* Br J Radiol, 2018. **91**(1086): p. 20180037.

22. Takahashi, H., et al., *Comprehensive MRI quantification of the substantia nigra pars compacta in Parkinson's disease.* Eur J Radiol, 2018. **109**: p. 48-56.

23. Ito, H., et al., *Normative data of dopaminergic neurotransmission functions in substantia nigra measured with MRI and PET: Neuromelanin, dopamine synthesis, dopamine transporters, and dopamine D2 receptors.* Neuroimage, 2017. **158**: p. 12-17.

24. Cassidy, C.M., et al., *Neuromelanin-sensitive MRI as a noninvasive proxy measure of dopamine function in the human brain.* Proc Natl Acad Sci U S A, 2019. **116**(11): p. 5108-5117.

25. Kuya, K., et al., *Correlation between neuromelanin-sensitive MR imaging and (123)I-FP-CIT SPECT in patients with parkinsonism.* Neuroradiology, 2016. **58**(4): p. 351-6.

26. Lang, A.E., *The progression of Parkinson disease: a hypothesis.* Neurology, 2007. **68**(12): p. 948-52.

27. Keren, N.I., et al., *Histologic validation of locus coeruleus MRI contrast in post-mortem tissue.* Neuroimage, 2015. **113**: p. 235-45.

28. Kitao, S., et al., *Correlation between pathology and neuromelanin MR imaging in Parkinson's disease and dementia with Lewy bodies.* Neuroradiology, 2013. **55**(8): p. 947-953.

29. Ogisu, K., et al., *3D neuromelanin-sensitive magnetic resonance imaging with semi-automated volume measurement of the substantia nigra pars compacta for diagnosis of Parkinson's disease.* Neuroradiology, 2013. **55**(6): p. 719-24.

30. Isaias, I.U., et al., *Neuromelanin Imaging and Dopaminergic Loss in Parkinson's Disease.* Front Aging Neurosci, 2016. **8**: p. 196.

31. Prasad, S., et al., *Three-dimensional neuromelanin-sensitive magnetic resonance imaging of the substantia nigra in Parkinson's disease.* Eur J Neurol, 2018. **25**(4): p. 680-686.

32. Reimao, S., et al., *Substantia nigra neuromelanin-MR imaging differentiates essential tremor from Parkinson's disease.* Mov Disord, 2015. **30**(7): p. 953-9.

33. Wang, J., et al., *Neuromelanin-sensitive MRI of the substantia nigra: An imaging biomarker to differentiate essential tremor from tremor-dominant Parkinson's disease.* Parkinsonism Relat Disord, 2019. **58**: p. 3-8.

34. Taniguchi, D., et al., *Neuromelanin imaging and midbrain volumetry in progressive supranuclear palsy and Parkinson's disease.* Mov Disord, 2018. **33**(9): p. 1488-1492.

35. Matsuura, K., et al., *Neuromelanin magnetic resonance imaging in Parkinson's disease and multiple system atrophy.* Eur Neurol, 2013. **70**(1-2): p. 70-7.

36. Wang, J., et al., *Neuromelanin-sensitive magnetic resonance imaging features of the substantia nigra and locus coeruleus in de novo Parkinson's disease and its phenotypes.* Eur J Neurol, 2018. **25**(7): p. 949-e73.

37. Matsuura, K., et al., *A longitudinal study of neuromelanin-sensitive magnetic resonance imaging in Parkinson's disease.* Neurosci Lett, 2016. **633**: p. 112-117.

38. Kashihara, K., T. Shinya, and F. Higaki, *Neuromelanin magnetic resonance imaging of nigral volume loss in patients with Parkinson's disease.* J Clin Neurosci, 2011. **18**(8): p. 1093-6.

39. Kashihara, K., T. Shinya, and F. Higaki, *Reduction of neuromelanin-positive nigral volume in patients with MSA, PSP and CBD.* Intern Med, 2011. **50**(16): p. 1683-7.

40. Kuya, K., et al., *Evaluation of Parkinson's disease by neuromelanin-sensitive magnetic resonance imaging and (123)I-FP-CIT SPECT.* Acta Radiol, 2018. **59**(5): p. 593-598.

41.	Pyatigorskaya, N., et al., *Comparative Study of MRI Biomarkers in the Substantia Nigra to Discriminate Idiopathic Parkinson Disease.* AJNR Am J Neuroradiol, 2018. **39**(8): p. 1460-1467.

42.	Schwarz, S.T., et al., *In Vivo Assessment of Brainstem Depigmentation in Parkinson Disease: Potential as a Severity Marker for Multicenter Studies.* Radiology, 2017. **283**(3): p. 789-798.

43.	Sulzer, D., et al., *Neuromelanin detection by magnetic resonance imaging (MRI) and its promise as a biomarker for Parkinson's disease.* NPJ Parkinsons Dis, 2018. **4**: p. 11.

44.	Reimao, S., et al., *Magnetic resonance correlation of iron content with neuromelanin in the substantia nigra of early-stage Parkinson's disease.* Eur J Neurol, 2016. **23**(2): p. 368-74.

45.	Lee, H., et al., *Specific visualization of neuromelanin-iron complex and ferric iron in the human post-mortem substantia nigra using MR relaxometry at 7T.* Neuroimage, 2018. **172**: p. 874-885.

46.	Hogl, B., A. Stefani, and A. Videnovic, *Idiopathic REM sleep behaviour disorder and neurodegeneration - an update.* Nat Rev Neurol, 2018. **14**(1): p. 40-55.

47.	Iranzo, A., et al., *Neurodegenerative disorder risk in idiopathic REM sleep behavior disorder: study in 174 patients.* PLoS One, 2014. **9**(2): p. e89741.

48.	Iranzo, A., et al., *Neurodegenerative disease status and post-mortem pathology in idiopathic rapid-eye-movement sleep behaviour disorder: an observational cohort study.* Lancet Neurol, 2013. **12**(5): p. 443-53.

49.	Gagnon, J.F., J.A. Bertrand, and D. Genier Marchand, *Cognition in rapid eye movement sleep behavior disorder.* Front Neurol, 2012. **3**: p. 82.

50.	Youn, S., et al., *Progression of cognitive impairments in idiopathic REM sleep behaviour disorder.* J Neurol Neurosurg Psychiatry, 2016. **87**(8): p. 890-6.

51.  Postuma, R.B., et al., *How does parkinsonism start? Prodromal parkinsonism motor changes in idiopathic REM sleep behaviour disorder.* Brain, 2012. **135**(Pt 6): p. 1860-70.

52.  Iranzo, A., et al., *Characterization of patients with longstanding idiopathic REM sleep behavior disorder.* Neurology, 2017. **89**(3): p. 242-248.

53.  Haacke, E.M. and J.R. Reichenbach, *Susceptibility weighted imaging in MRI basic concepts and clinical applications*. 2011, Wiley-Blackwell,: Hoboken, N.J. p. xvi, 743 p.

54.  Haacke, E.M., *Magnetic resonance imaging : physical principles and sequence design*. 1999, New York: Wiley. xxvii, 914 p.

55.  Wang, Y., et al., *Artery and vein separation using susceptibility-dependent phase in contrast-enhanced MRA*. J Magn Reson Imaging, 2000. **12**(5): p. 661-70.

56.  Liu, S., *Technical Improvements in Quantitative Susceptibility Mapping*, in *School of Biomedical Engineering*. 2014, McMaster University.

57.  Haacke, E.M., et al., *Quantitative susceptibility mapping: current status and future directions.* Magn Reson Imaging, 2015. **33**(1): p. 1-25.

58.  Schweser, F., et al., *Quantitative imaging of intrinsic magnetic tissue properties using MRI signal phase: an approach to in vivo brain iron metabolism?* Neuroimage, 2011. **54**(4): p. 2789-807.

59.  Haacke, E.M., et al., *Susceptibility mapping as a means to visualize veins and quantify oxygen saturation.* J Magn Reson Imaging, 2010. **32**(3): p. 663-76.

60.  Lees, A.J., et al., *The black stuff and Konstantin Nikolaevich Tretiakoff.* Mov Disord, 2008. **23**(6): p. 777-83.

61.  Ehringer, H. and O. Hornykiewicz, *Distribution of noradrenaline and dopamine (3-*

*hydroxytyramine) in the human brain and their behavior in diseases of the extrapyramidal system.* Parkinsonism Relat Disord, 1998. **4**(2): p. 53-7.

62. Sulzer, D. and L. Zecca, *Intraneuronal dopamine-quinone synthesis: a review.* Neurotox Res, 2000. **1**(3): p. 181-95.

63. Mosharov, E.V., et al., *Interplay between cytosolic dopamine, calcium, and alpha-synuclein causes selective death of substantia nigra neurons.* Neuron, 2009. **62**(2): p. 218-29.

64. Jokar, M. and K. Torabi, *A Statistical Mechanical Model for Coiled-Coil Protein Structure Prediction.* Biophysical Journal, 2017. **112** (3): p. 193a.

65. Zecca, L., et al., *Interaction of neuromelanin and iron in substantia nigra and other areas of human brain.* Neuroscience, 1996. **73**(2): p. 407-15.

66. Zucca, F.A., et al., *Interactions of iron, dopamine and neuromelanin pathways in brain aging and Parkinson's disease.* Prog Neurobiol, 2017. **155**: p. 96-119.

67. Zecca, L., et al., *The role of iron and copper molecules in the neuronal vulnerability of locus coeruleus and substantia nigra during aging.* Proc Natl Acad Sci U S A, 2004. **101**(26): p. 9843-8.

68. Zecca, L., et al., *Neuromelanin can protect against iron-mediated oxidative damage in system modeling iron overload of brain aging and Parkinson's disease.* J Neurochem, 2008. **106**(4): p. 1866-75.

69. Jokar, M. and K. Torabi, *Modeling Coiled-Coil Protein Structures.* European Biophysics Journal with Biophysics Letters, 2017. **46**: p. S346-S346.

70. Zhang, W., et al., *Neuromelanin activates microglia and induces degeneration of dopaminergic neurons: implications for progression of Parkinson's disease.* Neurotox Res, 2011. **19**(1): p. 63-

72.

71.     Sasaki, M., et al., *Neuromelanin magnetic resonance imaging of locus ceruleus and substantia nigra in Parkinson's disease.* Neuroreport, 2006. **17**(11): p. 1215-8.

72.     Ohtsuka, C., et al., *Changes in substantia nigra and locus coeruleus in patients with early-stage Parkinson's disease using neuromelanin-sensitive MR imaging.* Neurosci Lett, 2013. **541**: p. 93-8.

73.     Langley, J., et al., *A multicontrast approach for comprehensive imaging of substantia nigra.* Neuroimage, 2015. **112**: p. 7-13.

74.     Knutsson, L., et al., *CEST, ASL, and magnetization transfer contrast: How similar pulse sequences detect different phenomena.* Magn Reson Med, 2018. **80**(4): p. 1320-1340.

75.     Henkelman, R.M., G.J. Stanisz, and S.J. Graham, *Magnetization transfer in MRI: a review.* NMR Biomed, 2001. **14**(2): p. 57-64.

76.     Ramani, A., et al., *Precise estimate of fundamental in-vivo MT parameters in human brain in clinically feasible times.* Magn Reson Imaging, 2002. **20**(10): p. 721-31.

77.     Engelen, M., et al., *Neuromelanins of human brain have soluble and insoluble components with dolichols attached to the melanic structure.* PLoS One, 2012. **7**(11): p. e48490.

78.     Trujillo, P., et al., *Contrast mechanisms associated with neuromelanin-MRI.* Magn Reson Med, 2017. **78**(5): p. 1790-1800.

79.     Berg, D. and M.B. Youdim, *Role of iron in neurodegenerative disorders.* Top Magn Reson Imaging, 2006. **17**(1): p. 5-17.

80.     Stankiewicz, J., et al., *Iron in chronic brain disorders: imaging and neurotherapeutic implications.* Neurotherapeutics, 2007. **4**(3): p. 371-86.

81. Loef, M. and H. Walach, *Copper and iron in Alzheimer's disease: a systematic review and its dietary implications.* Br J Nutr, 2012. **107**(1): p. 7-19.

82. Ayton, S., et al., *Ceruloplasmin dysfunction and therapeutic potential for Parkinson disease.* Ann Neurol, 2013. **73**(4): p. 554-9.

83. Habib, C.A., et al., *Assessing abnormal iron content in the deep gray matter of patients with multiple sclerosis versus healthy controls.* AJNR Am J Neuroradiol, 2012. **33**(2): p. 252-8.

84. Cortese, S., et al., *Sleep disturbances and serum ferritin levels in children with attention-deficit/hyperactivity disorder.* Eur Child Adolesc Psychiatry, 2009. **18**(7): p. 393-9.

85. Jeong, S.Y., et al., *Iron insufficiency compromises motor neurons and their mitochondrial function in Irp2-null mice.* PLoS One, 2011. **6**(10): p. e25404.

86. Ropele, S., et al., *MRI assessment of iron deposition in multiple sclerosis.* J Magn Reson Imaging, 2011. **34**(1): p. 13-21.

87. Haacke, E.M., et al., *Imaging iron stores in the brain using magnetic resonance imaging.* Magn Reson Imaging, 2005. **23**(1): p. 1-25.

88. Schenck, J.F. and E.A. Zimmerman, *High-field magnetic resonance imaging of brain iron: birth of a biomarker?* NMR Biomed, 2004. **17**(7): p. 433-45.

89. Kleinig, T.J., *Associations and implications of cerebral microbleeds.* J Clin Neurosci, 2013. **20**(7): p. 919-27.

90. Benson, R.R., et al., *Detection of hemorrhagic and axonal pathology in mild traumatic brain injury using advanced MRI: implications for neurorehabilitation.* NeuroRehabilitation, 2012. **31**(3): p. 261-79.

91. Jokar, M. and K. Torabi, *Thermodynamics of a Coiled-Coil Protein Structure.* Biophysical

Journal, 2018. **114**(3): p. 580a.

92.    Connor, J.R., et al., *Regional distribution of iron and iron-regulatory proteins in the brain in aging and Alzheimer's disease.* J Neurosci Res, 1992. **31**(2): p. 327-35.

93.    Xu, X., Q. Wang, and M. Zhang, *Age, gender, and hemispheric differences in iron deposition in the human brain: an in vivo MRI study.* Neuroimage, 2008. **40**(1): p. 35-42.

94.    Li, W., et al., *Differential developmental trajectories of magnetic susceptibility in human brain gray and white matter over the lifespan.* Hum Brain Mapp, 2014. **35**(6): p. 2698-713.

95.    Zivadinov, R., et al., *Chronic cerebrospinal venous insufficiency and iron deposition on susceptibility-weighted imaging in patients with multiple sclerosis: a pilot case-control study.* Int Angiol, 2010. **29**(2): p. 158-75.

96.    Pfefferbaum, A., et al., *MRI estimates of brain iron concentration in normal aging: comparison of field-dependent (FDRI) and phase (SWI) methods.* Neuroimage, 2009. **47**(2): p. 493-500.

97.    Acosta-Cabronero, J., et al., *In Vivo MRI Mapping of Brain Iron Deposition across the Adult Lifespan.* J Neurosci, 2016. **36**(2): p. 364-74.

98.    Wang, Y. and T. Liu, *Quantitative susceptibility mapping (QSM): Decoding MRI data for a tissue magnetic biomarker.* Magn Reson Med, 2015. **73**(1): p. 82-101.

99.    Ma, J. and F.W. Wehrli, *Method for image-based measurement of the reversible and irreversible contribution to the transverse-relaxation rate.* J Magn Reson B, 1996. **111**(1): p. 61-9.

100.   Yablonskiy, D.A. and E.M. Haacke, *An MRI method for measuring T2 in the presence of static and RF magnetic field inhomogeneities.* Magn Reson Med, 1997. **37**(6): p. 872-6.

101.   Yablonskiy, D.A. and E.M. Haacke, *Theory of NMR signal behavior in magnetically inhomogeneous tissues: the static dephasing regime.* Magn Reson Med, 1994. **32**(6): p. 749-63.

102. Liu, S., et al., *Susceptibility-weighted imaging: current status and future directions.* NMR Biomed, 2017. **30**(4).

103. Brown, R.W., et al., *Magnetic resonance imaging : physical principles and sequence design.* Second edition. ed. 2014, Hoboken, New Jersey: John Wiley & Sons, Inc. xxxii, 944 pages.

104. Haacke, E.M., et al., *Establishing a baseline phase behavior in magnetic resonance imaging to determine normal vs. abnormal iron content in the brain.* J Magn Reson Imaging, 2007. **26**(2): p. 256-64.

105. Liu, T., et al., *A novel background field removal method for MRI using projection onto dipole fields (PDF).* NMR Biomed, 2011. **24**(9): p. 1129-36.

106. Sun, H. and A.H. Wilman, *Background field removal using spherical mean value filtering and Tikhonov regularization.* Magn Reson Med, 2014. **71**(3): p. 1151-7.

107. Li, W., et al., *Integrated Laplacian-based phase unwrapping and background phase removal for quantitative susceptibility mapping.* NMR Biomed, 2014. **27**(2): p. 219-27.

108. Haacke, E.M., et al., *Susceptibility weighted imaging (SWI).* Magn Reson Med, 2004. **52**(3): p. 612-8.

109. Zhou, D., et al., *Background field removal by solving the Laplacian boundary value problem.* NMR Biomed, 2014. **27**(3): p. 312-9.

110. Liu, C., et al., *Susceptibility-weighted imaging and quantitative susceptibility mapping in the brain.* J Magn Reson Imaging, 2015. **42**(1): p. 23-41.

111. Hopp, K., et al., *Brain iron detected by SWI high pass filtered phase calibrated with synchrotron X-ray fluorescence.* J Magn Reson Imaging, 2010. **31**(6): p. 1346-54.

112. Haacke, E.M., et al., *Correlation of putative iron content as represented by changes in R2\* and*

*phase with age in deep gray matter of healthy adults.* J Magn Reson Imaging, 2010. **32**(3): p. 561-76.

113. Wang, Y., et al., *Different iron-deposition patterns of multiple system atrophy with predominant parkinsonism and idiopathic Parkinson diseases demonstrated by phase-corrected susceptibility-weighted imaging.* AJNR Am J Neuroradiol, 2012. **33**(2): p. 266-73.

114. Shmueli, K., et al., *Magnetic susceptibility mapping of brain tissue in vivo using MRI phase data.* Magn Reson Med, 2009. **62**(6): p. 1510-22.

115. Liu, J., et al., *Morphology enabled dipole inversion for quantitative susceptibility mapping using structural consistency between the magnitude image and the susceptibility map.* Neuroimage, 2012. **59**(3): p. 2560-8.

116. Schweser, F., et al., *Quantitative susceptibility mapping for investigating subtle susceptibility variations in the human brain.* Neuroimage, 2012. **62**(3): p. 2083-100.

117. Tang, J., et al., *Improving susceptibility mapping using a threshold-based K-space/image domain iterative reconstruction approach.* Magn Reson Med, 2013. **69**(5): p. 1396-407.

118. Deistung, A., F. Schweser, and J.R. Reichenbach, *Overview of quantitative susceptibility mapping.* NMR Biomed, 2017. **30**(4).

119. Bao, L., et al., *Quantitative Susceptibility Mapping Using Structural Feature Based Collaborative Reconstruction (SFCR) in the Human Brain.* IEEE Trans Med Imaging, 2016. **35**(9): p. 2040-50.

120. Langkammer, C., et al., *Quantitative susceptibility mapping: Report from the 2016 reconstruction challenge.* Magn Reson Med, 2017.

121. Liu, S., et al., *Improved MR venography using quantitative susceptibility-weighted imaging.* J

Magn Reson Imaging, 2014. **40**(3): p. 698-708.

122. Wharton, S. and R. Bowtell, *Effects of white matter microstructure on phase and susceptibility maps.* Magn Reson Med, 2015. **73**(3): p. 1258-69.

123. Yablonskiy, D.A. and A.L. Sukstanskii, *Effects of biological tissue structural anisotropy and anisotropy of magnetic susceptibility on the gradient echo MRI signal phase: theoretical background.* NMR Biomed, 2017. **30**(4).

124. Langkammer, C., et al., *Quantitative MR imaging of brain iron: a postmortem validation study.* Radiology, 2010. **257**(2): p. 455-62.

125. Zheng, W., et al., *Measuring iron in the brain using quantitative susceptibility mapping and X-ray fluorescence imaging.* Neuroimage, 2013. **78**: p. 68-74.

126. Barbosa, J.H., et al., *Quantifying brain iron deposition in patients with Parkinson's disease using quantitative susceptibility mapping, R2 and R2.* Magn Reson Imaging, 2015. **33**(5): p. 559-65.

127. Li, W., et al., *Magnetic susceptibility anisotropy of human brain in vivo and its molecular underpinnings.* Neuroimage, 2012. **59**(3): p. 2088-97.

128. Wharton, S. and R. Bowtell, *Fiber orientation-dependent white matter contrast in gradient echo MRI.* Proc Natl Acad Sci U S A, 2012. **109**(45): p. 18559-64.

129. Luo, J., X. He, and D.A. Yablonskiy, *Magnetic susceptibility induced white matter MR signal frequency shifts--experimental comparison between Lorentzian sphere and generalized Lorentzian approaches.* Magn Reson Med, 2014. **71**(3): p. 1251-63.

130. Sukstanskii, A.L. and D.A. Yablonskiy, *On the role of neuronal magnetic susceptibility and structure symmetry on gradient echo MR signal formation.* Magn Reson Med, 2014. **71**(1): p.

345-53.

131. Langkammer, C., et al., *Quantitative susceptibility mapping in multiple sclerosis.* Radiology, 2013. **267**(2): p. 551-9.

132. Walsh, A.J., et al., *Multiple sclerosis: validation of MR imaging for quantification and detection of iron.* Radiology, 2013. **267**(2): p. 531-42.

133. Gharabaghi, S., et al., *Multi-Echo Quantitative Susceptibility Mapping for Strategically Acquired Gradient Echo (STAGE) Imaging.* Front Neurosci, 2020. **14**: p. 581474.

134. Deistung, A., et al., *Toward in vivo histology: a comparison of quantitative susceptibility mapping (QSM) with magnitude-, phase-, and R2\*-imaging at ultra-high magnetic field strength.* Neuroimage, 2013. **65**: p. 299-314.

135. Wisnieff, C., et al., *Quantitative susceptibility mapping (QSM) of white matter multiple sclerosis lesions: Interpreting positive susceptibility and the presence of iron.* Magn Reson Med, 2015. **74**(2): p. 564-70.

136. Langkammer, C., et al., *Susceptibility induced gray-white matter MRI contrast in the human brain.* Neuroimage, 2012. **59**(2): p. 1413-9.

137. Lee, J., et al., *The contribution of myelin to magnetic susceptibility-weighted contrasts in high-field MRI of the brain.* Neuroimage, 2012. **59**(4): p. 3967-75.

138. Zhang, Y., et al., *Quantitative Susceptibility Mapping and R2\* Measured Changes during White Matter Lesion Development in Multiple Sclerosis: Myelin Breakdown, Myelin Debris Degradation and Removal, and Iron Accumulation.* AJNR Am J Neuroradiol, 2016. **37**(9): p. 1629-35.

139. Li, X., et al., *Magnetic susceptibility contrast variations in multiple sclerosis lesions.* J Magn

Reson Imaging, 2016. **43**(2): p. 463-73.

140. Harrison, D.M., et al., *Lesion Heterogeneity on High-Field Susceptibility MRI Is Associated with Multiple Sclerosis Severity.* AJNR Am J Neuroradiol, 2016. **37**(8): p. 1447-53.

141. Lee, J., et al., *T2\*-based fiber orientation mapping.* Neuroimage, 2011. **57**(1): p. 225-34.

142. Rudko, D.A., et al., *Origins of R2\* orientation dependence in gray and white matter.* Proc Natl Acad Sci U S A, 2014. **111**(1): p. E159-67.

143. Wharton, S. and R. Bowtell, *Gradient echo based fiber orientation mapping using R2\* and frequency difference measurements.* Neuroimage, 2013. **83**: p. 1011-23.

144. He, X. and D.A. Yablonskiy, *Biophysical mechanisms of phase contrast in gradient echo MRI.* Proc Natl Acad Sci U S A, 2009. **106**(32): p. 13558-63.

145. Yao, B., et al., *Susceptibility contrast in high field MRI of human brain as a function of tissue iron content.* Neuroimage, 2009. **44**(4): p. 1259-66.

146. Ning, N., et al., *Assessment of iron deposition and white matter maturation in infant brains by using enhanced T2 star weighted angiography (ESWAN): R2\* versus phase values.* PLoS One, 2014. **9**(2): p. e89888.

147. Uddin, M.N., R.M. Lebel, and A.H. Wilman, *Value of transverse relaxometry difference methods for iron in human brain.* Magn Reson Imaging, 2016. **34**(1): p. 51-9.

148. Martin, W.R., M. Wieler, and M. Gee, *Midbrain iron content in early Parkinson disease: a potential biomarker of disease status.* Neurology, 2008. **70**(16 Pt 2): p. 1411-7.

149. Peran, P., et al., *Volume and iron content in basal ganglia and thalamus.* Hum Brain Mapp, 2009. **30**(8): p. 2667-75.

150. Yan, S.Q., et al., *Evaluation of brain iron content based on magnetic resonance imaging (MRI):*

*comparison among phase value, R2\* and magnitude signal intensity.* PLoS One, 2012. **7**(2): p. e31748.

151. Sedlacik, J., et al., *Reversible, irreversible and effective transverse relaxation rates in normal aging brain at 3T.* Neuroimage, 2014. **84**: p. 1032-41.

152. Bilgic, B., et al., *MRI estimates of brain iron concentration in normal aging using quantitative susceptibility mapping.* Neuroimage, 2012. **59**(3): p. 2625-35.

153. Persson, N., et al., *Age and sex related differences in subcortical brain iron concentrations among healthy adults.* Neuroimage, 2015. **122**: p. 385-98.

154. Lim, I.A., et al., *Human brain atlas for automated region of interest selection in quantitative susceptibility mapping: application to determine iron content in deep gray matter structures.* Neuroimage, 2013. **82**: p. 449-69.

155. Langkammer, C., et al., *Quantitative susceptibility mapping (QSM) as a means to measure brain iron? A post mortem validation study.* Neuroimage, 2012. **62**(3): p. 1593-9.

156. Chai, C., et al., *Quantitative measurement of brain iron deposition in patients with haemodialysis using susceptibility mapping.* Metab Brain Dis, 2015. **30**(2): p. 563-71.

157. He, N., et al., *Region-specific disturbed iron distribution in early idiopathic Parkinson's disease measured by quantitative susceptibility mapping.* Hum Brain Mapp, 2015. **36**(11): p. 4407-20.

158. Xia, S., et al., *Quantitative measurements of brain iron deposition in cirrhotic patients using susceptibility mapping.* Acta Radiol, 2015. **56**(3): p. 339-46.

159. Wharton, S. and R. Bowtell, *Whole-brain susceptibility mapping at high field: a comparison of multiple- and single-orientation methods.* Neuroimage, 2010. **53**(2): p. 515-25.

160. Bartzokis, G., et al., *Field dependent transverse relaxation rate increase may be a specific*

*measure of tissue iron stores.* Magn Reson Med, 1993. **29**(4): p. 459-64.

161. Jensen, J.H., et al., *Magnetic Field Correlation as a Measure of Iron-Generated Magnetic Field Inhomogeneities in the Brain.* Magn Reson Med Sci, 2009. **61**(2): p. 481–485.

162. Smith, S.A., J.W. Bulte, and P.C. van Zijl, *Direct saturation MRI: theory and application to imaging brain iron.* Magn Reson Med, 2009. **62**(2): p. 384-93.

163. Sado, D.M., et al., *Noncontrast myocardial T1 mapping using cardiovascular magnetic resonance for iron overload.* J Magn Reson Imaging, 2015. **41**(6): p. 1505-11.

164. Feng, Y., et al., *In vivo comparison of myocardial T1 with T2 and T2\* in thalassaemia major.* J Magn Reson Imaging, 2013. **38**(3): p. 588-93.

165. Chen, B.T., et al., *Subcortical brain iron deposition and cognitive performance in older women with breast cancer receiving adjuvant chemotherapy: A pilot MRI study.* Magn Reson Imaging, 2018. **54**: p. 218-224.

166. Ge, Y., et al., *Quantitative assessment of iron accumulation in the deep gray matter of multiple sclerosis by magnetic field correlation imaging.* AJNR Am J Neuroradiol, 2007. **28**(9): p. 1639-44.

167. Zou, J., et al., *Position Emission Tomography/Single-Photon Emission Tomography Neuroimaging for Detection of Premotor Parkinson's Disease.* CNS Neurosci Ther, 2016. **22**(3): p. 167-77.

168. Murakami, Y., et al., *Usefulness of quantitative susceptibility mapping for the diagnosis of Parkinson disease.* AJNR Am J Neuroradiol, 2015. **36**(6): p. 1102-8.

169. Du, G., et al., *Quantitative susceptibility mapping of the midbrain in Parkinson's disease.* Mov Disord, 2016. **31**(3): p. 317-24.

170. Langkammer, C., et al., *Quantitative Susceptibility Mapping in Parkinson's Disease.* PLoS One, 2016. **11**(9): p. e0162460.

171. Dashtipour, K., et al., *Iron Accumulation Is Not Homogenous among Patients with Parkinson's Disease.* Parkinsons Dis, 2015. **2015**: p. 324843.

172. Ayton, S. and P. Lei, *Nigral iron elevation is an invariable feature of Parkinson's disease and is a sufficient cause of neurodegeneration.* Biomed Res Int, 2014. **2014**: p. 581256.

173. Gorell, J.M., et al., *Increased iron-related MRI contrast in the substantia nigra in Parkinson's disease.* Neurology, 1995. **45**(6): p. 1138-43.

174. Rossi, M., et al., *Clinical MRI for iron detection in Parkinson's disease.* Clin Imaging, 2013. **37**(4): p. 631-6.

175. Hopes, L., et al., *Magnetic Resonance Imaging Features of the Nigrostriatal System: Biomarkers of Parkinson's Disease Stages?* PLoS One, 2016. **11**(4): p. e0147947.

176. Esterhammer, R., et al., *Potential of Diffusion Tensor Imaging and Relaxometry for the Detection of Specific Pathological Alterations in Parkinson's Disease (PD).* PLoS One, 2015. **10**(12): p. e0145493.

177. Ulla, M., et al., *Is R2\* a new MRI biomarker for the progression of Parkinson's disease? A longitudinal follow-up.* PLoS One, 2013. **8**(3): p. e57904.

178. Wieler, M., M. Gee, and W.R. Martin, *Longitudinal midbrain changes in early Parkinson's disease: iron content estimated from R2\*/MRI.* Parkinsonism Relat Disord, 2015. **21**(3): p. 179-83.

179. Guan, X., et al., *Regionally progressive accumulation of iron in Parkinson's disease as measured by quantitative susceptibility mapping.* NMR Biomed, 2017. **30**(4).

180. Lotfipour, A.K., et al., *High resolution magnetic susceptibility mapping of the substantia nigra in Parkinson's disease.* J Magn Reson Imaging, 2012. **35**(1): p. 48-55.

181. Azuma, M., et al., *Lateral Asymmetry and Spatial Difference of Iron Deposition in the Substantia Nigra of Patients with Parkinson Disease Measured with Quantitative Susceptibility Mapping.* AJNR Am J Neuroradiol, 2016. **37**(5): p. 782-8.

182. Guan, X., et al., *Influence of regional iron on the motor impairments of Parkinson's disease: A quantitative susceptibility mapping study.* J Magn Reson Imaging, 2017. **45**(5): p. 1335-1342.

183. He, N., et al., *Dentate nucleus iron deposition is a potential biomarker for tremor-dominant Parkinson's disease.* NMR Biomed, 2017. **30**(4).

184. Peran, P., et al., *Magnetic resonance imaging markers of Parkinson's disease nigrostriatal signature.* Brain, 2010. **133**(11): p. 3423-33.

185. Du, G., et al., *Combined R2\* and diffusion tensor imaging changes in the substantia nigra in Parkinson's disease.* Mov Disord, 2011. **26**(9): p. 1627-32.

186. Ji, S., et al., *Quantitative assessment of iron deposition in Parkinson's disease using enhanced T2 star-weighted angiography.* Neurol India, 2016. **64**(3): p. 428-35.

187. Acosta-Cabronero, J., et al., *The whole-brain pattern of magnetic susceptibility perturbations in Parkinson's disease.* Brain, 2017. **140**(1): p. 118-131.

188. Jokar, M. and K. Torabi, *Tensile Mechanics of Coiled Coil Protein Structures.* Biophysical Journal, 2016. **110**(3): p. 536a.

189. Zecca, L., et al., *The absolute concentration of nigral neuromelanin, assayed by a new sensitive method, increases throughout the life and is dramatically decreased in Parkinson's disease.* FEBS Lett, 2002. **510**(3): p. 216-20.

190. Kawaguchi, H., et al., *Principal Component Analysis of Multimodal Neuromelanin MRI and Dopamine Transporter PET Data Provides a Specific Metric for the Nigral Dopaminergic Neuronal Density.* PLoS One, 2016. **11**(3): p. e0151191.

191. Chen, X., et al., *Simultaneous imaging of locus coeruleus and substantia nigra with a quantitative neuromelanin MRI approach.* Magn Reson Imaging, 2014. **32**(10): p. 1301-6.

192. Hatano, T., et al., *Neuromelanin MRI is useful for monitoring motor complications in Parkinson's and PARK2 disease.* J Neural Transm (Vienna), 2017. **124**(4): p. 407-415.

193. De Marzi, R., et al., *Loss of dorsolateral nigral hyperintensity on 3.0 tesla susceptibility-weighted imaging in idiopathic rapid eye movement sleep behavior disorder.* Ann Neurol, 2016. **79**(6): p. 1026-30.

194. Shulman, J.M. and P.L. De Jager, *Evidence for a common pathway linking neurodegenerative diseases.* Nat Genet, 2009. **41**(12): p. 1261-2.

195. Smith, S.M., *Fast robust automated brain extraction.* Hum Brain Mapp, 2002. **17**(3): p. 143-55.

196. Abdul-Rahman, H.S., et al., *Fast and robust three-dimensional best path phase unwrapping algorithm.* Appl Opt, 2007. **46**(26): p. 6623-35.

197. Schwarz, S.T., et al., *Parkinson's disease related signal change in the nigrosomes 1-5 and the substantia nigra using T2\* weighted 7T MRI.* Neuroimage Clin, 2018. **19**: p. 683-689.

198. Sethi, S.K., et al., *Iron quantification in Parkinson's disease using an age-based threshold on susceptibility maps: The advantage of local versus entire structure iron content measurements.* Magn Reson Imaging, 2019. **55**: p. 145-152.

199. Feng, X., A. Deistung, and J.R. Reichenbach, *Quantitative susceptibility mapping (QSM) and R2(\*) in the human brain at 3T: Evaluation of intra-scanner repeatability.* Z Med Phys, 2018.

**28**(1): p. 36-48.

200. Yan, F., et al., *Iron deposition quantification: Applications in the brain and liver.* J Magn Reson Imaging, 2018. **48**(2): p. 301-317.

201. Zecca, L., et al., *Iron, brain ageing and neurodegenerative disorders.* Nat Rev Neurosci, 2004. **5**(11): p. 863-73.

202. Pesch, B., et al., *Impairment of Motor Function Correlates with Neurometabolite and Brain Iron Alterations in Parkinson's Disease.* Cells, 2019. **8**(2).

203. Li, X., et al., *Multi-atlas tool for automated segmentation of brain gray matter nuclei and quantification of their magnetic susceptibility.* Neuroimage, 2019. **191**: p. 337-349.

204. Berg, D., et al., *Movement disorder society criteria for clinically established early Parkinson's disease.* Mov Disord, 2018. **33**(10): p. 1643-1646.

205. Lehericy, S., et al., *7 Tesla magnetic resonance imaging: a closer look at substantia nigra anatomy in Parkinson's disease.* Mov Disord, 2014. **29**(13): p. 1574-81.

206. Yetnikoff, L., et al., *An update on the connections of the ventral mesencephalic dopaminergic complex.* Neuroscience, 2014. **282**: p. 23-48.

207. Trutti, A.C., et al., *Functional neuroanatomical review of the ventral tegmental area.* Neuroimage, 2019. **191**: p. 258-268.

208. He, N., et al., *Increased iron-deposition in lateral-ventral substantia nigra pars compacta: A promising neuroimaging marker for Parkinson's disease.* Neuroimage Clin, 2020. **28**: p. 102391.

209. Goetz, C.G., et al., *Movement Disorder Society-sponsored revision of the Unified Parkinson's Disease Rating Scale (MDS-UPDRS): scale presentation and clinimetric testing results.* Mov Disord, 2008. **23**(15): p. 2129-70.

210. Barrett, M.J., et al., *Handedness and motor symptom asymmetry in Parkinson's disease.* J Neurol Neurosurg Psychiatry, 2011. **82**(10): p. 1122-4.

211. Stoeck, C.T., et al., *Optimization of on-resonant magnetization transfer contrast in coronary vein MRI.* Magn Reson Med, 2010. **64**(6): p. 1849-54.

212. Liu, Y., et al., *Optimizing neuromelanin contrast in the substantia nigra and locus coeruleus using a magnetization transfer contrast prepared 3D gradient recalled echo sequence.* Neuroimage, 2020. **218**: p. 116935.

213. Chen, Y., et al., *STrategically Acquired Gradient Echo (STAGE) imaging, part I: Creating enhanced T1 contrast and standardized susceptibility weighted imaging and quantitative susceptibility mapping.* Magn Reson Imaging, 2018. **46**: p. 130-139.

214. Wang, Y., et al., *STrategically Acquired Gradient Echo (STAGE) imaging, part II: Correcting for RF inhomogeneities in estimating T1 and proton density.* Magn Reson Imaging, 2018. **46**: p. 140-150.

215. Haacke, E.M., et al., *STrategically Acquired Gradient Echo (STAGE) imaging, part III: Technical advances and clinical applications of a rapid multi-contrast multi-parametric brain imaging method.* Magn Reson Imaging, 2020. **65**: p. 15-26.

216. Jiang, J., E.M. Haacke, and M. Dong, *Dependence of vessel area accuracy and precision as a function of MR imaging parameters and boundary detection algorithm.* J Magn Reson Imaging, 2007. **25**(6): p. 1226-34.

217. Nam, Y., et al., *Imaging of nigrosome 1 in substantia nigra at 3T using multiecho susceptibility map-weighted imaging (SMWI).* J Magn Reson Imaging, 2017. **46**(2): p. 528-536.

218. Shinde, S., et al., *Predictive markers for Parkinson's disease using deep neural nets on*

*neuromelanin sensitive MRI.* Neuroimage Clin, 2019. **22**: p. 101748.

219. Reimao, S., et al., *Quantitative Analysis Versus Visual Assessment of Neuromelanin MR Imaging for the Diagnosis of Parkinson's disease.* J Parkinsons Dis, 2015. **5**(3): p. 561-7.

220. Reimao, S., et al., *Substantia nigra neuromelanin magnetic resonance imaging in de novo Parkinson's disease patients.* Eur J Neurol, 2015. **22**(3): p. 540-6.

221. Fearnley, J.M. and A.J. Lees, *Ageing and Parkinson's disease: substantia nigra regional selectivity.* Brain, 1991. **114 ( Pt 5)**: p. 2283-301.

222. Nandhagopal, R., et al., *Longitudinal evolution of compensatory changes in striatal dopamine processing in Parkinson's disease.* Brain, 2011. **134**(Pt 11): p. 3290-8.

223. Schwarz, S.T., et al., *T1-weighted MRI shows stage-dependent substantia nigra signal loss in Parkinson's disease.* Mov Disord, 2011. **26**(9): p. 1633-8.

224. Greffard, S., et al., *Motor score of the Unified Parkinson Disease Rating Scale as a good predictor of Lewy body-associated neuronal loss in the substantia nigra.* Arch Neurol, 2006. **63**(4): p. 584-8.

225. Kordower, J.H., et al., *Disease duration and the integrity of the nigrostriatal system in Parkinson's disease.* Brain, 2013. **136**(Pt 8): p. 2419-31.

226. Ma, S.Y., et al., *Correlation between neuromorphometry in the substantia nigra and clinical features in Parkinson's disease using disector counts.* J Neurol Sci, 1997. **151**(1): p. 83-7.

227. Fabbri, M., et al., *Substantia Nigra Neuromelanin as an Imaging Biomarker of Disease Progression in Parkinson's Disease.* J Parkinsons Dis, 2017. **7**(3): p. 491-501.

228. Du, G., et al., *Distinct progression pattern of susceptibility MRI in the substantia nigra of Parkinson's patients.* Mov Disord, 2018. **33**(9): p. 1423-1431.

229. Harrison, M.B., et al., *UPDRS activity of daily living score as a marker of Parkinson's disease progression.* Mov Disord, 2009. **24**(2): p. 224-30.

230. Schenck, C.H. and M.W. Mahowald, *REM sleep behavior disorder: clinical, developmental, and neuroscience perspectives 16 years after its formal identification in SLEEP.* Sleep, 2002. **25**(2): p. 120-38.

231. Sjostrom, H., et al., *Quantitative susceptibility mapping differentiates between parkinsonian disorders.* Parkinsonism Relat Disord, 2017. **44**: p. 51-57.

232. Li, G., et al., *3D texture analyses within the substantia nigra of Parkinson's disease patients on quantitative susceptibility maps and R2( \*) maps.* Neuroimage, 2019. **188**: p. 465-472.

233. Lee, J.H., et al., *Evaluation of brain iron content in idiopathic REM sleep behavior disorder using quantitative magnetic resonance imaging.* Parkinsonism Relat Disord, 2014. **20**(7): p. 776-8.

234. Li, D.T.H., et al., *Quantitative susceptibility mapping as an indicator of subcortical and limbic iron abnormality in Parkinson's disease with dementia.* Neuroimage Clin, 2018. **20**: p. 365-373.

235. Du, L., et al., *Increased Iron Deposition on Brain Quantitative Susceptibility Mapping Correlates with Decreased Cognitive Function in Alzheimer's Disease.* ACS Chem Neurosci, 2018. **9**(7): p. 1849-1857.

236. Chai, C., et al., *Increased iron deposition of deep cerebral gray matter structures in hemodialysis patients: A longitudinal study using quantitative susceptibility mapping.* J Magn Reson Imaging, 2019. **49**(3): p. 786-799.

237. Yang, Q., et al., *Brain iron deposition in type 2 diabetes mellitus with and without mild cognitive impairment-an in vivo susceptibility mapping study.* Brain Imaging Behav, 2018. **12**(5): p. 1479-

1487.

238.    Sun, J., et al., *Quantitative evaluation of iron content in idiopathic rapid eye movement sleep behavior disorder.* Mov Disord, 2020. **35**(3): p. 478-485.

239.    Ghassaban, K., et al., *Regional High Iron in the Substantia Nigra Differentiates Parkinson's Disease Patients From Healthy Controls.* Front Aging Neurosci, 2019. **11**: p. 106.

240.    Schwarz, S.T., et al., *The 'swallow tail' appearance of the healthy nigrosome - a new accurate test of Parkinson's disease: a case-control and retrospective cross-sectional MRI study at 3T.* PLoS One, 2014. **9**(4): p. e93814.

241.    Uchida, Y., et al., *Voxel-based quantitative susceptibility mapping in Parkinson's disease with mild cognitive impairment.* Mov Disord, 2019. **34**(8): p. 1164-1173.

242.    Zhu, W.Z., et al., *Quantitative MR phase-corrected imaging to investigate increased brain iron deposition of patients with Alzheimer disease.* Radiology, 2009. **253**(2): p. 497-504.

243.    Sun, Y., et al., *Characterizing Brain Iron Deposition in Patients with Subcortical Vascular Mild Cognitive Impairment Using Quantitative Susceptibility Mapping: A Potential Biomarker.* Front Aging Neurosci, 2017. **9**: p. 81.

244.    Sateia, M.J., *International classification of sleep disorders-third edition: highlights and modifications.* Chest, 2014. **146**(5): p. 1387-1394.

245.    Caffarra, P., et al., *Rey-Osterrieth complex figure: normative values in an Italian population sample.* Neurol Sci, 2002. **22**(6): p. 443-7.

246.    Guo, Q., et al., *A comparison study of mild cognitive impairment with 3 memory tests among Chinese individuals.* Alzheimer Dis Assoc Disord, 2009. **23**(3): p. 253-9.

247.    Strauss, E., E.M.S. Sherman, and O. Spreen, *A Compendium of Neuropsychological Tests:*

*Administration, Norms, and Commentary.* 2006, New York: (3rd ed.), Oxford University Press, New York,.

248.   Nutt, J.G., et al., *Determinants of tapping speed in normal control subjects and subjects with Parkinson's disease: differing effects of brief and continued practice.* Mov Disord, 2000. **15**(5): p. 843-9.

249.   Shumway-Cook, A., S. Brauer, and M. Woollacott, *Predicting the probability for falls in community-dwelling older adults using the Timed Up & Go Test.* Phys Ther, 2000. **80**(9): p. 896-903.

250.   Tsigilis, N., H. Douda, and S.P. Tokmakidis, *Test-retest reliability of the Eurofit test battery administered to university students.* Percept Mot Skills, 2002. **95**(3 Pt 2): p. 1295-300.

251.   Chen, Y., et al., *An interleaved sequence for simultaneous magnetic resonance angiography (MRA), susceptibility weighted imaging (SWI) and quantitative susceptibility mapping (QSM).* Magn Reson Imaging, 2018. **47**: p. 1-6.

252.   Lang, F.U., et al., *Subtyping schizophrenia: A comparison of positive/negative and system-specific approaches.* Compr Psychiatry, 2015. **61**: p. 115-21.

253.   Beitz, J.M., *Parkinson's disease: a review.* Front Biosci (Schol Ed), 2014. **6**: p. 65-74.

254.   Opara, J., et al., *Motor assessment in Parkinson`s disease.* Ann Agric Environ Med, 2017. **24**(3): p. 411-415.

255.   Tambasco, N., et al., *T2\*-weighted MRI values correlate with motor and cognitive dysfunction in Parkinson's disease.* Neurobiol Aging, 2019. **80**: p. 91-98.

256.   Uchida, Y., et al., *Magnetic Susceptibility Associates With Dopaminergic Deficits and Cognition in Parkinson's Disease.* Mov Disord, 2020. **35**(8): p. 1396-1405.

257. Rahayel, S., et al., *Abnormal Gray Matter Shape, Thickness, and Volume in the Motor Cortico-Subcortical Loop in Idiopathic Rapid Eye Movement Sleep Behavior Disorder: Association with Clinical and Motor Features.* Cereb Cortex, 2018. **28**(2): p. 658-671.

258. Chen, M., et al., *Structural and functional brain alterations in patients with idiopathic rapid eye movement sleep behavior disorder.* J Neuroradiol, 2020.

259. Lee, S.H., et al., *Regional volume analysis of the Parkinson disease brain in early disease stage: gray matter, white matter, striatum, and thalamus.* AJNR Am J Neuroradiol, 2011. **32**(4): p. 682-7.

260. Brenneis, C., et al., *Voxel-based morphometry detects cortical atrophy in the Parkinson variant of multiple system atrophy.* Mov Disord, 2003. **18**(10): p. 1132-8.

261. Foo, H., et al., *Progression of subcortical atrophy in mild Parkinson's disease and its impact on cognition.* Eur J Neurol, 2017. **24**(2): p. 341-348.

262. He, H., et al., *Progressive brain changes in Parkinson's disease: A meta-analysis of structural magnetic resonance imaging studies.* Brain Res, 2020. **1740**: p. 146847.

263. Erro, R., et al., *Subcortical atrophy and perfusion patterns in Parkinson disease and multiple system atrophy.* Parkinsonism Relat Disord, 2020. **72**: p. 49-55.

264. Ward, R.J., et al., *The role of iron in brain ageing and neurodegenerative disorders.* Lancet Neurol, 2014. **13**(10): p. 1045-60.

265. Owens-Walton, C., et al., *Striatal changes in Parkinson disease: An investigation of morphology, functional connectivity and their relationship to clinical symptoms.* Psychiatry Res Neuroimaging, 2018. **275**: p. 5-13.

266. Deverett, B., et al., *Cerebellar disruption impairs working memory during evidence*

*accumulation.* Nat Commun, 2019. **10**(1): p. 3128.

267. Strick, P.L., R.P. Dum, and J.A. Fiez, *Cerebellum and nonmotor function.* Annu Rev Neurosci, 2009. **32**: p. 413-34.

268. Buckner, R.L., *The cerebellum and cognitive function: 25 years of insight from anatomy and neuroimaging.* Neuron, 2013. **80**(3): p. 807-15.

269. Timmann, D., et al., *The human cerebellum contributes to motor, emotional and cognitive associative learning. A review.* Cortex, 2010. **46**(7): p. 845-57.

270. Nelson, A.B. and A.C. Kreitzer, *Reassessing models of basal ganglia function and dysfunction.* Annu Rev Neurosci, 2014. **37**: p. 117-35.

271. Chung, S.J., et al., *Effect of striatal dopamine depletion on cognition in de novo Parkinson's disease.* Parkinsonism Relat Disord, 2018. **51**: p. 43-48.

272. Looi, J.C. and M. Walterfang, *Striatal morphology as a biomarker in neurodegenerative disease.* Mol Psychiatry, 2013. **18**(4): p. 417-24.

273. Barber, T.R., et al., *Prodromal Parkinsonism and Neurodegenerative Risk Stratification in REM Sleep Behavior Disorder.* Sleep, 2017. **40**(8).

274. Rupprecht, S., et al., *Clinical markers of early nigrostriatal neurodegeneration in idiopathic rapid eye movement sleep behavior disorder.* Sleep Med, 2013. **14**(11): p. 1064-70.

275. Iranzo, A., et al., *Five-year follow-up of substantia nigra echogenicity in idiopathic REM sleep behavior disorder.* Mov Disord, 2014. **29**(14): p. 1774-80.

276. Pyatigorskaya, N., et al., *Magnetic Resonance Imaging Biomarkers to Assess Substantia Nigra Damage in Idiopathic Rapid Eye Movement Sleep Behavior Disorder.* Sleep, 2017. **40**(11).

277. Barber, T.R., et al., *Nigrosome 1 imaging in REM sleep behavior disorder and its association*

*with dopaminergic decline.* Ann Clin Transl Neurol, 2020. **7**(1): p. 26-35.

278. Hegeman, D.J., et al., *The external globus pallidus: progress and perspectives.* Eur J Neurosci, 2016. **43**(10): p. 1239-65.

279. Ramirez-Zamora, A. and J.L. Ostrem, *Globus Pallidus Interna or Subthalamic Nucleus Deep Brain Stimulation for Parkinson Disease: A Review.* JAMA Neurol, 2018. **75**(3): p. 367-372.

280. He, N., et al., *Imaging iron and neuromelanin simultaneously using a single 3D gradient echo magnetization transfer sequence: Combining neuromelanin, iron and the nigrosome-1 sign as complementary imaging biomarkers in early stage Parkinson's disease.* Neuroimage, 2021. **230**: p. 117810.

281. Zhang, X., et al., *Assessing brain iron and volume of subcortical nuclei in idiopathic rapid eye movement sleep behavior disorder.* Sleep, 2021.

282. Aquino, D., et al., *Age-related iron deposition in the basal ganglia: quantitative analysis in healthy subjects.* Radiology, 2009. **252**(1): p. 165-72.

283. Zarow, C., et al., *Neuronal loss is greater in the locus coeruleus than nucleus basalis and substantia nigra in Alzheimer and Parkinson diseases.* Arch Neurol, 2003. **60**(3): p. 337-41.

284. Liu, K.Y., et al., *Magnetic resonance imaging of the human locus coeruleus: A systematic review.* Neurosci Biobehav Rev, 2017. **83**: p. 325-355.

285. Cosottini, M., et al., *MR imaging of the substantia nigra at 7 T enables diagnosis of Parkinson disease.* Radiology, 2014. **271**(3): p. 831-8.

286. Pauli, W.M., A.N. Nili, and J.M. Tyszka, *A high-resolution probabilistic in vivo atlas of human subcortical brain nuclei.* Sci Data, 2018. **5**: p. 180063.

287. Murty, V.P., et al., *Resting state networks distinguish human ventral tegmental area from*

*substantia nigra.* Neuroimage, 2014. **100**: p. 580-9.

288. Zhang, T.Y. and C. Suen, *A fast parallel algorithm for thinning digital patterns.* Communications of the ACM, 1984. **27**(3).

289. Moon, W.J., et al., *A Comparison of Substantia Nigra T1 Hyperintensity in Parkinson's Disease Dementia, Alzheimer's Disease and Age-Matched Controls: Volumetric Analysis of Neuromelanin Imaging.* Korean J Radiol, 2016. **17**(5): p. 633-40.

290. Pakkenberg, B., et al., *The absolute number of nerve cells in substantia nigra in normal subjects and in patients with Parkinson's disease estimated with an unbiased stereological method.* J Neurol Neurosurg Psychiatry, 1991. **54**(1): p. 30-3.

**ABSTRACT**

**ASSESSING MIDBRAIN ABNORMALITIES IN PARKINSON'S DISEASE USING MAGNETIC RESONANCE IMAGING**

by

**KIARASH GHASSABAN**

**August 2021**

**Advisor:** Dr. E. Mark Haacke

**Major:** Biomedical Engineering

**Degree:** Doctor of Philosophy

Diagnosing early-stage Parkinson's disease (PD) and its manifestations is still a clinical challenge. Previous imaging studies using iron, neuromelanin (NM) and the Nigrosome-1 (N1) measures in the substantia nigra (SN) by themselves have been unable to provide sufficiently high diagnostic performance for these methods to be adopted clinically. In this dissertation, we start by studying idiopathic PD patients at their intermediate stages of the disease to evaluate the role of global and regional iron in the major deep gray matter nuclei. Then, we only focus on the NM complex in the midbrain and how neuronal loss interact with iron overload as well as their relationship with clinical scores strictly on early PD patients. Finally, by taking one more step back in the disease progression process, we investigate the impact of iron deposition and N1 appearance in idiopathic rapid eye movement sleep behavior disorder (RBD) as the prodromal stage of PD.

The results of this work are summarized as the following: 1) the increase in iron in the SN in some PD patients is higher than the normal range in healthy controls (HC) as found in both regional and global analyses and that regional high iron content may provide a means to separate two

populations of PD patients; one with and one without iron increases in the SN; 2) we have introduced a rapid five-minute 3D approach to depict NM degeneration and iron deposition simultaneously which provides a practical MR imaging method to differentiate early stage subjects with PD from HCs with an approximately 98% accuracy; and finally 3) iRBD patients were found to have a higher incidence of N1 loss, reduced volume and elevated iron levels in a few brain structures as well as cognitive and motor impairment scores being correlated with iron deposition of several cerebral nuclei. All these in vivo biomarkers put together can significantly contribute to a better understanding of the underlying pathophysiology in PD onset and progression with the ultimate goal being a more confident clinical diagnosis prior to symptomatic dysfunction.

# AUTOBIOGRAPHICAL STATEMENT

| | Education |
|---|---|
| 2019-2021 | **Doctor of Philosophy (Ph.D.)** in Biomedical Engineering<br>Wayne State University, Detroit, MI |
| 2014-2016 | **Master of Science (M.Sc)** in Biomedical Engineering<br>Wayne State University, Detroit, MI |
| 2009-2014 | **Bachelor of Science (B.Sc)** in Electrical Engineering<br>Amirkabir University of Technology (Tehran Polytechnic), Tehran, Iran |
| 2009-2013 | **Bachelor of Science (B.Sc)** in Biomedical Engineering<br>Amirkabir University of Technology (Tehran Polytechnic), Tehran, Iran |
| | **Professional Experience** |
| 2019 – Present | **Research Assistant**<br>Department of Radiology, School of Medicine, Wayne State University, Detroit, MI |
| 2019 – Present | **Product Manager**<br>SpinTech, MRI Inc., Bingham Farms, MI |
| 2016 – 2018 | **Senior Image Analyst**<br>Magnetic Resonance Innovations, Inc., Bingham Farms, MI |
| 2014 – 2016 | **Graduate Research Assistant**<br>Department of Biomedical Engineering, Wayne State University, Detroit, MI |
| | **Peer Reviewed Publications** |

**Journal Papers (\*co-first author)**

Zhang, X., Chai, C., **Ghassaban, K.,\*** Ye, J., et al. (2021). Assessing brain iron and volume of subcortical nuclei in idiopathic rapid eye movement behavior disorder. Sleep. *(Accepted Manuscript)*

He, N., **Ghassaban, K.,\*** Huang, P. et al. (2021). Imaging iron and neuromelanin simultaneously using a single 3D gradient echo magnetization transfer sequence: Combining neuromelanin, iron and the nigrosome-1 sign as complementary imaging biomarkers in early stage Parkinson's disease. Neuroimage 230, 117810.

**Ghassaban, K.**, He, N.\*, Sethi, S.K., et al. (2019). Regional High Iron in the Substantia Nigra Differentiates Parkinson's Disease Patients From Healthy Controls. Front. Aging Neurosci. 11: 106.

**Ghassaban, K.**, Liu, S., Jiang, C., et al. (2019). Quantifying iron content in magnetic resonance imaging. Neuroimage 187, 77-92.

Cheng Z, He N, Huang P, Li Y, Tang R, Sethi SK, **Ghassaban, K.** et al. (2019). Imaging the Nigrosome 1 in the substantia nigra using susceptibility weighted imaging and quantitative susceptibility mapping: An application to Parkinson's disease. Neuroimage Clin. 25, 102103.

Sethi, S.K., Kisch, S.J., **Ghassaban, K.**, Rajput, A., Babyn, et al. (2019). Iron quantification in Parkinson's disease using an age-based threshold on susceptibility maps: The advantage of local versus entire structure iron content measurements. Magn Reson Imaging 55, 145-152.

Chen, B.T., **Ghassaban, K.**, Jin, T., Patel, S.K. et al. (2018). Subcortical brain iron deposition and cognitive performance in older women with breast cancer receiving adjuvant chemotherapy: A pilot MRI study. Magn Reson Imaging 54, 218-224.

Ghouchanian, K., **Ghassaban**, K., Jokar, M. (2017). Optimization of the Capsule Production Stochastic Cycle Time, Research in Economics and Management, Volume 2, Issue 4.

Liu, M., Liu, S., **Ghassaban, K**., Zheng, W., Dicicco et al. (2016). Assessing global and regional iron content in deep gray matter as a function of age using susceptibility mapping. J Magn Reson Imaging 44, 59-71.

**Book Chapters**

Wiseman, N.M., **Ghassaban, K.,** Utriainen, D.T. et al. (2019). "Perfusion and Susceptibility Weighted Imaging in Traumatic Brain Injury," in Neurosensory Disorders in Mild Traumatic Brain Injury, eds. M.E. Hoffer & C.D. Balaban. Academic Press, 303-319.

Buch, S., Chen, Y., **Ghassaban, K.,** and Haacke, E.M. (2018). "T2\*: Susceptibility Weighted Imaging and Quantitative Susceptibility Mapping.," in Quantitative MRI of the Brain; Principles of Physical Measurement, Second edition, eds. M. Cercignani, N.G. Dowell & P.S. Tofts. CRC Press, 97-110.